UCL SCHOOL OF PHARMACY

Layered rare-earth hydroxide nanoparticles for theranostic applications and targeted drug delivery

MARGARITA ŠTRIMAITE

Thesis submitted for the degree of

DOCTOR OF PHILOSOPHY

Department of Pharmaceutics

UCL School of Pharmacy

University College London

March 2023

Declaration

I, Margarita Štrimaite, confirm that the work presented in this thesis is my own. Where information has been derived from other sources, I confirm that this has been indicated in the thesis.

Acknowledgements

I would like to express my deepest gratitude to my supervisors Prof Gareth Williams and Dr Gemma-Louise Davies for all their support, guidance, encouragement, and tuition. I am so grateful for the opportunity to have studied under their leadership, and the skills I have learned as part of their respective research groups have helped me to become a much better-rounded and confident young scientist. I have drawn a lot of inspiration from observing their diligence, ambition, and incredible scientific ability, and I can only hope that one day I will be able to pass on that kind of positive influence to someone else. I thank Gareth especially for all the additional opportunities he has kindly encouraged me to participate in, as well as his many words of support during this incredibly rewarding (but occasionally Sisyphean) undertaking.

I thank all the members (past and present) of the Davies' and Williams' research groups, who have provided me with mentorship, training, assistance, feedback, advice, and friendship throughout my time at UCL. I also thank my fellow CDT cohort members - Charis, Holly, Ines, and Neel – who have been a source of everything from practical lab tips, shoulders to lean on, as well as some unforgettable (and hilarious) memories throughout our time at the UCL and Nottingham schools of pharmacy. Thank you to my friends from the wider SOP and UCL Chemistry community – especially Diba, Corinna, Sara – for all the much-needed, light-hearted chats and great company. Special thanks to John Frost and Ryan Mellor with their practical assistance in designing and building the laser enclosure, to Stephen Boyer and Orla McCulloo (at London Metropolitan University) for conducting elemental analysis, and to Connor Wells (UCL Chemistry) for conducting ICP-OES measurements.

Finally, I would like to thank my life partner and best friend Scrim for his companionship and unwavering belief in me throughout the last decade, and to my lovely mum, Mira, for being my most enthusiastic and tireless supporter since 1994. Люблю и благодарю тебя за все, мама!

Abstract

This thesis centres around the synthesis of a family of structurally related nanoparticulate systems, based on layered rare-earth hydroxides, with a combination of properties that make them suitable for theranostic applications. These materials have the ability to carry drug cargo, provide contrast in magnetic resonance and luminescence imaging, and the possibility to incorporate photosensitizers to facilitate photothermal and photodynamic therapy. The use of these systems in the context of targeted cancer treatment will be explored. The possibility to deliver image-guided therapy directly to tumours is of particular interest in this field, as it has the potential to obviate issues with off target toxicity which very commonly arise with traditional chemotherapies.

Chapter 1 begins with a discussion of current chemotherapeutic treatments and their limitations. The concept of theranostic medicines is introduced, and the modalities of drug delivery, photo-responsive therapies, and imaging contrast are covered. The various material types employed in theranostic research are described, with a particular focus on inorganic materials. Finally, the layered double hydroxides and layered rare-earth hydroxides are discussed, along with a detailed overview of their intercalation chemistry and use in the literature in recent years. The rationale behind focusing on layered rare-earth hydroxides along with the aims of this project are laid out.

Chapter 2 concerns the synthesis and characterisation of layered terbium hydroxide $Tb_2(OH)_5]Cl{\cdot}1.5H_2O$ (LTbH-Cl). Intercalation compounds of LTbH-Cl and several non-steroidal anti-inflammatory drugs (diclofenac, ibuprofen, and naproxen) were prepared and their functional performance in terms of drug release, cytotoxicity, and luminescence was assessed. It was found that LTbH-Cl and its drug intercalates had high biocompatibility, exhibited luminescence properties potentially suitable for imaging applications, and released at least 60% of their drug cargo within 5 hours (in phosphate buffered saline, at 37 °C).

Chapter 3 considers the optimisation of a hydrothermal synthesis route to LTbH-Cl. It details a further series of experiments conducted to explore the relationship between the synthetic parameters and the resulting particle size of LTbH-Cl. An optimised method was thus developed and shown to consistently produce particles with a much narrower size distribution and smaller average size (152 ± 59 nm) than those produced by the method described in Chapter 2 (670 ± 564 nm), which are better suited to exploit the enhanced permeation and retention effect for passive tumour targeting.

In Chapter 4, the optimised synthetic method derived in Chapter 3 was used to produce a range of layered rare-earth hydroxide systems with alternative compositions, including the elements praseodymium, neodymium, gadolinium, erbium, and ytterbium. Based on the subsequent characterisation data of these systems, further LRH materials combining the elements gadolinium and terbium in varying ratios were synthesised in order to exploit their respective magnetic and luminescent properties to create a theranostic platform capable of bi-modal imaging contrast. A lead formulation ($LGd_{1.41}Tb_{0.59}$H-Cl) was selected for further study, based on having the highest relative luminesce intensity as well as relatively strong magnetic relaxivity for magnetic resonance imaging contrast.

Chapter 5 explores the potential photodynamic and photothermal response of the lead LRH formulation and several intercalate systems. First, the selection, design, assembly, and testing of a laser apparatus for this series of experiments is discussed. The lead LRH formulation, $LGd_{1.41}Tb_{0.59}H$, was loaded with the known photothermal/photodynamic sensitiser indocyanine green, and isophthalic acid, which has recently been reported to act as an efficient photodynamic therapy agent when intercalated into a structurally similar LDH system.[1] The resultant materials were characterised, and tested in terms of their performance as photodynamic agents by utilising a colorimetric approach, and as photothermal agents using thermometry. Though the photothermal response measurement of the generated materials was not successful, the LRH-indocyanine green composite showed promising photodynamic activity, with enhanced efficiency relative to free indocyanine green.

Chapter 6 is the concluding section of this report, which summarises the key findings and challenges encountered in the work herein and explores some future avenues for research that should be considered.

Impact statement

This thesis presents a family of structurally related nanoparticulate systems based on layered rare-earth hydroxides, which have the potential to be used in targeted cancer treatment. These systems are suitable for combined therapeutic and diagnostic applications as they can carry drug cargo, provide contrast in medical imaging, and incorporate photosensitizers to facilitate photo-triggered therapy. The use of such multi-faceted systems for cancer therapy could help to obviate issues with off-target toxicity which commonly arise with traditional chemotherapies.

The impact of the research presented herein can firstly be considered in relation to the field of theranostic research in academia. Specifically, this work contributes to the development of theranostic platforms using layered rare-earth hydroxides, advancing knowledge of their intercalation chemistry, and potential use in therapy and imaging applications. The novel findings discussed in this thesis have the potential to influence and guide future work by other academic participants, therefore widening the field and contributing to the current and future body of knowledge.

Secondly, outside academia, this work has the potential to impact clinical use and public health down the line, by contributing to the development towards providing an effective targeted cancer treatment with reduced toxicity as an alternative to conventional chemotherapies. Overall, further research and development of layered rare-earth hydroxide nanoparticulate systems has the potential to significantly improve the quality of life for cancer patients and advance the field of cancer therapy.

UCL Research Paper Declaration Form - 1

referencing the doctoral candidate's own published work(s)

Please use this form to declare if parts of your thesis are already available in another format, e.g. if data, text, or figures:

- *have been uploaded to a preprint server*
- *are in submission to a peer-reviewed publication*
- *have been published in a peer-reviewed publication, e.g. journal, textbook.*

This form should be completed as many times as necessary. For instance, if you have seven thesis chapters, two of which containing material that has already been published, you would complete this form twice.

1. For a research manuscript that has already been published

a) **What is the title of the manuscript?**
Layered terbium hydroxides for simultaneous drug delivery and imaging

b) **Please include a link to or doi for the work**
https://doi.org/10.1039/D1DT01251G

c) **Where was the work published?**
Dalton Transactions

d) **Who published the work?** (e.g. OUP)
Royal Society of Chemistry

e) **When was the work published?**
6th July 2021

f) **List the manuscript's authors in the order they appear on the publication**
Margarita Strimaite, Clarissa L. G. Harman, Huan Duan, Yuwei Wang, Gemma-Louise Davies, Gareth R. Williams

g) **Was the work peer reviewed?**
Yes

h) **Have you retained the copyright?**
No

i) **Was an earlier form of the manuscript uploaded to a preprint server?** (e.g. medRxiv). If 'Yes', please give a link or doi)
no

If 'No', please seek permission from the relevant publisher and check the box next to the below statement:

☒

*I acknowledge permission of the publisher named under **1d** to include in this thesis portions of the publication named as included in **1c**.*

UCL Research Paper Declaration Form - 2

referencing the doctoral candidate's own published work(s)

Please use this form to declare if parts of your thesis are already available in another format, e.g. if data, text, or figures:

- *have been uploaded to a preprint server*
- *are in submission to a peer-reviewed publication*
- *have been published in a peer-reviewed publication, e.g. journal, textbook.*

This form should be completed as many times as necessary. For instance, if you have seven thesis chapters, two of which containing material that has already been published, you would complete this form twice.

2. For a research manuscript that has already been published

j) **What is the title of the manuscript?**
Chapter 2: Inorganic materials in drug delivery

k) **Please include a link to or doi for the work**
https://doi.org/10.1039/9781788019293

l) **Where was the work published?**
Inorganic materials series

m) **Who published the work?** (e.g. OUP)
Royal Society of Chemistry

n) **When was the work published?**
8th December 2021

o) **List the manuscript's authors in the order they appear on the publication**
Fatma Demir Duman, Sophia S. Boyadjieva, Margarita Strimaite, Rachel Foulkes, Gareth R. Williams, Ross S. Forgan

p) **Was the work peer reviewed?**
No

q) **Have you retained the copyright?**
No

r) **Was an earlier form of the manuscript uploaded to a preprint server?** (e.g. medRxiv). If 'Yes', please give a link or doi)
no

If 'No', please seek permission from the relevant publisher and check the box next to the below statement:

☒

*I acknowledge permission of the publisher named under **1d** to include in this thesis portions of the publication named as included in **1c**.*

Table of contents

List of figures

List of tables

List of abbreviations

ANOVA	One-way analysis of variance
API	Active pharmaceutical ingredient
AS3	Arsenazo III
ASA	Aspirin
ATP	Adenosine triphosphate
BSA	Bovine serum albumin
Dic	Diclofenac (anion)
DDS	Drug delivery system
DLS	Dynamic light scattering
DOX	Doxorubicin
DBB	1,2-dibenzoylbenzene
DPBF	1,3-Diphenylisobenzofuran
(D)PBS	(Dulbecco's) phosphate buffered saline
EPR	Enhanced permeability and retention (effect)
EDXS	Energy dispersive x-ray spectroscopy
FTIR	Fourier transform infra-red (spectroscopy)
FWHM	Full width at half maximum
GI	Gastrointestinal
GO	Graphene oxide
HDS	Hydroxy double salt
Ibu	Ibuprofen (anion)
ICG	Indocyanine green
ICP-OES	Inductively coupled plasma optical emission spectroscopy
IMC	Indomethacin
IPA	Isophthalic acid
LDH	Layered double hydroxide
LRH	Layered rare-earth hydroxide
LM	Layered material
LTbH-X	Layered terbium hydroxide (X is an intercalated anion)
LPrH-X	Layered praseodymium hydroxide

LNdH-X	Layered neodymium hydroxide
LGdH-X	Layered gadolinium hydroxide
LDyH-X	Layered dysprosium hydroxide
LYbH-X	Layered ytterbium hydroxide
LErH-X	Layered erbium hydroxide
MMT	Montmorillonite
MOF	Metal organic framework
MPE	Maximum permitted exposure
MRI	Magnetic resonance imaging
MTX	Methotrexate
Na-dic	Sodium diclofenac
Na-ibu	Sodium ibuprofen
Na-nap	Sodium naproxen
Nap	Naproxen (anion)
NIR	Near infra-red
NIRF	Near infra-red fluorescence (imaging)
NMR	Nuclear magnetic resonance
NSAID	Non-steroidal anti-inflammatory drug
PEG	Polyethylene glycol
PDT	Photodynamic therapy
PTT	Photothermal therapy
RBC	Red blood cell
RMM	Relative molecular mass
ROS	Reactive oxygen species
SEM	Scanning electron microscopy
TGA	Thermogravimetric analysis
TMD	Transition metal dichalcogenide
TRF	Time-resolved fluorescence
XRD	X-ray diffraction
5-ALA	5-aminolevulinic acid
5-FU	5-fluorouracil

List of publications

Strimaite, M., Harman, C. L. G., Duan, H., Wang, Y., Davies, G. L., Williams, G. R. Layered terbium hydroxides for simultaneous drug delivery and imaging. *Dalt. Trans.* **50**, 10275-10290 (2021).

Duman, F. D., Boyadjieva, S. S., **Strimaite, M.**, Foulkes, R., Williams, G. R. Forgan, R. S. Inorganic Materials in Drug Delivery. *Biomedical Applications of Inorganic Materials,* 14 - 126 (Royal Society of Chemistry, 2021).

Oral presentation, “Layered rare earth hydroxide nanoparticles for theranostics”, Solid State Chemistry (SSC 2021) conference, virtual

1 Introduction

Theranostics is an emerging field of medicine which combines diagnostic imaging approaches with therapeutic methods. Theranostic platforms can be designed to act as contrast agents in magnetic resonance imaging, luminescence imaging, and positron/photon emission tomography.[2–5] In addition, chemotherapeutic drugs may be included, and it is possible to functionalise the platforms to act as photosensitisers for photothermal or photodynamic therapy (where the photosensitiser either converts light energy to heat, or produces reactive oxygen species *via* energy/electron transfer processes).[1,6] The combination of two or more of these features into a single platform could improve treatment efficacy relative to conventional therapies, and pave the way for personalised cancer treatment.

Sections 1.4 and 1.5 were published as part of a book chapter in 2021,[7] and are reproduced here with permission from the Royal Society of Chemistry.

1.1 Cancer and the need for personalised medicine

1.1.1 Prevalence and progression

Globally, due to a growing population and a variety of environmental and societal factors, cancer poses an increasingly large burden on the healthcare system and economy.[8] In 2018, 18.1 million new cases of cancer and 9.6 million cancer related deaths were reported, and if current trends continue, it is predicted by the Global Cancer Observatory that the number of new cases of cancer will increase by over 60 % by 2040.[9] Accordingly, substantial research interest is directed at continued development and innovation in cancer treatment technology.

There are many different types of cancers which occur in humans, and the prognosis can vary vastly between them. Cancers differ not only by the type of tissue affected,[10] but also by underlying cause(s),[11,12] degree of aggression,[13] responsiveness to treatment,[14] as well as likelihood of recurrence after remission.[15]

Staging and grading systems are commonly used to assess the progression of cancer. There is variation in categories and nomenclature between certain types of cancers, but in all cases, grading/staging aims to describe the extent of growth and spread of the disease. For the purposes of discussing a wide range of cancers on a population level, overall staging is a more useful tool than specific grading. Under the overall staging system,[16] stage 0 or sometimes the 'pre-cancerous' stage is where the cells in question have started to deviate from their normal growth pattern, eventually forming abnormal tissues which are at a higher risk of developing into cancer. Stages I-II describe cancer which is still localised in the area of origin, and stage III describes regionalised cancer which has begun to spread to nearby tissues and/or the lymphatic system. Stage IV, the most advanced stage, refers to cancers which have spread to distant parts of the body.

1.1.2 Conventional therapies

While cancers that are localised may be treated with locally administered therapy (such as by excision surgery, radiotherapy, or proton beam therapy), cancers which have begun to spread may require systemically administered treatments. The most established treatment for such cancers currently is traditional chemotherapy, which uses cytotoxic agents such as doxorubicin and methotrexate, delivered intravenously to target rapidly dividing cells within the body.[17] Often, these agents are used in combination to increase the efficacy of

the treatment. However, such ‘one-size-fits-all’ intravenously administered cytotoxic agents do not discriminate between healthy and diseased cells, and thus have a long list of adverse side-effects. For instance, chemotherapeutic drugs often negatively affect non-cancerous rapidly dividing cells, leading to negative effects in tissues within the bone marrow or central nervous system, or the characteristic hair loss seen in patients undergoing chemotherapy.[17] Targeted anticancer therapies, which can target proteins and genes associated with cancer, exhibit a reduced degree of off-target toxicity, but may still result in symptoms such as gastroenteritis, impaired liver function, and dermatitis[18] which are associated directly with their mechanism of action.

Such side effects have a great impact on both mental and physical patient wellbeing, and in some cases may prevent patients from undergoing treatment altogether due to avoidance or counterindications.[19,20] Therefore, it is important to develop novel treatments which seek to minimise side effects and increase treatment efficacy. Such an approach could help to improve the current gold-standard chemotherapeutic treatments by facilitating a more individualised, effective treatment, with fewer off-target effects, therefore leading to improved patient outcomes.

1.2 Theranostic approaches to the treatment of cancer

Theranostic platforms aim to combine multiple modalities of treatment and imaging contrast capability to enable synergistic treatment at the desired site of action. Therefore, theranostic technology aims to address the need to reduce off-target toxicity effects and increase treatment efficacy. This section will introduce the most utilised treatment and image contrast modalities seen in theranostic systems in the literature, including drug delivery, photothermal/photodynamic therapy, luminescence, and magnetic resonance imaging.

1.2.1 Drug delivery

Theranostic systems may be utilised to carry and deliver active pharmaceutical ingredients (APIs). The use of such a drug delivery system (DDS) may offer several advantages over pure drug administration.

Firstly, the use of a carrier enables the targeted delivery of API by exploiting either passive or active targeting, which are covered in more detail in Section 1.5.2. In this way, the use of a DDS can be an effective strategy to prevent off-target toxicity. Secondly, encapsulation of API within a DDS may enhance the bioavailability of poorly soluble APIs, by minimising the interaction between individual API molecules and enabling more efficient release into solution as compared with the pure API counterpart.[21,22] Additionally, the use of a DDS system may further enhance bioavailability and stability of the API by shielding it from the surrounding physiological environment and therefore preventing premature degradation.[23,24]

Depending on the nature of the carrier employed and any additional functionalisation, the release profile from a DDS can vary widely. For instance,

release can range from a burst over the course of a few minutes/hours up to extended release over several months. Release is sensitive to both the chemical and physical nature of the DDS, as those properties impact the affinity of the API molecule for the carrier matrix and the diffusion path it must take to exit into solution. Additionally, release profiles can be further modulated by use of coating strategies to slow release or enable release in response to some external trigger (such as changes in pH, the application of electromagnetic radiation, or the presence of bacterial enzymes).

For instance, a gold nanoparticle-based and aptamer/DNA-functionalised DDS has been reported which is capable of rapidly releasing over 80 % of its cytotoxic payload in under 20 minutes.[25] The DDS employs an antibody mimic to target cancer cells, and a dense, cross-linked DNA coating which rapidly breaks down in the presence of adenosine triphosphate (ATP) to release the cytotoxic doxorubicin.[25] This type of fast release is desirable in this scenario because the goal is to rapidly eliminate cancer cells before they proliferate and spread. In other cases, longer release times may be preferrable – for instance in the treatment of glaucoma, which often requires the application of daily eye drops to lower intraocular pressure. An example of such sustained release from a liposomal nanocarrier formulation was reported recently, where the release of latanoprost reached only 60 % after 20 days.[26]

1.2.2 Photothermal therapy

Photothermal therapy is a treatment which utilises the ability of some species, known as photosensitizers, to convert light (usually in the near-infrared or ‘NIR’ region) into heat. In the context of cancer treatment, the photosensitizer is first allowed to accumulate in the tumour tissue. The application of NIR light to the

tumour then excites the photosensitizer, which releases energy as heat upon relaxation to the ground state. This causes localised hyperthermia, ablating the cancer cells and thus eliminating the tumour. The photothermal response and the considerations regarding the choice of light wavelength will be discussed in more detail in Chapter 5.

Most commonly, gold-based nanoparticles are used to efficiently convert visible or NIR light to heat by exploiting their inherently strong surface plasmon resonance response. Gold nanoparticles are thus exceptionally good at absorbing electromagnetic radiation, and the absorption wavelength is highly tuneable by varying their shape and size.[27] These properties, combined with the inert and biocompatible nature of gold, make gold extremely attractive in the production of photothermal agents.

For example, a theranostic system has been reported[4] which consists of a lanthanide-doped core within a superparamagnetic iron oxide shell, and an outer layer of gold. The lanthanide-doped core acts as a luminescent imaging agent, the iron oxide shell acts as a magnetic resonance imaging contrast, whilst the outer layer of gold is used to provide photothermal functionality. It was demonstrated that these multi-functional nanoparticles could be directed into the tumour via magnetic field targeting, and subsequent irradiation with a NIR laser led to a localised temperature increase of over 40 °C and complete tumour elimination in mice (Figure 1.1a).[4]

Other materials which exhibit efficient photothermal conversion and have been investigated for theranostic applications include polymers such as polydopamine,[28] and a variety of two-dimensional materials including transition metal carbides/nitrides and dichalcogenides.[29,30] It is also possible to elicit a

photothermal response by functionalising theranostics with light-absorbing dyes, such as indocyanine green (a NIR absorbing dye, used widely in the clinic for imaging applications)[31] or methylene blue (a visible light absorbing dye).[32]

1.2.3 Photodynamic therapy

Unlike photothermal therapy, photodynamic therapy uses a photosensitiser to generate reactive oxygen species rather than heat. As the photosensitizer relaxes to the ground state, the energy released leads to the production of reactive oxygen species (ROS) such as free radicals and singlet oxygen. The ROS generation process is discussed in more depth in Chapter 5. These ROS are able to cause cell death directly, but can also disrupt the vasculature which supplies the tumour and elicit a localised immune response.[33] PDT is already used widely for cancer treatment, and there are a variety of commercially available photosensitisers, including porphyrin derivatives and chlorophyll mimics.[34]

Several very promising theranostic systems able to perform photodynamic therapy have been reported. For instance, a nanoparticle system was assembled from an amino acid (Fmoc-L-L) with Mn^{2+} and Chlorin e6 as magnetic resonance imaging contrast and photosensitiser respectively.[35] This system, abbreviated as FMCNP, and an analogue which does not contain Mn^{2+} (FLCNP), were both shown to result in efficient photodynamic therapy, leading to significant tumour size decrease, and in some cases complete tumour elimination in mice (Figure 1.1b)[35] following irradiation with NIR light.

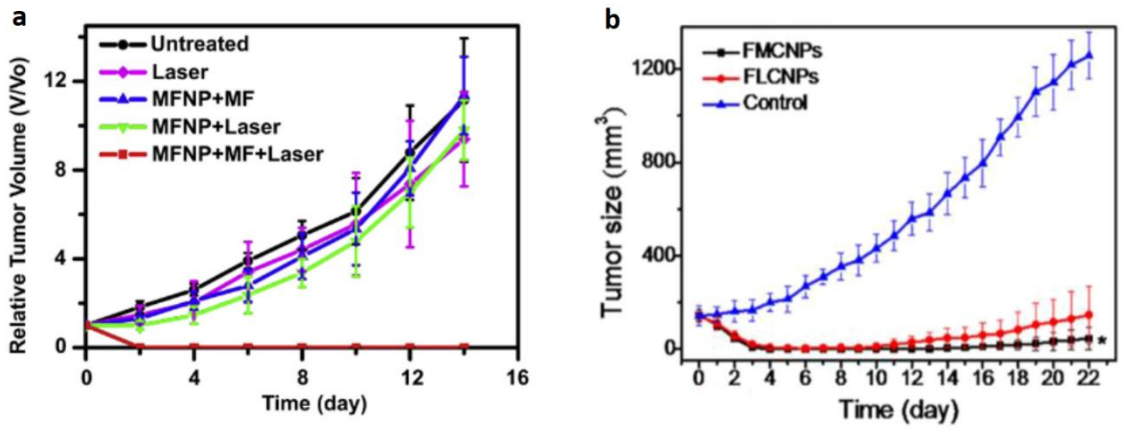

Figure 1.1 a.) Diagram (Reprinted from reference 4 with permission from Elsevier) showing tumour volume in mice under different combinations of photothermal treatment conditions, with or without injection with multifunctional nanoparticles (MFNPs), irradiation with a NIR laser, exposure to a magnetic field (MF) for tumour targeting; and the untreated control. b.) Diagram (reprinted with permission from reference 35. Copyright 2018, American Chemical Society) showing mass of excised mice tumours following photodynamic treatment with Fmoc-L-L/Chlorin e6/Mn^{2+} nanoparticles (FMCNPs) or Fmoc-L-L/Chlorin e6 nanoparticles (FLCNPs) coupled with NIR light irradiation, as compared to the control group (NIR light irradiation only).

1.2.4 Luminescence imaging

One property which can be exploited for medical imaging is photoluminescence. Photoluminescence occurs when a sample absorbs light, producing excited electrons which relax back to the ground state and emit photons. Typically, the emitted photons are of a lower wavelength than those of the excitation light, but some systems exist which are capable of absorbing two photons to re-emit a single photon of a higher wavelength.[36] This process is known as upconversion luminescence. The excitation/emission process can occur millions of times per second per atom, which makes photoluminescence imaging very sensitive. The types of photoluminescence and competing relaxation pathways are covered in more detail in Chapter 4.

Of particular interest for medical applications are fluorophores which can be excited by NIR light for near-infrared fluorescence imaging (NIRF). This is because NIR light is energetic enough to penetrate human tissue, but not so energetic that it elicits an auto-fluorescence response in tissues. This

dramatically lessens the fluorescence background in images and hence provides better contrast. There are many fluorophores which are able to absorb NIR light such as indocyanine green[37] and porphyrin derivatives.[38] There have also been many nanoparticle systems reported which contain[39] or are conjugated to[40,41] NIR fluorophores, and are therefore able to be used in diagnostic fluorescence imaging.

1.2.5 Magnetic resonance imaging

Magnetic resonance imaging (MRI) is one of the most common medical imaging methods and is based on the nuclear magnetic resonance (NMR) phenomenon. It can be used, for example, to diagnose cancers by imaging tissues,[42] to monitor brain activity by exploiting the different properties of oxygenated vs deoxygenated blood,[43] and even to observe physiological processes such as joint movement in real-time.[44] The application of an external magnetic field and a radiofrequency pulse causes nuclei in a sample to absorb and re-emit radiofrequency waves through a process called relaxation. The nature and mechanisms of relaxation in MRI and how they are used to construct images will be discussed in more detail in Chapter 4.

Due to their vast abundance in the body and high NMR sensitivity, ^{1}H atoms (protons) are often targeted for magnetic medical imaging applications. Nuclei will have different rates of nuclear relaxation (and therefore produce a higher or lower contrast) depending on their environment, which is why different tissues in the body can be distinguished in an MR image. In molecules of fat, for example, each proton benefits from magnetic shielding by neighbouring electron clouds. In contrast, protons in water molecules are de-shielded due to the electronegative oxygen atom, and so they are more affected by an external magnetic field.[45]

‘Positive’ contrast agents such as those containing Mn^{2+} and Gd^{3+} ions lead to enhanced brightness in the image; many theranostic systems containing Mn^{2+}/Gd^{3+} ions for MR contrast ability have been reported.[35,46] Currently, only Gd^{3+} based positive contrast agents are commercially available; however, the toxicity of free Gd^{3+} ions necessitates the use of chelating ligands, and ongoing concerns about accumulation in the body have encouraged the search for other effective and safe positive MRI contrasts.[47] Conversely, contrast agents which lead to decreased brightness in the image, such as barium sulphate or superparamagnetic iron oxide, are known as ‘negative’. While their use has been mostly phased out in clinical MRI, there exist reports of theranostic systems for negative MR contrast applications.[48,49]

1.2.6 Other modalities

There are several other imaging and therapeutic modalities which appear somewhat less commonly in the theranostic literature.

Positron emission tomography and single-photon emission computed tomography both employ radioactive tracers to produce images of the body by collecting the emitted gamma radiation. Theranostic systems may contain or be functionalised with such radioactive tracers to allow imaging functionality.[50–52] Radiation may also be used in a therapeutic capacity, and can be applied externally (for instance X-ray or proton beams) or internally (by using radiogenic species administered to the body). Theranostic systems can be used to directly produce internally applied radiation by inclusion of radioactive species,[53] or to enhance the effect of externally applied radiation by inclusion of a radiosensitiser.[54]

In addition to PDT, other methods of locally generating ROS species also exist that have been incorporated into theranostic systems. Sonodynamic therapy relies on the external application of ultrasound (rather than light, as in PDT) to activate the ROS generation process.[55] Conversely, in chemodynamic therapy, ROS generation occurs by means of chemical reaction – namely, the conversion of hydrogen peroxide (which is naturally elevated in some tumour tissues) to ROS.[56] The advantage of chemodynamic therapy over other ROS producing processes in this context is that it requires no externally applied trigger; however, it is limited in therapeutic effect due to rapid consumption of endogenous hydrogen peroxide, as well as inefficient reaction under physiological pH.[57]

Lastly, a variety of theranostic systems have been designed which can deliver genes,[58] functional nucleic acids,[59] proteins,[60] and antibodies.[61] These types of active ingredients have a broad range of biological applications, for instance to alter gene expression[62] or selectively target specific cancer proteins.[63]

1.3 Material types in theranostics

The vast majority of materials utilised in research for theranostic applications are nano- or micro-scale materials, which are suitable for administration by a variety of delivery routes (for instance as powders for inhalable delivery or particulate suspensions for injectable formulations).[64,65] There are also instances of macro-scale theranostic implant systems containing nanomaterials such as nanowires[66,67] or nanosheets,[68] though these are less commonly explored. A broad range of materials have been studied for theranostic applications to date, which can be categorised based on their composition (organic, inorganic, composite) or their dimensionality on the nanostructural scale (0D, 1D, 2D, or 3D materials).

1.3.1 Material dimensionality

Particles which do not extend more than 100 nm in any dimension are referred to as ‘0D’, for instance quantum dots or spherical nanoparticles with diameter less than 100 nm. Materials such as nanotubes or nanowires which extend over 100 nm in only one dimension are referred to as ‘1D’. Materials which extend over 100 nm in two dimensions (thus forming planes) and are referred to as ‘2D’. Such materials include graphene and layered double hydroxide nanosheets. The final class of materials are termed ‘3D’, and exhibit extension over 100 nm in every dimension – for instance particles of materials such as metal organic frameworks (MOFs) or giant covalent structures.

Dimensionality labels are used as a helpful shorthand rather than a strict classification system. For example, a sample of material which contains spherical nanoparticles of a wide size distribution (e.g. diameters of 50 – 200 nm) is

technically both 0D and 3D. A distinction is often made between single/few layers of layered materials (2D) and their bulk stacked structures (3D). While covalent bonding in 3D stacks of 2D materials is discontinuous in one dimension (i.e. perpendicular to the layer stacking direction), when the stacked assembly forms particles > 100 nm in all dimensions, it is most often considered to fall into the 3D category.

Recently, 2D materials and their bulk 3D structures have been receiving increasing amounts of attention in the theranostic literature owing in large part to their high available surface area for adsorption or chemical processes. In addition, layered materials can accommodate a wide range of guest species sizes, making them a versatile option as a theranostic platform. The advantages and properties of layered systems compared to other types of materials are explored in detail in Section 1.4.

The implications of overall particle size (and shape) on theranostic applications of materials will be dealt with in more detail in Chapter 3. Broadly, the particle size must be a compromise between acceptable properties in terms of biological fate (cell uptake behaviour, tissue/vasculature permeation, propensity for macrophagic elimination, etc.) and functional performance (surface area available for functionalisation, drug loading capacity, drug release kinetics, etc.).

1.3.2 Material composition

Material composition is arguably the most important consideration when designing theranostic systems. Firstly, composition influences the resultant functional properties of a material. Many inorganic materials possess inherent luminescence or magnetic properties. This allows novel systems to act as contrast agents simply by inclusion of such inorganic materials. On the other

hand, organic fluorophores, whilst many in number, are often complicated in structure, and frequently suffer from photobleaching.[69] Furthermore, the performance of inorganic materials can often be easily modified by changing their physical form or elemental composition (for instance by changing particle size[70] or by doping[71]).

Secondly, composition impacts the biocompatibility and biostability of materials. This extends not just to the theranostic platform itself, but to any possible metabolites and degradation products. For example, some free metal ions are known to exhibit toxicity by interfering with natural signalling pathways (for instance, free Gd^{3+} ions which can block Ca^{2+} ion channels).[72] Organic-based systems may be more susceptible to breakdown by the body's natural metabolic pathways, whereas many inorganic materials are less chemically reactive in the physiological environment.[73]

For these reasons, layered materials with an inorganic composition are of particular interest as potential theranostic matrices.

1.4 Inorganic layered materials for biomedical applications

1.4.1 Introduction

Inorganic materials which possess a layered internal structure are particularly attractive as candidates for drug delivery platforms. The structure of such layered materials (LMs) is based on two-dimensional sheets of material which are stacked into a three-dimensional array, and held together by ionic or van der Waals forces.[74] If the layers bear an overall charge, the interlayer space contains guest counterions which interact electrostatically with the charged layers. Materials with negatively charged layers include cationic guest species, whereas

those with positively charged layers are balanced by anionic species. If the counterions are not bound permanently to the layers, the material is termed ion-exchangeable, and the process of reversible guest uptake is called intercalation. This ability to reversibly intercalate ionic drugs allows such LMs to act as drug carriers (Figure 1.2).

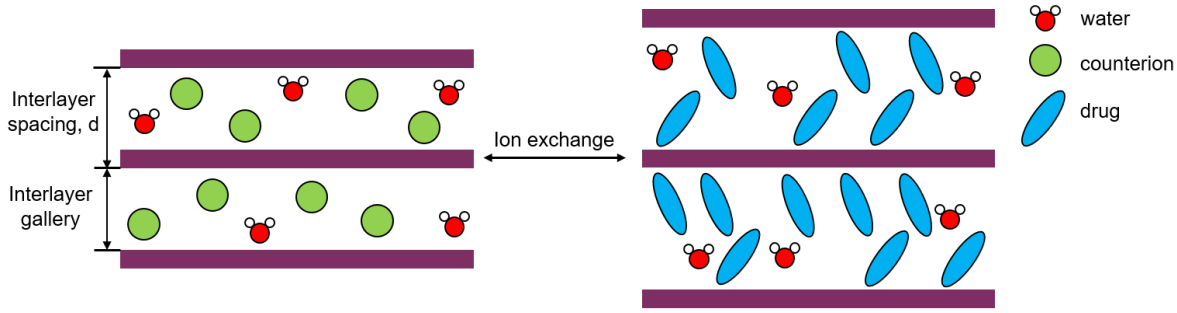

Figure 1.2 Schematic diagram illustrating the intercalation of drug molecules into a layered material by ion exchange, causing the interlayer separation to increase.

There exist many layered systems which comprise negatively charged layers and are therefore cation-exchangeable, for example cationic clays,[75–77] MXenes,[78] metal phosphates,[79,80] and metal chalcogenides.[29,81] Layered systems which are able to undergo anion exchange are fewer in number, and consist almost exclusively of layered metal hydroxides – a class of materials which includes layered double hydroxides (LDHs),[82–86] layered rare-earth hydroxides (LRHs),[87,88] and the hydroxy double salts (HDSs).[89,90] Of the aforementioned layered systems, LDHs are by far the most widely studied for drug delivery applications.

LMs can be designed to release their drug cargo in response to external stimuli, act as imaging contrast agents, and provide additional therapeutic functionalities such as light-triggered hyperthermia. Overall, there is ample scope for developing novel drug delivery platforms based on LMs, which benefit in particular from their diverse intercalation chemistry. This section will explore the applications of LMs

in drug delivery, their advantages over other types of systems, and cover notable examples of drug delivery platforms based on LMs in the literature.

1.4.2 Properties of layered materials

A useful property shared by all LMs is their high available surface area for adsorption relative to their volume as compared to conventional solid materials, which includes both the particle surface as well as the interlayer surface areas (Figure 1.3). In turn, this can be exploited to generate intercalates with very high drug loadings, thereby maximising formulation potency and reducing the minimum effective dose. However, with increasing LM particle size, adsorption towards the middle of the particles is diffusion rate limited, leading to lower than theoretical drug loadings. Therefore, delamination of LMs into nanosheets can be used to increase the effective surface area available for adsorption, leading to enhanced capacity relative to the bulk LM.[91]

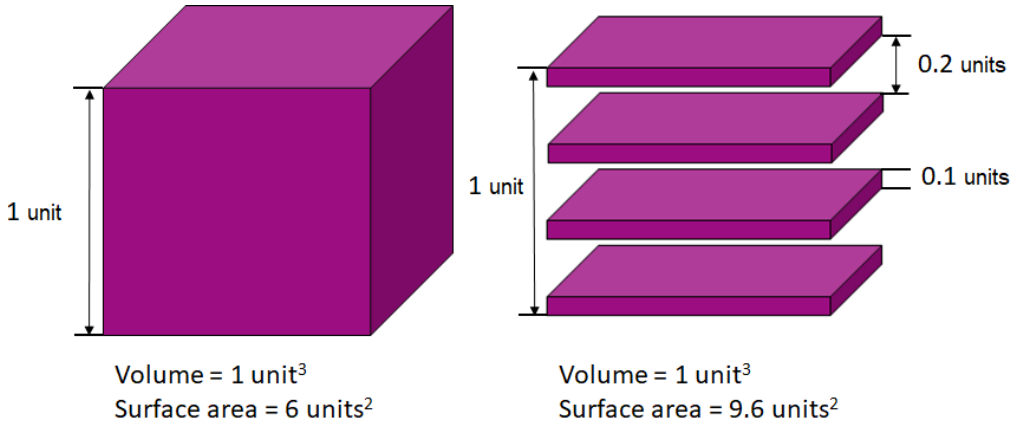

Figure 1.3 Schematic diagram illustrating the surface area available for guest adsorption in a unit cube crystal of solid material (left) as opposed to a layered material (right), assuming a layer thickness and interlayer gallery height of 0.1 and 0.2 units respectively.

Perhaps the most advantageous feature of LMs for drug delivery applications is their extensive intercalation chemistry. Inorganic materials which contain pores or channels (such as metal organic frameworks, zeolites, or silica) are rigid and only capable of accepting guest species of a narrow range of sizes. Therefore,

different materials would be required to deliver small molecule actives as opposed to proteins, for instance. Conversely, some LMs are capable or expanding/contracting their interlayer separation depending on the intercalated species. This makes it possible to use the same LM to load a broader range of guest species.

LMs give rise to a variety of particle shapes and sizes, and in some cases these can be controlled by adjusting the synthetic method. For instance it was demonstrated in one study that Mg/Al LDH particles produced using a hydrothermal route exhibited smooth spheroid particle shapes and a more uniform size distribution (85-340 nm) than those produced by co-precipitation, which were roughly hexagonal in shape with serrated edges and a much wider particle size distribution (860-4470 nm).[92] In addition, it is possible to synthesise LM particles which have a range of average particle sizes – from only several nanometres[93] up to micrometre size and beyond.[94,95] These features are very important in the context of drug delivery, because particle size and shape greatly influence the in-vivo behaviour of the formulation. Importantly, overall particle size affects how rapidly particles are removed by the immune system (and other biological mechanisms) and how well they penetrate different types of tissue. Particle shape, on the other hand, influences cellular uptake behaviour, and has even been shown to allow preferential targeting of sub-cellular features.[96]

1.4.3 Types of layered materials

1.4.3.1 Anion-exchangeable materials

The vast majority of anion-exchangeable LMs belong to the layered metal hydroxides group, which are sometimes referred to as the anionic clays. Of these, by far the most widely studied are the layered double hydroxides (LDHs). Their

brucite-type structure is based on two dimensional sheets of edge sharing octahedra (Figure 1.4A), composed of mixed metal ions (divalent and trivalent) coordinated to six hydroxide ions.[97] The sheets have a net positive charge[97] which causes them to electrostatically interact with anions and trap them between the sheets, forming a three dimensional assembly.[98] The basal spacing between the layers is able to adjust depending on the size of the guest anion[99] which allows a variety of species to be intercalated.

Another subset of the layered metal hydroxides which have been explored in drug delivery applications are the hydroxy double salts (HDS). Unlike LDHs, HDSs contain only divalent metal centres, octahedrally and tetrahedrally coordinated to hydroxide groups (Figure 1.4B). More recently, attention has turned towards the layered rare-earth hydroxides (LRHs), as they can exhibit magnetic and fluorescent properties useful for medical imaging arising from the rare-earth metal ions they contain.[100,101] It is possible to create LDH and HDS based materials which also exhibit these properties, for instance by incorporation of magnetic Fe^{3+} ions, however this often requires further functionalisation therefore complicating the synthetic procedure.[102,103] Structurally, LRHs are similar to LDHs/HDSs, but the sheets constitute trivalent rare-earth metal ions in two high coordination environments, with eight and nine vertices,[104] which arrange in an edge-sharing fashion (Figure 1.4C). Each metal centre is coordinated to one water molecule and either seven or eight hydroxide groups.

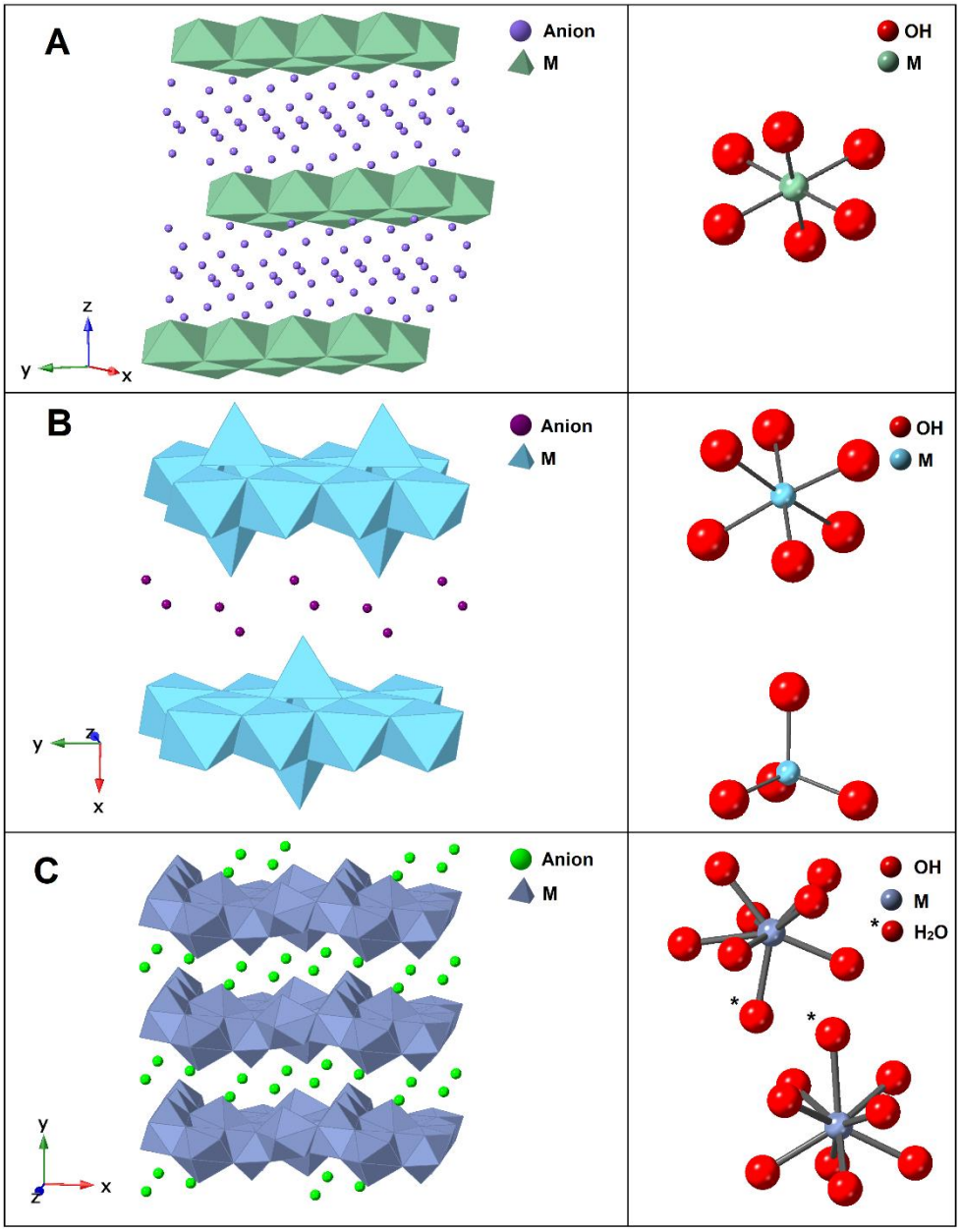

Figure 1.4 Polyhedral models of anionic clay materials A.) LDH, B.) HDS, and C.) LRH. Inset: coordination environments of metals within LDH/HDS/LRH materials.

1.4.3.2 Cation exchangeable materials

Cation exchangeable LMs span a much larger range of compositions than anion exchangeable LMs. The largest class of materials that fall into this category are the hydrated aluminium silicates, frequently referred to as cationic clays. Of particular interest in drug delivery applications are materials with a smectite-type structure, in which the interlayer distance is able to expand and contract depending on guest species. In the smectite structure, each solid layer is actually

composed of a layer of edge-sharing $Al_2(OH)_6$ octahedra, sandwiched between two layers of vertex-sharing SiO_2 tetrahedra (Figure 1.5). Both Al and Si can be substituted to alter the composition of the clay.

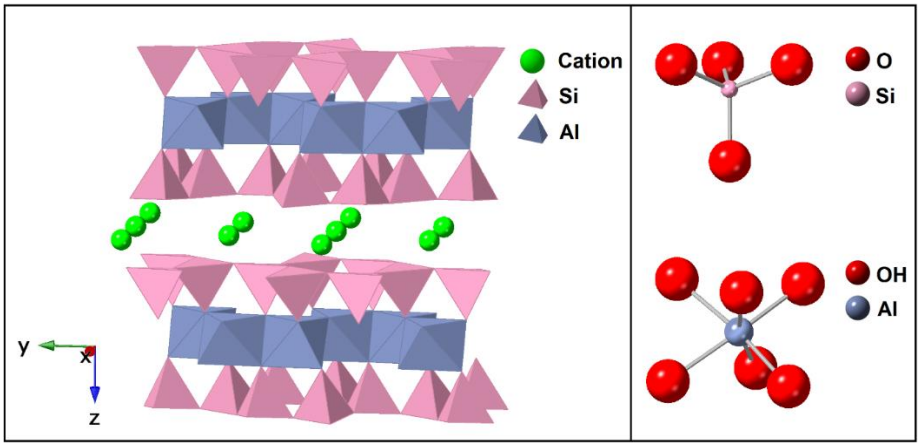

Figure 1.5 Polyhedral model of a smectite-type cationic clay. Inset: coordination environments of Si and Al within the cationic clay structure.

While a significant body of work exists around graphene (monolayers of graphite) and its related graphene oxide form within the biomedical field,[105,106] these materials and their bulk crystal counterparts do not exhibit ion exchange capacity. A relatively newly discovered type of LM similar in structure to graphene are the so-called MXenes, which are carbides or nitrides of transition metals derived from a parent MAX phase (where M is a transition metal, A is a group 13 or 14 element, and X is either C or N).[107] Unlike graphene, multi-layered MXenes have been shown to be capable of ion exchange[108], as well as adsorption (and subsequent release) of cationic drug on nanosheets of MXene.[109] Other types of LMs capable of cation exchange include some metal titanates, metal phosphates, and metal oxides, though they have been seldom mentioned in the literature in regard to their potential as drug delivery platforms.

Another notable type of LMs are the transition metal dichalcogenides (TMDs), where a transition metal centre is coordinated to a chalcogen (usually S or Se). TMDs most frequently exist in either a structure analogous to LDHs, with metal

centres in an octahedral coordination,[110] or in a trigonal prismatic configuration.[111] Their potential in theranostic applications has begun to attract attention, particularly owing to their favourable photothermal (light to heat) conversion properties.[112–114] In their unaltered form, the layers within TMDs are not charged, and thus do not exhibit ion exchange properties. However, a recent report into the application of TMDs for semiconductor purposes has shown that intercalation of hexylammonium cations into TMDs is possible under electrochemical conditions.[115] Briefly, the application of an electrical potential to a TiS_2 cathode caused the reduction of Ti^{4+} to Ti^{3+}, thereby giving the individual layers a negative charge.[115] Hexylammonium ions, dissolved in the electrolyte, were then intercalated into the TMD as a result of electrostatic interactions. It may therefore be feasible to drive ion-exchange in TMDs for drug delivery applications, using a similar reductive process.

1.4.4 General synthesis

LMs can be prepared by a variety of synthetic methods – most commonly by co-precipitation, hydrothermal, solvothermal, sonochemical, and sol-gel approaches. The co-precipitation method involves the mixing of two solutions, which react to form one precipitate. In the case of LDH materials, for example, a solution containing the metal cations is added to a basic solution of the anion to be intercalated.[116] Hydrothermal synthesis, as the name implies, is carried out in aqueous solution or suspension, and occurs during heating in a sealed reaction vessel. It is often used in combination with co-precipitation to improve the crystallinity of products obtained. The vapour pressure inside the reaction vessel can be controlled by selecting the appropriate temperature. This approach is

versatile, commonly employed to produce LDHs and LRHs,[117–123] and has also been used to produce layered chalcogenides, and metal oxides.[124,125]

Solvothermal synthesis is an analogous method employing solvents other than water, and can also be used to produce both cation and anion exchangeable LMs.[126–130] The main advantage of using hydro/solvothermal methods is that the reaction occurs at elevated temperatures and pressures, allowing the efficient synthesis of materials which may otherwise not form.[131] Less common methods to produce LMs include sonochemical[132–135] and mechanochemical synthesis.[136–140]

The production of nanosheet materials can be broadly classified into two strategies. ‘Top down’ approaches involve the delamination (also known as ‘exfoliation’) of layers from bulk LM particles. Most commonly this is achieved either via mechanical means,[141,142] or by chemical exfoliation.[143–146] Conversely, ‘bottom up’ methods aim to produce nanosheets in one step, for instance by chemical/physical vapour deposition,[147,148] or direct synthesis.[149–152]

Intercalation of the desired counterion can be achieved either during the initial LM synthesis (direct intercalation),[153–155] or after the formation of the LM (by ion exchange, reconstruction, or exfoliation-reassembly). During direct intercalation, a solution of metal salts is mixed with a solution of the desired species to be intercalated into the LM. This approach is advantageous because the final product is obtained in a single step but is not always possible as it requires that the desired species has a stronger electrostatic interaction with the layers of the LM than do the other species present in the reaction mixture. For instance, successful direct intercalation of amino acids into a Zn/Al LDH was shown to be

largely dependent on the overall charge and hydrophobic character of the amino acid.[154]

Post-synthetic intercalation methods can often be more practical to use. Most commonly, this is achieved by ion exchange, which is the diffusion of drug ions from a solution into the interlayer space to replace the initial guest ions.[87,156] Typically, particles of LM are submerged in a solution with the desired guest in molar excess, and ion exchange is allowed to proceed over the course of several hours, usually with heating. Another approach is to use reconstruction,[155,157] whereby the LM first undergoes calcination to remove any intercalated species. In the case of LDHs, this process causes the dehydroxylation and collapse of the layered structure, which is recovered upon submerging this calcined product in a solution of the desired guest. Similarly, the exfoliation-reassembly method can be used,[158–162] whereby the LM is delaminated and allowed to reassemble in a solution of the guest species. Co-precipitation and reconstruction methods also allow for intercalation of species which are not ionic, which is not possible to achieve using ion exchange. The exfoliation-reassembly approach is favoured where the guest species' size is prohibitive to efficient diffusion into the LM interlayer gallery.

1.4.5 Cytotoxicity

LDHs are well known to be highly biocompatible. Many in-vitro studies have reported very low cytotoxicity of LDH formulations in a wide range of human and murine cell lines, including healthy, cancerous, and stem cells.[163–169] Figure 1.6a shows the results from one such study, in which four different human cell lines were exposed to Mg/Al LDH for 72 hours, and in all treatment groups no significant cytotoxicity was observed.[163] In a study on rats, tablets made of

compressed Mg/Al and Zn/Al LDH powders were implanted into the abdominal muscles and assessed after 7 and 28 days.[170] At both time points, no signs of inflammation or microvasculature disruption were present (Figure 1.6b), irrespective of LDH composition.[170] Additionally, the nature of tissue repair around the implanted tablets was consistent with the type observed around highly biocompatible implants. Another study, in which Mg/Al LDH was used as a coating for middle-ear prostheses in rabbits,[171] also found no signs of inflammation 10 days following implantation. A clinical study on humans was performed on fluoride loaded LDH films for dental applications,[172] and found no evidence of irritation after several hours of exposure.

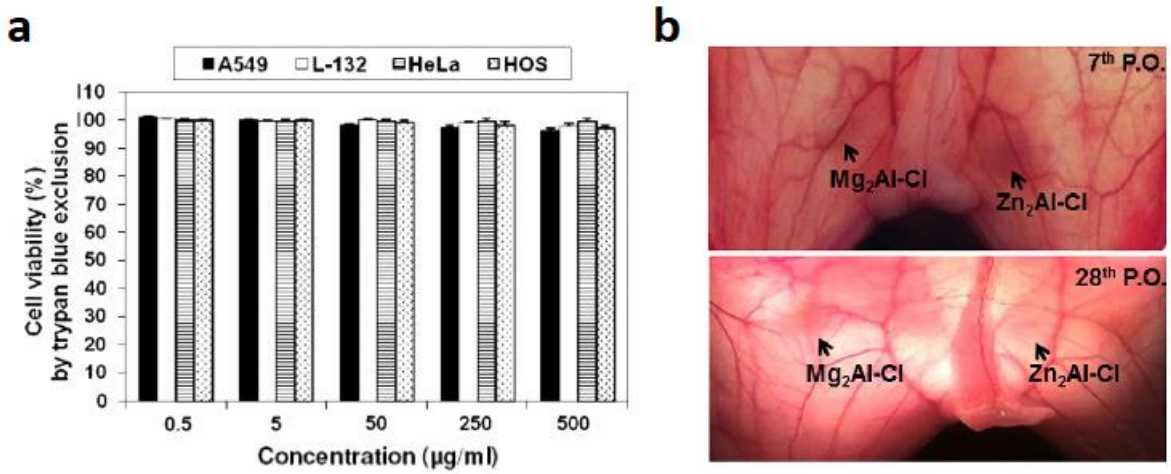

Figure 1.6 a.) Diagram (Reprinted from reference 163, with permission from Elsevier) showing the cell viability of four different human cell lines (normal lung (L-132) cells, lung cancer (A549) cells, cervical cancer (HeLa) cells, and osteosarcoma (HOS) cells) following 72 h exposure to Mg/Al LDH at various concentrations; b.) Photographs (reprinted from reference 98, with permission from Springer Nature) showing the implantation sites of LDH tablets within the abdominal muscles of rats, at 7 days (top) and 28 days (bottom) post operation.

On the other hand, there also exist multiple reports concerning the adjuvanticity of LDHs. Briefly, adjuvants are substances which enhance the immunological response of an organism when exposed to an antigen,[173] and are widely used in vaccine formulations for this purpose. There are many studies discussing the adjuvant activity of MgAl LDHs,[173–178] indicating that LDHs have the capacity to interact with the immune system - an important consideration when evaluating

the cytotoxicity of such systems. It has also been demonstrated that the chemical composition and physical properties of LDHs have an influence on adjuvanticity,[179,180] providing a pathway to modulate this response as desired for applications in drug delivery.

Several studies on LRHs have found very high biocompatibility in cell culture studies, and in some cases showed an apparent increase in cell viability relative to the untreated control cells.[87,101,181,182] HDSs are assumed to be biocompatible,[89] particularly those based on metals which are not toxic in their free ion form. A study testing Mg/Zn and Fe/Zn HDS systems on human prostate cancer cells reported no reduction in viability,[183] though no additional studies using other cell lines or HDS systems have been carried out to date. Cationic clays have shown generally good biocompatibility with evidence of some inhibitory effects on cell proliferation *in vitro*,[184–186] but *in vivo* studies in mice did not find any ill effects at concentrations of 1000 mg montmorillonite per kg body mass, much higher than what would typically be required for biological applications (100 mg/kg body mass).[184]

In vitro experiments on TMDs appear to show good biocompatibility, though there are some conflicting studies which report TMDs causing reduced cell viability by cell membrane disruption.[187–190] Cytotoxicity appears to be greatly influenced by the composition of the TMD.[191] *In vivo* tests, in which mice were injected with polyethylene glycol (PEG) functionalised MS_2, TiS_2, and WS_2 particles,[190] observed no cytotoxic effects over the course of 60 days, and subsequent histology on major organs did not show any signs of inflammation. In another study, dressings containing $MoSe_2$ were tested on mice with infected wounds,[192] with no reported ill effects and improved would healing. It has also been shown

that MoS_2 can be degraded by human myeloperoxidase enzymes,[193] which could help to prevent issues arising from accumulation.

There are a variety of *in vivo* studies on several graphene-based materials. Graphene nanosheets surface functionalised with PEG have been shown to exhibit no toxic effects in mice, as assessed by histological and blood analyses.[194,195] Graphene oxide (GO) nanosheets, on the other hand, have been shown to cause lung injury and inflammation in mice. For instance, this was shown to be the case for GO nanosheets with an average size of 158 nm,[196] as well as a formulation of GO sheets with a size range of 10-800 nm.[197] However, this toxicity was not observed in mice injected with graphene oxide formulated as quantum dots (3-5 nm diameter).[198] This finding was mirrored in another study, comparing the *in vivo* toxicity of graphene oxide nanosheets and quantum dots (20-40 nm diameter) in zebrafish.[199] Similarly, MXenes are also known to be highly biocompatible.[200–202] In an in-vivo study, mice were injected intravenously with a suspension of titanium carbide MXene nanosheets.[203] After 30 days, histological studies on the major organs revealed no damage, and toxicological assessment showed no significant difference from untreated mice.[203]

Metal phosphate materials are also highly biocompatible,[204] and calcium phosphate is a commonly used material for orthopaedic surgeries and dentistry.[205,206] Similarly, metal titanates have been demonstrated to cause no inflammation following implantation in rabbits and dogs.[207,208] Overall, many layered materials have good biocompatibility and are therefore suitable for drug delivery applications.

1.5 Inorganic layered materials in drug delivery

The concept of drug delivery from LMs is illustrated in Figure 1.7. Briefly, the introduction of a drug-loaded LM formulation into the physiological environment leads to the release of the drug cargo via a process of ion exchange. More specifically, drug anions diffuse out of the matrix of the LM following the concentration gradient and are replaced by physiological anions (such as chloride, hydrogen phosphate, or hydrogen carbonate). This process can occur either intra- or extracellularly, depending cellular uptake properties specific to the formulation used.

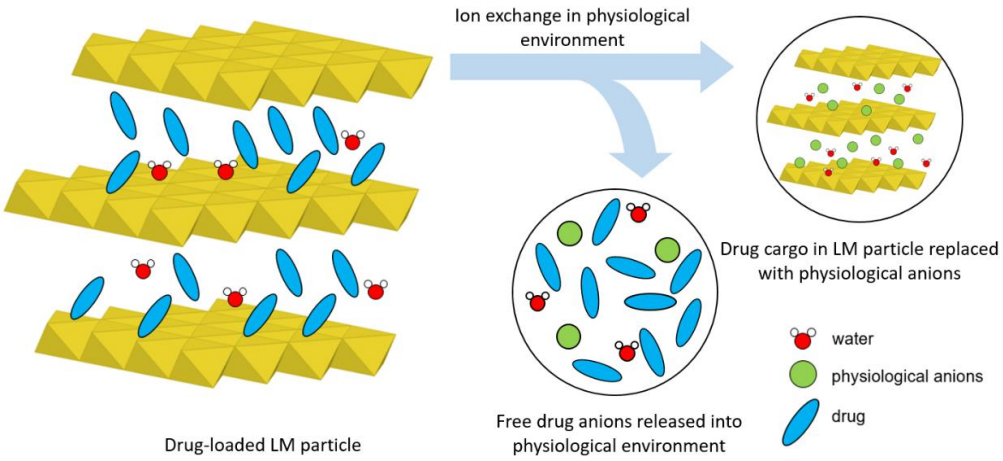

Figure 1.7 Schematic diagram illustrating the process of drug release from LMs into the physiological environment.

1.5.1 General examples

A wide variety of LDH-therapeutic intercalates have been reported in the literature to date, with guest species including anti-cancer drugs,[86,209,210] non-steroidal anti-inflammatory drugs (NSAIDs),[211–213] vitamins,[214,215] and DNA/RNA.[216,217] Some examples of these systems are summarised in Table 1.1.

Though the literature around LDH-drug delivery includes multiple types of formulations, including long-acting implants, injectables, and inhalable powders, a significant portion of work on LDH-drug delivery focuses on the oral delivery

route. It is widely accepted that LDH materials are unstable to degradation in acidic media as the hydroxyl links are readily hydrolysed, therefore use of an enteric coating is required where delivery further along the gastrointestinal tract is desirable. This is the case, for example, for protein and vaccine delivery applications, where the encapsulated cargo is itself unstable to the acidic environment in the stomach. In a recent work, Mg/Al LDH was loaded with protein antigens, and subsequently coated with chitosan and alginate (a pH responsive polymer).[218] Dissolution experiments showed that this system effectively protected the antigens from degradation in simulated stomach acid at pH = 1.5.[218]

It is possible to modulate the drug release behaviour of LDHs. In one study, rats with cranial bone defects were implanted with polymer plates containing Zn/Al LDH loaded with risedronate (a bone regenerative drug).[219] Owing to the protective nature of the polymer, exceptionally slow drug release was demonstrated (< 10 % of drug cargo released after 42 days),[219] which is favourable for bone regeneration applications as bone tissue grows very slowly. It was found that after 12 weeks, new bone tissue growth was significantly enhanced in rats which received implants containing LDH-risedronate complex compared to those which received polymer only or unloaded LDH implants.[219] Additionally, studies on Zn/Al LDH systems made by co-precipitation revealed that the identity of the initial counterion present in the LDH system seems to have a profound effect on the drug loading and drug release behaviour of the LDH. It was shown that LDH precursors containing nitrate anions released only 30-40 % of their simvastatin drug cargo within 60 h, compared to 80-90 % for carbonate containing LDH.[220]

Table 1.1 A summary table showing examples of previously reported LDH-drug intercalates categorised by their intended application, along with some of the key findings of these studies.

	LDH composition and guest species	*Key results*
Antimicrobial	**Mg/Al:** Enoxacin[221] **Zn/Al:** Cefazolin[85] Benzoate anion[222] **Zn/Al/Ti:** Dehydroabietic acid derivatives (DHADs)[223]	- Release profile of enoxacin from LDH was extended over 24 hrs by incorporation into a polymer hydrogel[221] - LDH-cefazolin showed enhanced antibacterial activity and chemical stability relative to free cefazolin[85] - LDH-DHAD produces bactericidal reactive oxygen species upon irradiation with visible light, and exhibits a protective effect against UV radiation *in vitro* and *in vivo*[223]
Anticancer	**Mg/Al:** 5-fluorouracil (5-FU), methotrexate (MTX)[86] 5-FU with cell death SiRNA[216] Raloxifene hydrochloride (RH)[210] Etoposide,[224,225] Doxorubicin,[226] Cisplatin[227] **Ca/Al:** Etoposide[209] **Zn/Al:** Isophthalic acid (IPA)[1]	- LDH-drug composites showed higher rates of cancer cell inhibition *in vitro* compared to free drugs 5-FU, MTX,[86] etoposide[209] - Co-delivery of 5-FU and cell death SiRNA from LDH matrix showed greatly enhanced cancel cell inhibition *in vitro* relative to 5-FU or SiRNA alone[216] - Administration of LDH-etoposide to pregnant mice showed greatly reduced foetal toxicity,[224] hematotoxicity, and enhanced tumour suppression[225] relative to free etoposide - LDH-DOX showed increased tumour inhibition and decreased cardiotoxicity compared to free DOX in mice[226] - LDH-cisplatin exhibited lower cytotoxicity and enhanced cancel cell targeting than free cisplatin[227] *in vitro* - LDH-IPA showed near-complete and in some cases complete tumour elimination due to photodynamic effect, compared to negligible tumour inhibition by free IPA or LDH alone in mice[1]
Bone regeneration	**Mg/Al/Yb:** Alendronate[228] **Zn/Al:** Simvastatin,[220] Risedronate[219]	- Administration of LDH-alendronate resulted in 1.41 times greater bone regeneration volume in rabbits, compared to free alendronate[228] - Rat studies on implants containing LDH-risedronate showed extended release properties (<10 % release over 42 days) and more than double the amount of new bone volume in 12 weeks compared to no treatment[219]
NSAIDs	**Zn/Al:** Sulindac[211] **Mg/Al:** Ibuprofen (IBU)[213] **Mg/Al/Fe:** Mefenamic and meclofenamic acids (MFAs), naproxen[212]	- Intramuscularly implanted pellet containing LDH-sulindac showed slow release of sulindac over approximately 21 days[211] - LDH-IBU showed pH dependent drug release in particle suspension, and diffusion limited drug release in a polymer hydrogel[213] - Intercalated formulations showed extended release relative to free drug (MFAs/NAP) in all cases[212]
Other	**Ca/Al:** Vitamin D3;[215] **Mg/Al:** DNA,[217] Vitamin C (VC)[214] Berberine,[229] Carnosine, gallic acid[230] Dexamethasone[231] **Zn/Al:** Gallic acid[160]	- LDH-DNA conjugate exhibited effective cell membrane permeation for intracellular DNA delivery[217] - Improved thermal stability of LDH-VC relative to free VC[214] - LDH loading improved solubility and oral bioavailability of berberine, leading to enhanced blood sugar lowering effect in diabetic mice[229] - Intercalation of carnosine and gallic acid into LDH matrices prevents premature oxidation and thereby allows extended release of the actives[230] - LDH-dexamethasone treated rats showed higher inflammatory inhibition than dexamethasone alone[231] - enhanced stability of gallic acid to UV irradiation when intercalated in LDH.[160]

Another challenge in drug delivery that has been addressed using LDHs is chemotherapy during early pregnancy. Chemotherapeutic treatment of cancer during the early stages of pregnancy is very challenging, as it has been shown to greatly increase the chances of miscarriage, deformities, and death.[232] In a recent study, it was shown that pregnant mice injected with Mg/Al LDH loaded with anticancer drug etoposide (also known as VP16) showed drastically reduced rates of foetal toxicity and developmental defects relative to free etoposide (Figure 1.8).[224] In a previous study by the same group, it was shown that delivery in Mg/Al LDH enhances the anti-tumour effect of etoposide relative to its free form, and decreases the associated off-target toxicity effect on the liver.[225] Together, these findings offer significant merit to continued exploration of LDH-based delivery systems for chemotherapeutic delivery.

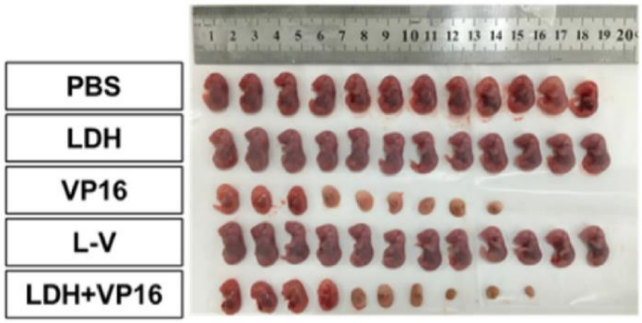

Figure 1.8 Diagram (Reprinted from reference 224, with permission from Elsevier) showing foetal mice after 12 days of maternal peritoneal injection with one of: phosphate buffered saline (PBS), unloaded Mg/Al LDH, free etoposide (VP16), Mg/Al LDH loaded with etoposide (L-V), or a physical mixture of Mg/Al LDH with etoposide (LDH+VP16).

Thus far, HDS systems have not been explored frequently for drug delivery applications in the literature. Several drug intercalate systems based on the HDS matrix have been reported to date, including vitamins A and C, [233,234] coumaric acid,[235] indole-3-acetic acid,[236] and several NSAIDs.[90,237] It was shown that drug release from HDS matrices is slower relative to LDH systems due to stronger guest-host interactions,[236] and that it is possible to modify the drug release profile by surface coating the HDS particles.[233,237]

Several studies exist on the use of LRHs for drug delivery applications. Layered gadolinium hydroxide (Gd-LRH) is a particularly attractive LRH system, because the inclusion of the gadolinium ion in the matrix allows these materials to exhibit strong magnetic resonance imaging (MRI) contrast. Many other rare-earth elements exhibit strong fluorescence and can be used as contrast agents for luminescence imaging, making LRHs particularly attractive in theranostic (simultaneous therapeutic and diagnostic) applications. Intercalation compounds of Gd-LRH with three NSAIDs (ibuprofen, diclofenac, and naproxen) have been reported.[87] It was found that both the parent material and intercalates exhibited good MRI contrast (Figure 1.9a), and were able to release their drug cargo in between 1-24 hours with the rate of drug release varying depending on guest species (Figure 1.9b).[87] It was also found that Gd-LRH was not stable in acidic media (pH = 1.5),[87] a property which could potentially be exploited for intratumoral delivery due to the acidic microenvironment of tumours.

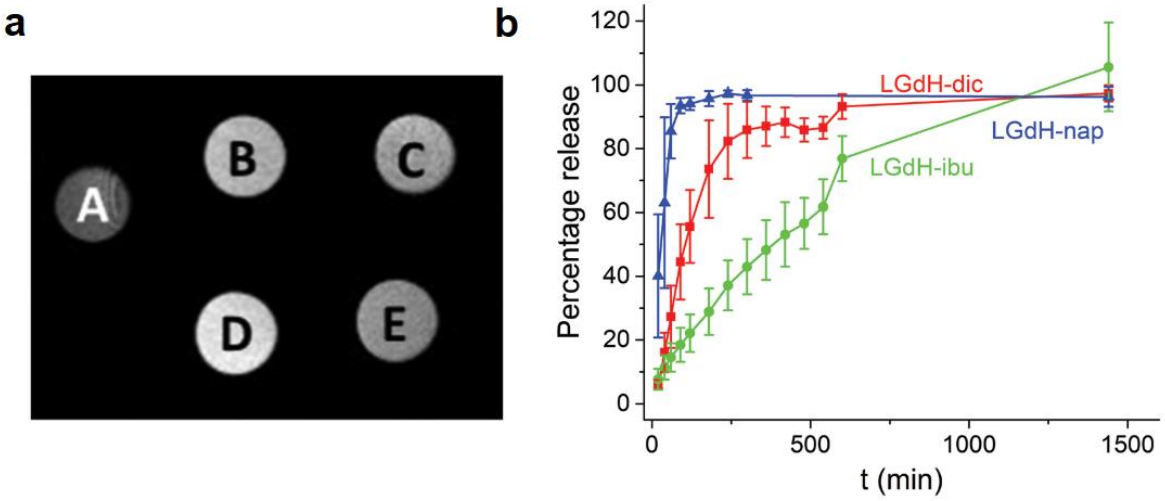

Figure 1.9 Diagram (reprinted from reference 87 with permission from the Royal Society of Chemistry) showing: a.) T1-weighted MRI images of agarose negative control (A); 0.5 and 0.25 mM suspensions of ibuprofen intercalated Gd-LRH (B and C respectively); 0.5 and 0.25 mM suspensions of diclofenac intercalated Gd-LRH (D and E respectively). b.) Drug release profiles of Gd-LRH intercalates.

Mixed rare-earth element LRHs have also been reported, including Gd-LRH doped with europium.[238] When intercalated with the amino acids phenylalanine

and tyrosine, it was shown that the fluorescence signal arising from Eu^{3+} was dampened, which the researchers suggested may be useful for sensing applications.[238] Conversely, if the signal was seen to change upon the release of the guest compound, it may be possible to use the change in signal intensity to track the rate of drug release. Other reported LRH systems include Eu-LRH intercalated with naproxen, and Tb-LRH loaded with aspirin, diclofenac, and indomethacin.[88,123,182] Intercalation with naproxen and aspirin were shown to cause an increase in the luminescence intensity of Eu-LRH and Tb-LRH, and rapid release within 3 hours,[88,123] whereas diclofenac and indomethacin were released from Tb-LRH over 24 hours with no reported change in luminescence properties.[182]

Montmorillonite (MMT), a cationic clay with a smectite structure, is a relatively commonly used excipient in medicines.[239,240] Many intercalation compounds of MMT and drug molecules have been studied. For instance, a study using promethazine and buformin[75] found that the drug release behaviour from MMT intercalates is dependent on the guest molecule size. Promethazine is a bulky polycyclic compound, whereas buformin is small and linear (Figure 1.10). The drug release profile from the intercalates was slower relative to the pure drug equivalent in both cases, but after 6 hours the promethazine-MMT intercalate reached only 30 % cumulative drug release, compared to 70 % for the much smaller buformin drug.[75] In another study, timolol intercalation and release from montmorillonite was investigated. The formulation exhibited sustained drug release with some pH dependence, reaching slightly higher cumulative drug release after 9 hours at pH 8.4 than at pH 1.2 (48 % vs 43 %).[76]

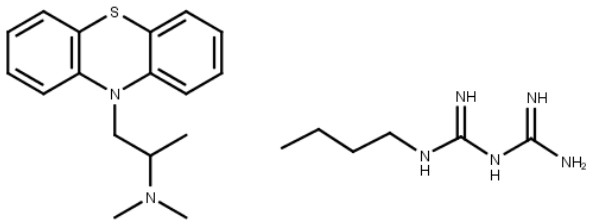

Figure 1.10 Chemical structures of drugs promethazine and buformin.

Another example is the use of montmorillonite to intercalate buspirone.[241] The intercalate showed a sustained release profile, reaching approximately 54 % release after 12 hours.[241] In addition, the release profile was further altered by coating the particles with a polymer, reaching only 23 % release after 12 hours.[241] A further potential application of montmorillonite in drug delivery is taste masking. The intercalation of sildenafil[242] into the clay matrix protects the drug from immediate dissolution in the saliva, therefore enabling taste masking. In addition, the intercalate was coated with an acid-soluble polymer, enabling additional protection from release in the oral environment, but rapid drug release in the acidic stomach environment.[242] Kaolinite, a naturally occurring smectite material, has also appeared in the literature in the context of drug delivery. It has been loaded with a variety of therapeutics including anticancer drugs, [243–247] and antibacterials.[248,249]

Materials based on graphene and graphene oxide (GO) have been well studied as potential drug delivery systems. For instance, GO coated with chitosan and co-loaded with two anti-cancer drugs[250] was shown to exhibit a synergistic tumour inhibiting effect in rats, as well as delayed and controlled release relative to the free drugs. Graphene and GO materials are also known to exhibit efficient photothermal conversion, and there exist multiple notable examples of multifunctional systems based on graphene. In one such study, GO was surface

functionalised with hyaluronic acid (a cancer cell targeting ligand) and loaded with doxorubicin (DOX).[251] This platform was shown to exhibit enhanced drug release rate in response irradiation with near infrared light as well as to a change in redox conditions (upon entry into cells), and displayed powerful tumour inhibition in mice.[251] In another work, fluorinated GO nanosheets were decorated with folic acid (also a cancer cell targeting ligand), and loaded with DOX.[252] The formulation exhibited high cytotoxicity due to the synergistic effect of combined chemo and phototherapy and the presence of fluorine allowed the system to fluoresce, for potential fluorescence imaging applications.

Other LMs which occasionally appear in the literature in the context of drug delivery include the layered metal phosphates and titanates. Several zirconium phosphate drug intercalates have been reported, [253–256] including a study investigating the potential of the material as a carrier for orally delivered insulin.[257] Sodium titanates have also been explored for drug delivery applications, most notably in a series of works which used titanate nanofibers and nanospheres to deliver Cerebrolysin (a neuroprotective agent) to rats and mice,[258,259] finding an enhanced neuroprotective effect relative to conventionally administered Cerebrolysin. Iron titanate has previously been intercalated with an enzyme, and showed magnetic properties suitable for targeting applications by applying an external magnetic field.[162]

1.5.2 Targeting mechanisms

Methods to target the desired drug delivery site can be broadly classified as either active or passive. Passive targeting involves taking advantage of the enhanced permeation and retention (EPR) effect seen in tumour tissue as compared to healthy tissue. Due to the rapid growth of cancerous tumours, the formation of

vasculature is much less organised than in healthy tissue, leading to ‘leaky’ blood vessels and poor lymphatic drainage.[260] As a result, intravenously administered nanoparticles in a particular size range are better able to exit the blood vessel into the tumour tissue (permeation), and are then trapped in this tissue due to poor lymphatic drainage (retention). To maximise the efficiency of targeting by using the EPR effect, it is common to employ a surface coating such as PEG or PLGA in order to prolong the circulation time of the nanoparticles.[261]

A common type of active targeting involves surface functionalisation with species which bind preferentially to target cells. For example, in an *in vivo* study on rabbits, a Mg/Al LDH system intercalated with heparin was successfully targeted to arterial injury sites by utilising antibodies conjugated to the particles.[262] In another work, Mg/Al LDH particles coated with folic acid were shown to preferentially target cells which overexpress folate receptors.[263] Overexpression of folate receptors in cancerous cells is fairly common, for instance in breast, lung, and ovarian cancers.[264,265] Intercalation of the folic acid decorated particles with methotrexate revealed that the drug was delivered preferentially to these cells.[263,266] A related study extended this concept to DOX loaded Mg/Al LDH nanosheets which were functionalised with folic acid. The study findings also indicated that cell uptake of the drug delivery platform was highly selective for cells which overexpress the folate receptor gene, and the cytotoxic effect of DOX was thereby effectively targeted to these cells.[267]

This strategy has also been employed in targeting other layered drug delivery systems to cancer cells. For instance, graphene/GO systems conjugated to cancer-targeting ligands including arginylglycylaspartic acid,[268] biotin,[269] folic acid,[270–273] and antibodies.[106,274–276] In one study, a glycyrrhetinic acid ligand was used to preferentially target DOX-loaded GO to the mitochondria of cancerous

cells,[277] leading to efficient tumour inhibition in mice. In a study on mice administered with paclitaxel loaded and hyaluronic acid functionalised zirconium phosphate,[278] it was demonstrated that this system could efficiently target cancer cells, and lead to a significant decrease in tumour volume relative to free paclitaxel.[278]

Chitosan-LDH complexes have been explored as targeted delivery systems for ocular drug delivery on a number of occasions.[279,280] *In vivo* studies on rabbits found that amino acid functionalised chitosan derivatives are able to target a peptide present on the ocular surface, and thereby increase the corneal permeation of drug-loaded LHD systems.[279] Moreover, the bioavailability of pirenoxine sodium intercalated within the LDH was increased up to 5 times that of commercially available counterpart.[279]

Another active targeting strategy is magnetic targeting, which is requires the inclusion of a magnetic species (most commonly iron oxide) in the drug delivery system. Targeting is then achieved by the application of an external magnetic field. Composite materials of iron oxide with LDH[281] or graphene oxide,[282] as well as inherently magnetic LMs such as iron titanate[162] have all shown the ability to be physically targeted using an external magnetic field. This has also been demonstrated *in vivo*, where a graphene/iron oxide composite loaded with a radiosensitiser drug was intravenously administered to mice.[283] After 1 h of exposure to an external magnetic field set up to target the tumour region, the formulation was shown to have accumulated within the tumour tissue (Figure 1.11).[283]

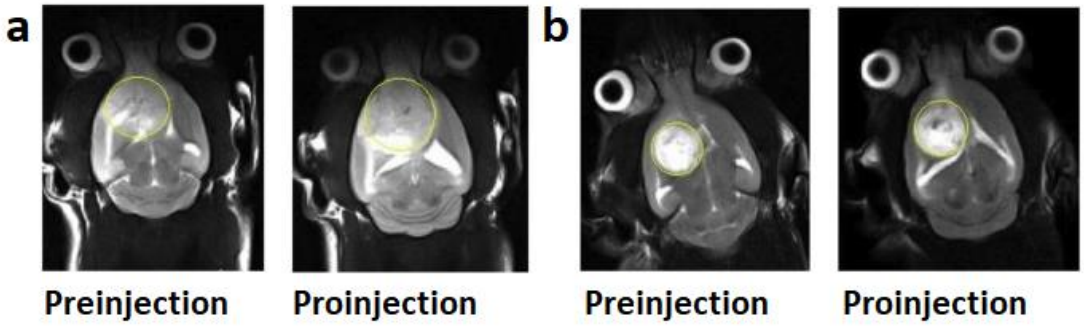

Figure 1.11 Figure (reprinted from reference 283, with permission from Elsevier) showing T_2-weighted magnetic resonance images of tumour bearing rats before and after injection with graphene/iron oxide composite, a.) In the absence of magnetic field targeting and b.) With external magnetic field targeting. Graphene/iron oxide composite appears as dark spots within the tumour tissue (circled in yellow).

Recently, *in vivo* tests of surface-functionalised LDH systems performed on mice showed that particles with a negative surface charge are rapidly cleared from the body via the liver, those with a positive surface charge seemed to accumulate preferentially in the lungs, and particles with a neutral surface showed enhanced circulation time and minimal accumulation in organ tissues. [284] These results indicate that surface functionalisation with charged moieties has a great influence on biodistribution, and therefore provides another viable route to active targeting.

1.5.3 Stimuli responsive release

Systems which are responsive to changes in pH are particularly useful for drug delivery to the gastrointestinal (GI) tract (due to the highly acidic medium in the stomach, which gradually gets neutralised by bile along the rest of the GI tract), as well as tumours, which often exhibit an acidic microenvironment relative to the surrounding healthy tissues. Metal hydroxide LMs (LDH, LRH, HDS) are all unstable with respect to dissolution in acidic media,[285] and therefore may release their drug cargo faster under such conditions. For instance, a composite system of iron oxide and Mg/Al LDH loaded with methotrexate[281] was shown to release over 80 % of the drug cargo in under 10 hours at pH = 3.5, whereas only 25 % release occurred in the same time at pH = 7.4.[281] On the other hand, a conflicting

report has found that the release of fluvastatin drugs from Mg/Al LDH at pH = 4.5 is negligible compared to release at pH = 7.4.[286] Another study, using naproxen loaded HDS systems formulated as tablets, showed negligible drug release during the course of two hours at pH 1, with rapid release occurring upon adjustment of pH to 6.8.[89] It is therefore unclear clear how metal hydroxide LM stability in acid may be affected through composition, guest identity, or formulation.

This property can, however, be modified by surface coating. An Mg/Al LDH system intercalated with ibuprofen and coated with carboxymethyl cellulose (a pH responsive polymer) was investigated for controlled drug release in the digestive tract.[287] At low pH in the stomach environment, the polymer protects the LDH-drug intercalate from degradation and slows drug release. As the formulation passes further through the digestive tract, and pH rises in the intestinal environment, the polymer swells and allows controlled drug release to occur.[287] Similar results were also demonstrated in a follow-up study using antibiotic cephalexin in place of ibuprofen.[288] There are many other examples of pH responsive drug release from LMs which are uncoated,[256,289] coated,[290–293] or otherwise functionalised.[80,294,295]

Electro-responsive drug release behaviour from LM systems has also been described in the literature. For instance, a GO and conductive polymer composite[296] has been reported, in which the release of adsorbed dexamethasone was triggered by applying a voltage. No release occurred without external triggering, and the magnitude of the applied voltage was shown to have a direct relationship with the rate of drug release.[296] Similarly, a study on an MMT-chitosan hydrogel reported changes in the release profile of vitamin b12 in response to electrical stimulation.[297]

MoS_2 nanosheets conjugated to cationic polymers were used to adsorb DNA fragments to deliver genes to both human and murine cancer cells.[298] It was shown that, after endosomal uptake of the platform into cells, release from the endosomes into the cytoplasm can be triggered photothermally. Moreover, the polymers desorbed from the MoS_2 nanosheets only in the presence of glutathione (an intracellular antioxidant), ensuring the DNA fragments are only released at the target site.[298] Another study reported greatly enhanced photothermal activity of MoS_2 when surface functionalised with CuS.[299] When loaded with DOX, this platform also exhibited pH and photothermally responsive drug release.[299]

1.5.4 Composite materials and combined therapies

Composite materials can exhibit additional functionalities and superior performance to simple LM systems. This allows for the simultaneous administration of multiple therapies (chemo-, photothermal, and photodynamic) to create a powerful, synergistic formulation.

A notable example of such a system is a Mg/Fe LDH doped with copper, and loaded with 5-fluorouracil.[300] In this instance, doping leads to coordinative unsaturation within the matrix, allowing the LDH to act as a charge carrier[300] and efficiently convert near-infrared light to heat. The powerful combination of this photothermal effect with pH sensitive drug release in the acidic tumour environment, lead to complete tumour elimination in mice (Figure 1.12a).[300] Moreover, the presence of paramagnetic iron ions within the LDH allows the system to act as a contrast agent in magnetic resonance imaging (Figure 1.12b). This enables the image-guided delivery and subsequent monitoring of the tumour site.

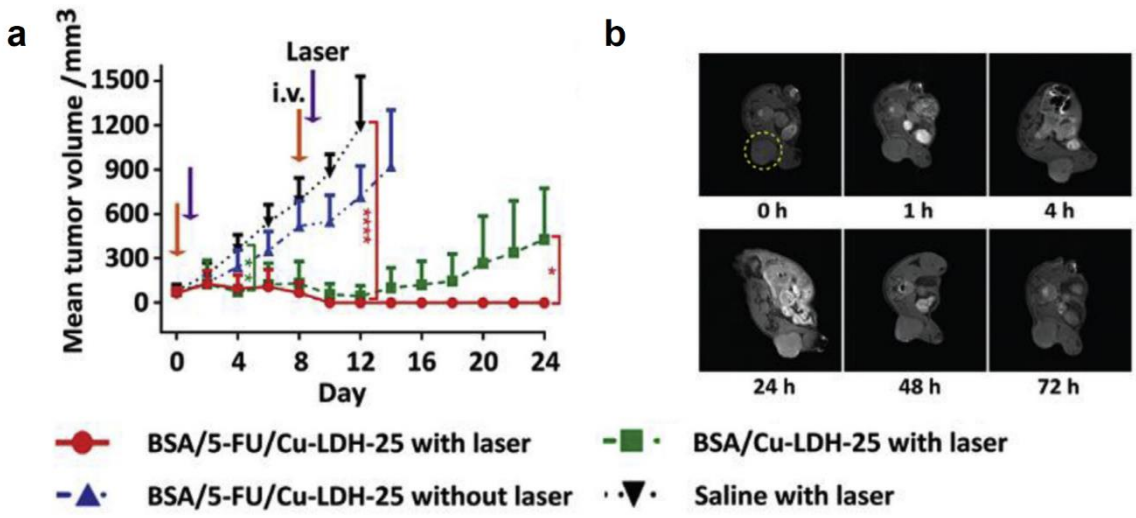

Figure 1.12 Diagram (reprinted from reference 300, with permission from Elsevier) showing: a.) Mean tumour volume under different combinations of treatment conditions, including: injection with LDH (without drug, green line) followed by irradiation with laser; injection of 5-FU loaded LDH followed by laser irradiation (red line) and no irradiation (blue line); injection with saline followed by laser irradiation (black line). (BSA = Bovine serum albumin, used to coat particles to prevent aggregation). b.) Change in T1-MRI contrast of a tumour (circled in yellow) at different time points after LDH injection, with the most intense contrast at 24 h post injection.

Alternatively, a photosensitiser can be intercalated into an LM to provide photothermal or photodynamic functionality. Briefly, photodynamic therapy involves energy/electron transfer from a photosensitiser to oxygen, producing cytotoxic reactive oxygen species and leading to cell death. For instance, a Zn/Al LDH was loaded with isophthalic acid (IPA), a photosensitiser which has the unique ability to absorb two near-infrared photons per molecule.[1] As such, IPA has a very high yield of ROS and therefore outperforms other reported photosensitisers in its photodynamic activity. It was shown that mice injected with LDH-IPA and subsequently irradiated with near-infrared light resulted in a significant decrease in tumour volume in all cases, and complete tumour elimination in several cases (Figure 1.13).[1]

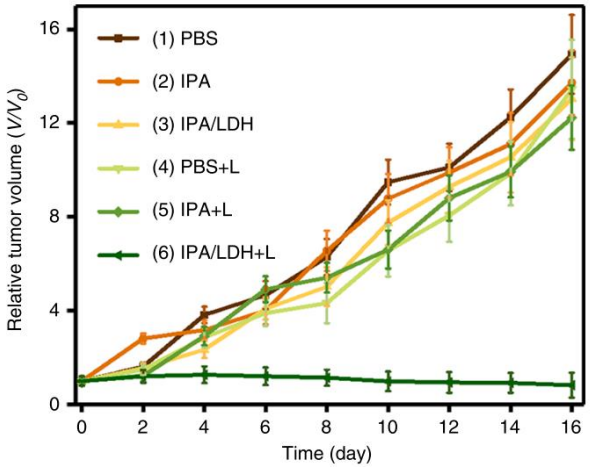

Figure 1.13 Diagram (reprinted from reference 1 with permission from Springer Nature) showing tumour volume in mice under different combinations of treatment conditions, including injection with phosphate buffered saline (PBS), isophthalic acid (IPA), isophthalic acid and LDH intercalate (IPA/LDH), and irradiation with a NIR laser (L).

Some LMs are inherently able to act as photosensitisers. Several studies have shown how effective MXenes can be as photothermal agents. For instance, a Ta_4C_3 and iron oxide composite showed very efficient photothermal conversion, leading to complete tumour elimination in mice without the need for chemotherapy.[30] Similarly, Nb_2C and Ti_3C_2 were shown to lead to complete tumour elimination in mice following NIR irradiation.[301,302] Interestingly, it was also demonstrated that Nb_2C is biodegradable in the presence of human myeloperoxidase enzyme,[301] which is an important consideration when evaluating the safety of injectable formulations.

The photothermal activity of MXenes in combination with drug delivery can therefore result in potent treatments for more complicated or aggressive cancers. A notable example of such a MXene based drug delivery platform is that of Ti_3C_2 loaded with DOX and decorated with cancer-targeting hyaluronic acid (HA).[109] In addition to acting as a pH responsive drug carrier, this platform was shown to be able to act as a photosensitiser for both photothermal and photodynamic therapy.[109] In tumour bearing mice, the nanosheets were shown to preferentially accumulate in tumours and lead to complete tumour elimination after irradiation

with NIR light.[109] In similar work, a composite of Ti_3C_2 and cellulose loaded with DOX was shown to exhibit NIR triggered drug release and photothermal activity (Figure 1.14a),[303] which together lead to tumour elimination with no relapse (Figure 1.14b, c).

Other LM systems reported to be photothermally active include a GO and iron oxide composite[282] loaded with DOX and coated with PEG, which was shown to be capable of acting as a photothermal sensitizer for thermal ablation, as well as exhibit good contrast in magnetic resonance imaging *in vivo*.[282] In another study, a composite including iron oxide, GO, and several polysaccharides loaded with DOX was shown to exhibit significant anti-tumour activity through the combination of chemotherapy and thermal ablation.[304]

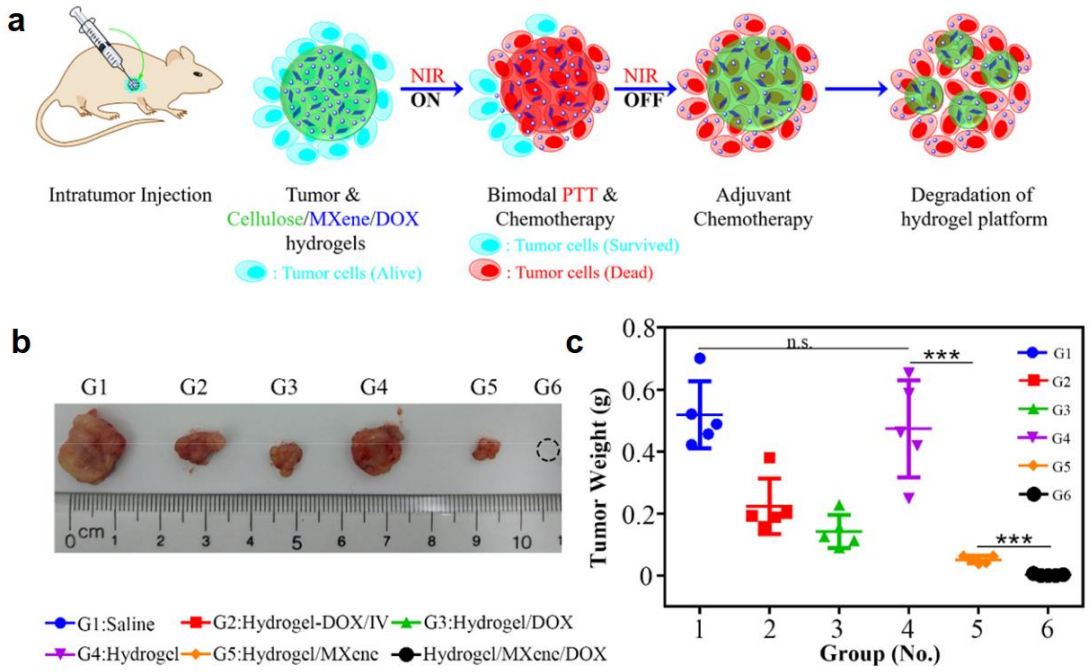

Figure 1.14 Diagram (adapted with permission from reference 303. Copyright 2018, American Chemical Society) showing: A.) schematic representation of the course of the therapy, consisting of: injection of the DOX loaded MXene composite into the tumour; NIR irradiation causing hyperthermia and simultaneous DOX release, leading to incomplete tumour cell death; continued drug release in the absence of NIR irradiation leading to complete tumour cell death; biodegradation of the composite. B.) Excised tumours representative of each treatment group G1-G6. C.) Tumour mass measurements (n=5) for each treatment group G1-G6.

In summary, inorganic layered materials hold great potential as drug delivery vehicles and have been the subject of many noteworthy works in the literature. LMs are tremendously versatile in terms of their composition, physical, and chemical properties and are therefore highly customisable. Their rich intercalation chemistry allows them to host a variety of therapeutic and functional guest species, and it is also possible to achieve additional features – such as effective targeting – through surface functionalisation. Moreover, the majority of inorganic LMs so far explored in biomedical applications have demonstrated exceptionally high biocompatibility, and in many cases impressive performance *in vivo*. It is therefore unsurprising that LMs are receiving increasing amounts of attention from the scientific community and will certainly play a part in the ongoing efforts to develop personalised medicines.

1.6 Layered hydroxide materials as theranostic agents

1.6.1 Layered double hydroxides

As the most widely studied anion-exchangeable class of layered materials, the layered double hydroxides (LDHs) have seen considerable interest in the field of theranostics. One example of an LDH with potential theranostic applications is based on manganese and iron.[305] This system makes use of the particles' instability in acidic media: this results in the release of paramagnetic Mn^{2+} and Fe^{3+} ions, which in turn enhance the T_1 MRI signal. The material could potentially be employed as a pH-responsive contrast agent able to give drug release in the slightly acidic environment of tumours. In this instance, the most suitable methods of administration are intravenous and intratumoral injections,[305] in order to avoid breakdown and premature drug release in the acidic environment of the upper

gastrointestinal tract. The biocompatibility of the platform and complexes, even after degradation in acidic media, was shown to be good in mice.

It is also possible to develop LDH materials which can act as photosensitisers in photothermal or photodynamic therapy. This is most commonly achieved by intercalation of a known photosensitiser molecule into the LDH matrix, for instance chlorin e6 or indocyanine green.[306,307] More recently, many LDH systems which exhibit inherent photosensitising ability as a result of lattice defects have been developed. In brief, instances of coordinative unsaturation within the crystal lattice of modified LDH materials change their resonant properties, and thereby their light-absorptive properties.[300] For instance, acid-etching (to introduce lattice defects) has been recently reported to cause a 97-fold increase in the photodynamic efficiency of Co/Mo LDH systems,[308] and subsequently elicit complete tumour suppression in tumour-bearing mice upon NIR laser irradiation.

Additionally, it is possible to delaminate LDHs into nanosheets by either mechanical or chemical means,[141,309] or to produce them directly by vapour deposition or sonochemical methods.[132,149,150] Nanosheets differ from the bulk LRHs in their shape, thickness and surface area to volume ratio, which can in turn influence properties such as cell uptake and drug release. For example, it was found that Mg/Al LDH nanorods are preferentially internalised into mammalian cell nuclei, whereas Mg/Al LDH nanosheets remain in the cytoplasm,[96] enabling sub-cellular targeting simply by altering LDH morphology.

1.6.2 Layered rare-earth hydroxides

The first LRHs capable of anion exchange were reported in 2006.[104] The initial publication by Monge *et al.* described such structures including the smaller

lanthanide ions (Dy, Ho, Yb, and Y) with organic counterions. Shortly after, Fogg *et al.* reported a series of fully inorganic, anion exchangeable, LRH systems intercalated with A = NO_3^-, Cl^-, Br^- for R = Y, Gd-Lu.[122,310] In 2008, Geng *et al.* extended this family to include the larger lanthanide ions (R = Nd, Sm, Eu) intercalated with Cl^-.[311]

As with LDHs, LRH sheets carry a net positive charge which causes them to assemble into stacks of sheets with intercalated anionic species in the interlayer space. The ability of LRHs to exhibit magnetic and luminescent properties arising from the rare-earth metal ions they contain has fostered increasing interest in their applications as theranostic agents. By far the most studied LRH systems for theranostic applications are those containing gadolinium, as Gd^{3+} is paramagnetic and exhibits strong positive contrast in MRI.

A theranostic platform based on layered gadolinium hydroxide (LGdH = $[Gd_2(OH)_5]Cl{\cdot}yH_2O$) has been previously reported by our group.[87] Hydrothermal treatment of a gadolinium chloride salt at 150 °C produced mixture of rod and plate like particles, ranging in size from 100 nm up to 2 μm. Through various intercalation methods, including ion exchange and co-precipitation, it was shown that drug intercalation into LGdH was facile using naproxen, ibuprofen, and diclofenac anions. The drug-particle complexes were shown to be unstable in acidic media, releasing toxic Gd^{3+} ions, but suitable for use with an enteric coating. In terms of MRI performance, LGdH and all of the drug intercalate compounds were shown to be able to act as negative contrast agents. In addition, the material was shown to be biocompatible, with the presence of LGdH-Cl and LGdH-ibu appearing to result in a higher cell count than untreated cells.

In a subsequent work, the effect of surface functionalisation on LGdH nanoparticles using SiO_2 nanodots was explored.[312] LGdH was first prepared by hydrothermal synthesis, and 5-fluorouracil (5-FU) and ibuprofen (ibu) were intercalated using ion exchange. The negatively charged SiO_2 nanodots were prepared by microemulsion,[313] and coated onto the positively charged LGdH nanoparticles to produce the composite LGdH@SiO_2. Coating was found to increase the colloidal stability of LGdH and LGdH-ibu particles relative to their uncoated analogues, whilst the opposite was true for LGdH-5FU. The biocompatibility of LGdH-ibu@SiO_2 was shown to be high, whereas LGdH-5FU@SiO_2 inhibited the growth of A459 (an adenocarcinoma cell line). Though coating decreased both r_1 and r_2 relaxivity in most cases, LGdH-ibu@SiO_2 had higher r_2 relaxivity than uncoated LGdH-ibu, and showed strong negative contrast properties in MRI studies.

It is also possible to produce mixed lanthanide LRH systems by doping. An LGdH system, with 5% of the Gd^{3+} sites replaced with Eu^{3+}, was reported by Gu *et al*., and was successfully intercalated with phenylalanine and tyrosine.[238] The uptake of the amino acids by the LGgH:Eu matrix resulted in a decrease in the luminescence signal arising from Eu^{3+}, thought to be a result of a relaxation pathway involving the amino and hydroxy groups of the guest species. Potentially, this property could have applications in amino acid detection. The same research group also reported LEuH intercalated with naproxen (nap), and LTbH intercalated with aspirin, diclofenac, and indomethacin (ASA, dic, and IMC).[88,123,182] LEuH and LTbH showed vastly increased luminescence intensities after intercalation with nap and ASA respectively, owing to efficient energy transfer between the host and guest species.[88,123] It was also demonstrated that LEuH-nap and the LTbH-drug intercalates have high biocompatibility (> 80%) in multiple

human cancer cell lines at concentrations up to 100 µg / ml. The majority of drug was released from LEuH-nap and LTbH-ASA in the first 3 hours,[88,123] whereas LTbH-dic and LTbH-IMC showed sustained release over 25 h.[182]

Like for LDHs, it is also possible to produce LRH based nanosheets,[146,314,315] a property which could be exploited to enhance the theranostic potential of LRHs. A group investigating the potential of LGdH systems as MRI contrast agents showed that hydrothermal treatment at 60 °C produces a suspension of LGdH-Cl nanosheets approximately 2.6 nm thick and around 100 nm wide.[101] This is in stark contrast with the particles obtained by our group via hydrothermal synthesis at 150 °C, which produced rod and plate like particles 100 nm – 2 µm in size. [87] This demonstrates that it is feasible to control the morphology of the LGdH particles using synthetic parameters, which may also be possible to do for other systems. These LGdH nanosheets were shown to exhibit both positive and negative MRI contrast properties, but the effect was particularly strong in T_1 weighted MR images even at low LGdH concentration (Figure 1.15).[101] The advantage of using nanosheets versus the bulk crystals in this context is that delamination allows water molecules easier access to the Gd^{3+} centres, thereby enhancing the MRI signal.[101]

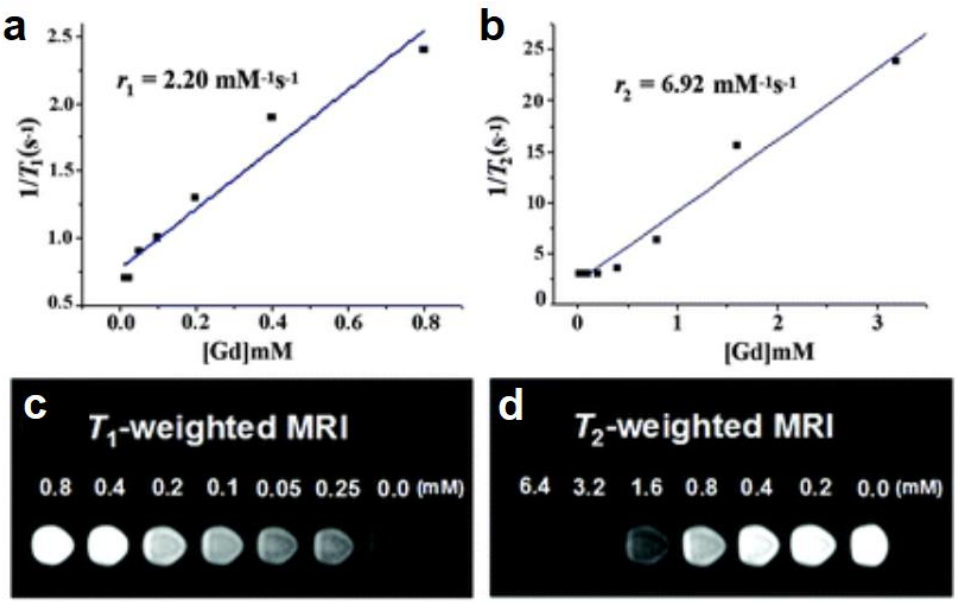

Figure 1.15 Plots (reproduced from reference 101, with permission from the Royal Society of Chemistry) showing a.) $1/T_1$ and b.) $1/T_2$ against LGdH concentration in aqueous suspension; c.) T_1 weighted and d.) T_2 weighted MR images at different concentrations of LGdH suspensions.

In a follow up study, the group explored the effects of polyethylene glycol (PEG) surface modification on the properties of LGdH.[181] It was found that PEG coating improved LGdH nanosheets' ability to form a uniform aqueous dispersion as well as significantly enhance the acid resistance of the system (from 55 % to 8 % dissolution after 1 hour at pH = 3.0).[181] Fluorescein was successfully intercalated into this surface functionalised LGdH system, potentially enabling multi-modal MRI and fluorescence imaging. Moreover, the group also demonstrated that it is possible to use the LRH matrix as an intermediate to produce rare-earth phosphate functionalised silica nanoparticles for multimodal imaging contrast applications.[316] In this study, nanosheets of LGdH doped with 11 % Eu^{3+} were conjugated to silica nanospheres, and subsequently annealed at 800 °C to induce a phase transformation of LGdH:Eu to $GdPO_4$:Eu. The resulting colloids displayed both strong red fluorescence as well as both T_1 and T_2 weighted MR contrast.[316] Though there are not yet any LRH systems reported which have been intercalated with photosensitizers for photodynamic/photothermal therapy, it is

entirely feasible that such functionality could be achieved as has been demonstrated for LDHs.[1,300]

In summary, LRH materials which can incorporate drug cargo, act as contrast agents for medical imaging, exhibit photothermal or photodynamic functionalities, and produce a range of particle morphologies hold great potential as theranostic platforms. There is ample scope for creating novel LRH based treatments incorporating multiple functionalities by using different combinations of metals and guest species. The use of inorganic systems in particular to achieve this goal exploits the properties inherent to the metals used – this substantially simplifies the synthetic process as compared to organic counterparts. For example, inorganic systems can act as MRI contrast agents simply by inclusion of superparamagnetic iron or gadolinium (III) species in a single synthetic step, as described above, whereas a fully organic MRI contrast agent[317] requires an initial synthesis and then subsequent conjugation to other functionalising moieties to create a theranostic platform.

1.7 Aims and objectives

This project aims to develop a family of structurally related nanoparticulate systems, based on layered rare-earth hydroxides, with a combination of properties that make them suitable for theranostic applications. Based on existing literature, the synthesis of these materials is expected to be facile, and yield systems capable of exhibiting high drug loadings, and providing high levels of contrast in MR/fluorescence imaging. Additionally, the ability to be functionalised with photosensitisers may endow such materials with photo-responsive treatment capabilities. The local application of a NIR laser could further enable photothermal/photodynamic therapy at the desired site leading to cell ablation and death.

This work begins by building on previous work within the group on a terbium based layered rare-earth hydroxide (LTbH). The anti-inflammatory drugs diclofenac (dic), ibuprofen (ibu), and naproxen are intercalated into LTbH *via* ion exchange, the intercalation products are characterised and their performance in terms of drug release, luminescence and biocompatibility is investigated. Subsequently, the influence of experimental parameters on particle morphology is investigated, with the aim of increasing sample homogeneity and optimising average size. Several related LRH systems based on praseodymium, neodymium, gadolinium, erbium and ytterbium are synthesised and characterised. Mixed metal (Gd/Tb) LRH systems are investigated for their bimodal (luminesce, MR) contrast ability, and a lead formulation is developed. Finally, the photothermal and photodynamic properties of the lead LRH system are explored by loading with known PTT/PDT agent indocyanine green and subsequent illumination using a NIR laser of 808 nm wavelength.

2 Synthesis, characterisation, and theranostic properties of layered terbium hydroxide

2.1 Introduction

Layered rare-earth hydroxides have begun to gather increasing attention as potential theranostic platforms owing to their extensive intercalation chemistry combined with magnetic and fluorescent properties. In this chapter, the potential of layered terbium hydroxide (LTbH, $[Tb_2(OH)_5]Cl{\cdot}yH_2O$) as a platform for simultaneous drug delivery and fluorescence imaging will be discussed. An abridged version of this chapter was published in 2021.[318]

A promising theranostic platform based on layered gadolinium hydroxide (LGdH-Cl, $[Gd_2(OH)_5]Cl{\cdot}yH_2O$) has been reported previously by our group.[87] Through several methods, including ion exchange and co-precipitation, it was shown that drug ion intercalation into LGdH was facile and reversible using diclofenac, ibuprofen, and naproxen as model drugs. In terms of MRI performance, LGdH and all the drug-intercalated compounds were shown to be able to function as negative contrast agents (reducing T_2 MRI signal intensity), and the materials were shown to have no significant cytotoxic effect on the Caco-2 cell line relative to untreated cells. Based on these findings, the exploration of other LRH materials for theranostic applications is attractive.

The luminescence behaviour of the lanthanide salts is a well-known phenomenon and could therefore be exploited (in lieu of magnetic resonance) for medical imaging applications. In a study comparing the luminescence behaviour of trivalent lanthanide ion chelates, it was shown that the strongest line emissions

(arising from the lanthanide centres as opposed to the attached ligand) were observed for Sm^{3+}, Eu^{3+}, Tb^{3+}, and Dy^{3+} chelates.[319] In brief, this has to do with the electronic energy level distribution within these ions, which allows the radiative (luminescent) relaxation pathway to dominate over non-radiative relaxation processes. This is discussed in more depth in Chapter 4.

The Tb^{3+} and Eu^{3+} ions exhibit the highest intensity emissions of all lanthanides, and therefore are dominant in the literature for luminescence applications. In general, Eu^{3+} systems are more widely explored than those based on Tb^{3+}. This extends to their respective layered hydroxides, with the search term 'layered europium hydroxide' yielding 119 exact match results on Google Scholar, as opposed to only 38 for 'layered terbium hydroxide' as of 2022. Additionally, reported luminescence lifetimes for a variety of Eu/Tb chelates/complexes have shown that in general, Tb^{3+} centred species show longer luminescence lifetimes (ca. 250 – 1900 µs) than do Eu^{3+} centred ones (ca. 50 – 1300 µs).[320,321] On this basis, the LTbH system was selected as the focus of further study, described in this chapter.

Intercalation into LRHs is a charge-driven process and requires anionic guest molecules to balance the charge of the positive LRH layers. Three model drugs – dic, ibu, nap – were chosen, as they are cheap, commonly used in similar studies, and their anionic sodium salt forms are readily available. Additionally, the three model drug molecules exhibit between them a variety of functional groups, including alkane, amine, carboxylate, ether, and aromatic rings, which may translate into distinct interactions with the host LRH matrix.

There are several reports in the literature of LTbH-NO_3 precursors exhibiting enhanced green luminescence after intercalation with benzene-containing

carboxylic acid sensitizers.[322,323] This increased luminescence effect is believed to be a result of host-guest energy transfer, and the extent of this effect has been shown to depend on the arrangement of the guest molecules within the interlayer gallery as well as energy level matching between the guest and Tb^{3+} within the host.[322] It is therefore feasible that such an energy transfer phenomenon may be observed for LTbH-drug intercalates generated in this chapter, as the chosen drugs are all benzene-containing carboxylic acids.

2.2 Aims

The work described in this chapter considers LTbH (Figure 2.1a) as a potential theranostic platform. The anti-inflammatory drugs diclofenac (dic), ibuprofen (ibu), and naproxen (nap; Figure 2.1b) will be intercalated into LTbH-Cl *via* ion exchange to form LTbH-dic, LTbH-ibu, and LTbH-nap respectively. These intercalation compounds will be characterised and their performance in terms of drug release, luminescence, and biocompatibility will be investigated.

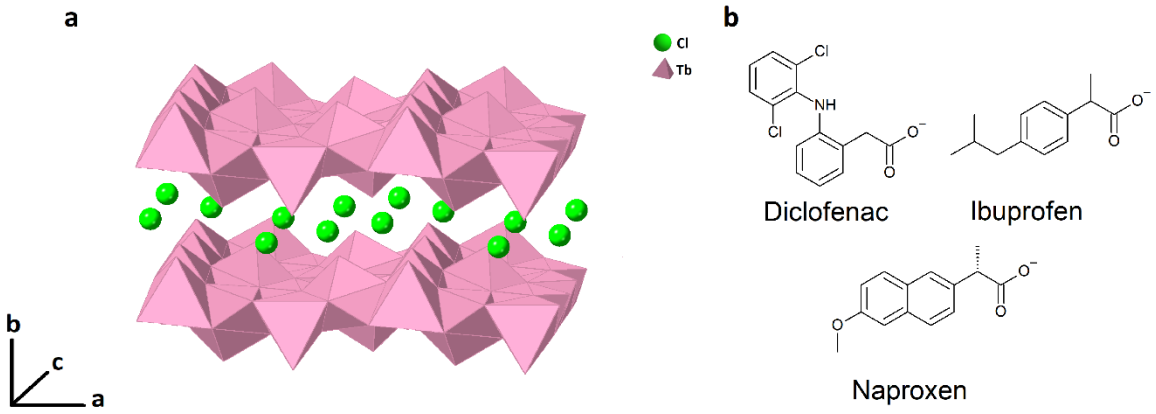

Figure 2.1 a.) A schematic diagram showing the lamellar structure of LTbH with intercalated Cl^- anions. b.) The chemical structures of the anions of diclofenac, ibuprofen, and naproxen.

2.3 Experimental

2.3.1 Materials

Terbium chloride hexahydrate and ibuprofen sodium were purchased from Sigma Aldrich. Diclofenac sodium was sourced from Cambridge Bioscience, and naproxen sodium from Fisher Scientific UK. All water used was deionised, and ethanol was of analytical grade.

2.3.2 Synthesis

2.3.2.1 Hydrothermal synthesis of layered terbium hydroxide (LTbH-Cl)

An aqueous solution of $TbCl_3 \cdot 6H_2O$ (0.4 M, 15 ml) was added dropwise to a stirring aqueous solution of NaCl/NaOH (1.4 M and 2.1 M respectively, 5 ml). The resultant suspension was stirred for 10 min and transferred to a Teflon lined hydrothermal reactor (23 ml). The reactor was heated to 150 °C for 15 h, at a heating and cooling rate of 10 °C / min, after which the white precipitate was collected by centrifugation. The product was washed with water (2 x 30 ml) and ethanol (2 x 30 ml), and subsequently dried at 60 °C for 24 h to yield the product, $[Tb_2(OH)_5]Cl \cdot yH_2O$ (LTbH-Cl). The product cake was briefly (<1 min) ground using a pestle and mortar to produce a fine powder.

2.3.2.2 Ion exchange reactions

LTbH-Cl (150 mg) was dispersed in water (15 ml), and the drug of interest was added to this solution in a three-fold molar excess (223 mg for ibuprofen sodium, 310 mg for diclofenac sodium, and 246 mg for naproxen sodium). The mixture was heated at 60 °C for 24 h, with stirring. The product was collected by

centrifugation, washed with water (2 x 30 ml) and ethanol (2x 30 ml), and subsequently dried at 60 °C for 24 h.

As diclofenac is poorly soluble in water, the intercalation mixtures contained a large amount of undissolved drug. However, it is highly soluble in ethanol and any remaining undissolved drug was removed in the washing step. The poor drug solubility during intercalation did not affect final drug loading.

2.3.3 Characterisation

2.3.3.1 Scanning electron microscopy (SEM)

Samples were sputter coated with gold and imaged using a JEOL JSM-6701F field emission scanning electron microscope. Particle size analysis on the resulting images was performed manually using ImageJ 1.52a software, and the results presented as mean ± standard deviation. The number of particles measured was 905, 771, 651, and 634 for LTbH-Cl, LTbH-dic, LTbH-ibu, and LTbH-nap respectively.

2.3.3.2 Dynamic light scattering (DLS)

The hydrodynamic size and zeta potential of the LTbH particles were analysed using a Zetasizer Ultra instrument and ZS Xplorer software (Malvern Panalytical). Suspensions of the particles (0.1 mg / ml) were prepared by re-dispersing the samples in water by ultrasonication (5 min). Disposable folded capillary zeta cells (DTS1070, Malvern Panalytical) were used. Each suspension was measured in triplicate, and the results are given as mean ± standard deviation.

2.3.3.3 X-ray diffraction (XRD)

X-ray diffraction analysis was performed using a Rigaku Miniflex 600 diffractometer with Cu Kα radiation (λ = 1.5418 Å). Patterns were collected over the 2θ range 3-60 °, at 40 kV and 15 mA.

2.3.3.4 Fourier-transform infrared spectroscopy (FTIR)

Fourier transform infrared spectra were collected on a Perkin Elmer Spectrum 100 FTIR spectrometer. Spectra were collected over the range 650-4000 cm^{-1} at a resolution of 1 cm^{-1}, and four scans.

2.3.3.5 Elemental microanalysis

Carbon/hydrogen/nitrogen content analysis was performed using flash combustion on a Carlo Erba CE1108 elemental analyser. Analysis of samples was performed at London Metropolitan University by Stephen Boyer and Orla McCulloo.

2.3.3.6 Thermogravimetric analysis (TGA)

Thermogravimetric analysis was performed using a TA instruments Discovery TGA instrument controlled by the TA Trios software. The samples were heated from 40-900 °C at a rate of 20 °C / min, under nitrogen gas at a flow rate of 25 ml / min.

2.3.3.7 Cytotoxicity assay

To assess the cytotoxicity of the formulations, human colorectal adenocarcinoma cells (Caco-2) and human embryonic kidney cells (HEK 293) were used. Caco-2 cells were cultured at 37 °C under 5 % CO_2, in high glucose Dulbecco's modified

Eagle's medium (DMEM-HG, 435 ml, Sigma Aldrich) supplemented with the following solutions: penicillin-streptomycin (5 ml, Life Technologies), L-glutamine (5 ml, Life Technologies), non-essential amino acid solution (5 ml, Life Technologies), and foetal bovine serum (50 ml, Gibco). HEK-293 cells were cultured at 37 °C under 5 % CO_2, in Dulbecco's modified Eagle's medium (DMEM, 440 ml, Sigma Aldrich) supplemented with the following solutions: penicillin-streptomycin (5 ml, Life Technologies), L-glutamine (5 ml, Life Technologies), and foetal bovine serum (50 ml, Gibco). The cell cultures were passaged at 50-75 % confluence by treatment with trypsin solution (0.25 % in EDTA, 2 ml, Sigma Aldrich). For cell viability experiments, the passage numbers used were 73-76 (Caco-2) and 9-12 (HEK 293).

Cell viability assessments were conducted using the CellTiter-Glo™ assay, in white 96-well plates (Corning). Cell suspension was prepared at a concentration of 5.6 x 10^4 cells / ml and deposited into the wells of the plate (180 µl each). To measure the cytotoxicity of the LTbH-drug intercalates, suspensions of LTbH-X (X = Cl, dic, ibu, nap) in culture medium (10 mg / ml) were prepared, and either 5 or 10 µl of these suspensions were added directly to the cells. To measure the cytotoxicity of the pure drug counterparts, solutions of each drug in culture medium (3 mg / ml, approximately equivalent to the amount present in the LTbH-X suspensions assuming a 30 % drug loading) were prepared, and either 5 or 10 µl of these suspensions were added directly to the cells.

For background luminescence measurements, wells were prepared using only cell culture medium in place of cell suspension. For control cell luminescence measurements, wells were prepared by using cell culture medium in place of LTbH-X suspensions. The plates were then incubated at 37 °C for 24 h. After incubation, CellTiter-Glo™ 2.0 assay reagent (100 µl, Promega) was added to

each well, and left to react at room temperature for 30 min. The luminescence of the plates was read over the range 250–850 nm using a SpectraMax M2e microplate reader. Cell viability for each well was calculated according to the equation:

$$Viability\ (\%) = \frac{(Sample\ luminescence - background\ luminescence)}{(Control\ luminescence - background\ luminescence)}\ x\ 100 \quad (2.1)$$

Three independent experiments were performed, each with treatment conditions in triplicate, and results presented as mean ± standard deviation.

2.3.3.8 Haemolysis assay

To assess the haemolytic activity of the formulations, an assay was performed using blood from adult female Wistar rats. Fresh whole blood (3.5 ml) was first centrifuged to separate the red blood cells (RBCs) from the plasma and buffy coat layers, which were discarded. The RBCs were then washed with Dulbecco's phosphate buffered saline (DPBS, 6 ml, Sigma Aldrich) three times, until the supernatant was colourless. The RBC suspension was then diluted with DPBS to a total volume of 50 ml.

Haemolysis assessments were conducted in clear 96-well plates (Corning). The RBC suspension was deposited into the wells of the plate (180 µl each). To measure the haemolytic activity of the LTbH-drug intercalates, suspensions of LTbH-X (X = Cl, dic, ibu, nap) in DPBS (10 mg / ml) were prepared, and either 5 or 10 µl of these suspensions were added directly to the cells, to final concentrations of 270 and 526 µg / ml respectively. For negative control haemolysis measurements, wells were prepared by using DPBS in place of LTbH-X suspensions. For positive control haemolysis measurements, wells were prepared by using a solution of Triton-X in DPBS (10 % v/v) in place of LTbH-X

suspensions. The plates were then incubated at 37 °C for 1 h. After incubation, the microplates were centrifuged, and 100 µl of the supernatant from each well was transferred to a clean microplate. The absorbance of the plates at 540 nm was read using a SpectraMax M2e microplate reader. Extent of haemolysis for each well was calculated according to the equation:

$$Haemolysis\ (\%) = \frac{(Sample\ absorbance)}{(Positive\ control\ absorbance)}\ x\ 100 \qquad (2.2)$$

Three independent experiments were performed, each in triplicate, and results are presented as mean ± standard deviation.

2.3.3.9 Stability assay

Stability of LTbH-Cl in aqueous suspension was evaluated over a range of pH values (pH = 1.5 - 10, in intervals of 0.5) using an Arsenazo-3 (AS-3) assay. A stock solution of AS-3 in water was prepared (2.5 mM) and stored in a container wrapped with foil until required. A calibration curve was generated using $TbCl_3.6H_2O$ in distilled water. In a typical experiment, 5 mg of LTbH-Cl was suspended in 10 ml of distilled water (acidified or basified to the required pH using HCl or NaOH solutions respectively) and stirred at 37 °C for 24 h.

After time intervals of 2 h and 24 h, samples of the supernatant (50 µl) were collected and were deposited into a clear 96-well plate. To each well AS-3 solution (50 µl) and distilled water (200 µl) were added. 50 µl of the resulting solution was then transferred to another well plate and diluted further by adding distilled water (200 µl). Background absorbance wells were prepared with distilled water in place of sample solution. Absorbance at 652 nm was read using a SpectraMax M2e microplate reader. The measured absorbance values were first corrected by subtracting the average background absorbance, and subsequently

converted to concentration of Tb^{3+} ions using the calibration curve. Finally, the extent of dissolution for each sample was calculated as follows:

$$Dissolution\ (\%) = \frac{[Tb^{3+}\ sample]}{[Tb^{3+}\ max]}\ x\ 100 \qquad (2.3)$$

The concentration [Tb^{3+} max] is the maximum possible concentration of Tb^{3+} ions if 5 mg of LTbH-Cl was completely dissolved in 10 ml of water. In this case, this value was calculated based on the formula $[Tb_2(OH)_5]Cl_{0.9}(CO_3)_{0.05}.1.5H_2O$ with a molecular mass of 464.82 g mol^{-1}, which gives [Tb^{3+} max] = 2.1514 mM. Three independent experiments were performed, each in triplicate, and results are given as mean ± standard deviation.

In order to investigate the effect of the change in pH on the performance of the AS-3 assay, supernatant from the suspensions of LTbH-Cl at pH 1.5 and pH 7.4 was removed after 24 hours of incubation. This supernatant was reacted with AS-3 and diluted as described above. Negative control solutions (unbound AS-3) were prepared with distilled water in place of sample supernatant. Positive control solutions (bound AS-3) were prepared with aqueous solution of $TbCl_3.6H_2O$ in place of sample supernatant. Absorbance was then recorded over the wavelength range 400 – 800 nm.

To assess the effect of pH change on the absorbance at 652 nm specifically, a single-point experiment was performed in which solutions of $TbCl_3.6H_2O$ (1.25 mM) in water at the appropriate pH were reacted with AS-3 and diluted as described above. The absorbance of each sample was then measured at 652 nm. Three independent experiments were performed, each in triplicate, and results are given as mean ± standard deviation.

2.3.3.10 Drug release

Low-volume drug release studies were conducted using a dialysis approach, with phosphate buffered saline (PBS, pH = 7.4) used as the release medium. The medium was prepared by dissolving 1 PBS tablet (Sigma Aldrich) in water (200 ml) and warming to 37 °C immediately prior to use. In a typical experiment, LTbH-drug intercalate (5 mg) was suspended in release medium (5 ml) and sealed in a length of dialysis tubing (3500 MWCO, Fisher Scientific). The sealed dialysis parcel was transferred to a centrifuge tube (50 ml) containing release medium (30 ml). The centrifuge tubes were placed in an incubator shaker at 50 rpm and 37 °C. Aliquots (100 µl) were taken at predetermined time intervals and analysed by UV-vis spectroscopy (Cary 100 spectrometer, Agilent) in a quartz semi-micro cell (Agilent) to determine absorbance. The measurements were conducted at λ_{max} values of 276 nm (diclofenac), 222 nm (ibuprofen) or 224 nm (naproxen). Absorbance was converted to drug concentration using calibration curves generated using solutions of pure drug salts in PBS. Release experiments were performed in triplicate, and results presented as a mean ± standard deviation.

Truncated drug release experiments were preformed using LTbH-ibu in groups of four samples per experiment. Each sample was set up as described above and designated to be terminated at one of the following time points: 15, 30, 60, or 270 minutes. The LTbH-ibu suspension was taken from the dialysis bag at the required time, and the supernatant of the suspension was removed immediately by centrifugation. The remaining solids were dried in an oven at 60 °C for 24 h, and subsequently analysed by solid state photoluminescence. Three independent experiments were performed.

2.3.3.11 Fluorimetry

Fluorescence spectroscopy was conducted on a Horiba Fluorolog 3 spectrofluorimeter, equipped with an R928P photomultiplier tube and InGaAs photodiode detector. Suspensions of the particles (0.1 mg / ml) were prepared by re-dispersing the samples in water by ultrasonication (5 min). The excitation source used was a 450 W xenon lamp. Measurements were conducted at room temperature, at an excitation wavelength of 375 nm. The excitation and emission slit width used was 3 nm.

2.3.3.12 Solid state photoluminescence

Photoluminescence measurements were performed on a Renishaw inVia Qontor microscope at an excitation wavelength of 325 nm, at 1 % laser intensity to prevent sample degradation. Measurements were taken over the range 326 - 700 nm at a resolution of 0.026 nm.

In order to determine the extent of drug release for the truncated drug release experiments, emission spectra were first normalised to the intensity at 542 nm (arising from the $^5D_4 \rightarrow {}^7F_5$ electronic transition in Tb^{3+}). The intensity of each spectrum at 512 nm (a wavelength chosen because it shows a marked change in intensity before and after intercalation of ibuprofen) was then used to calculate the release percentage according to Equation 2.4:

$$Cumulative\ release\ (\%) = 100 - \left[\frac{(Sample\ intensity - negative\ control\ intensity)}{(Positive\ control\ intensity - negative\ control\ intensity)}\ x\ 100\right] \qquad (2.4)$$

The negative control is the intensity (at 512 nm) of LTbH-Cl (which represents a theoretical cumulative release of 100 %), and the positive control is the intensity

(at 512 nm) of LTbH-ibu (which represents a theoretical cumulative release of 0 %).

2.3.3.13 Statistical analysis

One-way analysis of variance (ANOVA) was used to determine the statistical significance (at the p = 0.05 level) in the difference of means for viability and particle size measurements. Either a Tukey or Fisher's LSD (if sample means had unequal variance) post hoc test was used to determine which sample means differed significantly from the control. For particle size optimisation experiments, the mean particle size values for each synthetic group were input into JMP Pro 14 software for model fitting and effect screening.

2.4 Results and discussion

2.4.1 SEM

SEM images of LTbH-Cl and LTbH-drug intercalate particles are shown in Figure 2.2. In all formulations, the particles exhibit rod and plate shaped morphologies, with individual particle size ranging from around 100 nm up to 4.5 µm (Figure 2.2, Table 2.1). The average particle size measured for LTbH-Cl was 670 ± 564 nm. It can be seen that the morphology becomes less regular after intercalation. The particle sizes are similar to those previously reported for LGdH-Cl prepared using an identical synthetic protocol (which had sizes 100 nm – 2 µm).[87]

The particles were seen to aggregate to some extent in all formulations, but this was particularly evident for LTbH-ibu and LTbH-nap, with aggregates as large as 15 µm (Figure 2.3). Statistical analysis indicated that there is no significant difference in the particle size before and after drug intercalation, except in the case of LTbH-ibu where average particle size appears to increase relative to

LTbH-Cl. This is in contrast to what was reported for LGdH-Cl and its intercalation compounds, which were found to have decreased particle size after ion exchange.[87] However, this difference is most likely to be a result of particle aggregation, which increases the average size of the particles seen in SEM images, rather than a true increase in the primary particle size.

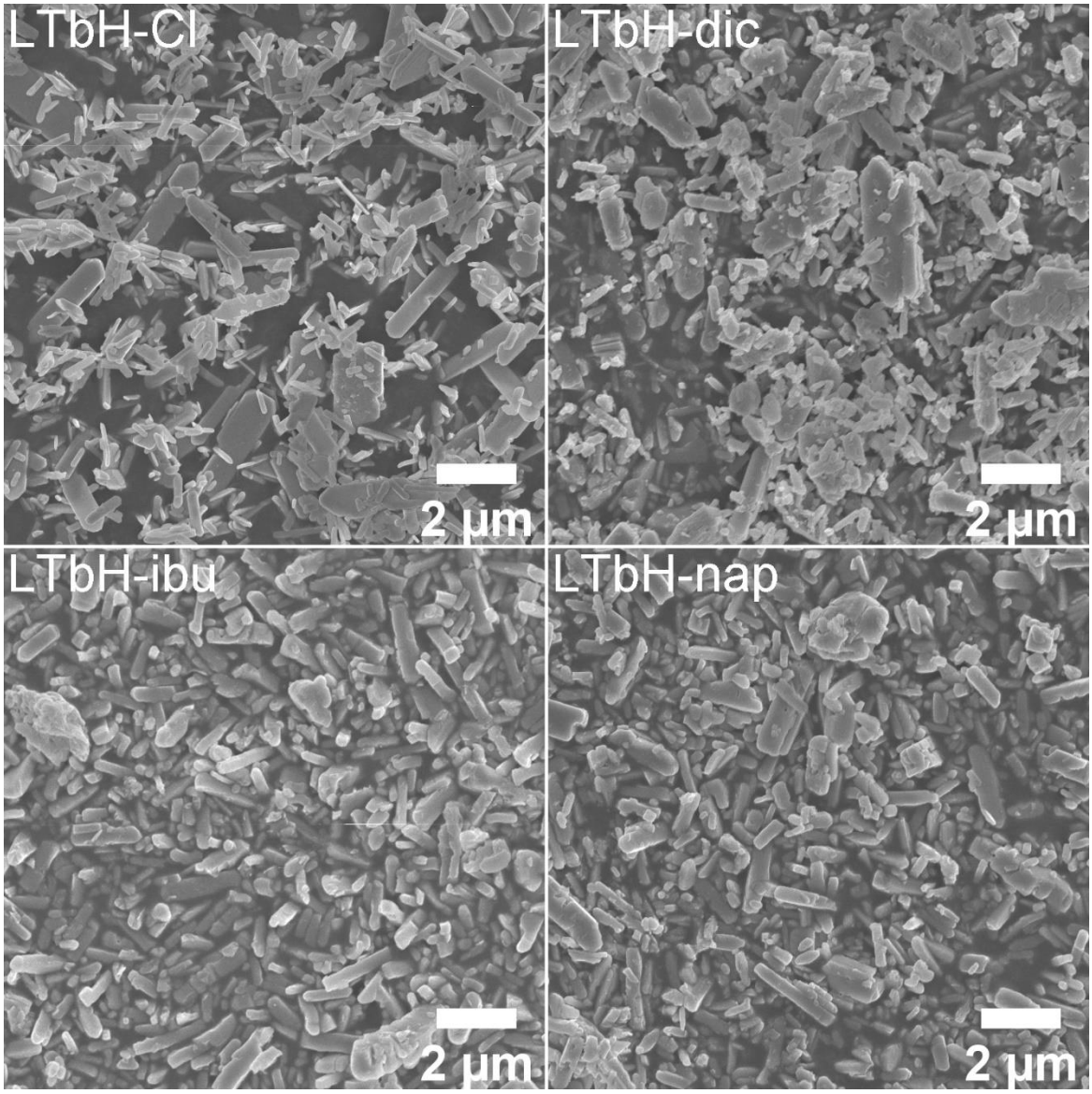

Figure 2.2 SEM images of the LTbH-Cl and LTbH-drug intercalates.

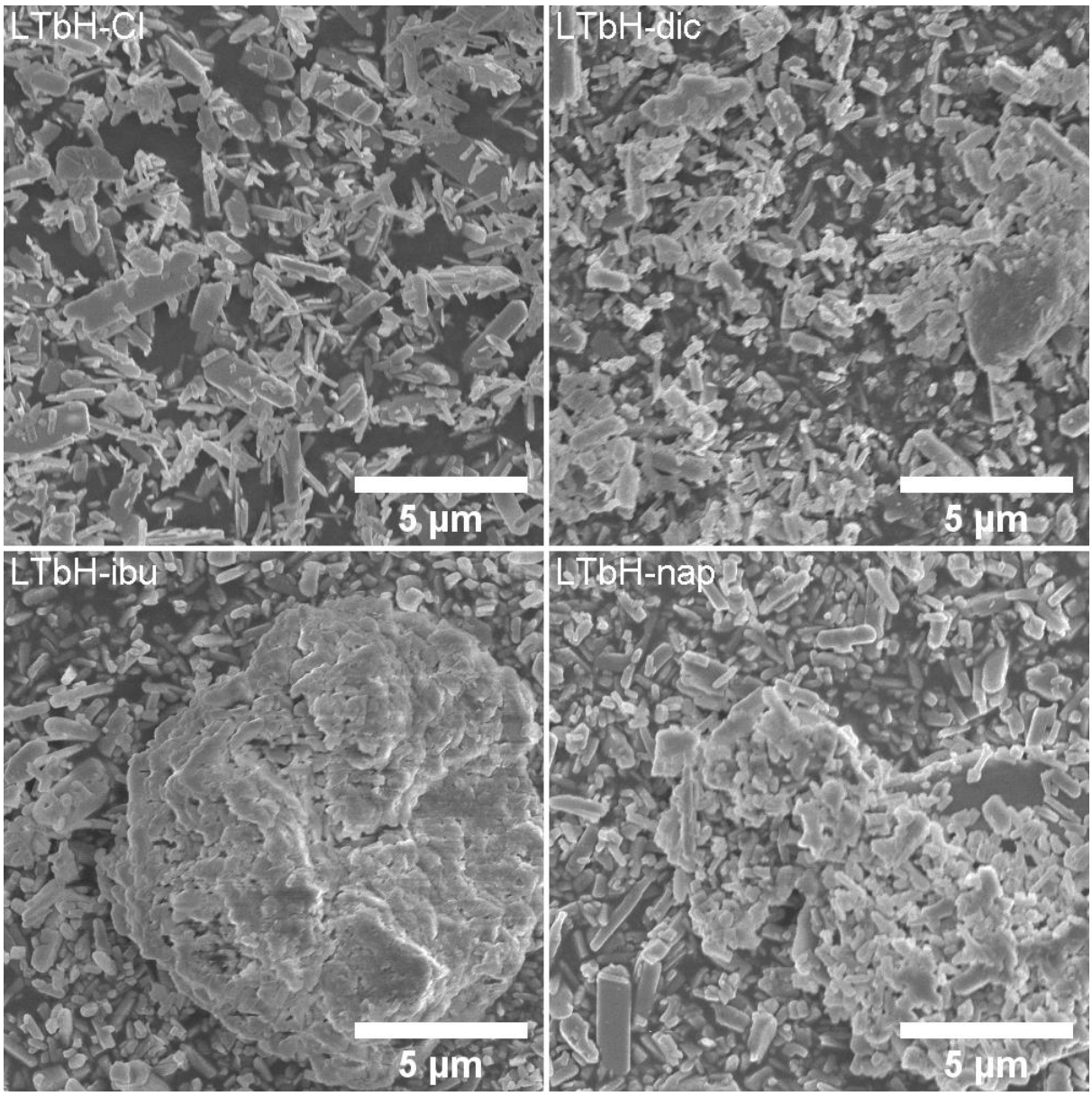

Figure 2.3 Additional SEM images of LTbH-Cl and LTbH-drug intercalates, showing aggregation seen in the samples.

2.4.2 DLS

DLS was used to determine the hydrodynamic size and zeta potential of aqueous suspensions of LTbH-Cl and LTbH-drug intercalates (Figure 2.4, Table 2.1). The hydrodynamic diameter of the particles is approximately 100 nm larger than the size measured from SEM images, which is to be expected as this diameter includes solvent molecules associated with the particles being measured. Therefore, the DLS and SEM data are in good agreement. All samples appear to exhibit some polydispersity, and in most cases a secondary population peak can be seen at around 5-6 microns (Figure 2.4). In all cases, the zeta potential of the suspended particles was positive, indicating a positively charged surface (as would be expected for LRH materials). For LTbH-dic, the zeta potential was markedly lower than the other samples, which suggests it is less stable with respect to aggregation in aqueous suspension. This is believed to be related to the highly hydrophobic nature of diclofenac and may explain why the hydrodynamic diameter measured for LTbH-dic was larger than that of the other samples.

Table 2.1 Summary of the data obtained by SEM and DLS. Data are shown as mean ± S.D. from three independent experiments.

Sample	*Size from SEM (nm)*	*Size from DLS (nm)*	*Polydispersity index*	*Zeta potential (mV)*
LTbH-Cl	670 ± 564	754 ± 58	0.38 ± 0.08	+ 28.7 ± 0.2
LTbH-dic	614 ± 480	903 ± 78	0.41 ± 0.07	+ 8.0 ± 0.4
LTbH-ibu	753 ± 474	858 ± 66	0.45 ± 0.05	+ 36.4 ± 0.4
LTbH-nap	730 ± 526	819 ± 40	0.49 ± 0.06	+ 31.6 ± 0.4

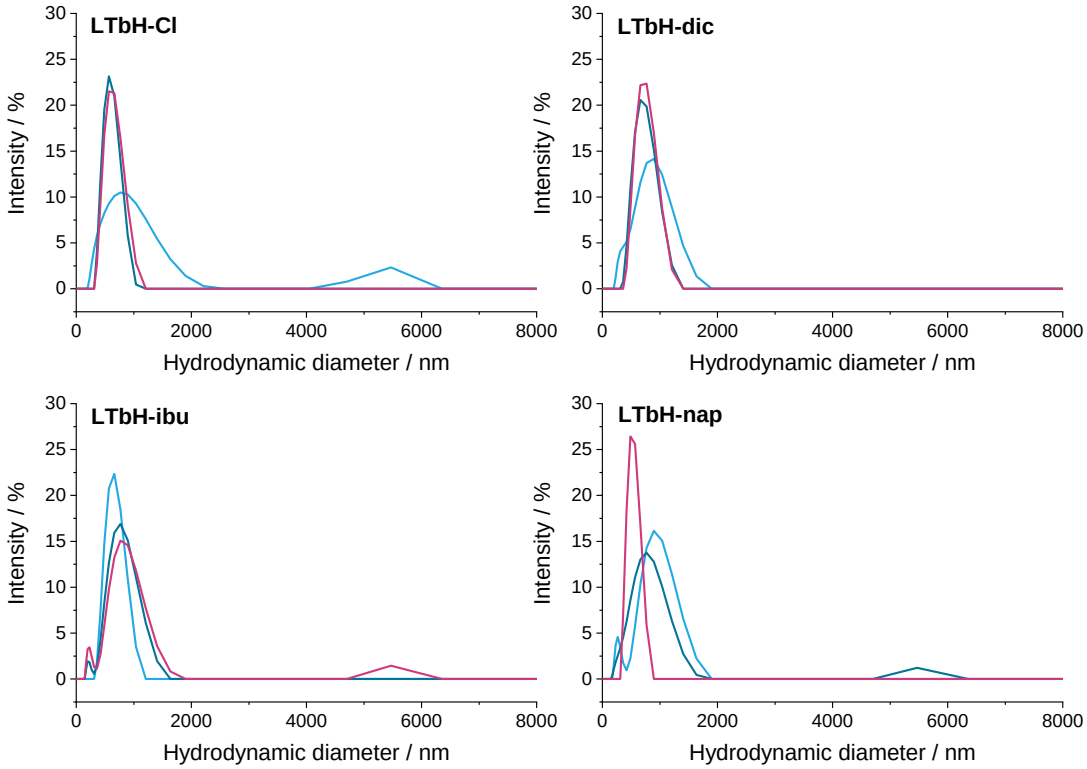

Figure 2.4 DLS plots for aqueous dispersions of LTbH and the LTbH-drug intercalates.

2.4.3 XRD

XRD patterns of the starting materials and the drug intercalation compounds of LTbH obtained by ion exchange are depicted in Figure 2.5. For LTbH-Cl, the pattern contains no residual peaks from the parent terbium salt, showing that a full conversion has taken place. The pattern is consistent with the calculated pattern based on the analogous reported structure[311] for an ytterbium based LRH. In all cases, the presence of strong basal reflections confirms the layered structure of LTbH. In the drug intercalation compounds, the basal reflections are broader and weaker compared to LTbH-Cl, indicating that a loss in crystallinity occurs as a result of the drug anion intercalation. Additionally, the reflections are seen to shift to lower diffraction angles, which is consistent with the layers moving farther apart to accommodate the larger drug anions.[87,120] The reflections arising from LTbH-Cl and the drugs used for intercalation are not visible in the patterns

for LTbH-dic, LTbH-ibu, and LTbH-nap, confirming that ion exchange was successful.

All intercalation compounds appear to be phase pure. The interlayer spacing for LTbH-Cl, LTbH-dic, LTbH-ibu, and LTbH-nap was calculated to be 8.35, 22.01, 25.27 and 22.04 Å respectively. In the case of LTbH-dic and LTbH-nap, these values are consistent with previous reports for LTbH-dic[182] and for similar LGdH systems.[87] A previously reported LGdH-ibu[87] material prepared by ion exchange revealed that two phases formed, with interlayer spacings of 23.46 and 20.73 Å. These are somewhat lower than the interlayer spacing found for LTbH-ibu (25.27 Å). All intercalates can be indexed to the orthorhombic $Pca2_1$ space group, and their refined unit cell parameters are summarised in Table 2.2.

Table 2.2 Summary of (010) reflection positions and unit cell parameters of LTbH-Cl and LTbH-drug intercalates.

Material	*(010) 2θ / °*	*a / Å*	*b / Å*	*c / Å*
LTbH-Cl	10.60	12.66 ± 0.01	8.33 ± 0.01	7.03 ± 0.01
LTbH-dic	4.00	12.37 ± 0.06	22.06 ± 0.07	7.04 ± 0.04
LTbH-ibu	3.52	12.37 ± 0.01	25.28 ± 0.03	7.01 ± 0.01
LTbH-nap	3.98	12.41 ± 0.02	22.04 ± 0.03	7.02 ± 0.01

Based on a model using the previously determined structure of an analogous ytterbium based LRH system,[311] the single layer thickness of LTbH can be approximated as 6.0 Å. Using this value, the gallery heights in LTbH-dic, LTbH-ibu, and LTbH-nap are approximately 16.1, 19.1, and 16.2 Å respectively. These values are 1.3-1.4 times greater than the molecular dimensions of dic and nap (11.8 Å, 10.3 Å)[87,324] and 1.9 times greater than that of ibu (12.9 Å).[87] This strongly suggests that the anions within the interlayer space adopt an intertwined bilayer arrangement (Figure 2.6), which has been previously posited for LRH systems.[87,325] The greater interlayer distance noted with ibu is likely due to the

amphipathic nature of the ibu molecule, which leads to a surfactant-like arrangement in which the hydrophobic hydrocarbon chains are clustered in the middle of the interlayer space while the hydrophilic anionic groups interact with the positive LRH layers above and below. In contrast, dic and nap have electronegative atoms at both ends of the molecule and are therefore able to adopt a more interdigitated arrangement, which results in a lower gallery height.

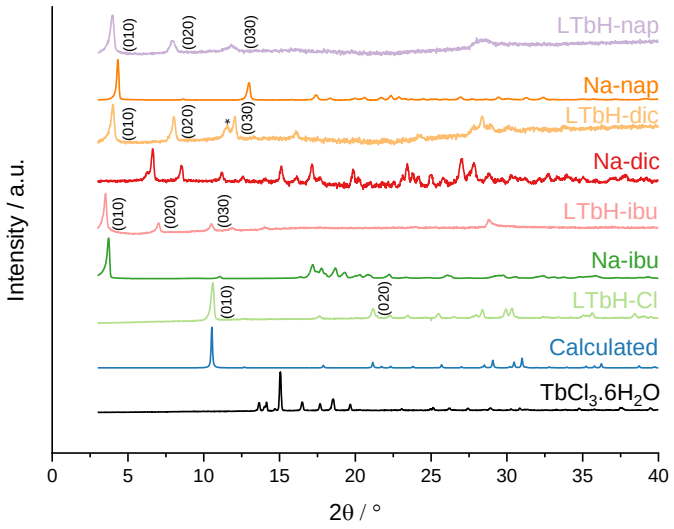

*Figure 2.5 XRD patterns for starting materials and intercalation compounds of LTbH prepared by ion exchange. *: The (030) reflection of LTbH-dic is seen to partially overlap with the (011) reflection. Calculated pattern based on LYbH-Cl (ICSD collection code 419745).*

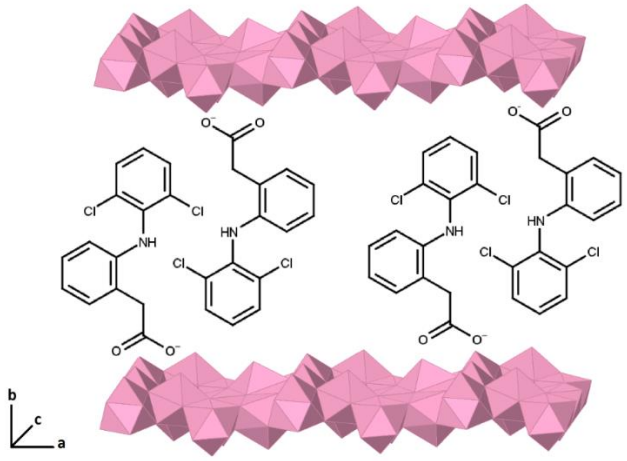

Figure 2.6 Schematic diagram illustrating the bilayer arrangement of intercalated diclofenac within the LTbH interlayer gallery.

2.4.4 FTIR

The FTIR spectra for all obtained intercalation compounds and reagents used are shown in Figure 2.7. The precursor compound LTbH-Cl exhibits multiple broad stretches over the range 3652-3336 cm^{-1} due to O-H stretching vibrations arising from intercalated water molecules and hydroxide groups coordinated to Tb^{3+}. An additional band at 1652 cm^{-1} is seen (Figure 2.7a), which is attributed to O-H bending vibrations. This is consistent with values reported for a similar system based on gadolinium.[87] In addition, the stretch at 1616 cm^{-1}, associated with the O-H δ-bend in $TbCl_3.6H_2O$, is not seen, which confirms that no residual reagent is present.

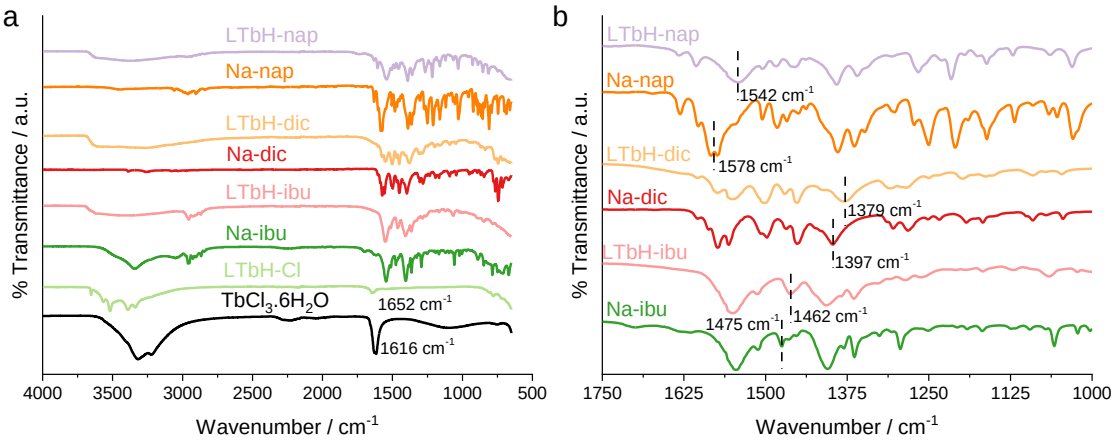

Figure 2.7 a.) FTIR spectra for starting materials and the intercalation compounds of LTbH prepared by ion exchange. b.) Enlarged view showing band shifting in LTbH-drug intercalate spectra relative to the pure drug spectra.

All drug intercalation compounds exhibit the broad O-H stretching seen in LTbH-Cl. Additionally, the intercalates show similar features to the pure drug spectra, particularly in the fingerprint region. In some cases, the band positions in the drug intercalates are shifted to lower wavenumbers. This is particularly evident in the LTbH-nap intercalate, where the 1578 cm^{-1} carboxylate band is seen to shift to 1542 cm^{-1} after intercalation (Figure 2.7b). These shifts are a result of electrostatic interactions between the anionic carboxylate groups on the drug and the cationic LRH layers[120].

2.4.5 TGA

Thermograms of LTbH-Cl and LTbH-drug intercalates are given in Figure 2.8. For all compounds, mass loss below 350 °C occurs in two or three distinct stages, as has been previously reported for LDH systems.[326,327] The first mass loss event between 100-170 °C is attributed to the loss of interlayer water (Table 2.3). This corresponds to 1.5 water molecules per formula unit in LTbH-Cl/ibu/nap, and 2 water molecules per formula unit in LTbH-dic. The second mass loss event, between 200-250 °C, is attributed to the dehydroxylation[328] of the LTbH layers to the terbium oxide form Tb_2O_3 and a residual proton, which is subsequently used to liberate intercalated Cl^- and CO_3^{2-} as HCl and CO_2 gases[328,329] above approximately 500 °C. In the case of LTbH-dic, the second mass loss event overlaps with the loss due to thermal decomposition of intercalated diclofenac, whereas for LTbH-ibu and LTbH-nap the thermal decomposition of intercalated drug is visible as a separate event above approximately 400 °C.

2.4.6 Chemical formulae

Elemental analysis and TGA data (Table 2.3, Figure 2.8) were used to derive the formulae of the intercalation compounds (Table 2.4). It is presumed that residual Cl^- anions are present in the structures of LTbH-dic and LTbH-nap, due to incomplete ion exchange. This leads to drug anions and Cl^- anions being distributed within the same layers of LTbH,[87] as there is no evidence of any remaining LTbH-Cl phase present in the respective XRD patterns. In addition, in the case of LTbH-Cl and LTbH-dic, the elemental analysis data indicate the presence of CO_3^{2-} anions between the layers. This is believed to be due to the dissolution of atmospheric carbon dioxide into the solution during the synthetic or ion exchange process, which is a problem previously reported for LDH

systems.[118,330] The average drug loading in the formulations is approximately 33 % by mass, which corresponds to 80-100 % of the maximum capacity as determined by charge balance considerations.

Loading capacity of 33 % w/w would be adequate to deliver single doses of dic, ibu, and nap (75 mg, 400 mg, and 500 mg respectively).[331–333] In regards to intravenously delivered chemotherapeutic drugs such as doxorubicin or paclitaxel, which are usually administered at a minimum dosage of 60 mg and 135 mg per m^2 of body surface area respectively,[334,335] the loading capacity of LTbH is more than sufficient given that the effective dose for intratumoral delivery is expected to be lower than that for systemic delivery.

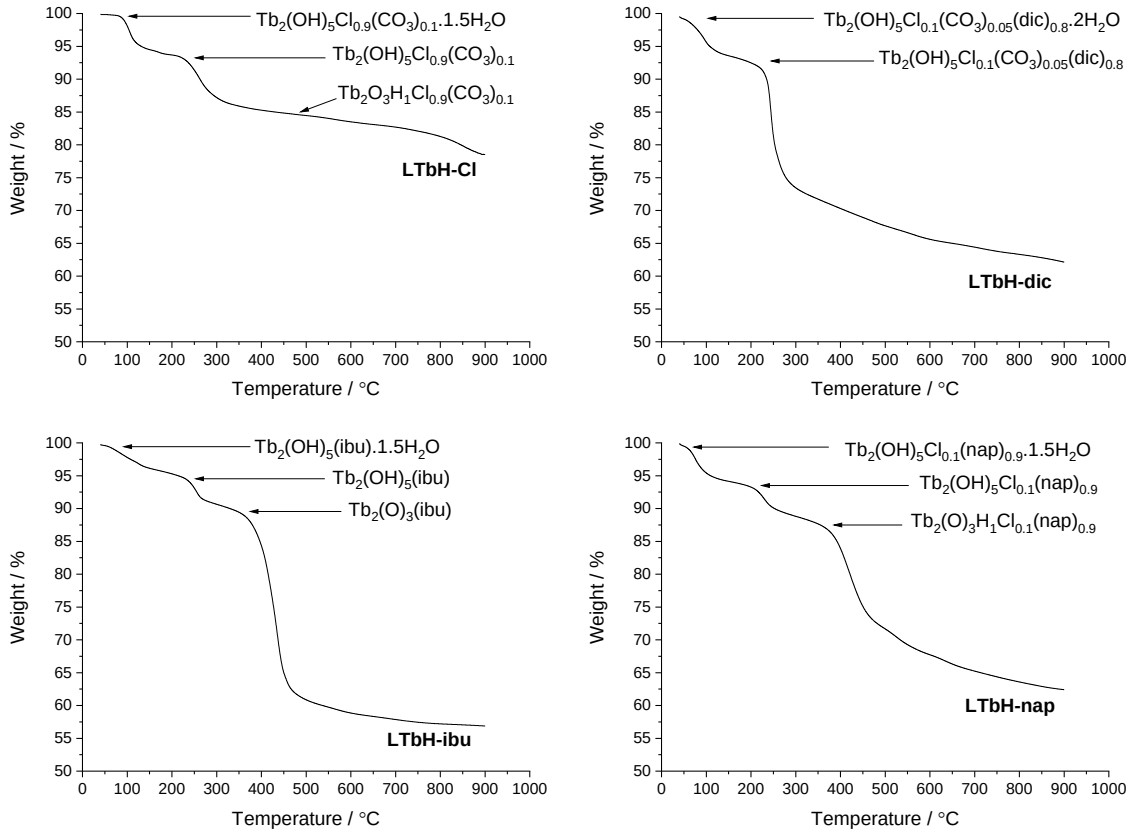

Figure 2.8 Thermograms of LTbH-Cl and LTbH-drug intercalates, showing intermediate phases calculated based on % mass loss.

Table 2.3 Summary of observed (and calculated from formulae, Table 2.4) values for elemental analysis and TGA data.

Material	*%C*	*%H*	*%N*	*Mass loss % (H_2O)*
LTbH-Cl	0.29 (0.13)	1.48 (1.73)	-	5.78 (5.81)
LTbH-dic	20.12 (19.82)	2.12 (2.51)	1.66 (1.64)	5.26 (5.29)
LTbH-ibu	24.81 (24.58)	2.65 (3.97)	-	4.25 (4.25)
LTbH-nap	23.96 (23.65)	2.61 (3.10)	-	5.82 (4.22)

Table 2.4 Summary of formulae derived from TGA/elemental analysis data.

Material	*Formula*	*Drug loading / % mass*
LTbH-Cl	$[Tb_2(OH)_5]Cl_{0.9}(CO_3)_{0.05}\cdot 1.5H_2O$	0
LTbH-dic	$[Tb_2(OH)_5]Cl_{0.1}(CO_3)_{0.05}(C_{14}H_{10}Cl_2NO_2)_{0.8}\cdot 2H_2O$	34.6
LTbH-ibu	$[Tb_2(OH)_5](C_{13}H_{17}O_2)\cdot 1.5H_2O$	32.3
LTbH-nap	$[Tb_2(OH)_5]Cl_{0.1}(C_{14}H_{13}O_3)_{0.9}\cdot 1.5H_2O$	32.2

2.4.7 Cytotoxicity assay

Cytotoxicity of the LTbH formulations was evaluated using *in vitro* cell viability experiments on Caco-2 and HEK 293 cell lines, the results of which are presented in Figure 2.9. For the Caco-2 cell line, there is some cell death seen in all treatment groups as compared to the untreated cells control. At the higher concentration of 526 µg / ml, all three drug intercalate formulations show statistically significant cytotoxicity, with the viability of cells treated with LTbH-dic decreasing the most to an average of 71%. LTbH-Cl does not appear to be significantly cytotoxic at either concentration. This suggests that the cytotoxicity seen arises from the intercalated drug anions. However, this contrasts with findings from a previous study on LGdH-Cl, LGdH-dic, and LGdH-ibu, which reported an increase in Caco-2 cell viability in the presence of these materials at a concentration of 270 µg / ml.[87] The precise source of this difference is not known, but it may be related to differences in cell uptake or drug release rate.

For the HEK 293 cell line, a degree of cytotoxicity is seen in the LTbH-Cl and LTbH-nap treatment groups at both concentrations, which is comparable to the slight decrease in cell viability seen in the Caco-2 cell line. Conversely, the LTbH-dic and LTbH-ibu groups appear to encourage cell proliferation, even at the higher concentration of 526 µg / ml, with average cell viabilities statistically higher than those of the untreated control. Overall, the biocompatibility of the formulations appears to be good even at high concentrations of the formulations.

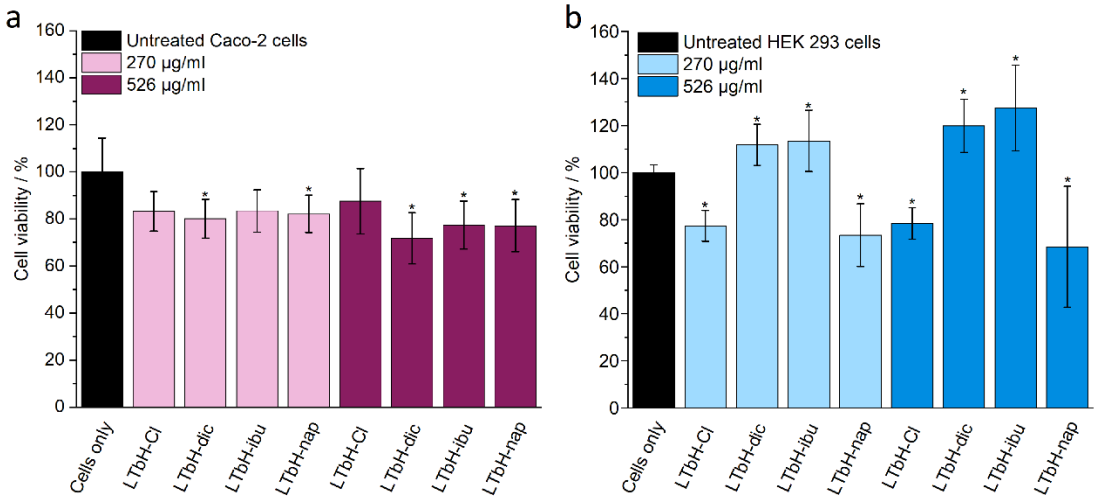

*Figure 2.9 The results of in vitro cell viability assays a.) Caco-2 and b.) HEK 293 cell lines, performed with LTbH intercalates at two concentrations (270 µg / ml and 526 µg / ml). The assay experiment was performed three separate times, each in triplicate. Results are presented as mean ± standard deviation. * denotes groups with a significantly different mean viability from the control, at the p = 0.05 level.*

The treatment of cancer cell lines (HeLa, fibroblast, and rhabdomyosarcoma) with diclofenac has been reported to cause significant decreases in cell viability at a concentration of just 11 µM.[336] Likewise, the cytotoxicity of ibuprofen has been previously studied using adenocarcinoma gastric cell line (AGS), and cell viability found to decrease after 24 h exposure to ibuprofen at a concentration of just 100 µM.[337] Naproxen has been reported to cause significant cell death compared to untreated cells controls in urinary bladder cancer cell lines (UM-UC-5 and UM-UC-14) at a concentration of 500 µM.[338] The findings of these studies therefore seem to support the assertion that the cytotoxicity exhibited by the LTbH-drug

intercalates may in fact arise from the intercalated drug ions as opposed to the presence of the particles themselves.

To probe if this is the case, a further cytotoxicity experiment was conducted using pure drug solutions at a concentration approximately equivalent to the LTbH-drug intercalates (assuming 30 % drug loading). The results of this experiment are shown in Figure 2.10.

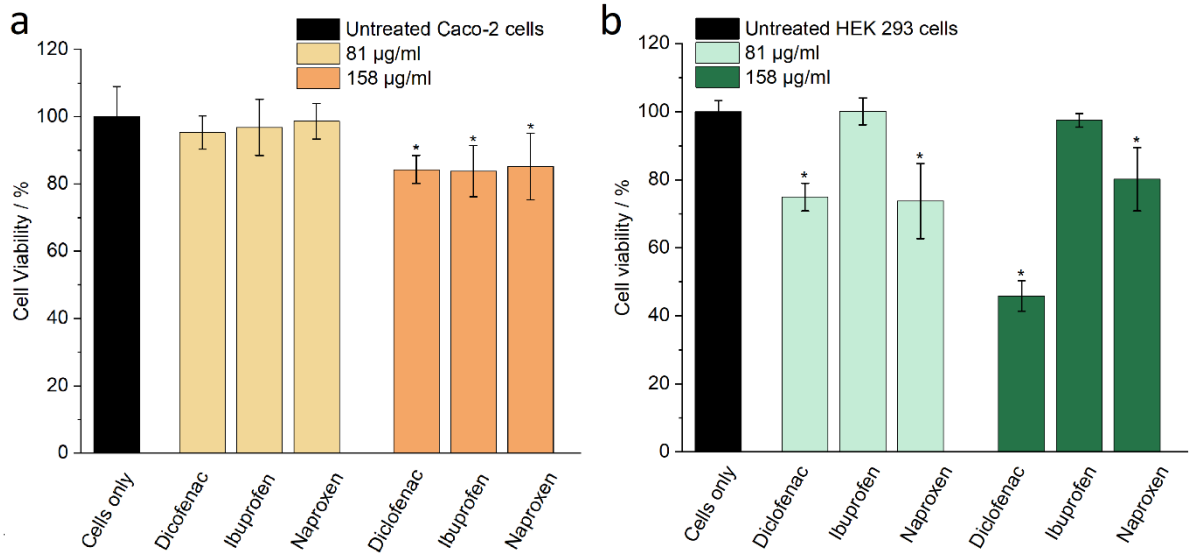

*Figure 2.10 Graphs showing the results of in-vitro cell viability assay of a.) Caco-2 and b.) HEK 293 cell lines, with diclofenac, ibuprofen, and naproxen at two concentrations (81 µg / ml and 158 µg / ml). The assay experiment was performed three separate times, each in triplicate. Results are presented as mean ± standard deviation. * denotes groups with a significantly different mean viability from the untreated cells control, at the p = 0.05 level.*

It was found that for Caco-2, all three drugs exhibited a mild cytotoxic effect at the higher drug concentration of 158 µg / ml, but cell viability was not significantly affected at the lower drug concentration of 81 µg / ml. In the case of HEK 293 cells, ibuprofen was well tolerated and showed no cytotoxic effect at either concentration, whereas diclofenac and naproxen showed a statistically significant impact on viability. When taken together, the data seem to suggest any cytotoxic effects seen may be due to the presence of a relatively high concentration of LTbH particles which may interfere with the growth of cells, along with contributing effects arising from the presence of the pure drugs.

2.4.8 Haemolysis assay

The haemolytic potential of the LTbH intercalates on red blood cells (RBCs) from rats was studied, and the outcome of this investigation is shown in Figure 2.11. Compared to the untreated RBCs and the RBCs treated with the surfactant Triton-X, it can be seen that the presence of LTbH-Cl or any of the LTbH-drug intercalates does not cause any substantial degree of haemolysis. This is the case at both concentrations of 270 and 526 µg / ml. This indicates that LTbH particles do not disrupt the membrane of RBCs, and therefore supports the idea that formulations containing LTbH could be used for intravenous or intratumoral administration without haemotoxic effects.

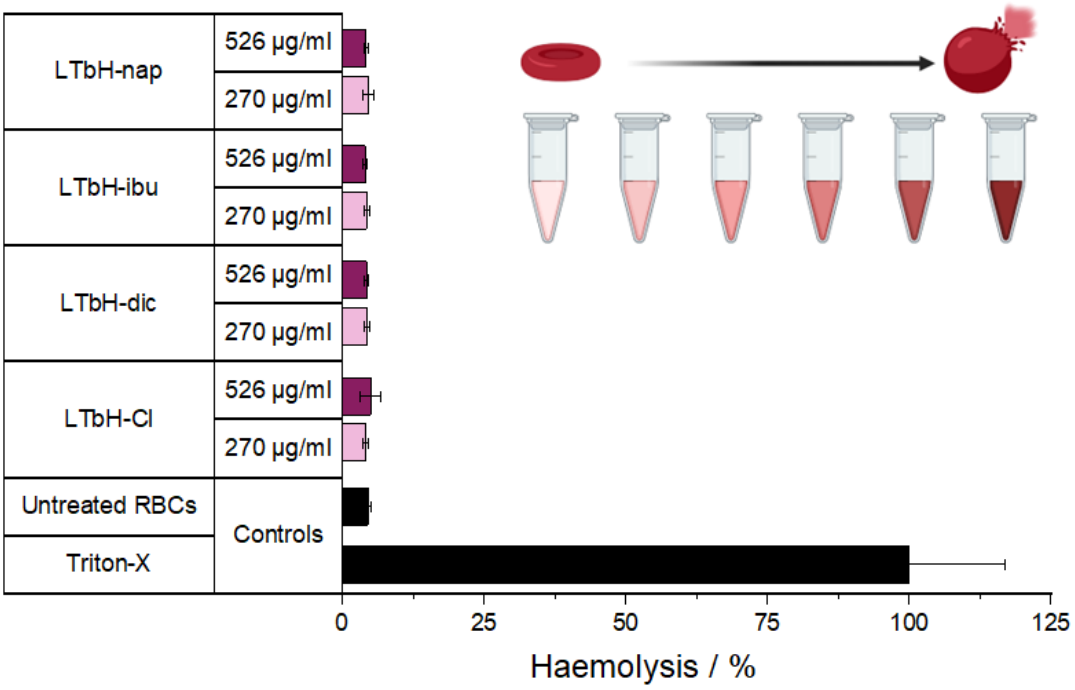

Figure 2.11 The results of in vitro haemolysis assays with LTbH intercalates at two concentrations (270 µg / ml and 526 µg / ml). The assay experiment was performed three separate times, each in triplicate. Results are presented as mean ± standard deviation. All treatment groups differed significantly from the Triton-X treated RBC control at the p = 0.05 level. Inset: graphical representation of the basis of the colorimetric haemolysis assay. RBCs which remain intact after treatment with LTbH produce a colourless supernatant, whereas lysed RBCs release haemoglobin that remains in the supernatant after centrifugation and produces a deep red colour.

2.4.9 Stability assay

It is known that LDH materials are unstable in acidic suspensions,[339] as metal hydroxides undergo acid hydrolysis which results in the dissolution of the LDH and the subsequent release of free metal ions into the solution. As LRH materials are also a metal hydroxide system, it was of interest to establish the pH range over which LTbH-Cl is stable in aqueous suspension. This is particularly important because the toxicology of Tb^{3+} has not been evaluated in detail, but free Gd^{3+} ions are well known to be toxic to humans.[340] For biomedical applications, it is necessary to minimise the release of free ions with potential toxicity issues. For this reason, a stability assay using arsenazo-3 (AS-3) was conducted on LTbH-Cl in aqueous suspensions at a range of pH values (pH = 1.5-10).

It is important to note that the performance of the AS-3 assay is known to be pH dependant.[341] An experiment to probe this change in performance was conducted, and the results are displayed in Figure 2.12. The characteristic absorbance peaks for both complexed and unbound AS-3 were seen to appear at a slightly lower wavelength at pH = 1.5 than at pH = 7.4. This difference in absorbance maxima positions does not reduce the ability of the assay to qualitatively verify whether LTbH-Cl dissolves at given pH. A further experiment was conducted to probe the change in absorbance at 652 nm as a factor of pH, and the outcome of this experiment is shown in Figure 2.13. It was found that the average absorbance across the pH range = 1.5 – 10 remains consistent, with no significant difference in absorbance seen between the extremes of the range. Therefore, for the purposes of quantifying the extent of dissolution of LTbH across

this range of pH values, the performance of the AS-3 assay appears to be satisfactory.

The extent of dissolution of LTbH-Cl in each sample at 2 and 24 hours after immersion was then quantified using a colorimetric assay which tests for the presence of free Tb^{3+} ions. The results of this assay are given in Figure 2.14.

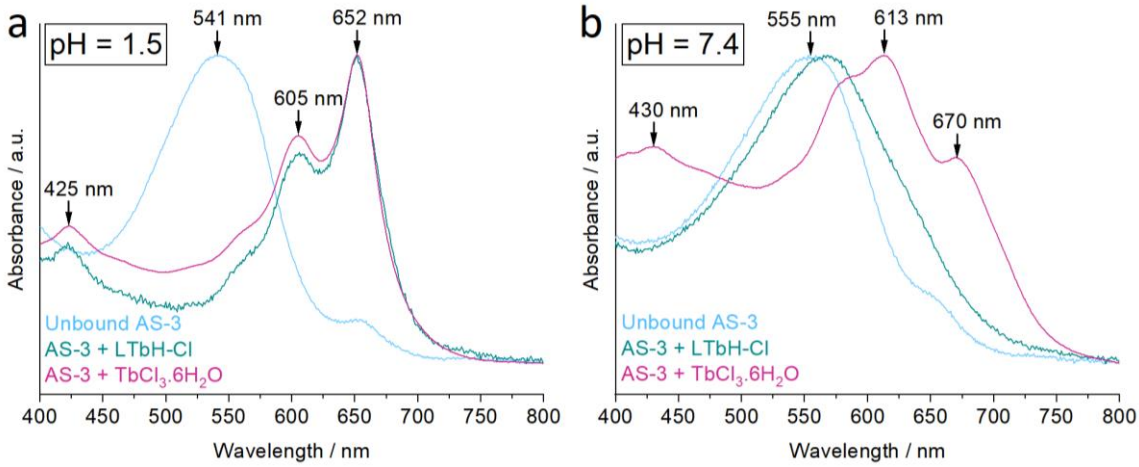

Figure 2.12 Graphs showing the absorbance spectra of unbound AS-3, AS-3 with LTbH-Cl, and AS-3 with $TbCl_3.6H_2O$ at a.) pH 1.5 and b.) pH 7.4. It can be seen that the characteristic peaks of both unbound and bound AS-3 appear at a slightly lower wavelength in acidic media relative to media at pH = 7.4.

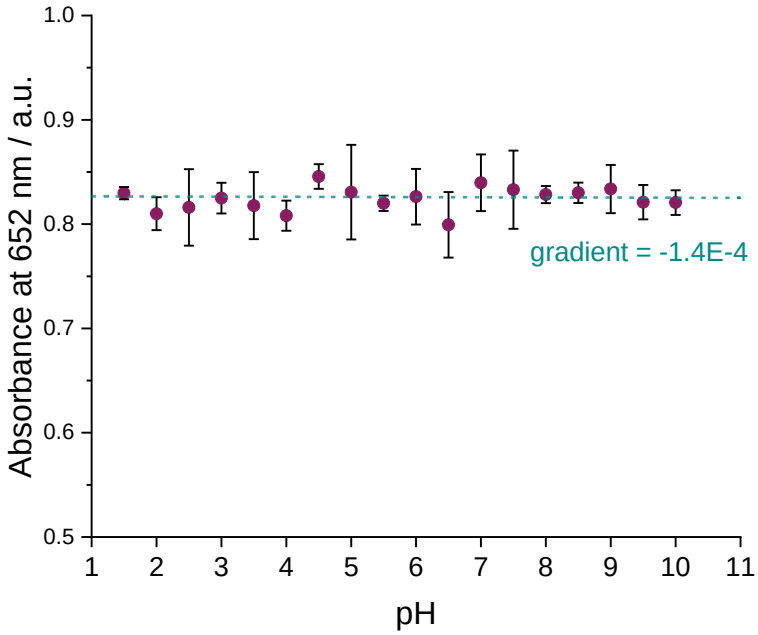

Figure 2.13 Plot showing the absorbance data at 652 nm of 1.25 mM solutions of $TbCl_3.6H_20$ in water (reacted with equal volumes of a 2.5 mM solution of AS-3) across a range of pH values. The experiment was performed three separate times, each in triplicate. Results are presented as mean ± standard deviation. The line of best fit (dashed) and associated gradient demonstrates negligible change in absorbance over pH range.

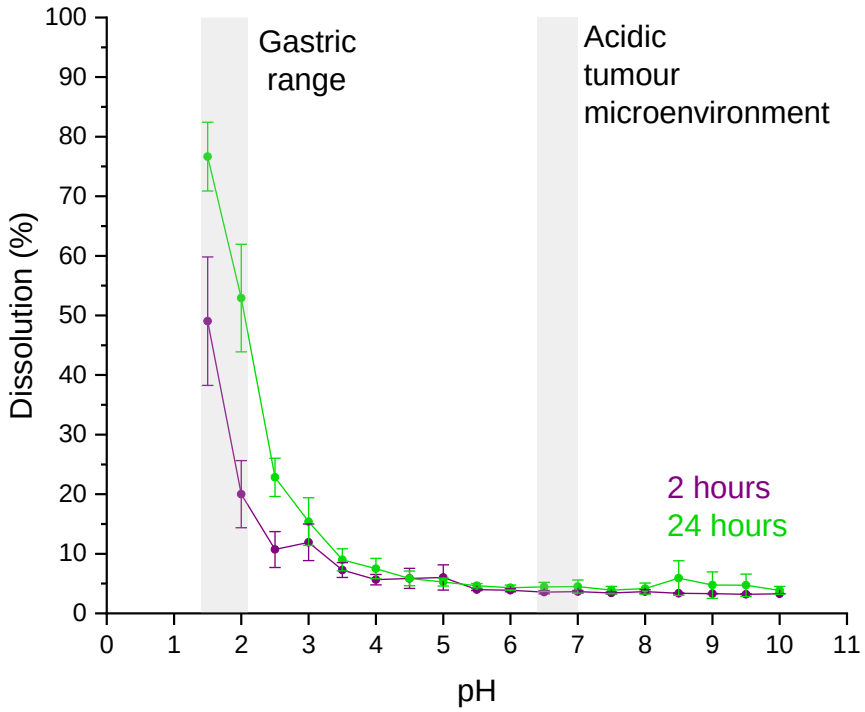

Figure 2.14 pH stability assay of LTbH-Cl in aqueous suspension, after 2 and 24 hours. Three independent experiments were performed, each in triplicate, and the results are shown as mean ± standard deviation.

Significant dissolution of LTbH-Cl is seen in the pH range 1-5-3.0, which corresponds to the typical pH values seen in the gastric environment (pH = 1.0 - 2.0 in the fasted state, up to a median pH = 5.0 in the fed state).[342] Therefore, formulations containing LTbH materials which are designed for oral delivery may require the use of an enteric coating to prevent degradation and the release of free Tb^{3+} ions. Above this pH range, however, the suspensions exhibit high stability with minimal dissolution (approximately 5 %) seen after 24 hours. This includes the average physiological pH (7.4)[343] as well as the slightly acidic extracellular environment often found in tumours (pH = 6.4 – 7.0).[344] Assuming a theoretical LTbH-ibu dose of 1300 mg (which contains the equivalent of a single dose of ibuprofen), 5 % dissolution would equate to 33 mg of free Tb^{3+} ions released. In a person weighing 60 kg, this is equivalent to 0.55 mg Tb^{3+} per kg body mass – several orders of magnitude below the reported LD_{50} for intravenously injected $GdCl_3$ (100 mg per kg body mass in mice,[345] equivalent to

60 mg of free Gd^{3+} ions per kg body mass). Whilst discussion of how Tb^{3+} ions may behave *in vivo* is beyond the scope of this study, the cytotoxicity studies and dissolution stability data seem to indicate that LTbH-based drug delivery systems may be safe to use for short-term treatments where accumulation of free lanthanide ions would be limited.

2.4.10 Drug release

Drug release from LTbH-dic, LTbH-ibu, and LTbH-nap was studied using phosphate buffered saline (PBS, pH = 7.4) as the release medium. The results are given in Figure 2.15. It can be seen that the drug release profiles are very similar in the three formulations, with the majority of release occurring rapidly within the first 5 hours. Further release after around 6 hours is negligible. The mean final release percentage in all cases is between 91 – 96 %.

These release profiles are consistent with previous reports for LTbH-asa (approx. 85 % release in 6 hours),[88] and LEuH-nap (complete release within 200 minutes).[123] However, previously reported release profiles for LTbH-dic and LTbH-imc (approx. 35 % and 30 % in 6 hours respectively)[182] differ significantly. This may be related to the particle morphology of LTbH used in those studies – though no particle size analysis was presented in the previous study,[182] SEM images showed large and clustered crystals which may introduce a longer diffusion path to the intercalated drug molecules and therefore lead to extended release kinetics.

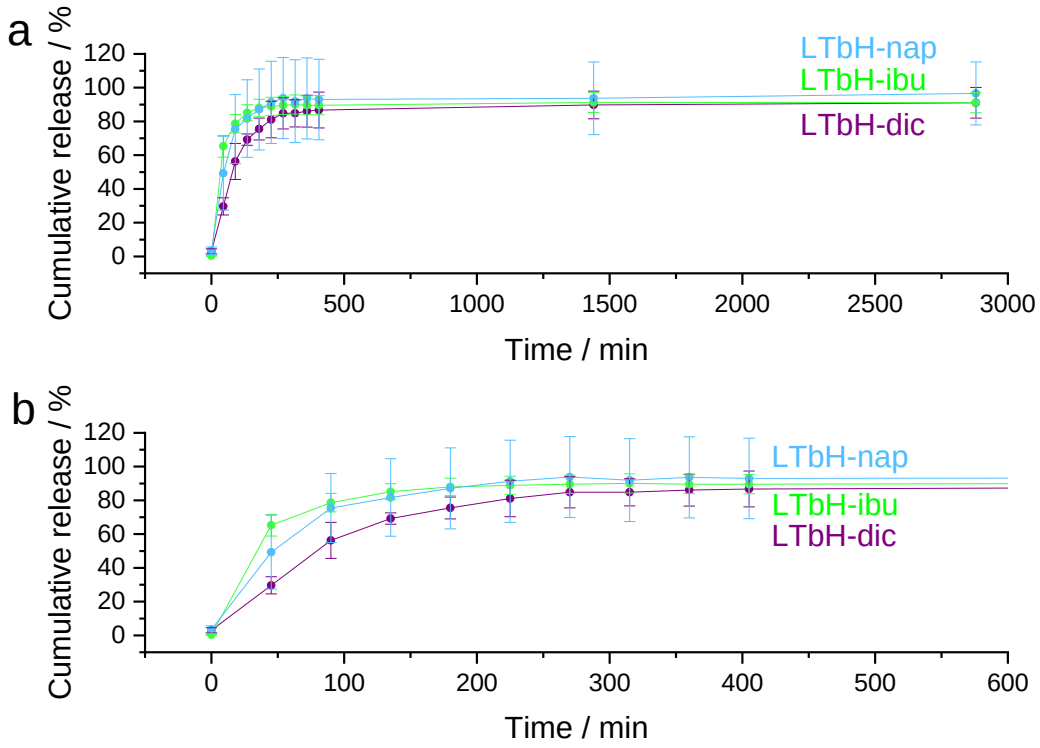

Figure 2.15 Drug release curves for LTbH-dic, LTbH-ibu, and LTbH-nap in phosphate buffered saline (PBS, pH = 7.4) a.) over 48 h and b.) an enlarged view of the first 10 h. Results are presented as mean ± standard deviation.

The drug release data were fitted with the Bhaskar and Avrami models (Equations 2.5 and 2.6 respectively); α is extent of reaction, equivalent to the fraction of intercalated drug released, k is the rate constant, t is time, and n is a coefficient related to the reaction mechanism.

$$\ln(1-\alpha) = kt^{0.65} \tag{2.5}$$

$$\ln(-ln(1-\alpha)) = nln(t) + \ln(k) \tag{2.6}$$

Fits of the Avrami and Bhaskar models to the LTbH-drug intercalates are shown in Figure 2.16. The Avrami equation can be used to describe a wide range of solid-state kinetic processes (usually involving the generation and growth of nuclei) and appears to be a good fit to the drug release data from LTbH. n values, derived from the slope of the line of best fit in the plots, are all close in value to 1. Whilst this does not definitely determine the precise release mechanism, it is

consistent with a 2D diffusion controlled process in which the rate of nucleation is zero.[87,346,347] In the context of the LTbH-drug intercalates, this is sensible because new nucleation sites (the positively charged layers with associated drug molecules) are not generated during the course of the reaction. The rate of reaction is thus controlled by the diffusion of the drug ions between the layers (hence, 2D).

The Bhaskar model was originally developed to describe the diffusion of drug cations out of an ion exchangeable resin,[348] and is therefore a good approximation for the diffusion of drug anions out of LRH particles. The model is based on the assumption that rate of release is controlled by diffusion of the drug through the particle, and the good fit of this model to the LTbH-drug release data strongly suggests that this is also the case in LTbH systems. These findings are in good agreement with those for LGdH-drug intercalates.[87] If it was desired to increase the length of time over which sustained release occurs from LTbH, a possible approach would be to use a polymeric coating to increase the diffusion path for the drug molecule, as has been demonstrated on many occasions with other materials – including LDHs.[349,350]

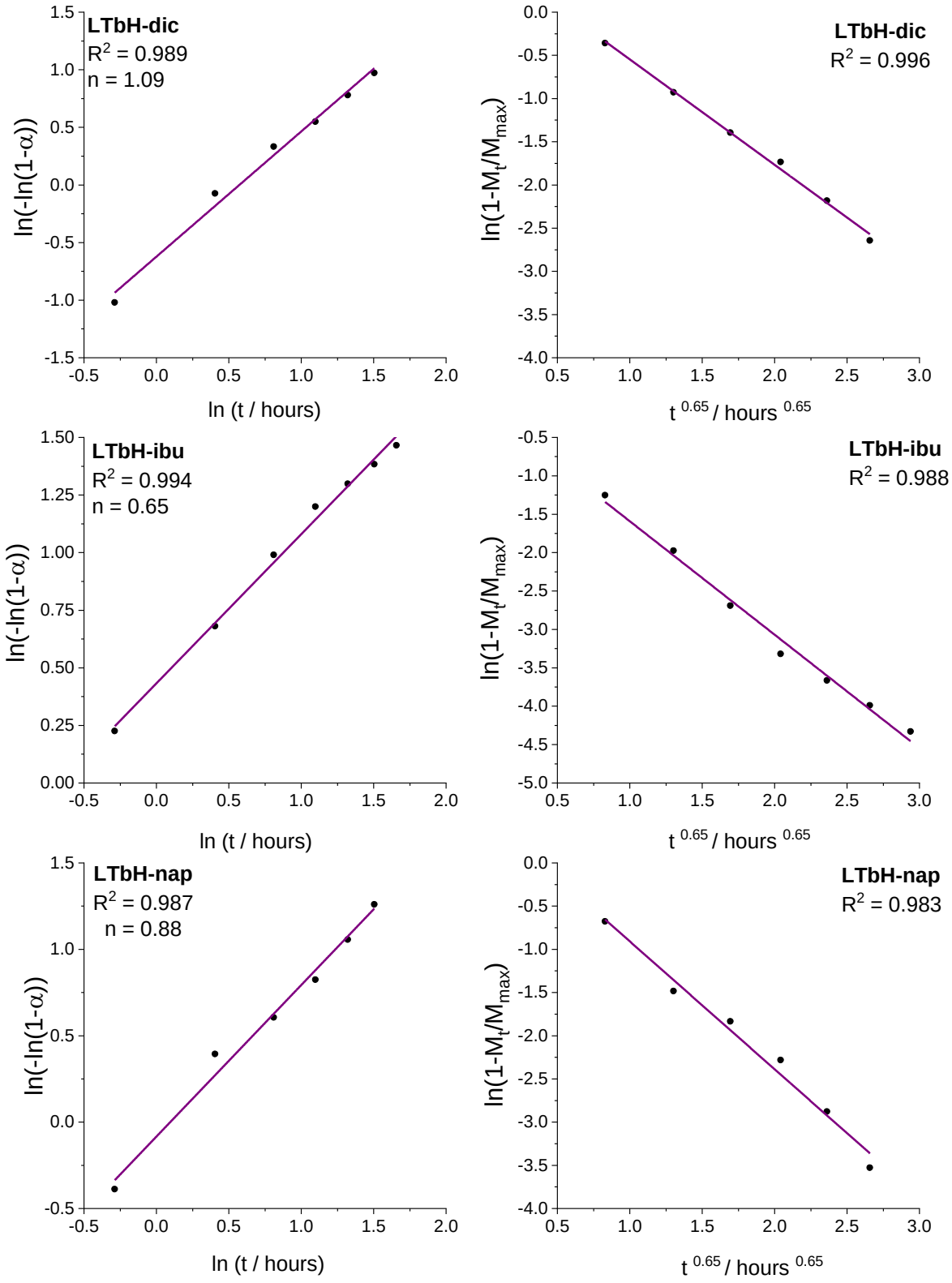

Figure 2.16 Fits of the Avrami (left) and Bhaskar (right) models to drug release data from LTbH-dic, LTbH-ibu, and LTbH-nap.

2.4.11 Fluorimetry

Emission spectra of suspensions of LTbH-Cl and LTbH-drug intercalates measured at an excitation wavelength of λ = 375 nm, are presented in Figure 2.17. In each case, the characteristic Tb^{3+} f-f transitions ($^5D_4 \rightarrow {}^7F_6$ at 490 nm, $^5D_4 \rightarrow {}^7F_5$ at 545 nm, $^5D_4 \rightarrow {}^7F_4$ at 586 nm) are visible and in good agreement with peak positions reported[323] for LTbH-NO_3. The emission spectrum of LTbH-Cl shows evidence of peak splitting by the presence of a shoulder to the right of each peak, which is consistent with the presence of both 8 and 9 coordinate sites for Tb^{3+} within the LTbH structure.[311,323] The amount of sample used during measurement was not controlled, and therefore quantitative comparisons between sample luminescence intensities cannot be drawn. However, it is evident from the data before normalisation (Figure 2.17a) that the intercalation of dic, ibu, and nap appears to cause significant dampening in the signals with respect to the baseline, with this effect being most pronounced in LTbH-nap and least evident in LTbH-ibu. After normalisation (Figure 2.17b), it can also be seen that nap generates some background interference below approximately 480 nm and above approximately 560 nm, but no additional features arising from the intercalated drugs can be seen. The source of the curved baseline in the spectra is not known but is believed to be instrument related.

These results demonstrate firstly that both LTbH and LTbH-drug intercalates exhibit the expected characteristic Tb^{3+} luminescence features which could be exploited for medical imaging applications. Secondly, it appears that luminescence intensity of LTbH may vary depending on the intercalated guest species, which may make it possible to monitor drug release via signal change.

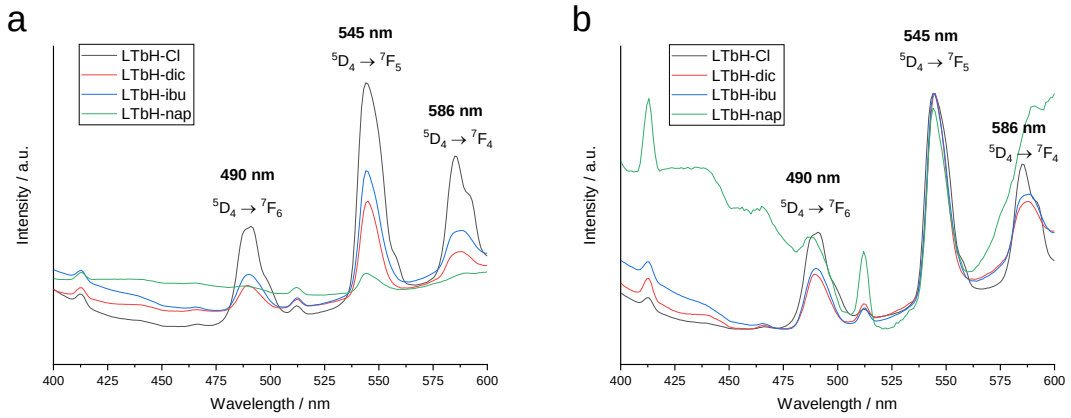

Figure 2.17 Solid state luminescence emission spectra for LTbH-Cl and LTbH-drug intercalates, collected with an excitation wavelength of 375 nm. a.) Raw data and b.) Normalised data.

2.4.12 Solid-state photoluminescence

In order to obtain emission spectra of a higher quality (stable baseline, presence of fine features, no confounding effect from drug release), solid state emission spectra of LTbH-Cl, the LTbH-drug intercalates, and the pure drug salts (Na-dic, Na-ibu, Na-nap) were measured at an excitation wavelength of λ = 325 nm (Figure 2.18a-d). Solid state measurements eliminate vibrational energy loss to solvent molecules, leading to enhanced signal (and therefore greater fine feature resolution).[351] The excitation wavelength used for these experiments was more energetic (325 nm instead of 375 nm as in the suspension fluorescence experiments), because the instrument used possesses only fixed-wavelength lasers, of which 325 nm was the closest matched. The photoluminescence emission spectrum of LTbH-Cl shows well resolved fine features and clear evidence of peak splitting arising from the low symmetry coordination environment[311] of Tb^{3+}.

As it was not possible to control for the mass of sample used in each measurement (in each case, *ca.* 5 mg), the differences in intensity between samples cannot be quantified. However, it can be assumed that small differences in mass of sample would not fully account for the large difference in the

magnitude of intensity between LTbH-ibu or LTbH-nap relative to LTbH-Cl or LTbH-dic in the data before normalisation (Figure 2.18a). This indicates that the interaction between the LTbH matrix and dic differs in nature to that of LTbH with ibu or nap, leading to a different relaxation pathway. This is also supported by the significant shift in peaks arising from dic after intercalation, which can be seen in the spectra after normalisation, and the much-reduced degree of drug peak shifting in LTbH-ibu and LTbH-nap (Figure 2.18b-c). The decreased luminescence intensity of LTbH-dic is in contrast with a previous study, which reported increased luminescence intensity after intercalation of dic.[182] However, due to significant differences in the synthetic method and the excitation wavelength used 352 nm vs 325 nm) the emission spectra obtained in the previous study cannot be directly compared to those in the present work.

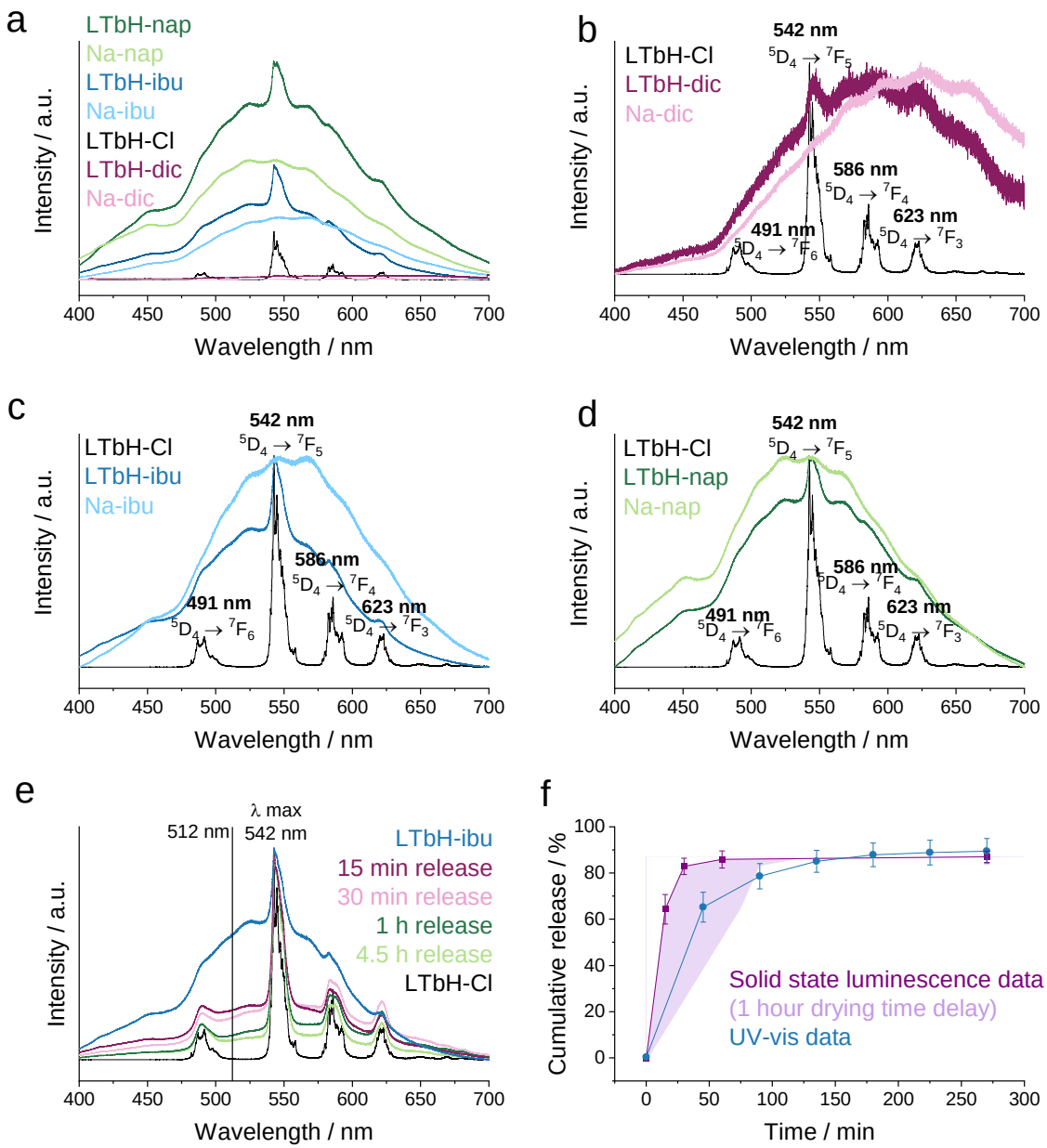

Figure 2.18 Solid state photoluminescence emission spectra of LTbH-Cl, LTbH-drug intercalates, and the pure drug salts (Na-dic, Na-ibu, Na-nap) obtained at an excitation wavelength of 325 nm and laser power of 1 %. a.) Raw data, b-d.) Normalised data. e.) Normalised solid state photoluminescence emission spectra of LTbH-ibu (pure) and LTbH-ibu at different stages of release (15 min, 30 min, 1 h, and 4.5 h) as compared to LTbH-Cl. f.) Drug release curve obtained from photoluminescence compared to the drug release curve obtained by UV-vis. Three independent experiments were performed, and the results presented as mean ± standard deviation.

Since the spectra for the LTbH-drug intercalates show a combination of features from the pure drugs and a strong peak at 542 nm arising from Tb^{3+}, it was thought that it may be possible to use the ratio between the height of the 542 nm peak and the height of the surrounding background to establish the extent of drug release. Presumably, as more drug is released from the formulation, the height

of the peak arising from Tb^{3+} would increase relative to the signal arising from the drug, and the spectrum would become increasingly similar to the spectrum of LTbH-Cl. Similar real-time tracking of drug release has been reported before, for instance for doxorubicin release from silica nanoparticles (using fluorescence resonance energy transfer),[352] or rhodamine release from a hydrogel (by multispectral fluorescence imaging on live mice).[353]

To test this hypothesis, further drug release experiments were conducted using LTbH-ibu, in which the experiment was terminated at specific time points and the solids recovered for photoluminescence analysis. The results of one such experiment are given in Figure 2.18e. It can be seen that the spectra from samples that have the shortest release times (15 min, 30 min) are more similar in character to the spectrum of LTbH-ibu, whereas those with a longer release time (1 h, 4.5 h) more closely resemble that of LTbH-Cl. The halo-like intensity arising from the presence of the drug appears to decrease in magnitude with length of release time. This is particularly evident in the region between the first two Tb^{3+} transition peaks, and the intensity of each sample at 512 nm was chosen as a reference point for further calculations.

Assuming the spectra of LTbH-ibu and LTbH-Cl represent the theoretical 0 % and 100 % release respectively, the cumulative release in each of the experimental samples was calculated using their intensity at 512 nm. The resultant drug release curve obtained is shown in Figure 2.18f. It can be seen that this release curve closely resembles the one obtained by UV-vis, and therefore it is feasible to use the change in luminescence emission to quantify drug release from LTbH-ibu. It should be noted that due to the nature of the experiment, it is not possible to truly terminate drug release at exactly the required time point: release will continue to some extent whilst the sample is wet. Therefore, the extent of release

obtained in this manner is likely to be an overestimate of the true extent of release at a particular point. This is believed to be the reason why the release curve obtained from photoluminescence measurements appears to be shifted to the left relative to the release curve obtained by UV-vis. Nevertheless, it is clear that there is a high degree of correlation between the luminescence properties and the extent of drug release, and thus the distinct possibility of using the LTbH formulations for theranostic applications.

2.5 Conclusions

This work considers the theranostic applications of the layered rare-earth hydroxide LTbH-Cl. The hydrothermal synthesis of LTbH-Cl and subsequent intercalation of the model drugs diclofenac, ibuprofen, and naproxen (dic, ibu, and nap) *via* ion exchange, is confirmed by XRD and FTIR characterisation. Elemental microanalysis and TGA experiments revealed high drug loadings of 80-100 % based on charge balance considerations (or *ca.* 33 wt %). Most of the drug cargo was released over approximately 5 h when the formulations were incubated in phosphate buffered saline at pH = 7.4.

The haemo- and cytocompatibility of all formulations was found to be high, even at concentrations far exceeding those that would be required for therapeutic applications (up to 526 µg / ml). Photoluminescence studies revealed characteristic peaks associated with Tb^{3+} and the presence of two different coordination environments in LTbH-Cl, consistent with previous reports in the literature. It was shown that intercalation of ibu and nap resulted in a significant increase in luminescence intensity, whereas the intercalation of dic lead to the quenching of the luminescence signal associated with Tb^{3+}. These findings imply that the LTbH-intercalates could act as fluorophores for luminescence imaging.

Moreover, it was demonstrated using LTbH-ibu that it is feasible to use the changing luminescence emission spectrum upon drug release to quantify the extent of drug which had de-intercalated. This property could provide a non-invasive way to quantify the real-time drug release kinetics *in vivo*, determine the precise location where drug release is taking place, as well as derive the required delivery frequency to maintain the local therapeutic levels of drug. The LTbH formulations developed in this work hence have great potential for use as theranostic agents and bolster the recent interest in LRH materials towards personalised medicine applications.

To ensure consistent performance and safety for potential *in vivo* applications, homogeneous particles with an average size below ca. 500 nm are required. The particles prepared in this chapter are non-uniform and exceed this size requirement. Building on the promising findings from this work, Chapter 3 will seek to devise ways to accurately control LRH particle size and ensure it falls in the desired range for theranostic applications.

3 Particle size optimisation of layered terbium hydroxide

A promising theranostic platform based on layered gadolinium hydroxide (LGdH-Cl, $[Gd_2(OH)_5]Cl{\cdot}yH_2O$) has been reported previously by our group.[87] A mixture of nano and microparticles of the material was synthesised from a gadolinium chloride salt *via* hydrothermal synthesis. Subsequent synthesis of layered terbium hydroxide (LTbH) by an analogous method[318] as detailed in Chapter 2, also produced particles which suffered from poor size-uniformity. The lack of homogeneity in the generated products is problematic, as both the size and geometry of particulate formulations affect their ultimate performance *in vivo*. In this chapter, the hydrothermal synthesis method used to generate LTbH particles is optimised to reproducibly yield particles with a smaller average particle size, a narrower particle size distribution and higher morphological consistency.

3.1 Introduction

3.1.1 Particle morphology considerations

Injectable formulations must be able to avoid rapid elimination by the body's biological mechanisms to prolong circulation time and increase the effectiveness of the intended treatment. The main route of elimination of particles from the blood stream is *via* phagocytosis by macrophages; while there is no clear consensus, there is some evidence in the literature that larger particles (ca. 400 nm upwards) are more susceptible to macrophage uptake than smaller particles (200 nm and below).[354] Moreover, very large nanoparticles and microparticles (~500 nm and above) injected intravenously are known to become mechanically

entrapped in the lung vasculature,[355–357] making them a less favourable choice for drug delivery to other tissues.

In relation to cancer therapy, it is also important to consider particle size as it relates to tumour vasculature and therefore the ability of the particles to pass from nearby blood vessels into the tumour tissue. Due to the rapid growth of cancerous tumours, the formation of vasculature is often much less organised than in healthy tissue, leading to 'leaky' blood vessels and poor lymphatic drainage. These blood vessels have been reported to have intracellular gaps larger than 200 nm,[358] whereas the separation between endothelial cells in healthy tissue is between 12-150 nm.[359,360] This is the basis for passive targeting of particles to tumour tissue *via* the EPR effect. Though the reported particle size limit for effective EPR targeting varies widely by tumour type and is the subject of some contention, it is generally accepted to be around 200 nm.[361] Ultimately, to enable particles to preferentially accumulate in tumour tissue, particle size should be small enough to avoid rapid removal by macrophages (< 200 nm), but large enough not to penetrate the vasculature of healthy tissues (> 150 nm).

The shape and size of particles also influence how they migrate towards blood vessel walls (margination), and their intracellular uptake. In the context of nanoparticulate drug delivery, stronger margination is a desirable property as particles flowing closer to the blood vessel walls are better able to passively target tumour tissues *via* the EPR effect. A very basic approximation of margination dynamics is that spherical particles experience less margination and flow linearly within the blood vessel, whereas non-spherical particles with a higher aspect ratio exhibit tumbling effects which allow them to drift laterally (Figure 3.1).[362–364]

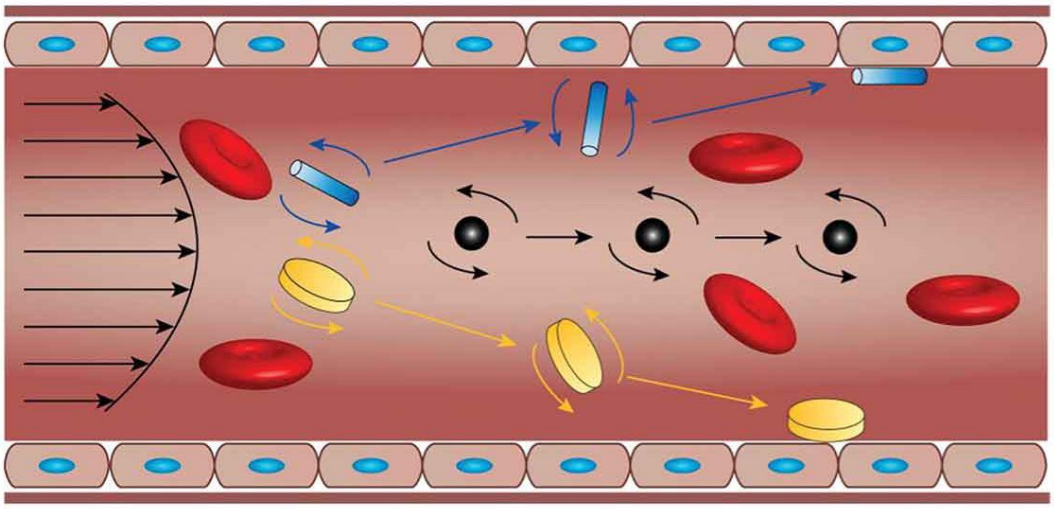

Figure 3.1 Diagram (reproduced from reference 364 with permission from Taylor & Francis) showing the effect of particle shape on margination. Spherical particles (black) flow with the bloodstream, whereas disc (yellow) and rod (blue) shaped particles experience tumbling and tend to flow towards the blood vessel walls.

It has also been demonstrated that an increase of aspect ratio is inversely proportional to cell uptake efficiency in several cancer cell lines, with spherical particles being taken up more readily than rods.[365] However, rod shaped particle uptake was reported to be more efficient than sphere-shaped particle uptake in healthy intestinal cells,[366] so this effect may vary depending on the type of cell line used. It may also be possible to utilise particle morphology to target subcellular features. It was demonstrated in a study on Mg_2Al-LDH that rod-shaped particles are effectively internalised into the nuclei of three mammalian cell lines (mouse, hamster, and human), whereas their hexagonal plate-shaped counterparts were seen to remain in the cytoplasm.[96] It is therefore feasible that sub-cellular targeting can be achieved by exploiting particle morphology, and thus serve to increase the treatment efficacy if the target is intracellular. Therefore, the ability to control the shape of nanoparticles during synthesis may be an important factor when designing theranostic platforms.

3.1.2 Particle size evaluation considerations

There are several methods of particle size evaluation in the nanosized range which are used within the pharmaceutical field. Most commonly, electron microscopy (in scanning or transmission mode, SEM and TEM respectively) or dynamic light scattering (DLS) methods are employed. In brief, electron microscopy generates digital images of samples with a known magnification, which may then be used to measure the dimensions of individual particles (either manually or by using a software script). DLS, on the other hand, derives particle size information by relating the speed of Brownian motion of particles in suspensions to their size.

While DLS equipment is much less costly to purchase and operate than electron microscopes (and is therefore a more widely accessible particle size characterisation technique), it suffers from several shortcomings compared to electron microscopy.[367] Firstly, as Brownian motion is also affected by temperature fluctuations and solvent viscosity, these properties must be precisely known and controlled during measurement, which may not always be possible. Secondly, results may be inconsistent/inaccurate depending on sample concentration and sedimentation of larger particles during the measurement. In addition, non-spherical particles exhibit rotational effects which must be corrected for in order to obtain accurate size results, and this may also not always be possible especially if the sample exhibits low homogeneity (as is the case for LTbH-Cl generated according to the method described in Section 2.3.2.1). On the other hand, since DLS characterisation is done automatically, this eliminates potential user bias which may be present with manual measurement of particles in SEM/TEM images.

SEM preparation requires samples to be in the solid state, which may be disadvantageous when characterising particles intended for medical applications where a suspension may be more representative of the effective particle size *in vivo* (due to association with charged entities such as ions, proteins, or amino acids).[368] However, as demonstrated in Section 2.4.2, there is generally very good agreement between the average particle size derived by SEM and DLS for LTbH-Cl (within 100 nm), though the standard deviation is much lower in DLS derived measurements (ca. ± 560 vs 60 nm, presumably due to sedimentation effects). Moreover, as the aim of this series of experiments is to improve particle homogeneity and reduce average particle size, particle size measurements from SEM images are sufficient for characterisation purposes. While TEM is conducted on suspensions of particles, it is much more expensive and samples are typically very dilute, making it difficult to procure images with a sufficient number of particles for reliable average particle size measurements (even more so for a large number of samples). Electron microscopy also provides a convenient way to observe and study particle shape. Though it is theoretically possible to derive some particle shape information by using DLS methods,[369] it involves complex data analysis and is impractical for characterising a large number of samples. Based on these factors, SEM was chosen as the optimal method of size characterisation for this series of experiments.

3.1.3 Hydrothermal synthesis parameter considerations

As described in Chapter 2, the synthesis of LTbH involves hydrothermal treatment of an aqueous mixture of precursor salts (NaCl, NaOH, $TbCl_3.6H_2O$). The parameters of reaction temperature, reaction time, and reactor fill volume

were chosen to systematically investigate in terms of their influence on resultant particle morphology.

3.1.3.1 Temperature

When water is gradually heated in a partially filled, sealed container (as is the case during hydrothermal synthesis), thermal energy is provided to the liquid molecules, which subsequently become more mobile. Therefore, an increase in temperature results in a decrease in both the viscosity and density of water (Figure 3.2a), which in turn increases the kinetics of product formation as the mobility of the reactant species increases. This is particularly evident at temperatures approaching the critical temperature (T_c = 374 °C) of water, whereafter a sharp decline in density is observed as the liquid and gaseous phases merge into a supercritical fluid. In this way, the rate of product formation is related to synthetic temperature. Where processes are carried out below the critical temperature (as in this chapter), they are referred to as 'subcritical'.

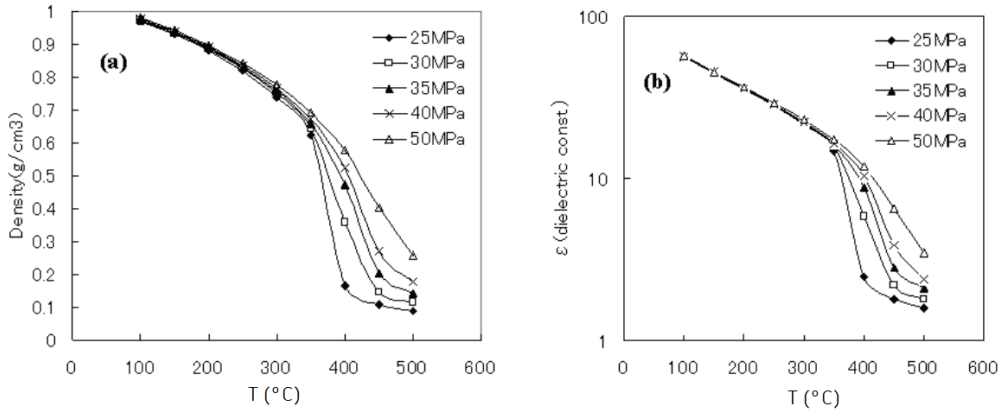

Figure 3.2 Graphs (reproduced from reference [370]) depicting the effect of temperature on the a.) density and b.) dielectric constant of pure water, subjected to differing pressure conditions..

Another important consequence of increasing the temperature of water during hydrothermal synthesis is the resultant decrease in its relative permittivity (a property which is frequently referred to as the 'dielectric constant', ε, in the

literature; Figure 3.2b). As it pertains to solvents, relative permittivity is effectively a measure of the polarity of the solvent. As with density, this effect becomes particularly strong at temperatures approaching T_c, after which point the relative permittivity of water is comparable to organic solvents such as dichloromethane (ε_{DCM} = 9.04).[371] On this basis, synthetic temperature may also be expected to have effects on solubility of the reactant, intermediate, or product species.

Lastly, elevated synthetic temperatures ensure that the product generated is more likely to be thermodynamically stable, as there is sufficient energy within the system to decompose any competing metastable phases.[372]

3.1.3.2 Time

The length of reaction time also contributes to selectivity towards the thermodynamic product, as kinetically favoured phases (given sufficient time) will gradually be converted into thermodynamically favoured phases.[373] Additionally, as described by the La Mer particle growth mechanism (Figure 3.3), time plays a crucial role in determining the resultant particle size: longer growth phases correspond to larger particles.[374] Moreover, longer aging times are associated with higher degrees of crystallinity, as has been demonstrated for LDH systems.[375]

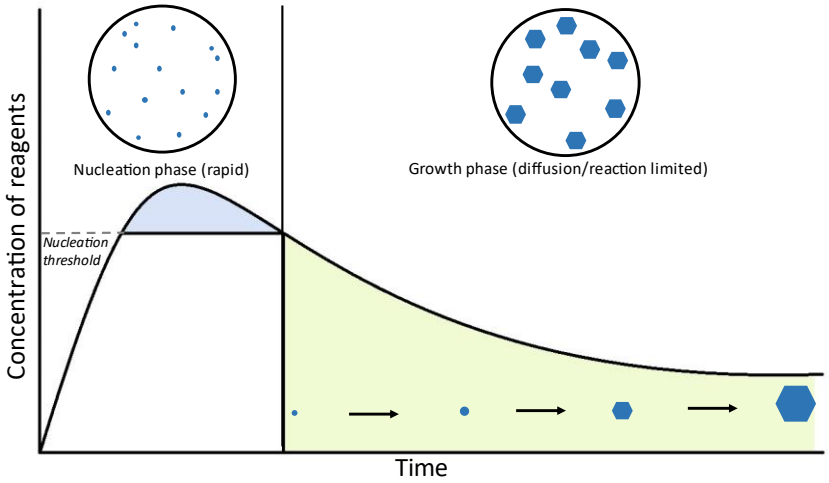

Figure 3.3 La Mer diagram illustrating the nucleation and growth stages of nanoparticles growing from a solution.

3.1.3.3 Pressure

Pressure is an important parameter to consider because it affects both the density and dielectric constants (albeit only marginally below the critical temperature, Figure 3.2a-b), as well as having potential effects on the crystallisation behaviour of LRHs in solution. The mechanism of formation of LRHs (and LDHs) is poorly understood at present, but there is some evidence to imply it may be an oriented attachment process (whereby building blocks of LRH nucleate instantly and subsequently assemble into a 3D structure).[376] There is evidence in the literature of similar oriented attachment processes being influenced by the pressure during synthesis.[377] Additionally, pressure during synthesis may influence the resultant product phase, as more dense phases tend to be preferred at higher pressures.[378]

During heating, water molecules evaporate, producing water vapour. The corresponding increase in pressure within the sealed container due to the increase in water vapour is referred to as ‘autogenous’, because it is generated within the system (in contrast to hydrothermal reactors which can apply external pressure to the system). The degree of fill within the sealed container is a

determinant factor for the internal system pressure during synthesis – a higher degree of fill leaves a lower available volume for water molecules to evaporate into, and therefore a greater pressure generated at a given temperature. This effect is illustrated in Figure 3.4.[379] It can be noted from this graph that autogenous pressure in all cases is very low/negligible below ca. 150 °C, and subsequently rises steeply for reactors with a high fill volume (e.g. up to approximately 700 bar at 200 °C for 90 % fill volume). Therefore, fill volume is an effective way to modulate autogenous pressure within a hydrothermal reactor.

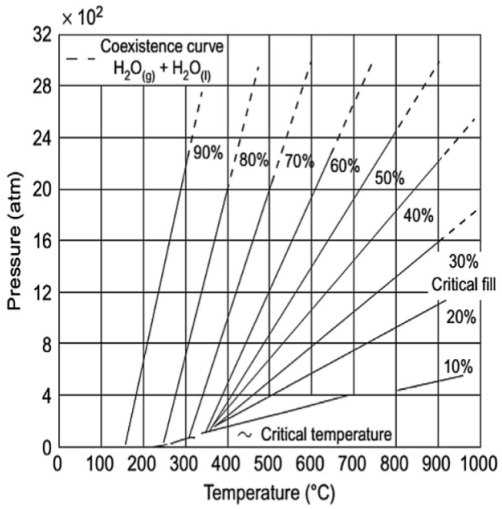

Figure 3.4 Graph (reprinted from reference [379], with permission from Elsevier) illustrating the effect of fill volume (%) on autogenous pressure of pure water inside a sealed autoclave.

3.1.3.4 Concentration

The concentration of reagents in a hydrothermal synthesis are known to affect the morphological properties of products formed for some classes of materials, for instance metal phosphates and oxides.[380,381] However, the literature suggests that this factor is less important in the case of metal hydroxides. In a study on the hydrothermal synthesis of boehmite (a layered oxyhydroxide material composed of edge-sharing $Al(O)_4(OH)_2$ octahedra), it was found that while temperature and pressure exhibited a statistically significant effect on the resultant particle

size/morphology, the initial reactant concentration did not.[382] It is therefore reasonable to expect that in the synthesis of LRHs the effects of temperature and pressure may dominate over those of concentration.

3.2 Aims

The following series of experiments aims to establish whether it is feasible to control the average particle size and morphology of LTbH-Cl by adjusting the conditions during hydrothermal synthesis. In particular, the parameters of temperature, time, and fill volume will be systematically investigated. A series of experiments will be generated using design of experiments software to establish which (if any) of the above parameters have influence over the resulting particle size/shape of LTbH. The results of these experiments will then be used to optimise the necessary conditions to yield particles of the desired size (150 - 200 nm), to be amenable to theranostic applications. Finally, the optimised LTbH formulation will be compared with the pre-optimisation LTbH formulation in terms of cytotoxicity, uptake, and fluorescence performance.

3.3 Experimental

3.3.1 Materials

Terbium chloride hexahydrate was purchased from Sigma Aldrich. All water used was deionised, and ethanol was of analytical grade.

3.3.2 Synthesis

3.3.2.1 Hydrothermal synthesis of LTbH with systematically varied parameters

Reaction parameters were determined using JMP Pro 14 software and are summarised in Table 3.1 and Table 3.2. An aqueous solution of $TbCl_3.6H_2O$ (0.4 M, either 7.5 ml or 13.5 ml) was added dropwise to a stirring aqueous solution of NaCl/NaOH (1.4 M and 2.1 M respectively, either 2.5 ml or 4.5 ml), such that the total volume was either 10 ml or 18 ml. The resultant suspension was stirred for 10 min and transferred to a Teflon lined hydrothermal reactor (23 ml). The reactor was heated to the desired temperature (90, 100, 140, or 200 °C) for the required length of time (4, 8, 10, or 24 h), at a heating and cooling rate of 10 °C / min, after which the precipitate was collected by centrifugation. The product was washed with water (2 x 30 ml) and ethanol (2 x 30 ml), and subsequently dried at 60 °C for 24 h to yield the product. The product cake was briefly (< 1 min) ground using a pestle and mortar to produce a fine powder.

3.3.2.2 Attempted intercalation into unknown terbium material synthesised at 200 °C

The material produced during hydrothermal synthesis at 200 °C was determined by XRD to be an unknown phase. To investigate if the unknown terbium material

has ion exchange capabilities, an experiment was conducted using a method analogous to the one described in Section 2.3.2.2. The unknown material (100 mg) was dispersed in water (15 ml), and ibuprofen sodium (300 mg) was added to this solution. As the formula of the unknown material is not known, a three-fold excess by weight was used instead of a three-fold molar excess. The mixture was heated at 60 °C for 24 h, with stirring. The product was collected by centrifugation, washed with water (2 x 30 ml) and ethanol (2x 30 ml), and subsequently dried at 60 °C for 24 h.

3.3.3 Characterisation

Characterisation procedures used in this chapter are identical to those described in Section 2.3.3; any differences and additional methods are described explicitly in this section.

3.3.3.1 Scanning electron microscopy (SEM)

All particles were measured along their longest dimension. The number of particles measured per sample is indicated in Table 3.2 and Table 3.5.

3.3.3.2 Cytotoxicity assay

Cell viability assessments were conducted according to the protocol described in Section 2.3.3.7; the samples used in this series of experiments were the unoptimized and size-optimised LTbH-Cl particles (samples 150-15-23 and 90-4-18 respectively). Suspensions of LTbH-Cl in culture medium (10 mg / ml) were prepared, and either 5 or 10 µl of these suspensions were added directly to the cells, to final concentrations of 270 and 526 µg / ml respectively.

Three independent experiments were performed, each with treatment conditions in triplicate, and results presented as mean ± standard deviation.

3.3.3.3 Cell uptake and live/dead staining assay

Cells were grown according to the same protocol as for cytotoxicity studies, detailed in Section 2.3.3.7. For uptake and live/dead experiments, the passage numbers used were 7-12 (Caco-2) and 9-13 (HEK 293).

Live/dead staining was conducted using the LIVE/DEAD™ C12 Resazurin/SYTOX™ Green assay (Invitrogen), in tissue-culture treated clear-bottom black 96-well plates (Thermo Fisher Scientific), T75 flasks, or glass-bottom petri dishes. Cell suspension was prepared at a concentration of 5.6×10^4 cells / ml and deposited into the wells of a black 96-well plate (180 µl per well), into a T75 flask (5 ml per flask), or into a 35 mm glass bottom petri dish (1.5 ml per dish). Suspensions of LTbH-Cl in culture medium (10 mg / ml) were prepared. For microplate experiments, 10 µl of these suspensions were added directly to the treatment wells. For T75 flask experiments, 275 µl of the suspensions were added to each flask. For petri dish experiments, 85 µl of the suspensions were added to each dish. The cells were allowed to adhere and grow for 24 hours after seeding.

Working solutions of the C12 Resazurin and SYTOX green™ dyes were prepared according to manufacturer instructions in sterile dimethyl sulfoxide. After 24 hours, the supernatant was carefully aspirated and retained for subsequent staining with Trypan blue (using equal parts supernatant to dye) to test for detached cells (data not presented). The remaining adhered cells were washed once using sterile PBS (100 µl for wells, 3 ml for flasks, 1 ml for dishes). Fresh PBS was then added to cover the cells, and the working dye solutions added (0.5

µl per well and 5 µl per flask for each dye). The plates/flasks/dishes were then incubated at 37 °C for 15 minutes. Cell imaging was performed using a fluorescence microscope (EVOS® FL Cell Imaging System, ThermoFisher Scientific) equipped with GFP, DAPI, and Texas red filters.

3.3.3.4 Suspension photoluminescence

Fluorescence measurements were carried out in black 96-well plates using a SpectraMax M2e microplate reader (excitation = 250 nm, emission = 545 nm, or scanned across a range of wavelengths where required). LTbH-Cl samples (29.6 mg) were resuspended in water (10 ml), and 150 µl of these suspensions was transferred to a 96-well plate. Time-resolved fluorescence measurements were taken after a delay of 50 µs and measured up to 1450 µs (in increments of 250 µs).

3.3.3.5 Statistical analysis

One-way analysis of variance (ANOVA) was used to determine the statistical significance (at the $p = 0.05$ level) in the difference of means for particle size measurements. A Fisher's LSD post-hoc test was used to determine which sample means differed significantly. The mean particle size values for each set of experimental parameters were input into JMP Pro 14 software for model fitting and effect screening.

3.4 Results and Discussion

3.4.1 First generation experiments

For initial experiments, the reaction parameter values were chosen manually and input into JMP Pro 14 software to design combinations for testing. The

temperatures were selected as 100 °C and 200 °C (50 °C above and below the reported method, described in Section 2.3.2.1),[318] with incubation times of 10 and 24 h (compared to 15 h originally). The fill volumes chosen were approximately half the capacity of the reactor (10 ml) and full capacity (18 ml), whilst leaving some room for air to avoid vessel leakage. These parameters and their combinations are summarised in Table 3.1 (samples 100-X-Y and 200-X-Y, where X = incubation time, and Y = fill volume).

Table 3.1 Summary of reaction parameters generated using JMP Pro 14 software, and precursor solution volumes for 100 °C and 200 °C samples. Sample names are designated as T-X-Y, where T = temperature during synthesis, X = incubation time, and Y = fill volume.

Sample name	*Temperature (°C)*	*Incubation time (h)*	*Total Volume (ml)*	*Volume of $TbCl_3.6H_2O$ solution (ml)*	*Volume of NaCl/NaOH solution (ml)*
100-10-10	100	10	10	7.5	2.5
100-10-18	100	10	18	13.5	4.5
100-24-10	100	24	10	7.5	2.5
100-24-18	100	24	18	13.5	4.5
200-10-10	200	10	10	7.5	2.5
200-10-18	200	10	18	13.5	4.5
200-24-10	200	24	10	7.5	2.5
200-24-18	200	24	18	13.5	4.5

Comparison of XRD patterns (Figure 3.5) to that of LTbH synthesised at 150 °C, confirmed that all samples produced at 100 °C were also LTbH, whereas those produced at 200 °C were a different material. There are no reflections present in the 200 °C samples which correspond to LTbH, showing that a new phase has formed. It was not possible to search-match this material to any known material in the ICDD (International centre for Diffraction Data) database. As the XRD pattern exhibits several strong harmonic reflections it is likely also layered, perhaps able to ion-exchange like LTbH-Cl. It is also possible that this material is a mixture of phases, though this is unlikely as the number of reflections is rather low.

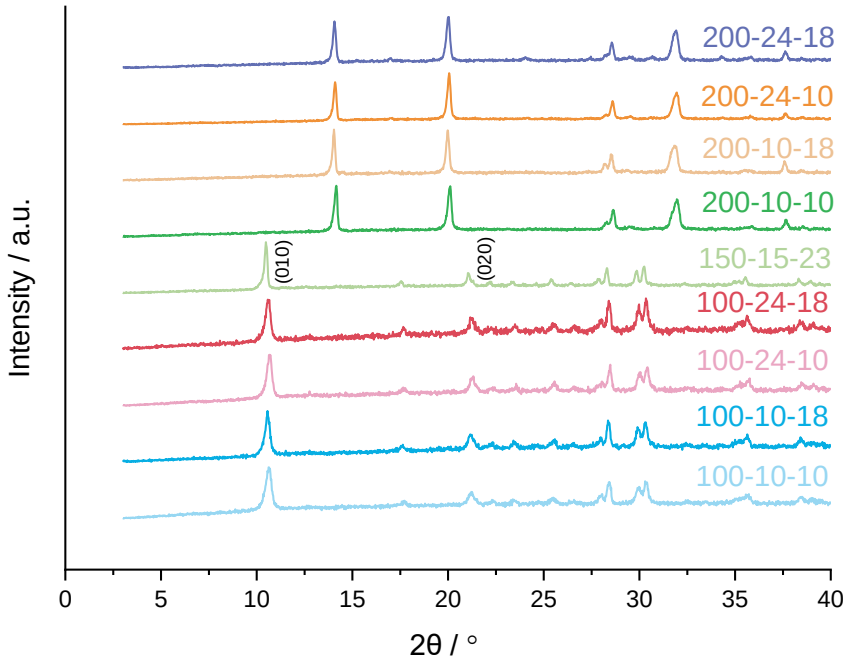

Figure 3.5 XRD patterns for LTbH-Cl synthesised according to the reported procedure (sample 150-15-23),[318] described in Chapter 2, and Tb based materials produced under various experimental conditions as described in Table 3.1. Samples are denoted as temperature-time-fill volume. The LTbH system is indexed to the orthorhombic $Pca2_1$ space group.

To test whether this material exhibits ion exchange capability, an ion exchange experiment with ibu-Na was attempted. The XRD pattern of the resultant material is shown in Figure 3.6. No peak shifting occurs, and no additional peaks arising from ibu-Na/interactions with ibu-Na are seen. It can therefore be concluded that this material does not appear to show any intercalation behaviour.

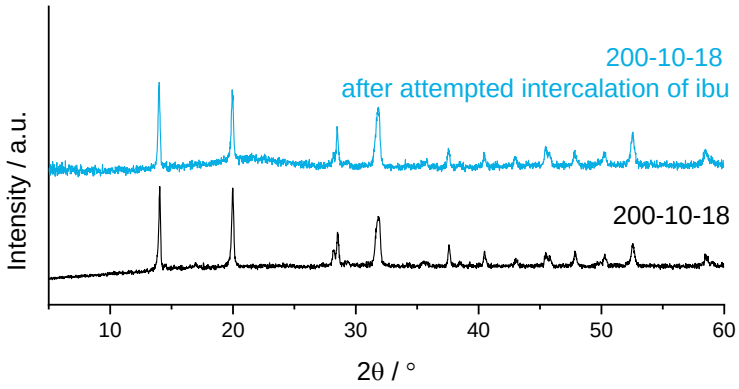

Figure 3.6 XRD patterns of unknown material obtained at 200 °C, before and after attempted intercalation. No intercalation appears to have occurred based on the lack of change seen in the pattern.

SEM images of LTbH-Cl samples synthesised at 100 °C are shown in Figure 3.7. Each sample appears to be a mixture of plate and rod-shaped particles. The average particle sizes measured for each sample (along with hydrodynamic size measurements) are summarised in Table 3.2.

The 100-10-10 sample appears to have the lowest overall mean particle size of 293 ± 126 nm. When the volume of reactant solution is increased to 18 ml (sample 100-10-18), the mean particle size appears to increase slightly to 308 ± 128 nm. A similar increase is seen when the incubation time is increased to 24 hours (sample 100-24-10), giving a mean particle size of 307 ± 127 nm. However, as determined by statistical analysis, none of the samples are significantly different form each other at the $p = 0.05$ level.

When both the incubation time and volume of reactant solution are increased (sample 100-24-18, mean size 344 ± 130 nm), the resultant mean particle size is statistically larger than those of the remaining treatment groups. This indicates that there may be an additive or synergistic effect on particle size of the fill volume and incubation time parameters. However, this size difference between the treatment groups is not apparent from the DLS data. In fact, in each sample, the hydrodynamic diameter is slightly smaller than the average particle size measured from SEM – which in in contrast to what is expected given that the hydrodynamic diameter also includes the spatial contribution of associated water molecules. This difference is slight and is likely explained by sampling error due to higher aggregation in the solid samples versus the dispersions. Overall, size differences produced by altering fill volume and incubation time at 100 °C appear to be insignificant.

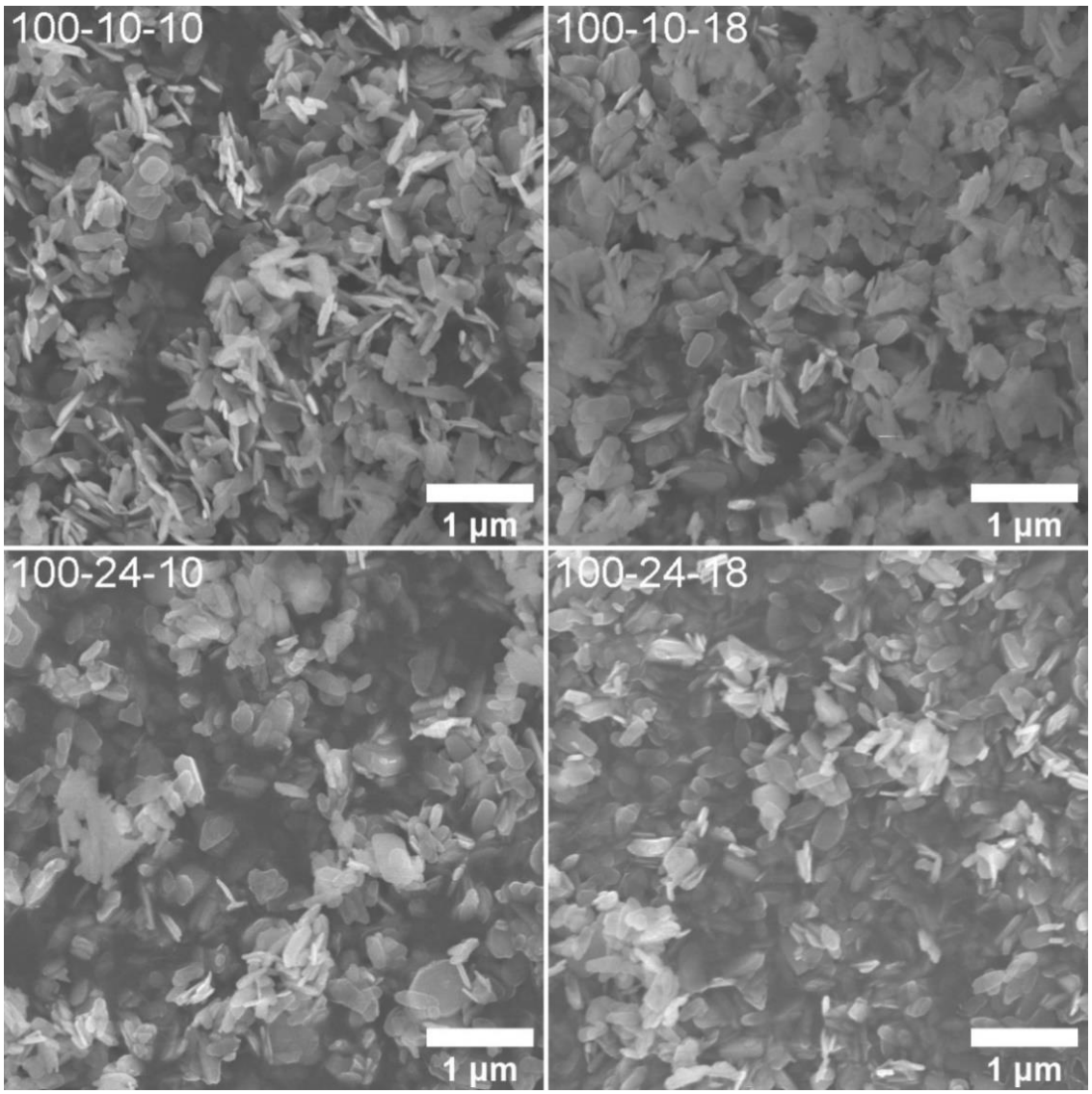

Figure 3.7 SEM images of LTbH-Cl samples synthesised at 100 °C and various fill volumes/incubation times as described in Table 3.1.

*Table 3.2 Summary of the average particle size and number of particles measured for LTbH-Cl samples synthesised at 100 °C. Results are presented as mean ± standard deviation *: Significantly different from the remaining samples at the p = 0.05 level.*

Sample name	*Size by SEM / nm*	*Particles measured*	*Hydrodynamic diameter / nm*	*Polydispersity index*
100-10-10	293 ± 126	391	278 ± 6	0.18 ± 0.01
100-10-18	308 ± 128	246	289 ± 15	0.22 ± 0.06
100-24-10	307 ± 127	247	259 ± 13	0.22 ± 0.01
100-24-18	*344 ± 130	205	270 ± 2	0.22 ± 0.01

SEM images of the unknown material synthesised at 200 °C are shown in Figure 3.8. Unlike LTbH-Cl, this material exhibits uniform particle morphology, consisting entirely of needle-shaped crystals. Particle length varied between approximately 1 – 120 µm, with a median value of 24 µm. Due to their very large size potentially causing issues with mechanical entrapment *in vivo*, as described in Section 3.1.1, these particles would not be suitable for use as injectables. Furthermore, it is well known that particles with a very high aspect ratio can cause disruption to cell membranes and elicit an inflammatory immune response.[383–385] In any case, as the identity of this material cannot be established at present, further exploration was not undertaken.

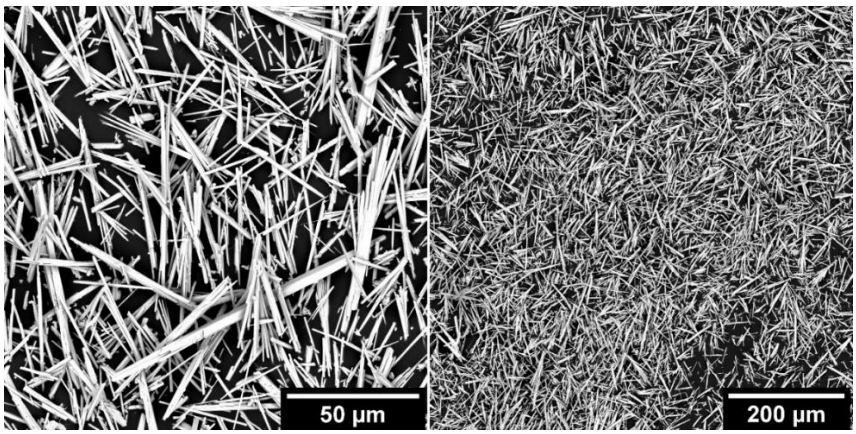

Figure 3.8 SEM images of the unknown crystalline material synthesised at 200 °C (sample 200-24-10). Particle length varied between approximately 1 – 120 µm, with a median value of 24 µm.

Though it is not possible to directly measure the internal pressure within a simple hydrothermal reactor (such as those used for synthesis in this chapter), it is possible to compare the *relative* pressure conditions at different temperatures by considering the vapour pressure generated by water at those temperatures. Vapour pressure is defined as the amount of pressure exerted by a vapour of a substance which is in equilibrium with its condensed phase(s) in a closed system. The vapour pressure for pure water can be approximated by the Arden Buck equation:

$$Vp\ (kPa) = 0.61121\exp((18.678 - \frac{T}{234.5})(\frac{T}{257.14 + T}) \qquad (3.2)$$

Where V_p is the equilibrium vapour pressure over liquid water at a given temperature, T (°C). Though the addition of solutes to water affects the boiling point of the solution (an effect known as boiling point elevation),[386] this is not an necessary consideration in this case because all sample solutions used have the same molality (moles of solute per kg of solvent), which in turn determines the magnitude of boiling point elevation. Therefore, V_p values for pure water are an acceptable way to relatively compare the V_p in systems at different temperatures.

The V_p values obtained for the range of temperatures in the current series of experiments are listed in Table 3.3. The magnitude of V_p at 100 °C is, by virtue of being at the boiling point, equivalent to atmospheric pressure. At 150 °C, the V_p is approximately 4.6 times higher than atmospheric pressure, whilst at 200 °C the V_p is significantly increased (over thrice the V_p at 150 °C, and a nearly 15-fold increase over the V_p at 100 °C). This could help to explain the formation of the unknown material at 200 °C – likely, it is a higher density phase which is thermodynamically favoured by the higher-pressure environment.[372]

Table 3.3 Vapour pressure (Vp) of pure water across the range of temperatures employed in the first-generation size-optimisation experiments, as calculated by the Equation 3.2, rounded to the nearest 100 Pa.

Temperature / °C	*100*	*150*	*200*
Vapour pressure (V_p) / Pa	101,300	470,300	1,489,500

Compared to the LTbH-Cl sample synthesised as described in Section 2.3.2.1, with an average particle size of 670 ± 564 nm, both the average particle sizes and the standard deviation in all the samples synthesised at 100 °C are significantly reduced. Overall, these data would seem to suggest that temperature has the most significant influence on resultant particle size, but that reaction time and fill volume, particularly at higher temperatures, may also contribute to some degree.

3.4.2 Second generation experiments

As it was shown that the particles produced at 150 °C are irregular in size, and a phase transition occurs somewhere between 150-200 °C, further experiments were carried out at reduced temperatures of 90 °C and 140 °C. In addition, the incubation time was shortened to 4 h and 8 h, both to increase time-efficiency and potentially further reduce particle size by limiting growth time. These parameters and their combinations are summarised in Table 3.4 (samples 90-X-Y and 140-X-Y). A design of experiments approach was used to decide on the combinations of experimental parameters (temperature, fill volume, incubation time) based on the outcome of the first-generation experiments.

Table 3.4 Experimental conditions chosen for second generation experiments to determine effect of synthetic parameters on particle size. Summary of reaction parameters generated using JMP Pro 14 software, and precursor solution volumes for all samples. Sample names are designated as T-X-Y-Z, where T = temperature during synthesis, X = incubation time, and Y = fill volume.

Sample name	*Temperature (°C)*	*Incubation time (h)*	*Total Volume (ml)*	*Volume of $TbCl_3.6H_2O$ solution (ml)*	*Volume of NaCl/NaOH solution (ml)*
90-8-10	90	8	10	7.5	2.5
90-4-18	90	4	18	13.5	4.5
140-4-10	140	4	10	7.5	2.5
140-8-18	140	8	18	13.5	4.5

XRD data (Figure 3.9) confirmed that all samples produced at 90 °C and 140 °C were LTbH-Cl. SEM images of the samples synthesised at 90 °C and 140 °C are shown in Figure 3.10. It can be seen that at lower temperature, the particles display a predominantly rod-shaped geometry, whereas at higher temperature the particles are almost exclusively plate shaped. The mean size of the particles in each sample is summarised in Table 3.5. Statistical analysis showed that the mean particle size of the samples generated at 90 °C are statistically equivalent to each other, but significantly different to those generated at 100 °C and 140 °C. The mean size of the particles in the two samples generated at 140 °C were shown to be statistically different to each other, and the smaller 140-4-10 sample particles we statistically equivalent to all samples generated at 100 °C. All samples (90 °C, 140 °C) had a mean particle size significantly smaller than that of samples synthesised as described in Section 2.3.2.1 at 150 °C.

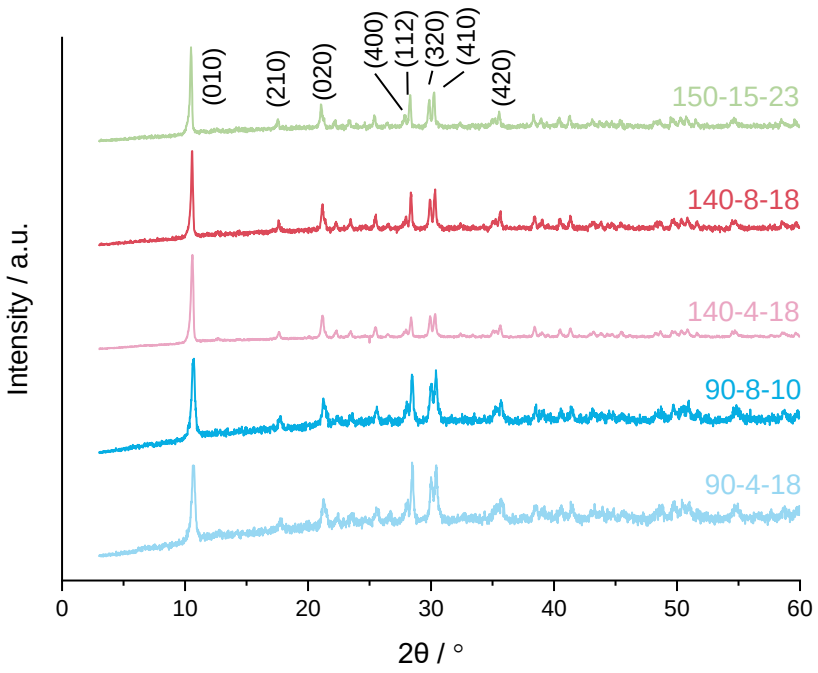

Figure 3.9 XRD patterns for LTbH-Cl synthesised according to the procedure in Section 2.3.2.1 (sample 150-15-23) and LTbH-Cl samples produced by various experimental conditions described in Table 3.4. Samples are denoted as temperature-time-fill volume. The LTbH system is indexed to the orthorhombic $Pca2_1$ space group.

*Table 3.5 Summary of the mean particle size and number of particles measured for LTbH-Cl samples synthesised at 90 °C and 140 °C. *: Significantly different at the p = 0.05 level.*

Sample	*Size by SEM / nm*	*Particles measured*
90-8-10	206 ± 80	293
90-4-18	178 ± 63	253
*140-4-10**	312 ± 135	251
*140-8-18**	413 ± 209	227

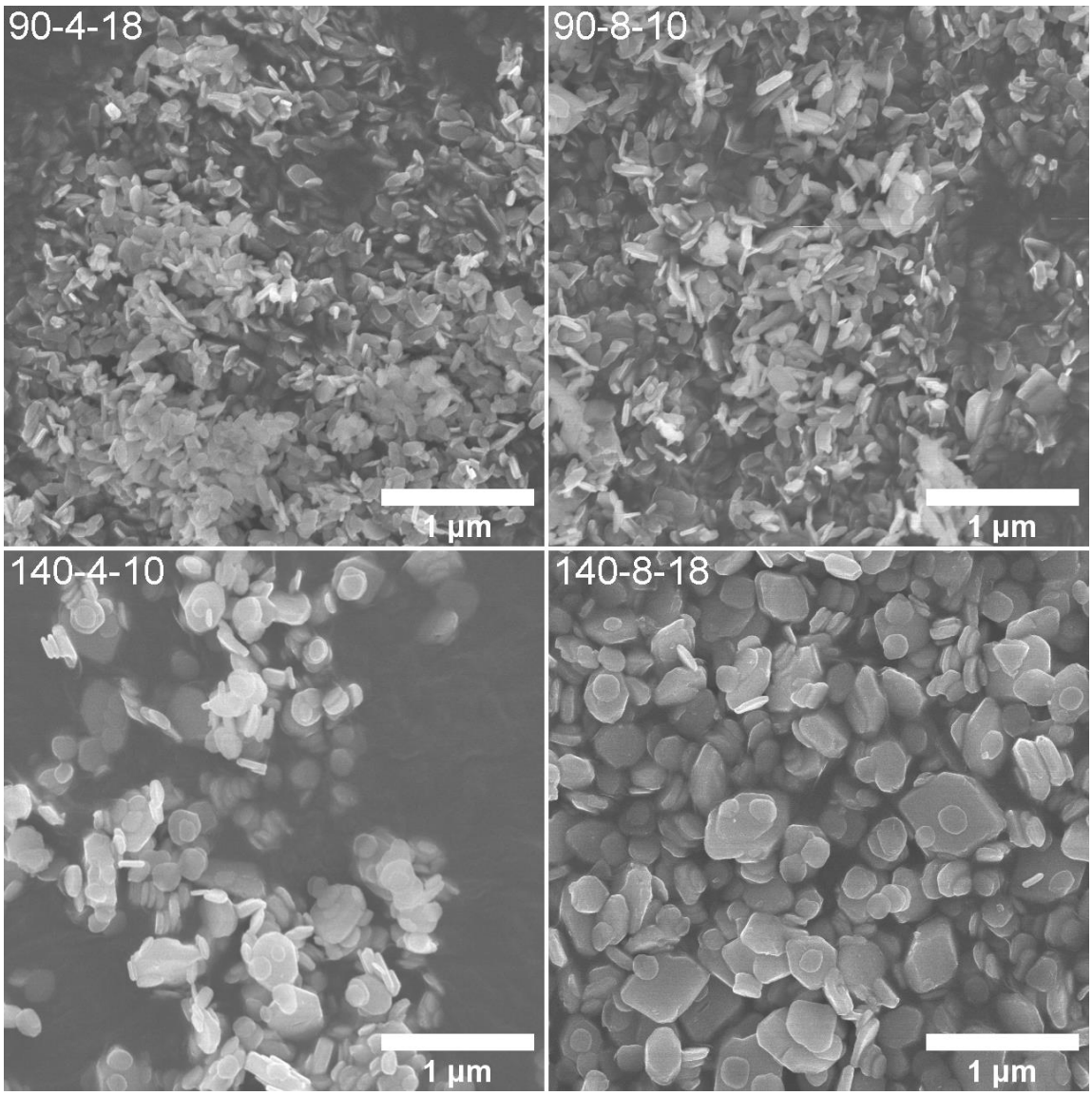

Figure 3.10 SEM images of LTbH-Cl samples synthesised at 90 °C and 140 °C, and various fill volumes/incubation times described Table 3.4.

Overall, the data imply that at lower temperatures (90 °C and 100 °C) the effect of incubation time and fill volume has almost no bearing on the resultant particle size. For fill volume, this aligns with the fact that the vapour pressure generated by water at such temperatures is less than or equal to atmospheric pressure, as shown in Table 3.3. At higher temperature (140 °C), it appears that resultant particle size is more sensitive to fill volume and/or incubation time.

When compared to the particles synthesised at 150 °C as described in Section 2.3.2.1, samples generated at 140 °C with reduced incubation time show

decreased intra-sample variance. Additionally, change in synthetic temperature shows good selectivity for particle shape, with plate morphology prevailing over rod morphology at higher temperatures. As discussed in Section 3.1.1, particle shape and size have important implications on the properties of nanoscale drug-delivery platforms. Therefore, the ability to control both by simply changing the conditions during synthesis is an especially useful property. Based on the reasoning laid out in Section 3.1, the experimental parameters producing the smallest average particle size of 178 ± 63 nm (90 °C, 4-hour incubation, and 18 ml fill volume) were chosen for further experiments.

3.4.3 Size-optimised method

The experimental parameters producing particles smaller than 200 nm (90 °C, 4-hour incubation, and 18 ml fill volume) were chosen as optimal for cancer theranostics. To verify that this method can consistently produce particles with a predictable size distribution and an average size of less than 200 nm, the experiment was replicated 5 additional times (samples 90-4-18-Z, where Z = replicate number). Particle size data measured by SEM are summarised in Table 3.7 and statistical analysis results from all treatment groups are presented in Table 3.6. XRD data (Figure 3.11) verified the material was LTbH in all cases. Statistical analysis showed that the mean particle sizes (by SEM) of the replicates are not statistically different. Therefore, the present method shows good reproducibility in terms of mean particle size and size distribution, compared to other hydrothermally synthesised LRH hydroxychlorides, such as LGdH-Cl (rods and platelets, 100 nm – 2 μm)[87] and LYH-Cl (layered yttrium chloride, platelets, 200 – 500 nm).[387]

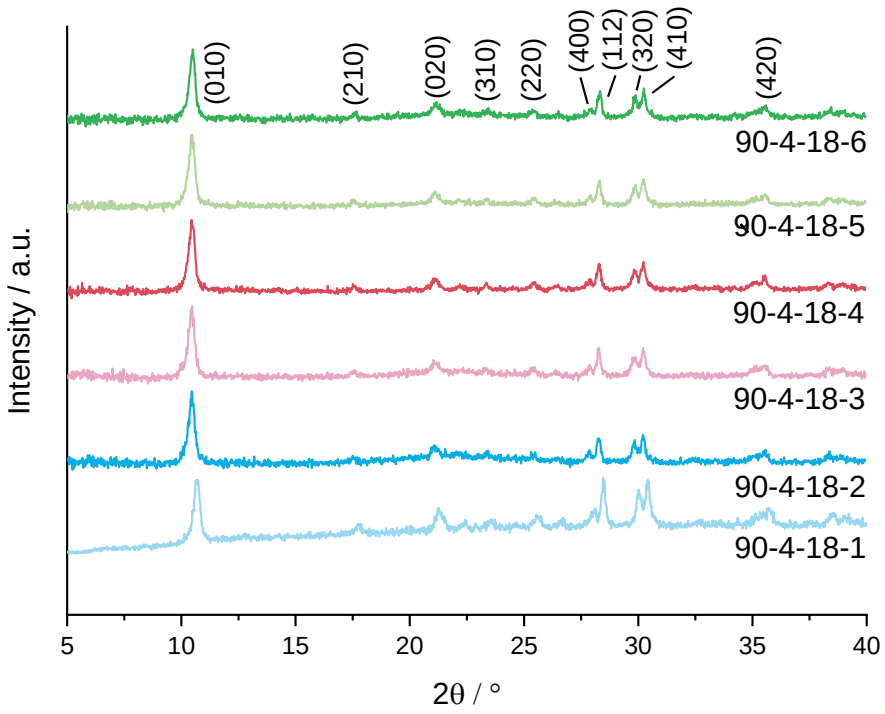

Figure 3.11 XRD patterns for the replicates of LTbH synthesised at the optimised conditions (90 °C, 4-hour incubation time, 18 ml fill volume). The LTbH system is indexed to the orthorhombic $Pca2_1$ space group.

The reverse microemulsion method has also previously been applied to generate more monodisperse LGdH-Cl particles (200 – 300 nm),[388] though the particle morphology in that case was less regular than reported here, and the use of surfactants introduced additional components into the system (which are potentially undesirable in pharmaceutical formulations).

3.4.4 Overall model

The mean particle sizes and statistical analysis results for each LTbH sample are summarised in Table 3.6. Overall, there appears to be a strong correlation between synthetic temperature and resultant particle size measured by SEM (Figure 3.12a), with a contributing effect from reaction time, and no significant influence from fill volume (Figure 3.12b). All LTbH samples in the present study had a mean particle size significantly smaller than that of samples synthesised according to the previously reported method (at 150 °C).[318] Furthermore, particles

from samples 90-8-10 and 90-4-18-1 (90 °C) were significantly smaller than those from samples synthesised at 100 and 140 °C, and particles from sample 140-8-18 (140 °C, with longer incubation time and higher fill volume) were statistically the largest. There are also statistical differences within each temperature group, which are explained by secondary effects from the differences in reaction time and fill volume.

*Table 3.6 Statistical analysis of the particle sizes measured by SEM. One-way analysis of variance (ANOVA) was used to determine the statistical significance (at the p = 0.05 level) in the difference of means for particle size measurements. A Fisher's LSD (if sample means had unequal variance) post hoc test was used to determine which sample means differed significantly. Samples which share a group number are not statistically different. * Data from previously published work, reference [318].*

Sample name	*Size by SEM / nm*	*Groups of statistical equivalence*					
*150-15-23 **	670	1					
90-8-10	206		2				
90-4-18-1	**162**			**3**			
90-4-18-2	**151**			**3**			
90-4-18-3	**159**			**3**			
90-4-18-4	**146**			**3**			
90-4-18-5	**147**			**3**			
90-4-18-6	**152**			**3**			
100-10-10	293				4		
100-10-18	308				4	5	
100-24-10	307				4	5	
100-24-18	344					5	
140-4-10	312				4	5	
140-8-18	413						6

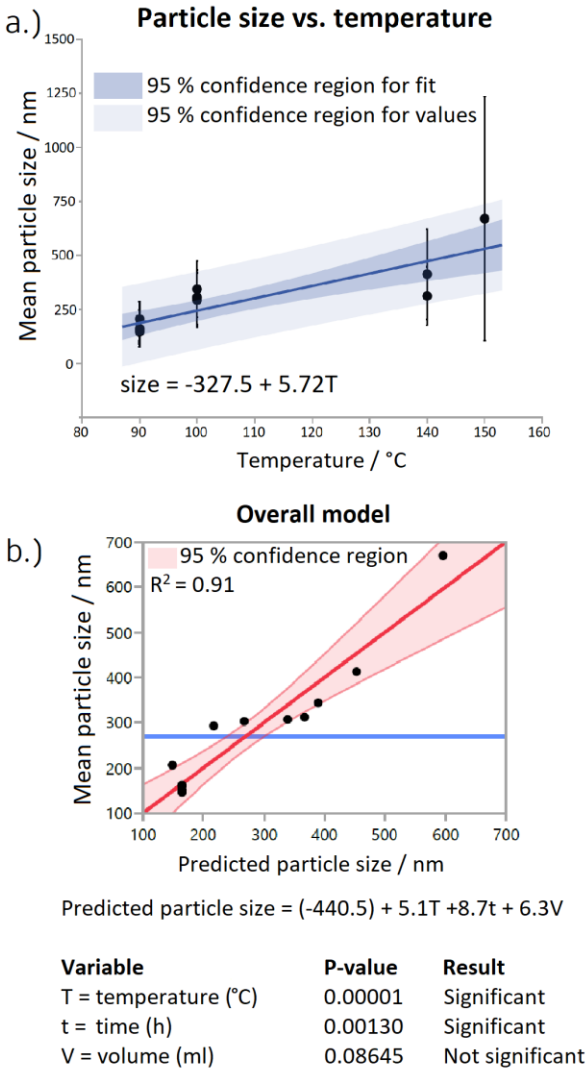

Figure 3.12 a.) Plot showing the relationship between synthetic temperature and mean particle size; b.) Plot showing the complete model (which includes T, t, and V as variables) fitted to the data, and the statistical impact of each variable on the model. Plots D and E were generated using JMP Pro 14 software.

The average particle sizes in all samples generated by the optimised method (90-4-18-X, X = repeat number) are within only ~ 20 nm of each other, and the ranges and magnitudes of their errors are very similar. Considering also that particle analysis from SEM images is inherently flawed (as many particles cannot be measured due to overlap), it can be said that the present samples show a high degree of reproducibility in terms of average particle size and size distribution, compared to LRHs and LDHs in the literature.[389,390]

The hydrodynamic diameter of the size-optimised particles, measured by DLS (Figure 3.13 and Table 3.7), is approximately 50 nm larger than the size

measured from SEM images, which is to be expected as this diameter includes water molecules associated with the particles being measured. Therefore, the DLS and SEM data are in good agreement. All samples have low polydispersity, though in some cases a small secondary population was observed around 4-6 µm (Figure 3.13). This is believed to be a result of aggregates which were not sufficiently broken up by sonication.

Table 3.7 Summary of particle size data from SEM and DLS for LTbH samples synthesised at 90 °C.

Sample name	*Size by SEM / nm*	*Particles measured*	*Hydrodynamic diameter / nm*	*Polydispersity index*
90-4-18-1	162 ± 85	460	199 ± 3	0.15 ± 0.04
90-4-18-2	151 ± 56	472	196 ± 2	0.18 ± 0.02
90-4-18-3	159 ± 52	515	199 ± 2	0.17 ± 0.03
90-4-18-4	146 ± 49	398	194 ± 6	0.15 ± 0.05
90-4-18-5	147 ± 47	849	194 ± 1	0.18 ± 0.04
90-4-18-6	152 ± 61	840	201 ± 2	0.20 ± 0.02
Overall	152 ± 59	3534	197 ± 4	0.17 ± 0.04

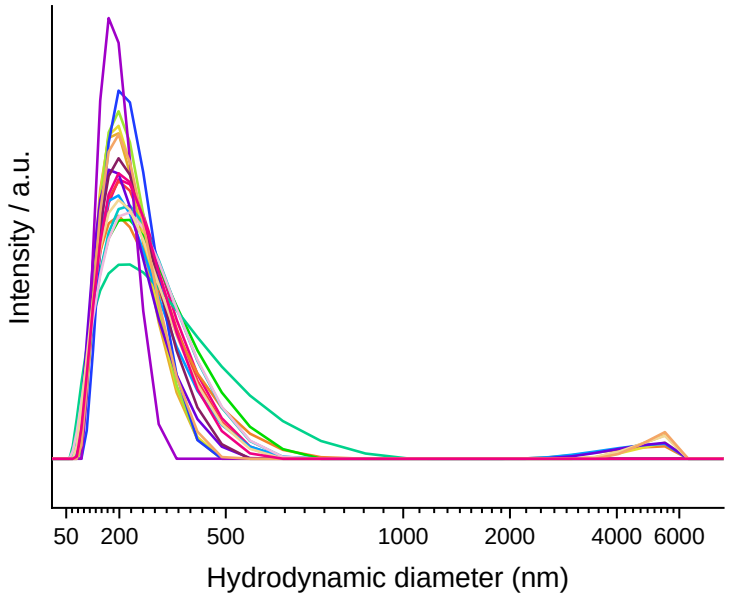

Figure 3.13 Superimposed hydrodynamic diameter data from DLS experiments on all size optimised LTbH samples (each sample suspension was prepared once and measured in triplicate).

3.4.5 Cytotoxicity assay

Cytotoxicity of the size-optimised and unoptimised LTbH formulations was evaluated using *in vitro* cell viability experiments on Caco-2 and HEK 293 cell lines, the results of which are presented in Figure 3.14.

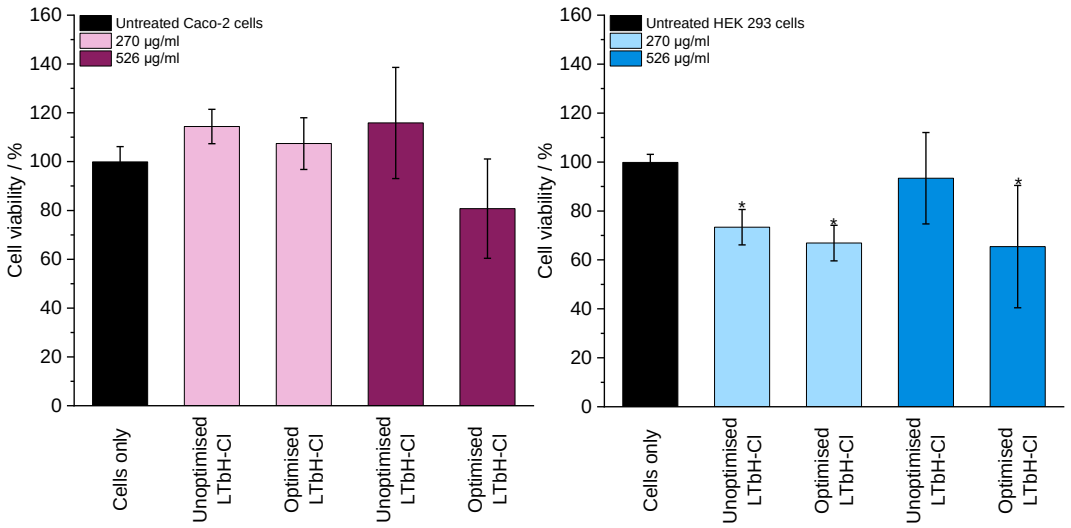

*Figure 3.14 The results of in vitro cell viability assays on a.) Caco-2 and b.) HEK 293 cell lines, performed with both optimised (90-4-18) and unoptimised (150-15-23) LTbH-Cl at two concentrations (270 µg / ml and 526 µg / ml). The assay experiment was performed three separate times, each in triplicate. Results are presented as mean ± standard deviation. * denotes groups with a significantly different mean viability from the control, at the p = 0.05 level.*

For the Caco-2 cell line, no treatment group appears to show a statistically significant change in cell viability relative to the untreated control. This agrees with results from Section 2.4.7, which also showed no statistically significant change in Caco-2 cell viability from treatment with LTbH-Cl. However, at the higher concentration of 526 µg / ml, the viability of cells treated with size optimised LTbH particles is statistically lower than the viability of cells treated with unoptimised LTbH particles. It is therefore possible that there may be some modest size-related effect on viability. Overall, LTbH-Cl does not appear to be significantly cytotoxic to Caco-2 cells at either concentration, irrespective of size.

The results of the viability experiment for the HEK 293 cell line are somewhat less clear. Some cytotoxicity (70 – 75 % viability relative to the untreated control) is

seen in both the optimised and unoptimised LTbH-Cl treatment groups at the lower concentration of 270 µg / ml. At the higher concentration of 526 µg / ml, however, the unoptimised treatment group exhibits high viability (95 %) compared to the optimised treatment group, which showed a further reduction in viability to ca. 65 %. This is mostly consistent with the results from Section 2.4.7, which showed HEK-293 cell viability was approximately 75 % relative to the control for LTbH-Cl at both concentrations. Overall, it seems HEK-293 cells are somewhat more sensitive to the presence of LTbH-Cl than Caco-2 cells, with a notable reduction in viability in three out of four treatment groups.

The assay employed measures cell viability indirectly by quantifying the amount of ATP (adenosine triphosphate) present, which is only produced by living cells. However, change in the quantity of ATP present may also arise due to cell damage rather than death. It may be that smaller particles (optimised LTbH) are better able to penetrate Caco-2 cells and disrupt their metabolic activity/cause cell death, leading to reduced quantities of ATP produced. There may also be differences between uptake behaviour between the cell lines which may help to explain the difference seen in viability. A live/dead staining assay was therefore conducted to investigate this further. Since the differences in behaviour are mainly seen at the higher treatment concentration of 526 µg / ml, this concentration was selected for the live/dead staining assay.

3.4.6 Live/dead assay and cell uptake studies

The CellTiter Glo assay underestimates the viability of cells, because metabolically inactive cells do not contribute to the resultant luminescence during the assay. Therefore, to verify the viability found by CellTiter Glo, a live/dead staining assay was conducted.

The live/dead staining kit consists of two components, the first of which is a resazurin stain which stains metabolically active cells by reacting with reduced nicotinamide adenine dinucleotide (NADH, an intermediate in several biological pathways, including glycolysis[391]) to produce a red fluorescence signal. The second component is a green nucleic acid stain (which is impenetrable to live cells), and as such it only stains dead cells. As with CellTiter Glo, the resazurin stain detects metabolic activity rather than true viability, so metabolically inactive cells will exhibit low (or nil) red fluorescence. The green nucleic acid stain, however, stains all dead cells. Therefore, dead cells will always exhibit green fluorescence emanating from the nucleus. In this way, the live/dead stain can show a.) living, metabolically active cells (bright red); b.) living, metabolically inactive cells (dim red or dark); and c.) dead cells (bright green).

3.4.6.1 Studies on Caco-2 cell line

The results of the live/dead assay conducted in 96-well plates for Caco-2 cells are shown in Figure 3.15. The staining process requires a rinse with PBS, which washed away most of the LTbH particles in the treatment groups and caused the cells to become rounded in the images. The images were used to derive viability data, shown in Table 3.8. Overall, the percentage viability reflects what is observed by the CellTiter Glo assay, showing no significant difference in viability between the treatment groups and the untreated control. The microscope used automatically adjusts fluorescence brightness, so while direct and quantitative comparisons of fluorescence intensity are not possible, it does seem that the treatment groups (Figure 3.15b, c) exhibit somewhat more intense red emission than the control. This is consistent with high levels of NADH, which in turn indicates high metabolic activity.[392] On this basis, it seems that the presence of

LTbH particles, size-optimised or not, does not seem to exhibit a cytotoxic effect on Caco-2 cells.

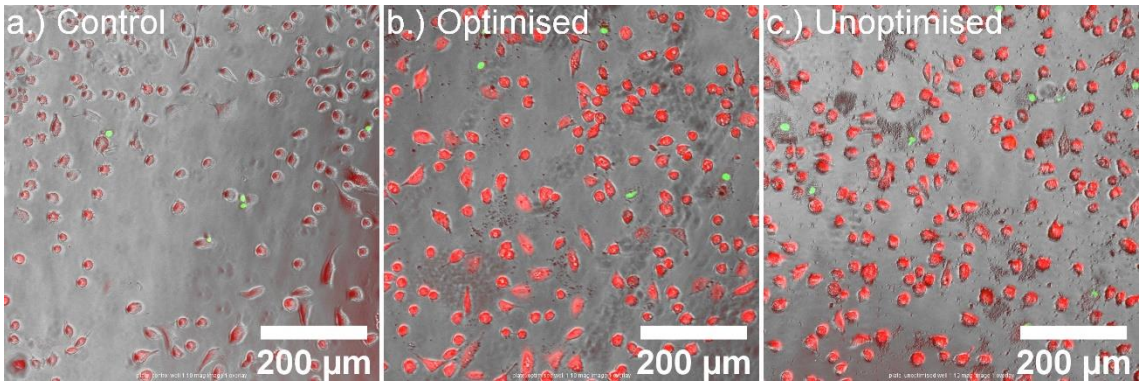

Figure 3.15 Fluorescence microscopy images in 96-well plates of live/dead staining of a.) untreated Caco-2 cells; b.) Caco-2 cells treated with size-optimised LTbH; and c.) Caco-2 cells treated with unoptimised LTbH. Live cells are stained red, dead cells are stained green.

Table 3.8 Summary of results of live/dead staining assay in 96-well plates of Caco-2 cells treated with LTbH.

Treatment	*Live cells*	*Dead cells*	*Viability / %*
Control	342	7	97.95
Optimised LTbH	310	9	97.10
Unoptimised LTbH	302	21	93.05

The magnification and resolution possible in a 96-well plate is restricted by the shape of the plate and the shadows cast by the black plate walls, so further experiments were conducted in glass-bottom petri dishes, which were easier to manoeuvre and could be used for further imaging by confocal scanning laser microscopy if desired.

Images of the cells grown and treated in glass-bottom petri dishes prior to washing and staining are shown in Figure 3.16, to illustrate cell growth and spreading. In both LTbH treated groups (Figure 3.16b, c) some cells exhibit bubble-like cavities within the cell membrane (cytoplasmic vacuolation). Though a detailed discussion on the cell mechanisms involved is beyond the scope of this

work, this phenomenon has been observed in the treatment of mammalian cells with high concentrations of inorganic nanoparticles on a number of occasions, and may be associated with the endocytosis process.[393,394] Alternatively, it may be evidence of autophagy, which is often characterised by the formation of autophagic vacuoles intended to digest damaged organelles within the cell.[395,396] Autophagy may eventually lead to cell death where the damage in cells is extensive, but is primarily a protective mechanism experienced by cells during stress.

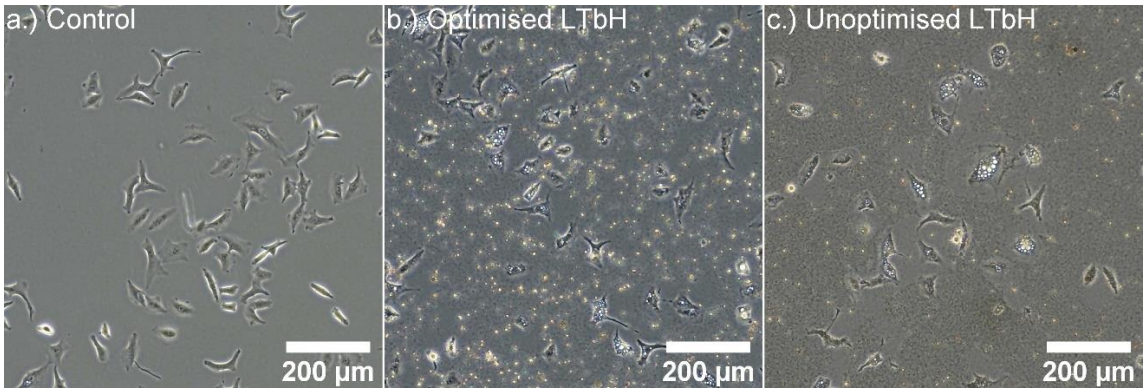

Figure 3.16 Microscopy images in glass-bottom petri dishes of a.) untreated Caco-2 cells; b.) Caco-2 cells treated with size-optimised LTbH; and c.) Caco-2 cells treated with unoptimised LTbH, all prior to washing and staining to illustrate cell spreading and vacuolation.

The outcome of the staining experiment conducted in a glass-bottom petri dish is shown in Figure 3.17. It is important to note that, due to lower cellular adherence on glass, the washing of samples with PBS was done very gently, leading to many particles being left over and therefore appearing in the images. Additionally, LTbH particles exhibit auto-luminescence in both the green and red channels, which is useful because they can be easily seen within cells. It is not expected that the autofluorescence of LTbH particles would confound the results of the CellTiter Glo assay, as it is a luminescence assay with no external excitation source, whereas LTbH autofluorescence occurs in response to excitation by the light source in the microscope.

The size optimised LTbH treatment group (Figure 3.17b) shows examples of live cells with endosomal cell uptake (shown by green arrows) as well as membrane attachment and/or uptake without associated endosomes (shown by red arrows). There are also examples of dead cells which show internalised particles (shown by white arrows), the bottom one of which also shows several large vacuoles containing particles. Overall, this seems to indicate that, while most cells experience no ill effects even after uptake several particles, there is potential to produce enough damage to eventually cause cell death *via* autophagy in a small number of cells. This may even be desirable if the cells in question are cancer cells – providing a potential route to passive cancer treatment.[397]

Images of cells treated with unoptimised LTbH are shown in Figure 3.17c. Due to the higher degree of rounding of cells in this sample, it was difficult to focus on the cells/particles simultaneously. This made it hard to evaluate uptake, but there are some cells which appear to contain LTbH particles (shown by the red arrows). There are multiple large particles/agglomerates of LTbH (example shown by white arrow), which due to their red auto-luminescence and similar size may be confused with live cells in the red channel. They are easily distinguishable in the brightfield channel because they appear dark. Additionally, there appear many areas surrounding cells (example shown by the green arrow) where there does not seem to be any particle density. It is possible that these empty areas were where cells had previously been adhered but contracted away from during the washing step.

Overall, due to the difficulties in the experimental process involved with the live/dead staining and uptake experiments presented in this section, it is not possible to draw any meaningful conclusions about how the size-optimisation of LTbH particles influences their effect on Caco-2 cells. However, viability data

derived from the live/dead staining assay supports the idea that the presence of LTbH particles does not appear to cause additional cell death (at the point of testing), relative to the untreated control, which agrees with viability data obtained using the CellTiter Glo assay.

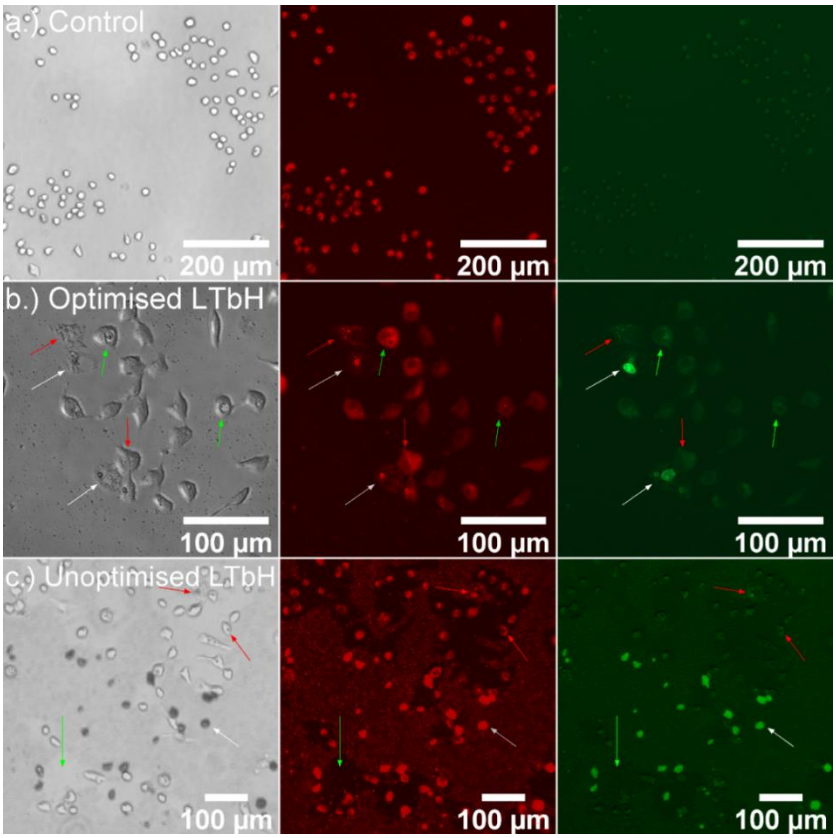

Figure 3.17 Microscopy images in glass-bottom petri dishes of Caco-2 cells stained with live/dead reagents, shown in brightfield view, and with Texas red/GFP filters. a.) Untreated Caco-2 cells; b.) Caco-2 cells treated with size-optimised LTbH - red arrows show cells with non-internalised LTbH particle adherence, green arrows indicate cells with endosomal LTbH uptake, and white arrows show necrotic cells with internalised LTbH; c.) Caco-2 cells treated with unoptimised LTbH – red arrows show cells with possible LTbH internalisation, the white arrow indicates and example of an agglomerate of LTbH, while the green arrow shows an empty region around a cluster of cells which is likely to have been the site of cell attachment prior to washing with PBS.

3.4.6.2 Studies on HEK-293 cell line

The 96-well live/dead staining procedure was replicated several times using the HEK-293 cell line. However, none of the experiments were successful due to issues encountered with cell attachment and aggregation, which made it impossible to glean meaningful information about the cells' response to the presence of LTbH.

In the 96-well plate, the HEK-293 cells did not adhere to the bottom of the wells (example overlay images are shown in Figure 3.18), making it impossible to perform a PBS rinse to remove the cell culture medium prior to staining. In turn, this raises the possibility of cell culture medium interference with the resazurin (red, metabolic activity stain) assay reagent, which is well known to be sensitive to the presence of many compounds, particularly amines and thiols.[398] Indeed, this seems to be the case as the red fluorescence intensity in the 96-well plate experiments was either very low or undetectable in all cases.

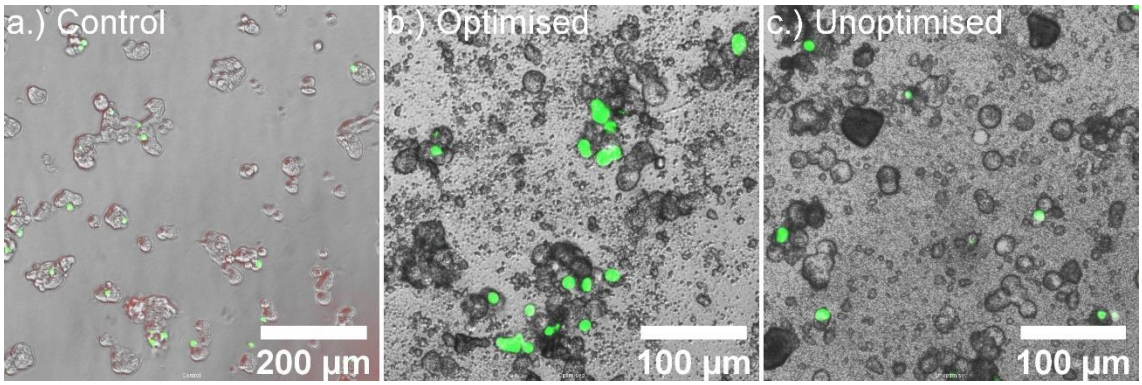

Figure 3.18 Example overlay microscopy images in 96-well plates of a.) untreated HEK-293 cells; b.) HEK-293 cells treated with size-optimised LTbH; and c.) HEK-293 cells treated with unoptimised LTbH, all stained with live/dead reagents. The low fluorescence intensity of the live (metabolic activity) red stain is likely low due to interference by cell culture media, which was not possible to wash away due to poor cell adherence.

Additionally, the cells were seen to form aggregates and exhibited a high degree of cell death, even in the control samples. This is typical for aggregates of cells, as the inner cells experience restricted access to culture medium containing essential nutrients and oxygen. Both poor adherence and aggregation are well known issues for the HEK-293 cell line.[399,400]

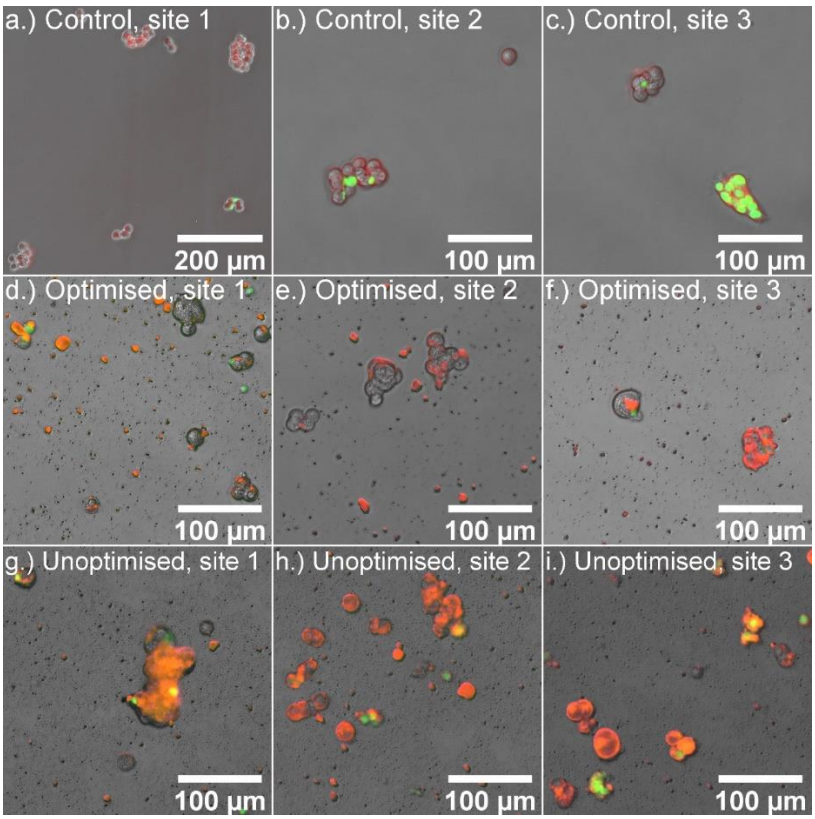

Figure 3.19 Example overlay microscopy images in T75 flasks of a-c.) untreated HEK-293 cells; d-f.) HEK-293 cells treated with size-optimised LTbH; and g-i.) HEK-293 cells treated with unoptimised LTbH, all stained with live/dead reagents.

As cell adherence to tissue culture treated glass is even more challenging for poorly adherent cell lines, the glass-bottom petri dish was substituted for a T75 cell culture flask for further imaging. 24 hours after seeding, the cells were attached to the flask, enabling a gentle PBS rinse to remove cell culture medium prior to staining. The PBS rinse caused the cells to detach, but the intensity of the resazurin stain was enhanced greatly by the removal of the cell culture medium prior to staining. Example overlay microscopy images are shown in Figure 3.19. Cell death and cell aggregation is seen to some degree in all groups. Though there does not seem to be additional cell death in the LTbH-treated groups relative to the untreated control, cell counting is precluded due to the significant level of cell overlap.

3.4.7 Suspension photoluminescence

The photoluminescence response of size-optimised and unoptimised LTbH samples was compared in aqueous suspension by using time-resolved fluorescence (TRF), the results of which are shown in Figure 3.20. Briefly, TRF allows the measurement of luminescence output after a specified time delay following the flash of the excitation lamp. Moreover, the luminescence output can be collected for a specified length of time (called 'integration time'), which is particularly useful for samples that exhibit phosphorescence rather than fluorescence, as is the case for terbium-containing species. Phosphorescence is a slower process than fluorescence (this will be discussed in more detail in the introduction section of Chapter 4), and therefore TRF measurements may offer more insight into the photoluminescence response than traditional fluorescence measurements. Lastly, the use of suspensions rather than solid-state samples allows quantitative comparisons as the concentration of the suspensions can be precisely controlled.

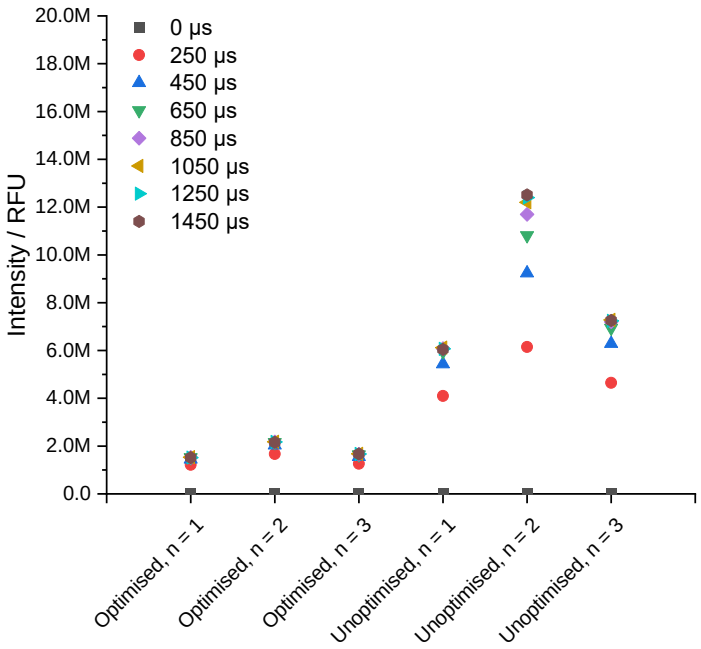

Figure 3.20 Plot showing the luminescence intensity (ex/em = 250/545 nm) in size-optimised vs. unoptimised LTbH, at different integration times (0 – 1450 µs).

The maximum luminescence intensity reached after 1450 µs appears to be higher in the unoptimised samples than those generated according to the size-optimised procedure (ca. 6-13M vs. 2M relative fluorescence units). Additionally, the inter-sample variability in maximum luminescence intensity is much higher in the unoptimised samples than in the size-optimised samples. Since the mean particle size distribution was shown to be higher in samples generated by the unoptimised method, it stands to reason that if the photoluminescence response is particle size-related, that these samples would have higher luminescence behaviour variability. Additionally, the size-optimised samples appear to reach saturation intensity faster (just above 250 µs) than the unoptimised samples (just above 450 - 850 µs).

While it is not certain that this effect is a consequence of particle size alone, size can influence luminescence intensity when surface defects in particles are present. For instance, the introduction of surface defects in terbium oxide nanoparticles by ball milling generates a ‘dead’ layer wherein excitation is quenched *via* non-radiative (thermal) pathways along the surface of the particles.[401] For smaller particles, the distance over which this ‘dead layer’ may effectively quench luminescence may be comparable to the particle size, therefore leading to a decreased luminescence intensity relative to samples with a larger average particle size, even at the same concentration. Since the LRH samples generated hydrothermally in this chapter all dry into a solid cake, each sample must undergo a brief mechanical grinding process in a pestle and mortar to separate the particles and produce a powder prior to further experiments. Though this process is not thought to influence the particle size (as particles appear whole and unbroken in SEM images), it may well introduce stress/strain defects along the surface of the particles and therefore facilitate defect-

quenching, which would be particularly evident for particles with a smaller average size population.

Overall, though the presented size-optimised method produces particles with a notably reduced luminescence intensity, it is still detectable and shows more inter-sample consistency than LTbH-Cl samples generated according to the protocol reported in Section 2.3.2.1.

3.5 Conclusions

The particle size and morphology of LTbH was shown to be responsive to the hydrothermal synthetic parameters of temperature, incubation time, and vessel fill volume. Optimisation of these conditions led to a significant reduction in both mean particle size and particle size distribution from that discussed in Section 2.4[318] (from 670 ± 564 nm to 152 ± 59 nm). This new method developed here was demonstrated to be highly consistent and reproducible. It is possible to use synthetic parameter control to achieve a high degree of particle shape selectivity. LTbH particles exhibit a predominantly rod-shaped morphology when synthesised at low temperature (90 °C), whereas at higher temperature (140 °C) the particles preferentially adopt a platelet geometry.

Overall, it was shown in this chapter that alteration of synthetic parameters is a viable route towards morphological control of LTbH. A method to achieve homogeneous LTbH particles with an average size below 200 nm was successfully developed. Chapter 4 will seek to apply this method to generate a family of LRH systems incorporating other lanthanide elements, which may be of interest for theranostic applications.

4 Potential theranostic systems based on layered rare-earth materials with alternative compositions

It was shown in Chapter 3 that the morphology and size of LTbH particles can be effectively controlled by varying time, temperature, and fill volume during hydrothermal synthesis. In this way, the resultant LTbH particle morphology was optimised to achieve a homogeneous population with a narrow mean particle size distribution (152 ± 59 nm), which is ideally suited in size to theranostic requirements.

This chapter explores applying the optimised synthetic method to generate LRHs based on a selection of other rare-earth elements – praseodymium, neodymium, gadolinium, dysprosium, erbium, and ytterbium. Furthermore, LRH systems with mixed composition (terbium/gadolinium) with potential for bimodal imaging capacity will be synthesised and evaluated in terms of their contrast ability.

4.1 Introduction

The rare-earth elements are typically defined as the set of 15 elements from lanthanum to lutetium. They are the first of two series of elements in the periodic table which are part of the f-block, the other being the actinides. Rare-earth elements are also commonly known as the lanthanides (or more formally, the lanthanoids, ‘lanthanum-like’), because their chemical behaviour remains remarkably uniform across the period. Conversely, the luminescence and magnetic properties of the lanthanides vary broadly, as a consequence of the unique electronic properties of these elements.

All lanthanide elements in their ground state possess electrons in 4f orbitals (apart from lanthanum, which has none). Additional valence electrons in lanthanide elements occur in the 6s orbitals (and in some cases, a single electron in the 5d orbital).[402]

An additional quirk of the electronic configuration of lanthanides is that the 5s and 5p orbitals lie lower in energy than do the 4f orbitals, which contain the valence electrons. However, because the 5s and 5p orbitals have a more distal spatial probability distribution, they effectively shield the 4f electrons from the surrounding environment. Because of this, the 4f electrons are relatively unaffected by the coordination or ligand field effects experienced by the Ln^{3+} ion.[402] Conversely, the ability of 4f electrons to shield the outer 5s and 5p electrons from the positive nuclear charge is poor.[403] As a result, lanthanide ions display a phenomenon known as the lanthanide contraction. Briefly, the ionic radii of the lanthanides contract along the period to a greater extent than might be expected based on the increasing nuclear charge alone. This happens because the poor shielding provided by the 4f electrons exposes the outer 5s and 5p electrons to a higher effective nuclear charge with successive additions of protons, and the resulting electrostatic interaction causes a contraction in the ionic radius (Figure 4.1).[404]

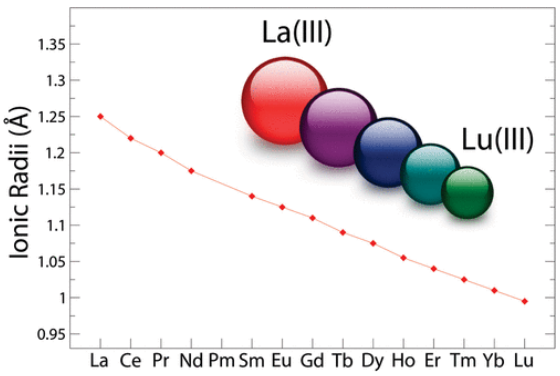

Figure 4.1 Ionic radii of the trivalent lanthanide ions, reprinted with permission from reference [404]. Copyright 2011, American Chemical Society.

Therefore, heavier lanthanide elements form smaller, more charge dense ions. This phenomenon, in turn, affects the final LRH structure due to the way the hydroxide anions are able to pack around the central metal ion. This is because Ln^{3+} centres bind primarily through ionic interactions (as a consequence of the well-shielded 4f valence electrons) rather than covalently, so their coordination environment is largely determined by steric considerations.[402] The LRH structure contains both 8 and 9 coordinate centres, with larger Ln^{3+} ions more able to accommodate higher coordination and therefore favouring the 9-coordinate environment.

To date, many LRH materials have been successfully synthesised, with a wide range of counter ions such as chlorides,[310,311,405] nitrates,[122,325] as well as drug anions.[87,88,123] Many initial attempts to synthesise LRH materials comprising the lighter lanthanide ions La, Ce, Pr, and Nd were unsuccessful, forming exclusively the $Ln(OH)_3$ phase.[311] Since then, successful syntheses of nanosheets of LRHs with Ln = La, Pr, and Nd have been reported,[101,406] though occasionally a secondary hydroxide phase may form, as in the case of LNdH.[311]

A Gd-based LRH doped with Eu ($LGd_{0.95}Eu_{0.05}H$) was reported, which exhibited a reduction in fluorescence intensity arising from Eu^{3+} when intercalated with amino acids, and thus was proposed to have potential applications in diagnostic sensing.[238] More recently, composite systems of polymers and Eu/Tb based LRHs demonstrated tuneable luminescence emission (red, green, or yellow) by varying the Eu and Tb content.[407] There are also reports of mixed-lanthanide systems containing Tb^{3+} and organic sensitizers, such as Gd/Tb/Eu LRH and Tb/Y LRH for colour tuneable luminescence,[408,409] and a Gd-doped LTbH-NO_3 system showing vastly enhanced luminescence arising from the synergistic interaction of Gd^{3+} and Tb^{3+}.[410] Most recently, “high-entropy” mixed-metal LRH

systems including up to 7 different rare-earth ions (Y, Eu, Gd, Er, Nd, Sm, and Tb)[411] have been reported. Attempts to include La^{3+} in these high-entropy systems were not successful, presumably as a result of lattice mismatch due to the large La^{3+} cation radius.[411]

Additionally, LRH composition may affect the resultant particle morphology, as has been explored on several occasions. One study on LRH-NO_3 materials synthesised via homogeneous precipitation reported a decrease in particle size for the heavier lanthanides, though the reasons behind this were not discussed.[412] In another study, LRH-Cl materials with different Ln^{3+} centres were found to form particles with differing geometries (ranging from rectangular to hexagonal plates).[311]

4.1.1 Rare-earth luminescence

The unique luminescence behaviour associated with many lanthanide elements arises from electronic transitions within partially filled 4f orbitals. Because of the shielding effect provided by 5s and 5p electrons, the f-f electronic transitions are relatively unaffected by the coordination environment of the Ln^{3+} ion. Therefore, multiple formulations including a particular Ln^{3+} ion might therefore be expected to have a very similar emission profiles, which is a useful property when formulating with different therapeutic moieties.

The balance of radiative vs. non-radiative relaxation pathways within a system ultimately determines the presence and strength of the luminescent response of a system. In a study comparing the fluorescence behaviour of Ln^{3+} chelates, it was shown that particularly strong line emission was observed for Sm^{3+}, Eu^{3+}, Tb^{3+}, and Dy^{3+} ions.[319] For these ions, the f-orbital splitting is such that: 1.) there are several low energy levels below the main emitting excited state; 2.) the

emitting energy levels have a relatively large energy separation from those lower energy levels.

This energy level distribution allows the radiative (luminescent) relaxation pathway to dominate over non-radiative relaxation processes (which are more efficient when the energy separation is low).[319] This is particularly evident in the Tb^{3+} and Eu^{3+} ions, compounds of which produce among most intense emissions of all lanthanide ions. In the case of Gd^{3+}, which has an electronic configuration of [Xe] $4f^7$, there is a supplementary stability imparted by the half-filled f-orbitals. As each orbital holds exactly one electron, the repulsion between electrons is minimised whilst the symmetry of the arrangement is maximised. As a result, these orbitals lie very high in energy and the lowest possible energy emission is within the UV region (310 nm). This property limits the medical uses of the luminescence behaviour of Gd^{3+}, as UV radiation is damaging to living tissue.

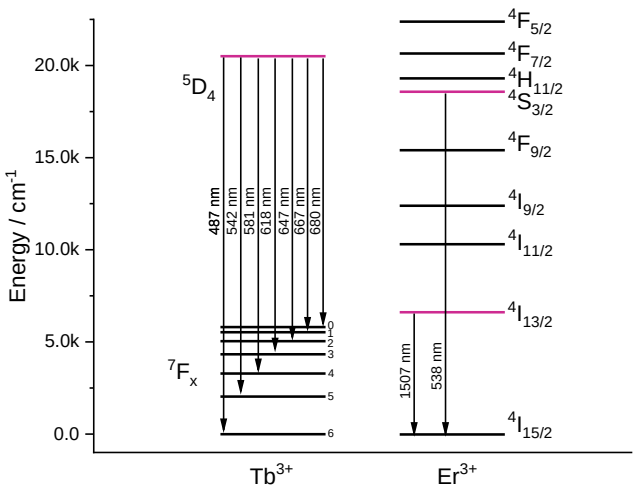

Figure 4.2 Term diagrams for the Tb^{3+} and Er^{3+} ions with the main emissive states highlighted in pink.

Strictly speaking, luminescent lanthanide ion emissions can be classified as either phosphorescence or fluorescence – phosphorescence arises from transitions which cause a change in spin multiplicity, whereas in a fluorescent process the spin multiplicity remains the same. For example, in Tb^{3+} (Figure 4.2),

for transitions from the $^5D_4$ state to one of the ^7F_x (x = 0-6) multiplet states, the spin multiplicity changes from 5 to 7, which formally makes these emissions phosphorescent. In Er^{3+}, transitions from the $^4S_{3/2}$ state to $^4I_{15/2}$ state, the spin multiplicity remains the same and therefore it is a fluorescence process (Figure 4.2). When spin-orbit coupling is not considered, a transition which results in the change of spin multiplicity is forbidden due to the conservation of angular momentum. However, when spin-orbit coupling is significant (such as in lanthanides), this restriction is not as prohibitive – for this reason, phosphorescence processes tend to happen on much slower timescales than do fluorescent processes. There are also other selection rules which govern the f-f transitions in lanthanides, but these are outside of the scope of this work.

Two other phenomena which must be mentioned in the context of lanthanide luminescence for biomedical applications are sensitisation and quenching effects. As many of the f-f transitions are forbidden by selection rules, direct excitation of Ln^{3+} is inefficient because both the absorption and emission are weak. Furthermore, each free Ln^{3+} ion can absorb only a very narrow range of wavelengths and may require expensive and powerful lamps. A way around this is to couple Ln^{3+} with molecules which can more efficiently absorb light (chromophores) across a broader range of wavelengths, and then transfer that absorbed energy to the emitting levels of the Ln^{3+} ion. In this way, indirect excitation (sensitisation) of the Ln^{3+} ion is more efficient than direct excitation and leads to higher luminescence yields – this is sometimes also referred to as the ‘antenna effect’. As demonstrated in Section 2.4.12 using LTbH, small organic molecules such as ibuprofen may act as chromophores to enhance the luminescence response in LRH systems in this manner.

There are several mechanisms of luminescence quenching that are relevant to lanthanide ion systems. As stated earlier, the smaller gap between the lowest emissive level and highest low energy levels in some Ln^{3+} ions (for instance Nd^{3+}, Er^{3+}, Yb^{3+}) increases the efficiency of non-radiative relaxation processes. Specifically, this is because the energy of those transitions happens to be closely matched to several vibrational modes in C-H and O-H bonds, enabling their efficient transfer. Consequentially, lanthanide ions which have resonant emissions in the NIR region are very efficiently quenched if surrounded by such bonds. In the context of medical applications, this is problematic because living tissue is rich in sources of O-H and C-H bonds.

Another undesirable pathway of relaxation involves energy transfer between a pair of Ln^{3+} ions. Essentially, when a Ln^{3+} ion with an electron excited into an emissive level comes into contact with a Ln^{3+} ion in its ground state, the excitation energy is redistributed leading to both ions occupying some intermediate energy (non-emissive) level, and subsequently relaxing via internal conversion. Such pair interactions prevent the eventual release of a photon via luminesce, and therefore lower the luminescence yield. As this process requires proximity of the Ln^{3+} ions, it is concentration dependant – and may be mitigated against using strategies such as doping or mixing with other species.

4.1.2 Rare-earth magnetism

In brief, MR imaging works by exploiting the response of hydrogen atoms (protons) in the human body to an externally applied magnetic field to build an image. Each proton has an associated spin magnetic moment, and in the absence of an externally applied magnetic field, the orientation of the magnetic moments of protons in a sample is random. When an external magnetic field is

applied, the magnetic moment of a proton may align with or against the direction of the external field, the former being a lower energy configuration and therefore resulting in a natural excess of protons aligned with the external field. Therefore, when an external magnetic field is applied, the protons in a sample generate a non-zero net magnetisation vector, which cannot be measured directly.

To measure the magnetic response of protons from a sample, therefore, the net magnetisation must be displaced away from the direction of the external field. The Larmor precession is a phenomenon which occurs for protons as a result of the torque generated by the external field, and manifests as the rotation of the magnetic moment of each proton around the direction of the applied field. A radiofrequency pulse can be used to confer energy to the protons and cause their magnetic moments to 'flip' into the higher energy state, aligned against the external magnetic field. In addition, the pulse causes the precession of the magnetic moments to begin to precess in phase with each other. After each pulse, the system returns to equilibrium by relaxation, which can occur in two distinct pathways. T_1 relaxation, also called 'longitudinal' relaxation, is the gradual return of magnetic moments to the lower energy state (aligned with the external field). T_2 or 'transverse' relaxation, on the other hand, is the gradual loss of resonance from the in-phase precession of protons within the sample. The energy loss associated with relaxation gives rise to signal, which can be monitored and translated into greyscale images.

As tissues within the body differ in composition, the local environment of protons between different tissues results in variable relaxation times, allowing the differences in measured signal to be used to construct images. However, the natural contrast of tissues is not always sufficient for therapeutic applications, so contrast agents are often utilised to improve the contrast of MR images. Contrast

agents work by further altering the local magnetic environment of protons within target tissues, changing their T_1 and/or T_2 relaxation times, and thereby changing their brightness relative to surrounding tissues. Contrast agents which decrease the T_1 relaxation time, such as Mn^{2+} and Gd^{3+} ions, are known as 'positive', and lead to enhanced brightness in the image.[35,46] Contrast agents which decrease the T_2 relaxation time, such as barium sulphate or superparamagnetic iron oxide, are known as 'negative', and they lead to decreased brightness in the image.

The Gd^{3+} ion, which contains the maximum possible number of unpaired 4f electrons, is a special case amongst the lanthanides, because of the highly symmetrical arrangement of these electrons. This results in a very high energy excited state, and therefore exceptionally slow electronic spin relaxation relative to the other lanthanide elements. The slow relaxation times of Gd^{3+} ions (10^{-7} s)[413] make them particularly efficient at enhancing the T_1 relaxation of nearby protons, for reasons which are beyond the scope of this study and will not be covered here. Conversely, due to the asymmetry in the unpaired electron distribution (and subsequently, shorter relaxation times of 10^{-13} s)[414] in other paramagnetic lanthanide ions, they act primarily to reduce the T_2 relaxation time of nearby protons. The ability of a contrast agent to enhance the relaxation rate of surrounding protons is quantified by a property termed 'relaxivity', which describes the change in either T_1 or T_2 relaxation rates as a function of contrast agent concentration. The ratio of relaxivities (r_2/r_1) for a particular contrast agent is a convenient way to express their predominant mode of action – with positive (T_1) agents generally having a low r_2/r_1 ratio (around 1-2), and predominantly negative (T_2) agents exhibiting higher r_2/r_1 ratios.[415]

4.2 Aims

The work in this chapter aims to apply the optimised synthetic method derived in Chapter 3 to generate LRHs based on a selection of other rare-earth elements – namely praseodymium, neodymium, gadolinium, dysprosium, erbium, and ytterbium. It is predicted based on available literature, that the synthesis of these LRH systems will be facile but may exhibit ion-size related effects on resultant particle morphology.

Additionally, LRH systems capable of bimodal imaging contrast with mixed composition (Gd/Tb) will be synthesised and evaluated in terms of their luminescent and magnetic properties. It is expected based on previously reported LGdH[87] that Gd-containing LRH systems will exhibit T_1 type relaxivity, and the inclusion of Tb (a predominantly T_2 affecting lanthanide) may enhance T_2 relaxivity.

4.3 Experimental

4.3.1 Materials

Terbium, dysprosium, erbium, and ytterbium chloride hexahydrate salts were purchased from Sigma Aldrich. Praseodymium and gadolinium chloride hexahydrate salts were purchased from Alfa Aesar, and neodymium chloride hexahydrate from Chem Cruz. All water used was deionised, and ethanol was of analytical grade.

4.3.2 Hydrothermal synthesis of LRH-Cl (R = Pr, Nd, Gd, Dy, Er, Yb)

An aqueous solution of $RCl_3.6H_2O$ (0.4 M, 13.5 ml, R = Pr, Nd, Gd, Dy, Er, Yb) was added dropwise to a stirring aqueous solution of NaCl/NaOH (1.4 M and 2.1 M respectively, 4.5 ml), such that the total volume was 18 ml. The resultant suspension was stirred for 10 min and transferred to a Teflon lined hydrothermal reactor (23 ml). The reactor was heated to 90 °C (150 °C for LYbH) for 4 h, at a heating and cooling rate of 10 °C / min, after which the precipitate was collected by centrifugation. The product was washed with water (2 x 30 ml) and ethanol (2 x 30 ml), and subsequently dried at 40 °C for 24 h to yield the product.

4.3.3 Hydrothermal synthesis of Gd:Tb LRH

A solution of $TbCl_3.6H_2O$ (0.X M, X = 0.3, 0.2, or 0.1) and $GdCl_3.6H_2O$ (0.4-X M) in water (13.5 ml) was added dropwise to a stirring aqueous solution of NaCl/NaOH (1.4 M and 2.1 M respectively, 4.5 ml), such that the total volume was 18 ml. The resultant suspension was stirred for 10 min and transferred to a Teflon lined hydrothermal reactor (23 ml). The reactor was heated to 90 °C for 4 h, at a heating and cooling rate of 10 °C / min, after which the white precipitate

was collected by centrifugation. The product was washed with water (2 x 30 ml) and ethanol (2 x 30 ml), and subsequently dried at 40 °C for 24 h to yield the product.

4.3.4 Characterisation

Characterisation procedures used in this chapter are identical to those described in Section 2.3.3; any differences and additional methods are described in this section.

4.3.4.1 SEM and electron dispersive x-ray spectroscopy

Samples were sputter coated with gold and imaged using a JEOL JSM-6701F field emission scanning electron microscope. Particle size analysis on the resulting images was performed manually using ImageJ 1.52a software, and the results presented as mean ± standard deviation. The number of particles measured is indicated in Table 4.1. Electron dispersive X-ray spectroscopy (EDXS) was performed using the same microscope fitted with an INCAx-Act detector from Oxford instruments.

4.3.4.2 ICP-OES

To determine the concentrations Ln^{3+} (Ln = Gd/Tb) in suspensions, inductively coupled plasma optical emission spectroscopy (ICP-OES) was conducted on a Varian 720-ES ICP-OES instrument. Stock suspensions of samples were prepared at a concentration of 29.6 mg in 10 ml distilled water. 1 ml of these stock suspensions was then acid digested using hot nitric acid and diluted with distilled water to 10 ml. The samples were then measured against a standard containing either Gd^{3+} or Tb^{3+} (100 mg / dm^3 in 5 % HNO_3 and 1000 mg / dm^3 in 2% HNO_3 respectively). The standard was diluted to aliquots of 2, 4, 6, and 8 ppm to make

a calibration curve for the measurements. Analysis of samples was performed by Connor Wells.

4.3.4.3 Relaxometry

Stock suspensions of samples were prepared at a concentration of 29.6 mg in 10 ml distilled water. The precise Ln^{3+} content of these samples was determined by ICP-OES. Aliquots (0.5 ml) of these suspensions and water (0.5 ml) were then transferred to NMR tubes (1 cm diameter) and prewarmed to 37 °C. Measurements of T_1 and T_2 relaxation times were conducted using an MQC+ benchtop NMR analyser (Oxford Instruments), operating at 23 MHz, O.47 T, and 37 °C. The inversion-recovery method was used for T_1 measurements (90° pulse calibration of 250 µm) and the Carr-Purcell-Meiboom-Gill (CPMG) method for T_2, with 4 scans per sample in both cases. Serial dilutions were performed for each sample by adding 100 µl of water between measurements; five different Ln^{3+} concentrations were measured for each sample. The suspensions were sonicated prior to each measurement.

The measured relaxation times were then used to calculate corresponding relaxation rates, $1/T_x$ (x = 1 or 2, as appropriate). The observed relaxation rate can be expressed according to Equation 4.1, where r_x is the relaxivity, and $[Ln^{3+}]$ is the concentration of Ln^{3+} ions (in mM), and $(1/T_x)_w$ is the relaxation rate of pure water.

$$\left(\frac{1}{T_x}\right)_{obs} = r_x \times [Ln^{3+}] + \left(\frac{1}{T_x}\right)_w \qquad 4.1$$

The relaxivities (r_1 and r_2) were derived from the gradients of the plots of relaxation rate ($1/T_x$) against $[Ln^{3+}]$ for each sample.

4.3.4.4 Suspension fluorescence

Fluorescence measurements were carried out in black 96-well plates (Thermo Fisher Scientific) using a SpectraMax M2e microplate reader (excitation = 325 nm, emission = 500 – 570 nm). Stock suspensions of LGd/TbH-Cl prepared for ICP-OES as described in Section 4.3.5.3 were used (150 µl per well).

4.3.4.5 Solid state photoluminescence

Photoluminescence measurements were performed on a Renishaw inVia Qontor microscope at an excitation wavelength of 325 nm, at 1 % laser intensity to limit sample degradation. Measurements were taken over the range 326 - 700 nm at a resolution of 0.026 nm.

4.3.4.6 Cytotoxicity assay

Cell viability assessments were conducted according to the protocol described in Section 2.3.3.7; the samples used in this series of experiments were LRH-Cl (R = Pr, Nd, Gd, Dy, Er, and Gd/Tb). Suspensions of LRH-Cl in culture medium (10 mg / ml) were prepared, and either 5 or 10 µl of these suspensions were added directly to the cells, to final concentrations of 270 and 526 µg / ml respectively. Three independent experiments were performed, each with treatment conditions in triplicate, and results presented as mean ± standard deviation.

4.4 Results and discussion

4.4.1 Single-metal LRHs

4.4.1.1 SEM

SEM images of the synthesised LRH materials are shown in Figure 4.3, and average particle sizes obtained from these images are summarised in Table 4.1. In general, there appears to be a loosely inverse relationship between decreasing Ln^{3+} ion size and particle size under the present synthetic conditions. The literature, however, presents a somewhat conflicting picture of how lanthanide ion size relates to LRH particle dimensions. The seminal works, which first reported the hydrothermal synthesis of LRH materials based on yttrium and the lanthanides Gd-Lu[416] did not note differences in resultant particle size. In another study, using the homogeneous precipitation method, lateral particle size of LRHs was seen to decrease across the period (from Sm – Tm).[412] Conversely, in a study on the effects of Ln^{3+} doping on the resultant size of layered yttrium hydroxide (synthesised hydrothermally), it was found that inclusion of lighter lanthanide dopants led to smaller overall particle size.[417]

LRHs based on Nd, Gd, and Dy exhibit very similar rod and plate shaped particles to the analogous LTbH material (sample 90-4-18, discussed in Section 3.4.2). Particles in the LPrH sample were highly aggregated, making sample preparation for SEM more difficult. It was therefore also more challenging to resolve individual particles in the images, though they appear to be of similar dimensions to LRHs with R = Nd – Dy, with particle sizes for these materials ranging between 100 - 200 nm. LErH is seen to form thin, plate shaped particles with serrated edges, which bear very little resemblance to those of any other LRH materials generated,

including the plate shaped LTbH particles synthesized at 140 °C (Section 3.4.2). The average size of LErH particles was found to be 442 ± 246 nm, which is significantly larger than the other LRH materials generated using the optimised protocol at 90 °C.

Crystalline LYbH could not be prepared at 90 °C, instead forming a colloidal dispersion. The synthetic temperature was therefore increased to 150 °C. The particles of LYbH produced are several orders of magnitude larger than the other LRH samples – though a direct comparison cannot be made due to the difference in synthetic temperature. The majority of LYbH particles are plate shaped, but some crystals are seen which exhibit unidirectional growth – this may be due to a presence of a secondary phase.

Table 4.1 Summary of mean particle size and number of particles measured for various LRH materials (R = Pr, Nd, Gd, Tb, Dy, Er, Yb) synthesised at 90 °C (: In the case of LYbH synthesis was carried out at 150 °C).*

Sample	*Size from SEM*	*Particles measured*
LPrH	138 ± 109 nm	89
LNdH	102 ± 33 nm	84
LGdH	171 ± 67 nm	99
LDyH	169 ± 56 nm	75
LErH	442 ± 246 nm	101
LYbH *	20 ± 14 µm	81

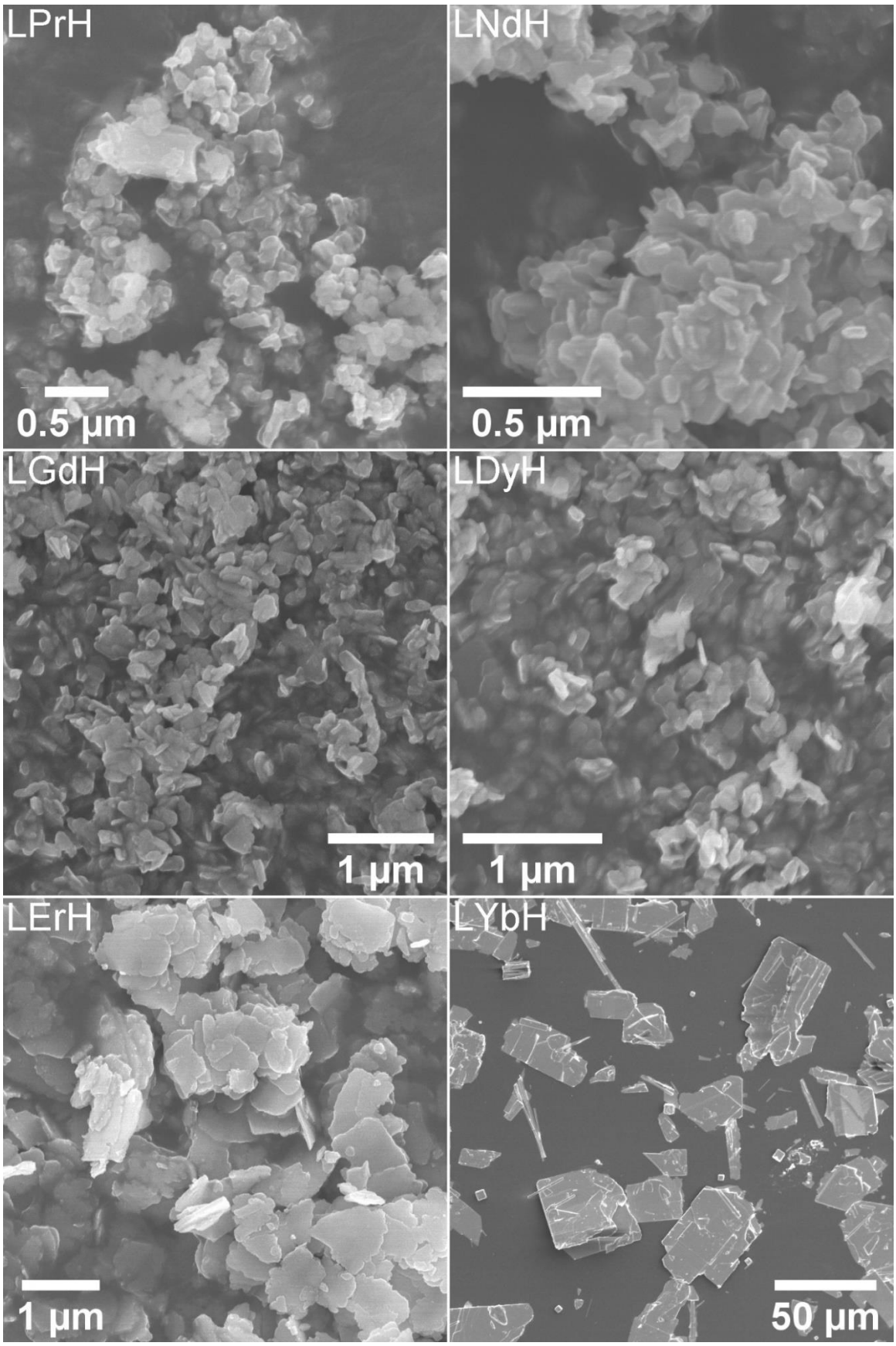

Figure 4.3 SEM images of the LRH materials (R = Pr, Nd, Gd, Dy, Er, Yb) synthesised at 90 °C (150 °C in the case of LYbH).

4.4.1.2 XRD

XRD patterns of the LRH materials (R = Pr, Nd, Gd, Dy, Er, Yb) are shown in Figure 4.4. All patterns exhibit the expected (010) reflection just above $2\theta = 10°$ and can be indexed to the orthorhombic $Pca2_1$ space group (refined unit cell parameters are summarised in Table 4.2). Interlayer spacing is seen to decrease slightly with decreasing ionic size as previously reported.[311] All samples also exhibit prominent reflections arising from the (400), (112), (320), and (410) planes, with the exception of LYbH in which they are not intense. In general, most reflections shift to higher diffraction angles as the lanthanide ion size decreases, which is due to the resultant decrease in Ln-O distances within the layers.[311]

All samples appear to be phase pure, except LYbH in which a small reflection can be seen next to the (010) reflection (Figure 4.4). This peak corresponds to a secondary phase, with a smaller interlayer spacing of 7.96 Å, and has been reported previously.[310] This is also consistent with the observation of two distinct morphologies for LYbH in the SEM images (Figure 4.3).

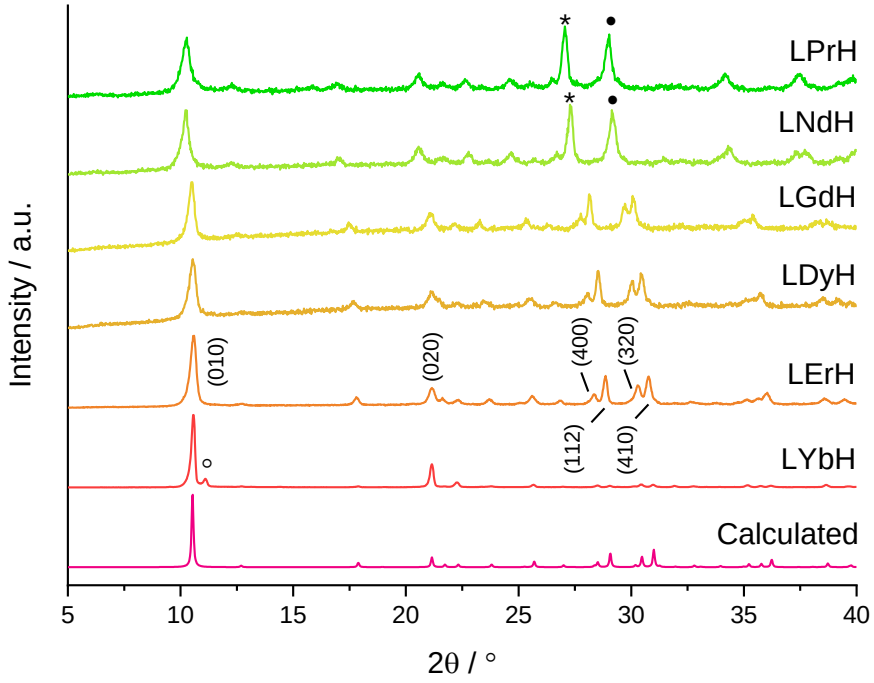

*Figure 4.4 XRD patterns for the LRH materials. (R = Pr, Nd, Gd, Dy, Er, Yb). *: (202) and (400) plane reflections are overlapping, •: (212) and (410) plane reflections are overlapping, °: Peak arising from secondary phase of LYbH. Calculated pattern based on LYbH (ICSD collection code 419745).*

Table 4.2 A summary of (010) reflection positions and refined unit cell parameters of LRH materials. (R = Pr, Nd, Gd, Dy, Er, Yb). Note: LYbH was not phase pure, data shown is for most abundant phase.

Material	*2θ / °*	*a / Å*	*b / Å*	*c / Å*
LPrH	10.24	12.49 ± 0.02	8.60 ± 0.01	7.14 ± 0.01
LNdH	10.24	12.54 ± 0.02	8.70 ± 0.01	7.02 ± 0.02
LGdH	10.50	12.71 ± 0.02	8.42 ± 0.01	7.047 ± 0.01
LDyH	10.52	12.52 ± 0.02	8.37 ± 0.02	7.05 ± 0.02
LErH	10.58	12.60 ± 0.01	8.41 ± 0.00	7.12 ± 0.00
LYbH	10.58	12.56 ± 0.03	8.38 ± 0.01	7.02 ± 0.03

4.4.1.3 TGA and chemical formulae

Thermograms of the various LRH materials are given in Figure 4.5. All compounds exhibit the expected triphasic mass loss as discussed in Section 2.4.6. The first mass loss event below ca. 200 °C is attributed to the loss of interlayer water, and the corresponding mass loss (along with elemental analysis data) is summarised in Table 4.3. This corresponds to between 1 and 1.75 molecules of water per formula unit, summarised in Table 4.4. Overall, there does not appear to be any trend in the hydration level of the LRH materials. It is likely that the interlayer water content is sensitive to drying and storage conditions, causing natural variability between samples.

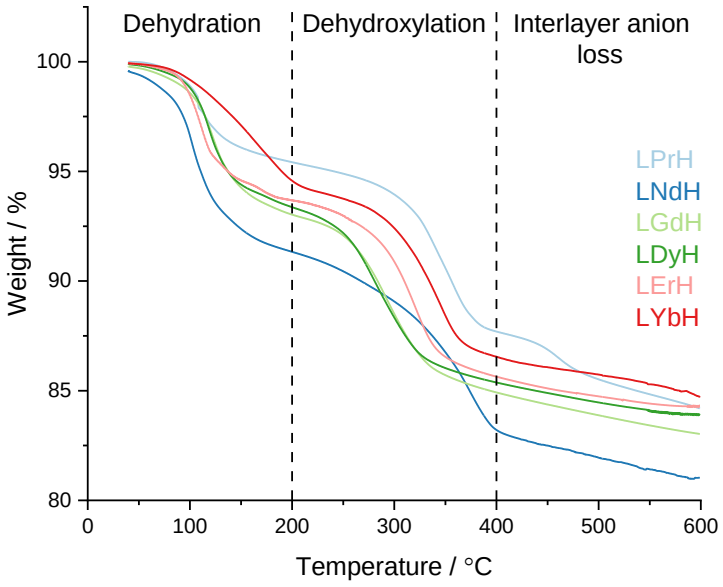

Figure 4.5 Thermograms of the various LRH materials (R = Pr, Nd, Gd, Dy, Er, Yb).

The results of the elemental analysis and water content as determined by TGA (Table 4.3) were used to calculate the approximate formulae of the LRH materials (Table 4.4). The carbon content of LPrH and LNdH indicated the presence a higher-than-expected amount of carbonate anions, making up 90 % of the anions within the interlayer gallery. It is not known why this might be the case – but it may be related to differences in charge density of the anions and lanthanide

cations. This is supported by the fact that carbon content seemingly decreases with Ln^{3+} ion size – with carbonate ions accounting for only 5 % of the interlayer anions in LYbH. No clear trend in carbonate content was reportedly observed for homogeneously precipitated LRHs with R = Nd – Tm,[311] but previous studies on LDH materials have shown a strong relation between anion selectivity and the charge density of the constituent LDH layers.[418]

Table 4.3 Summary of observed (and calculated from formulae, Table 4.4) values for elemental analysis and TGA data.

Material	*%C*	*%H*	*Mass loss % (H_2O)*
LPrH-Cl	1.24 (1.30)	1.53 (1.70)	4.77 (4.34)
LNdH-Cl	1.22 (1.24)	1.77 (1.97)	8.15 (7.24)
LGdH-Cl	0.42 (0.39)	1.59 (1.84)	6.83 (6.78)
LDyH-Cl	0.44 (0.39)	1.56 (1.53)	6.45 (5.74)
LErH-Cl	0.24 (0.25)	1.64 (1.68)	6.35 (5.62)
LYbH-Cl	0.07 (0.06)	1.63 (1.63)	6.03 (5.48)

Table 4.4 Summary of formulae derived from TGA/elemental analysis data.

Material	*Formula*
LPrH-Cl	$Pr_2(OH)5Cl_{0.1}(CO_3)_{0.45}\cdot H_2O$
LNdH-Cl	$Nd_2(OH)5Cl_{0.1}(CO_3)_{0.45}\cdot 1.75H_2O$
LGdH-Cl	$Gd_2(OH)_5Cl_{0.7}(CO_3)_{0.15}\cdot 1.75H_2O$
LDyH-Cl	$Dy_2(OH)_5Cl_{0.7}(CO_3)_{0.15}\cdot H_2O$
LErH-Cl	$Er_2(OH)_5Cl_{0.8}(CO_3)_{0.1}\cdot 1.5H_2O$
LYbH-Cl	$Yb_2(OH)_5Cl_{0.95}(CO_3)_{0.025}\cdot 1.5H_2O$

4.4.1.4 Cytotoxicity assay

Cytotoxicity of the LRH formulations was evaluated using *in vitro* cell viability experiments on Caco-2 and HEK 293 cell lines, the results of which are presented in Figure 4.6. LYbH was not tested due to unsuitable particle morphology (mean particle size 20 ± 14 μm, which is undesirable for theranostic applications due to reasons outlined in Section 3.1.1). In the Caco-2 cell line experiments, all treatment groups appear to show no statistically significant cytotoxicity at the p = 0.05 level, though in some cases (particularly for LDyH and LGdH) the standard deviation was relatively high (> ± 15 %). Conversely, for the HEK 293 cell line, a degree of cytotoxicity is seen in all treatment groups at both concentrations (with mean viability of less than 90 %). LErH appears to exhibit the most adverse effect on the HEK 293 cells, with ca. 50 % or less cells surviving after 24 hours, even at the lower testing concentration (270 μg / ml). This effect may be due to particle morphology, as LErH exhibits a mean particle size of 442 ± 246 nm, which is larger than the Pr/Nd/Gd/Dy LRHs (mean particle size under 200 nm). Additional factors, such as Ln^{3+} ion identity or differences in LRH solubility may also contribute, though erbium compounds are not known to be particularly toxic relative to the rest of the lanthanides.[419]

Overall, the biocompatibility of the formulations appears to differ depending on the cell line used. In Caco-2 cells, all LRH formulations (R = Pr, Nd, Gd, Dy, Er) exhibit good biocompatibility (over 80 % viability in all cases), even at high concentration (526 μg / ml). In contrast, HEK 293 cells were sensitive to the presence of all LRH formulations, at both testing concentrations (less than ca. 85 % viability in all cases). This effect was particularly strong in the case of LErH, with average cell viability of approximately 50 %. Though the apparently

enhanced cytotoxicity of the LRH formulations towards healthy (HEK 293) rather than cancerous (Caco-2) cells is not desirable, it must be noted that both the treatment concentrations considered here are higher than those which might be used therapeutically, and those reported in comparable studies (e.g., up to 100 µg / ml LRH).[420]

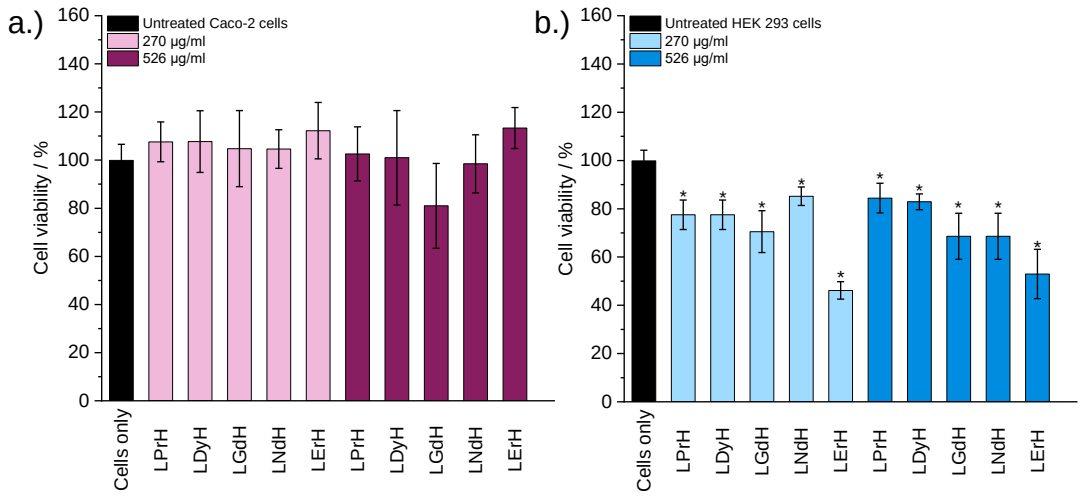

*Figure 4.6 The results of in vitro cell viability assays a.) Caco-2 and b.) HEK 293 cell lines, performed with aqueous LRH suspensions at two concentrations (270 µg / ml and 526 µg / ml). The assay experiment was performed three separate times, each in triplicate. Results are presented as mean ± standard deviation. * Denotes groups with a significantly different mean viability from the control, at the p = 0.05 level.*

4.4.1.5 Lead element selection

In an endeavour to develop a theranostic platform with the most promising combination of features, the lanthanide elements gadolinium and terbium were selected for further study. Terbium exhibits strong luminescence, with the most intense emission at 542 nm, which is ideally suited to avoid overlap with human tissue autofluorescence. This will be explored in more detail in Section 5.1.1. Gadolinium, on the other hand, exhibits by far the strongest magnetic effect of all lanthanide elements, as laid out in Section 4.1.2. Previous studies have demonstrated that LTbH systems doped with Gd exhibit a dramatic enhancement in the luminescence intensity arising from Tb,[410] and such a synergistic interaction could be exploited for biomedical imaging applications. SEM images revealed

that both LGdH and LTbH form homogeneous particles of similar size under the optimised synthetic conditions. Moreover, their similar ionic size would likely result in high compatibility in a combined crystal system. Lastly, both LGdH and LTbH have demonstrated high biocompatibility in the Caco-2 cell line (> ca. 80 % viability), and acceptable biocompatibility in the HEK 293 cell line (> ca. 65 % viability) at concentrations in excess of what would be expected for therapeutic applications.

4.4.2 Mixed-metal LRHs

4.4.2.1 ICP-OES

LRH systems containing three different ratios of Gd and Tb were synthesised using feedstock ratios of 1:3, 1:1, and 3:1. Inductively coupled plasma optical emission spectroscopy (ICP-OES) was used to verify the precise Gd/Tb composition of each material, and the data are summarised in Table 4.5.

Table 4.5 The Gd/Tb fractions of mixed-metal LRH materials ($LGd_{2-x}Tb_xH$-Cl), as determined by ICP-IOS (and expected based on concentrations in the synthetic feedstock). Each value is the average of three separate samples.

Feedstock ratio (Gd:Tb)	*Tb fraction (x)*	*Gd fraction (2 - x)*
3:1	1.590 ± 0.003 (1.50)	0.410 ± 0.003 (0.50)
1:1	1.121 ± 0.007 (1.00)	0.879 ± 0.007 (1.00)
1:3	0.591 ± 0.006 (0.50)	1.409 ± 0.006 (1.50)

In each formulation, the Tb content is slightly higher than expected based on the ratio of salts present during synthesis. It is possible that this effect is related to ion size/effective nuclear charge effects, with the slightly smaller, more charge dense Tb^{3+} ions crystallising into the LRH matrix more readily. However, since the chloride hexahydrate salts used in the synthesis of the present LRH materials

are highly hygroscopic, it is also possible that the Gd concentration in the feedstock solutions was underestimated. It may be that the $GdCl_3.6H_2O$ salt is more hygroscopic than the $TbCl_3.6H_2O$ salt; it has previously been reported that hygroscopicity across the period decreases in lanthanide oxides.[421] Nevertheless, the final Gd/Tb ratios in the synthesised LRH materials are very close to those intended, and therefore suitable for further study.

4.4.2.2 XRD

XRD patterns of the LRH materials (R = Gd/Tb) with varying composition are shown in Figure 4.7. In all cases, the patterns are very similar to each other and to the single-metal LRH materials (LTbH and LGdH). All mixed-metal LRH sample XRD patterns exhibit the expected (010) reflection just above $2\theta = 10°$. The (010) reflection, which corresponds to the interlayer spacing, is seen to shift very slightly to higher diffraction angles with higher Tb content. This is consistent with the expectation that the interlayer distance should decrease for heavier lanthanides with a smaller ionic size.[311] There are no prominent (h0l) reflections, but it is expected that they too would shift to higher reflection angles with increased Tb content due to the shorter average Ln-O distance within the layers. The presence of a single basal spacing reflection provides some evidence that both Gd and Tb ions are incorporated into a single phase.

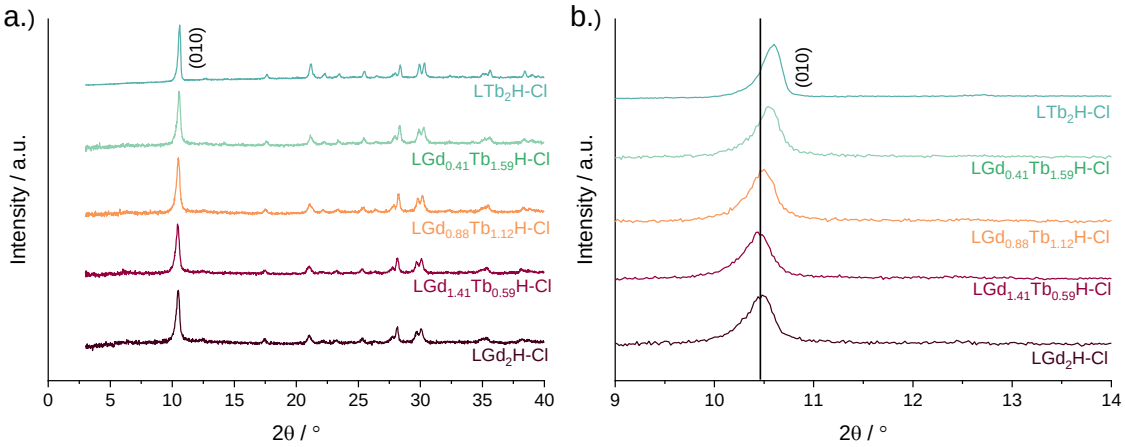

Figure 4.7 XRD patterns for various compositions of LRH materials. (R = Gd, Tb).

4.4.2.3 EDXS

Attempts were made to use energy dispersive X-ray spectroscopy (EDXS) to further study the Gd/Tb distribution within the mixed-metal LRH materials. Their respective spectra are shown in Figure 4.8. As the energy bands arising from Gd and Tb overlap significantly, and the equipment available did not contain the necessary software to deconvolute this overlap, it was not possible to use the spectra to quantify the metal ratios within the samples. Nevertheless, the overlapping peaks seem to exhibit slight differences in intensity distribution, which are consistent with the composition determined by ICP.

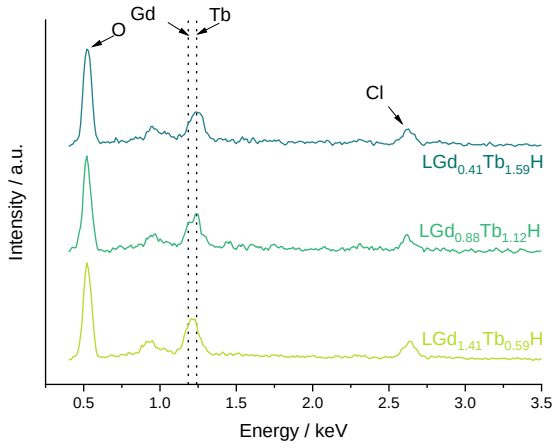

Figure 4.8 EDXS spectra of LRH (R = Gd/Tb) materials with varying composition.

Additionally, due to the poor spatial resolution in the images used during EDXS analysis (Figure 4.9), it was only possible to analyse large agglomerates rather than individual particles. Because of this, no information can be derived about the elemental distribution on the particle size scale. However, the images did not show any evidence of phase segregation at the micro scale, and taken together with other data, support the formation of a mixed-metal phase.

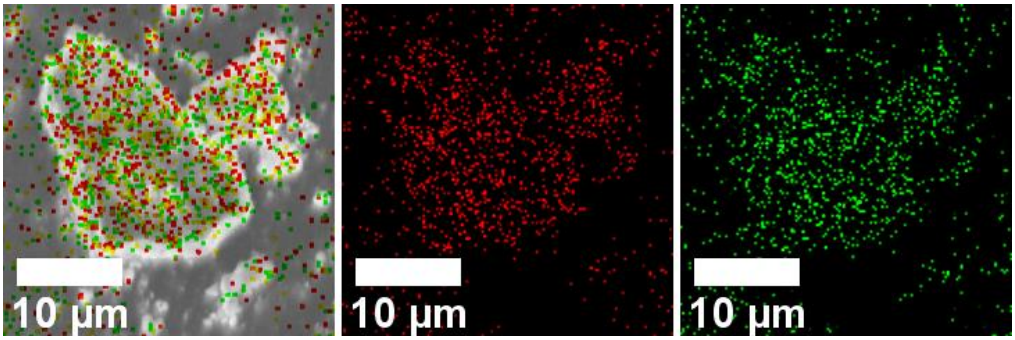

Figure 4.9 Representative SEM image used for EDXS analysis (sample $LGd_{1.41}Tb_{0.59}H$-Cl). Gadolinium and terbium atoms detected are shown in red and green respectively; yellow indicates sites which are either Gd or Tb.

4.4.2.4 TGA and chemical formulae

Thermograms of the LRH materials (R = Gd/Tb) are given in Figure 4.10. The ICP-OES, TGA, and elemental analysis data (Table 4.5 and Table 4.6) were used to derive the formulae of the three LRH materials (Table 4.7). All three compounds exhibit an initial mass loss event below ca. 200 °C which is attributed to the loss of interlayer water, in each case equivalent to approximately 1.6 molecules of water per formula unit. The subsequent mass loss event between ca. 200 – 400 °C is caused by dehydroxylation as discussed previously. Overall, the water and interlayer anion content are uniform across the three compositions.

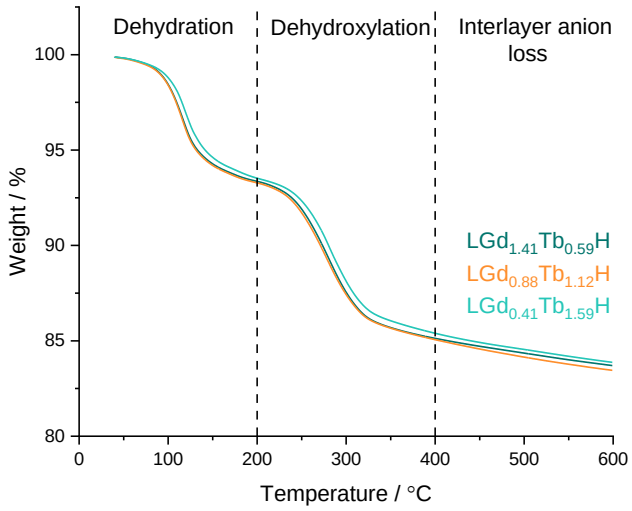

Figure 4.10 Thermograms of mixed LRH materials with varying composition (R = Gd/Tb).

Table 4.6 Summary of observed (and calculated from formulae, Table 4.7) values for elemental analysis and TGA data.

Sample	*% C*	*% H*	*Mass loss % (H_2O)*
$LGd_{1.41}Tb_{0.59}H$-Cl	0.30 (0.28)	1.62 (1.78)	6.14 (6.22)
$LGd_{0.88}Tb_{1.12}H$-Cl	0.30 (0.28)	1.60 (1.78)	6.18 (6.21)
$LGd_{0.41}Tb_{1.59}H$-Cl	0.35 (0.32)	1.58 (1.74)	5.94 (5.83)

Table 4.7 Summary of formulae derived from ICP-OES/TGA/elemental analysis data.

Sample	*Formula*
$LGd_{1.41}Tb_{0.59}H$-Cl	$Gd_{1.41}Tb_{0.59}(OH)_5Cl_{0.78}(CO_3)_{0.11}\cdot 1.6H_2O$
$LGd_{0.88}Tb_{1.12}H$-Cl	$Gd_{0.88}Tb_{1.12}(OH)_5Cl_{0.78}(CO_3)_{0.11}\cdot 1.6H_2O$
$LGd_{0.41}Tb_{1.59}H$-Cl	$Gd_{0.41}Tb_{1.59}(OH)_5Cl_{0.75}(CO_3)_{0.125}\cdot 1.6H_2O$

4.4.2.5 Relaxometry

Aqueous suspensions of the mixed-metal LRH materials (as well as LTbH and LGdH) were evaluated in terms of their potential MRI contrast ability using relaxometry. The relaxivity of samples can be determined from the gradient of a plot of relaxation rate ($1/T_1$ or $1/T_2$) against the concentration of MRI active

component (Ln^{3+}, in mM) during serial dilutions (as outlined in Section 4.3.4.3). Both Gd and Tb are magnetically active, with Gd primarily affecting T_1 and Tb predominantly affecting T_2. Since the samples tested have varying Gd/Tb content, the relaxation rate may be plotted against the total Ln^{3+} ion concentration (Gd + Tb) to compare their performance directly. The mean r_1 and r_2 relaxivities (and the resultant r_2/r_1 ratios) for the various formulations derived in this manner are shown in Figure 4.11a-c, and the data are summarised in Table 4.8.

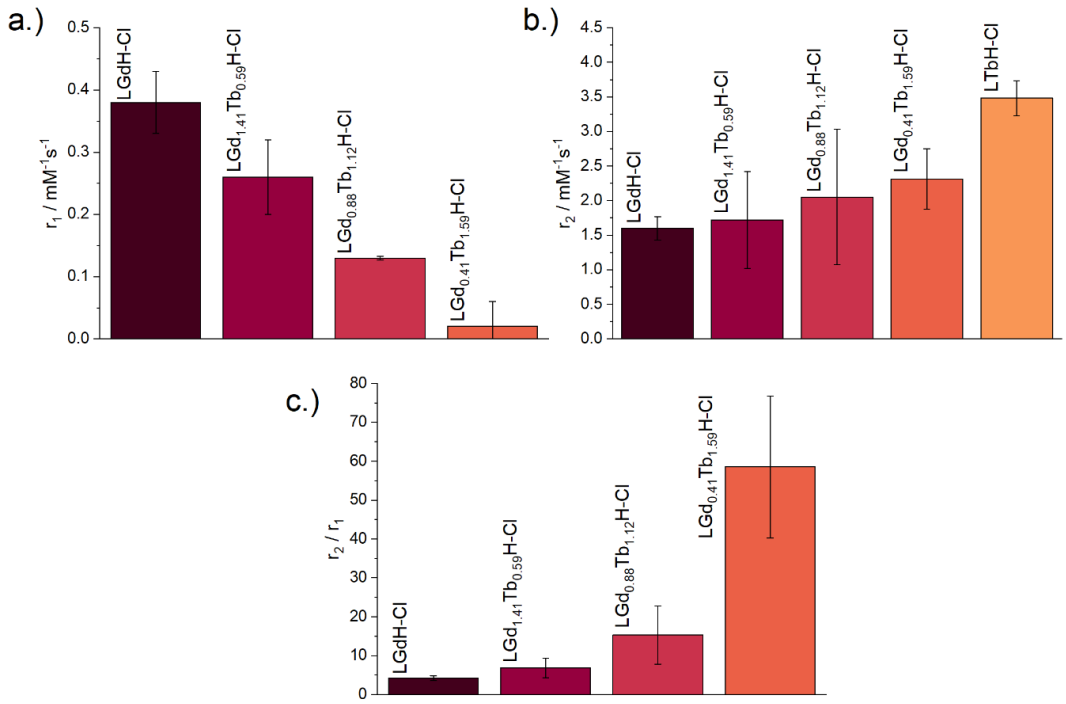

Figure 4.11 a-b.) Relaxivities (r_1 and r_2) for LRH materials with varying Gd/Tb compositions. c.) The r_2/r_1 ratio of the LRH materials. Data are presented as mean ± standard deviation, from three separate samples for each formulation.

Considering first the T_1 data plotted against the total lanthanide ion concentration (Figure 4.11a), the expected pattern is seen – samples with higher Gd content exhibit higher r_1 values which are associated with positive contrast agents. Moreover, since the relaxivity values are normalised to the total Ln^{3+} content rather than Gd^{3+} only, higher content of Tb (which is less active as a T_1 agent) is expected to result in a lower observed r_1 relaxivity. The highest mean r_1 value is seen for LGdH (0.38 ± 0.05 $mM^{-1}s^{-1}$), and the lowest for $LGd_{0.41}Tb_{1.59}H$ (0.02 ±

0.04 $mM^{-1}s^{-1}$); it was not possible to measure LTbH samples because their T_1 relaxation was not detectable. The previously reported r_1 relaxivity for LGdH-Cl is somewhat higher (0.51 $mM^{-1}s^{-1}$),[87] though in that instance the synthetic protocol produced particles with a larger mean size, and samples were suspended in agarose gel rather than water, both of which affect water access to the Gd centres and therefore the apparent relaxivity. Compared to commercially available agent Gd-DPTA (r_1 = 3.8 $mM^{-1}s^{-1}$ in aqueous suspension, at 0.47T),[422] the r_1 relaxivities of the present materials are very low. This is believed to be a consequence of the layered nature of the LRHs – with only the surface Gd-OH polyhedra able to efficiently partake in proton exchange with the surrounding bulk water, thus contributing to T_1 relaxation. The remaining Gd centres, which are exposed only to the interlayer environment, may not have sufficient bulk water access to contribute to T_1 relaxation. This is analogous to reports of non-layered Gd-phosphate nanoparticles,[423] where r_1 relaxivities were shown to depend on surface to volume ratio (with samples containing proportionally more Gd surface sites exhibiting higher relaxivities).

The T_2 relaxation rate data (Figure 4.11b) revealed that LTbH-Cl exhibited the highest r_2 values overall (3.48 ± 0.25 $mM^{-1}s^{-1}$), which is unsurprising as Tb^{3+} is predominantly a negative contrast agent. This is comparable to the r_2 relaxivity of commercially available Gd-DPTA (r_2 = 4.2 $mM^{-1}s^{-1}$ in aqueous suspension, at 0.47T).[422] The remaining formulations appeared to show a loosely positive correlation between Tb content and r_2 relaxivity. However, these relaxivity values are broadly comparable (ca. 2 $mM^{-1}s^{-1}$) irrespective of composition when the standard deviations are considered. The T_2 relaxation behaviour of Tb is thought to be predominantly determined by water diffusion effects,[424] which in turn are affected by the dynamic behaviour of the particles in suspension. Therefore, it is

not certain whether any differences in r_2 relaxivity in the present data are an effect of composition or of particle morphology/aggregation behaviour. The r_2 relaxivity of Tb-containing materials has been previously shown to be more effective at higher magnetic field strengths (10.4 and 48.5 $mM^{-1}s^{-1}$ at 1.44T and 9.4T respectively),[425] suggesting that the relaxivities of the present LRH materials may potentially be improved if measured at higher field strengths.

The r_1, r_2, and r_2/r_1 values for all formulations are summarised in Table 4.8. As the r_2/r_1 ratios in all cases are higher than 1, it can be tentatively said that all formulations act predominantly to affect T_2 relaxation. $LGd_{0.88}Tb_{1.12}H$-Cl and $LGd_{0.41}Tb_{1.59}H$-Cl show particularly high r_2/r_1 ratios (15.32 and 58.52 respectively) and may therefore be candidates as negative contrast agents for MRI; however, these ratios are enhanced primarily due to their very poor T_1 relaxivity, rather than good T_2 performance. The $LGd_{1.41}Tb_{0.59}H$-Cl system may offer a more reasonable compromise between r_1 and r_2 relaxivity.

Table 4.8 Summary of r_1, r_1, and r_2/r_1 values for various LRH materials (R = Gd/Tb). Results are shown as the mean ± standard deviation of three separate, independent samples.

Sample	*r_1 / $mM^{-1}s^{-1}$*	*r_2 / $mM^{-1}s^{-1}$*	*r_2/r_1 (unitless)*
LGdH-Cl	0.38 ± 0.05	1.60 ± 0.17	4.21 ± 0.64
$LGd_{1.41}Tb_{0.59}H$-Cl	0.26 ± 0.06	1.72 ± 0.7	6.83 ± 2.50
$LGd_{0.88}Tb_{1.12}H$-Cl	0.13 ± 0.00	2.05 ± 0.98	15.32 ± 7.47
$LGd_{0.41}Tb_{1.59}H$-Cl	0.02 ± 0.04	2.31 ± 0.44	58.52 ± 18.26
LTbH	n/a	3.48 ± 0.25	n/a

4.4.2.6 Suspension photoluminescence

The photoluminescence response of the various compositions of LRH (R = Gd, Tb) was compared in aqueous suspension by using time-resolved fluorescence (TRF), the results of which are shown in Figure 4.12. By far the highest maximum luminescence intensity reached after 1450 µs is seen in $LGd_{1.41}Tb_{0.59}H$-Cl (ca. 4

– 6M relative fluorescence units). The remaining mixed-metal LRH samples and LTbH-Cl exhibit comparable luminescence intensity, though the luminescence of $LGd_{0.88}Tb_{1.12}H$-Cl is marginally more intense than LTbH-Cl.

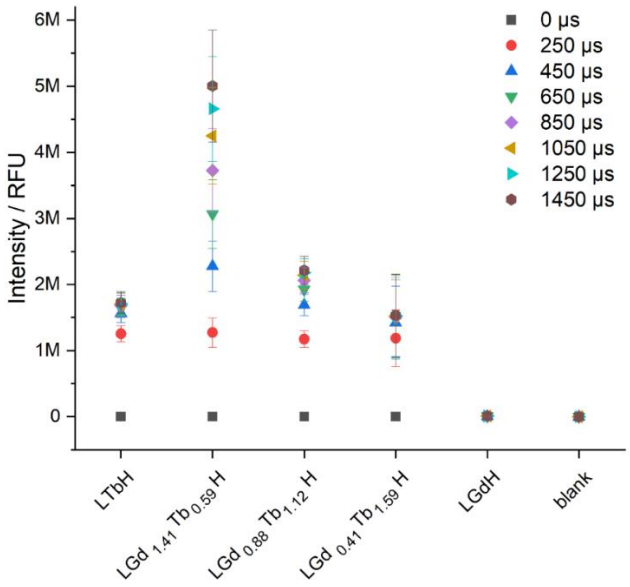

Figure 4.12 Plot showing the luminescence intensity (ex/em = 250/545 nm) in LRH materials with varying composition, at different integration times (0 – 1450 µs). Results are presented as mean of three separate samples ± standard deviation.

Overall, this is likely a combination of two effects – firstly, Tb-Tb quenching effects are minimised with higher Gd content (as there is more separation between Tb centres on average). Secondly, additional energy transfer from Gd to Tb occurs, resulting in a higher population of excited states in the Tb centres and thence higher luminescence production, as has been reported in several types of systems containing both Tb and Gd.[410,426] This also helps to explain the longer time to reach saturation intensity in $LGd_{1.41}Tb_{0.59}H$-Cl compared to the other Tb containing samples (over 1450 µs vs. less than ca. 1050 µs). as the additional energy transfer from Gd-Tb is not instantaneous and therefore occurs for some time after the excitation flash.

4.4.2.7 Cytotoxicity

Cytotoxicity of the mixed Gd/Tb LRH formulations was evaluated using *in vitro* cell viability experiments on Caco-2 and HEK 293 cell lines, the results of which are presented in Figure 4.13.

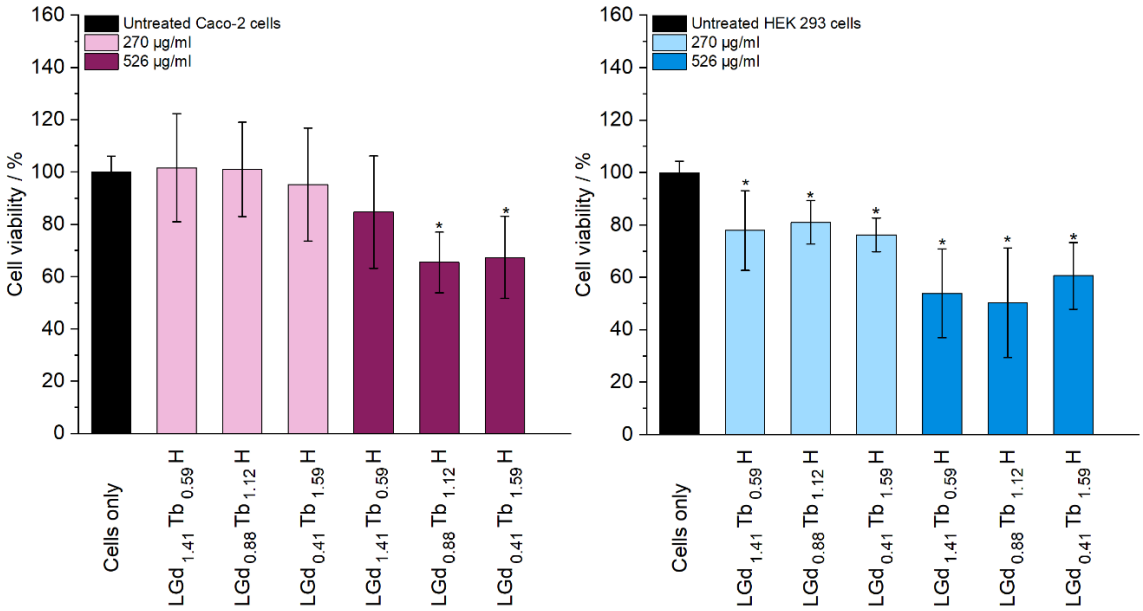

*Figure 4.13 The results of in vitro cell viability assays on a.) Caco-2 and b.) HEK 293 cell lines, performed with LRH materials of varying composition at two concentrations (270 µg / ml and 526 µg / ml). The assay experiment was performed three separate times, each in triplicate. Results are presented as mean ± standard deviation. * Denotes groups with a significantly different mean viability from the control, at the p = 0.05 level.*

For the Caco-2 cell line, no LRH (R = Gd, Tb) composition appears to show a statistically significant change in cell viability relative to the untreated control at the lower treatment concentration (270 µg / ml). At the higher concentration of 526 µg / ml, the viability of cells treated with $LGd_{0.88}Tb_{1.12}H$-Cl and $LGd_{0.41}Tb_{1.59}H$-Cl declines slightly to approximately 70 % relative to the untreated control. The marginally higher cell viability after treatment with $LGd_{1.41}Tb_{0.59}H$-Cl may be related to the slightly higher Gd content, as has been reported for LGdH-Cl previously.[87] Overall, LRH composition does not appear significantly affect the viability of Caco-2, but may have some influence at higher treatment concentrations.

Some cytotoxicity (75 – 80 % viability relative to the untreated control) is seen in all HEK 293 cell treatment groups at the lower concentration of 270 µg / ml. At the higher concentration of 526 µg / ml, the cell viability reduces further to ca. 50 – 60 %. It seems that HEK-293 cells are more sensitive to the presence of LRH materials than Caco-2 cells; this is broadly in agreement with cytotoxicity data presented for LTbH-Cl and LGdH-Cl in Sections 3.4.5 and 4.4.1 respectively.

Overall, these results are not dissimilar to other reported Ln-containing systems explored for biomedical applications, for instance Gd-containing quantum dots (ca. 70 % viability in Caco-2 at 400 µg / ml)[427] and Gd/Tb containing silica nanoparticles (ca. >75 % viability in Caco-2 at 100 µg / ml).[428] The HEK 293 cell line has been previously demonstrated to be more sensitive than cancerous HeLa cells to the presence of silver nanoparticles,[429] as well as experiencing mild inhibition (ca. 95 % viability) in the presence of only 10 µg / ml of Gd/Tb-containing nanoparticles.[430]

4.5 Conclusions

The size-optimised hydrothermal synthesis method derived in Chapter 3 (Section 3.4.3) was applied to generate a series of LRH materials with alternate composition (R = Pr, Nd, Gd, Dy, Er, Yb). The synthesis was successful for R = Pr, Nd, Gd, and Dy, in all cases yielding particles with mean size under 200 nm, which is suitable for theranostic applications. For LErH, though the synthesis itself was facile, mean particle size in the resultant product was over 400 nm, indicating that further optimisation may be necessary if LErH was to be used for theranostic purposes. The synthetic temperature according to the optimised protocol (90 °C) was insufficient to generate LYbH; subsequent synthesis at 150 °C yielded a biphasic material with average particle size of 20 µm, which was deemed

unsuitable for further studies. The cytocompatibility of the various LRH materials was assessed and was found to be high in Caco-2 cells (over 80 % viability in all cases). On the other hand, HEK 293 cells were more sensitive to the presence of all LRH formulations – this was particularly true of LErH, with average cell viability of only 50 %.

Lead elements Gd and Tb were selected based on their favourable properties for theranostic applications – high magnetic activity, intense photoluminescence, similarity in ion dimensions and resultant particle size, as well as relatively high biocompatibility. Three additional formulations containing the elements Gd and Tb were created, at varying composition ratios. The synthesis of these mixed-metal LRHs was found to be facile, with the resultant materials likely forming a single phase, as evidenced by XRD and EDXS. Relaxometry studies revealed that while the LRH materials exhibit low r_1 relaxivities (r_1 = 0.02 – 0.38 $mM^{-1}s^{-1}$), their r_2 relaxivities are promising (r_2 = 1.6 – 3.48 $mM^{-1}s^{-1}$). The photoluminescence of the various LRH formulations was assessed in aqueous suspension, and it was found that $LGd_{1.41}Tb_{0.59}H$-Cl exhibited higher than expected fluorescence intensity, which was attributed to the minimised Tb-Tb quenching and additional energy transfer from Gd to Tb.

Based on these results, a lead formulation ($LGd_{1.41}Tb_{0.59}H$-Cl) was selected for photodynamic and photothermal capacity testing in Chapter 5.

5 Photodynamic and photothermal properties of layered rare-earth hydroxide materials

5.1 Introduction

A range of LRH materials has been successfully synthesised in previous chapters and found to exhibit favourable properties for theranostic applications. Specifically, the ability of these materials to act as luminescent/magnetic resonance contrast agents and drug delivery systems has been explored, in addition to their cytocompatibility.

Of particular interest were terbium and gadolinium containing LRHs, for their abilities to act as luminescent and magnetic resonance probes respectively. Notably, a mixed metal LRH system ($LGd_{1.41}Tb_{0.59}H$-Cl) showed vastly enhanced luminescence relative to LTbH, as well as showing comparable MR contrast ability to LGdH. This mixed system is therefore a promising bimodal imaging platform and lead formulation for this work.

It is of interest to explore whether such systems have potential to exhibit further treatment modalities – namely photothermal and photodynamic responses, which are introduced in Section 1.2. Based on the significant drug-dependant change in the luminescent profile of LTbH after intercalation, as outlined in Section 2.4.12, the guest molecules and the LRH matrix are able to interact electronically. Therefore, it is feasible that LRH systems loaded with a suitable chromophore may be able to utilise externally applied light to produce heat/energy for reactions to generate ROS, and thereby elicit localised cell death. This ability may be enhanced relative to the unbound photosensitiser by way of synergistic electronic

interaction with the LRH matrix. LRH-photosensitiser intercalates will be prepared and tested in terms of their photothermal and photodynamic effects.

5.1.1 Choice of laser

5.1.1.1 Wavelength

For theranostic applications, the ideal wavelength should be minimally damaging, have good penetration depth, and elicit minimal autofluorescence in human tissues for maximal contrast. For these reasons, longer wavelengths which are less energetic and therefore less likely to elicit damage are generally preferred.[431] Additionally, autofluorescence in human tissues is particularly strong in the UV-visible region, owing in large part to the high absorbance of haemoglobin.[432] The concept of a biological window for imaging purposes aims to define a range of wavelengths which offer higher transparency (and therefore deeper penetration) for incoming light.[433] The most commonly used are the first and second windows (Figure 5.1),[434] which lie in the NIR region, between the absorbance maxima of haemoglobin (below 600 nm) and those of haemoglobin and water (above 1400 nm). Many NIR-absorbing molecules, including indocyanine green (the only NIR dye approved by the European Medicines Agency for diagnostic use in humans),[435] operate in the first NIR window, and this region has therefore received the most attention in the literature.[436,437] Within this window, by far the most commonly employed wavelength for PTT/PDT applications is 808 nm, which is the wavelength selected for the present work.

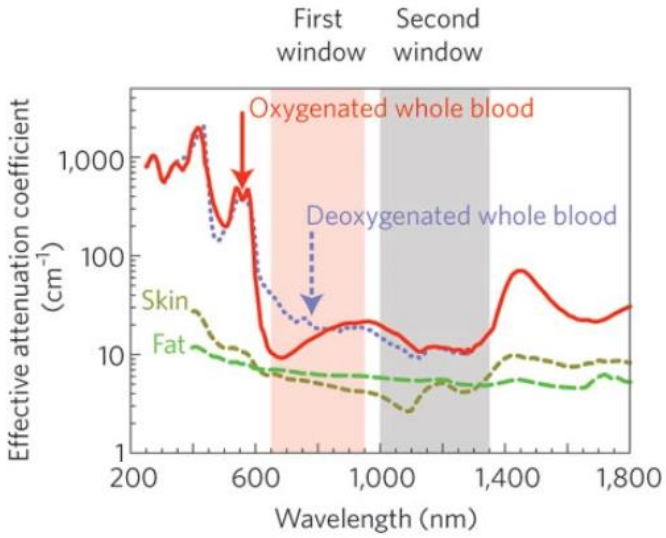

Figure 5.1 Graph (Reproduced from reference [434] with permission from Springer Nature) showing the attenuation coefficients (which govern absorbance) of whole human blood, skin, fat, and water across a range of NIR wavelengths.

However, it should be noted that melanin (a pigment occurring in human skin and hair) has been shown to absorb wavelengths in the NIR region. In a series of experiments on mice of different colours (ranging from black to white/hairless) it was shown that darker mice exhibited slightly higher skin autofluorescence across the whole NIR range, but particularly under 750 nm (Figure 5.2a).[438] Interestingly, irradiation with 808 nm also exhibited a marked photothermal response (> 50 °C, Figure 5.2b)[438] that was ascribed specifically to absorption by melanin in hair (as this effect disappeared when the mice were shaved).[438] Therefore, in terms of theranostic applications, while a laser operating at 808 nm is certainly preferable over UV-vis wavelengths, the degree of background noise (autofluorescence) may be subject dependant.

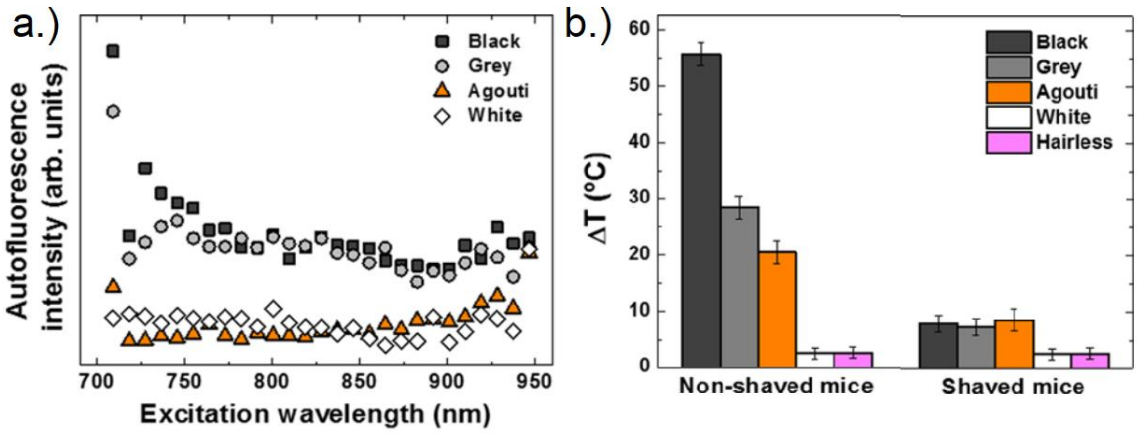

Figure 5.2 Graphs (reproduced from reference [438] with permission from John Wiley and Sons) showing a.) the autofluorescence in response to irradiation at NIR wavelengths in differently coloured mice; b.) observed photothermal effect on differently coloured mice with and without hair.

5.1.1.2 Laser type and operation mode

Many types of lasers exist, and the type required is highly application dependent. The most commonly used lasers in medicine are the CO_2 laser (10,600 nm) and the Nd:YAG (1064 nm) laser, for surgical and ablation applications.[439] PDT frequently employs metal vapour or dye lasers, the latter of which are particularly advantageous because they are wavelength tunable.[439]

More recently, diode lasers have begun gaining popularity as the laser of choice for PDT/PTT applications, particularly in research. Diode lasers are highly energy efficient, relatively cheap, and compact compared to other types of lasers. This makes them a good choice for both research purposes and for use in medical applications. Diode lasers can operate in both continuous wave mode and pulsed mode. A continuous wave laser emits a beam with constant power, whereas a pulsed laser emits pulses of light of short duration (as short as a couple femtoseconds, but more commonly in the ns – s range) at regular intervals.

The pulses in a pulsed laser are of much higher powers than the beam in a continuous wave laser because the power rating for a pulsed laser is commonly expressed as the average power (accounting for both time on and off). Therefore,

pulsed lasers and continuous wave lasers with the same power rating in fact may operate at different peak powers.

The power density is a measure of the laser power delivered per unit area and is an important comparative measure between different lasing setups. The laser selected for this series of experiments has a maximum theoretical power density of 0.4 W/cm^2, calculated using Equation 5.1 (using power of 0.025 W and a gaussian beam spot area of 12.5 cm^2). This is in line with guidance describing the maximum permitted exposure (MPE)[440] values for laser irradiation of skin at exposure times between 10 – 30,000 seconds. The MPE describes the maximum power density applied which will not cause irreversible damage and is tissue specific. For an 808 nm laser, at this exposure time range, the MPE for skin exposure is 0.33 W/cm^2 (calculated according to Equation 5.2, where λ is the laser wavelength in microns). Many literature reports, particularly for PTT applications, utilise power densities in vast excess of this value (for instance, 104 W/cm^2),[441] which could be potentially prohibitive for medical applications. Therefore, it is important to investigate systems which enable lower power density to be used.

$$Gaussian\ beam\ power\ density\ \left(\frac{W}{cm^2}\right) = 2\ x\ \frac{power}{beam\ spot\ area} \qquad (5.1)$$

$$MPE\ (skin, 808\ nm, > 10\ s) =\ 0.2\ x\ 10^{2(\lambda - 0.700)} \qquad (5.2)$$

Additionally, pulsed lasers inflict photoacoustic damage to irradiated tissue, and they therefore have a lower MPE than continuous wave lasers, even at the same peak power. However, determination of MPE for pulsed lasers differs substantially depending on the pulsing parameters chosen, and therefore direct comparisons with many literature sources are difficult. Continuous wave lasers

have been more commonly employed for photothermal applications in the literature historically. Pulsed lasers are becoming more commonly used in the literature in recent years, and there are instances in the literature which demonstrate higher rates of PDT/PTT efficiency in pulsed lasers compared to continuous wave lasers.[442,443] However, this increase in efficiency is seen only as a direct repercussion of the aforementioned photoacoustic effect of pulses, which is potentially damaging to surrounding tissue. For the reasons outlined above, a continuous wave laser was considered the optimal choice for this series of experiments.

5.1.2 Photodynamic response

5.1.2.1 Reactive oxygen species generation in photodynamic therapy

In conventional photodynamic therapy, a photosensitising molecule is utilised alongside a source of photons at the appropriate wavelength to elicit excitation of the photosensitising molecule. Generally, the ground state of photosensitising molecules is a singlet state, and excitation leads to the formation of an excited singlet state. This excited state is short lived because the transition back to the singlet ground state is spin-allowed and therefore efficient. In some cases, it is possible for the excited singlet to instead undergo a transition to an excited triplet – a process known as intersystem crossing. Triplet states are generally longer lived than singlet states because the transition back to the singlet ground state is now a spin-forbidden process (and is therefore inefficient).

Such intersystem crossing processes are important as they pertain to photodynamic therapy because the existence of the photosensitiser in a long-lived excited triplet state allows it time to undergo photochemical processes that eventually generate reactive oxygen species. Broadly, there are two mechanisms

by which this occurs – type 1, which is a complicated electron transfer mechanism generating a series of radicals; and type 2, a mechanism which involves the direct transfer of energy from the photosensitiser to nearby molecular oxygen, generating reactive singlet oxygen. The type 2 mechanism is predominant in PDT applications,[444] and will therefore be the focus of discussion in this chapter. Furthermore, because the ground state of molecular oxygen exists as a triplet state, the interaction between an excited triplet photosensitiser and the ground state triplet of molecular oxygen becomes a spin-allowed, efficient process.

In LRH intercalates where terbium luminescence is enhanced by intercalation (such as LTbH-ibu), additional energy transfer is assumed to occur from the intercalated molecule to the terbium centres within the LRH matrix, which then predominantly relax *via* a radiative process. For PDT applications, this is undesirable as the radiative relaxation pathway competes with energy transfer to the photosensitising molecule, and the subsequent non-radiative relaxation which eventually gives rise to the production of singlet oxygen. By contrast, in LRH intercalates where terbium luminescence is quenched by intercalation (such as LTbH-dic), net transfer of energy likely occurs from the LRH matrix to the intercalated molecule. In such intercalates, there may be more available energy for non-radiative relaxation, which is potentially favourable for PDT.

If LRH-Intercalated photosensitisers can show higher rates of singlet oxygen production as opposed to the unintercalated photosensitiser at 808 nm irradiation, it is likely that additional energy transfer from the LRH matrix to the photosensitiser is occurring. It also implies that energy absorbed by the photosensitiser is not efficiently transferred to the LRH. In that scenario, it is likely that there will be reduced terbium luminescence under UV excitation (as the energy will again be transferred efficiently to the photosensitiser, rather than lost

radiatively). There therefore may be a trade-off between terbium luminescence contrast and photodynamic ability of the resultant LRH.

The required wavelengths for eliciting luminescence in terbium containing LRH materials tested in Chapters 2 and 3 are in the UV region, which is somewhat undesirable due to the dangers of UV radiation and high autofluorescence of tissues as outlined in Section 5.1.1.1. Therefore, even if an intercalate system in this Chapter exhibits a predominantly radiative relaxation pathway using 808 nm and low/no singlet oxygen production, it may still be useful as a NIR luminescent probe. It is also possible that the PDT/PTT/fluorescence behaviour of a given LRH-photosensitiser may change as the result of de-intercalation when in suspension.

5.1.2.2 Detecting singlet oxygen

As discussed in Section 5.1.2.1, the photodynamic response of a substance is its ability to produce singlet oxygen in response to irradiation by light of a wavelength compatible with that substance. The relaxation of singlet oxygen to its triplet ground state can be seen directly as it is a phosphorescent process, emitting light at a wavelength of around 1270 nm.[445] However, most spectroscopic equipment does not possess a detector capable of measuring emissions so far into the NIR region. Therefore, indirect detection of singlet oxygen by using fluorescent or absorbent dyes is more frequently utilised.

A common dye used for this purpose is 1,3-diphenylisobenzofuran (DPBF, Figure 5.3), which reacts with singlet oxygen to form 1,2-dibenzoylbenzene (DBB). DPBF exhibits a strong absorbance peak at 412 nm, whereas DBB does not – the resulting decrease in absorbance of this peak in response to irradiation can therefore be used to quantify the photodynamic response. DPBF is not strictly

specific to singlet oxygen, and can react with other ROS species (for instance, hydroxyl and superoxide radicals).[446] However, for the purposes of establishing the presence and extent of photodynamic response in simple (non-biological) systems, this is sufficient and widely used in the literature.[447,448] In addition, DPBF is cheap, readily available, and has good solubility in H_2O/EtOH systems, unlike many other singlet oxygen probes.

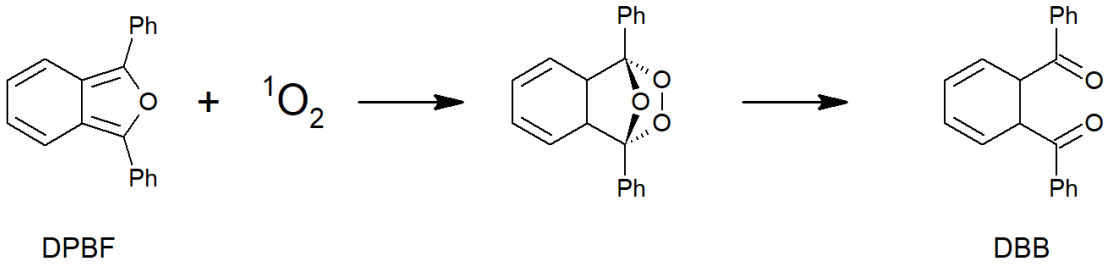

Figure 5.3 Reaction of DPBF with singlet oxygen, via an endoperoxide intermediate, producing DBB.

5.1.3 Photothermal response

As explained in Section 5.1.2.1, NIR absorbing entities with strong spin-orbit coupling, which predominantly relax *via* the intersystem crossing pathway (thereby generating a long-lived triplet excitation state) are particularly suitable for PDT applications. Conversely, PTT applications favour entities which preferentially relax *via* vibrational relaxation/internal conversion.[449]

Vibrational relaxation occurs when an excited molecule transitions to a lower energy vibrational mode and dissipates the excess energy kinetically (to other vibrational modes or by collision with surrounding molecules). In some molecules, where vibrational energy levels are coupled to electronic energy levels, such relaxations may be accompanied with an electronic state transition, in which case the process is referred to as internal conversion. In both cases, kinetic energy is released by the molecule to its surroundings, thus generating heat which can be

exploited for PTT. Because of this, systems which allow frequent molecular collisions are conducive to this relaxation pathway.[450]

Molecules intercalated within the LRH matrix may benefit from enhanced collisional heat loss, as the guest molecules within the LRH are arranged in close proximity to both each other and to the host layers. For instance, increased photothermal conversion efficiency has been reported in MXenes intercalated with polymer molecules relative to unintercalated MXenes.[451] Alternatively, it may also be the case that intercalation may restrict some molecular motion modes (particularly rotation) and thereby reduce the photothermal efficiency of the photosensitising molecule.[452,453]

5.1.4 Choice of NIR-absorbing guest species

Indocyanine green (ICG, Figure 5.4) is a NIR absorbing dye which has been used as a fluorescent angiography contrast for diagnostic applications since the late 1950s, when it was first approved for human use. It is generally well tolerated, with rare instances of allergic reactions,[454] and is still in wide use today. In addition to being an effective photosensitiser for photodynamic applications, ICG has been known to generate heat in response to irradiation (photothermal effect) since the mid-1990s.[455] Moreover, ICG is anionic and therefore a good candidate for intercalation into LRH systems.

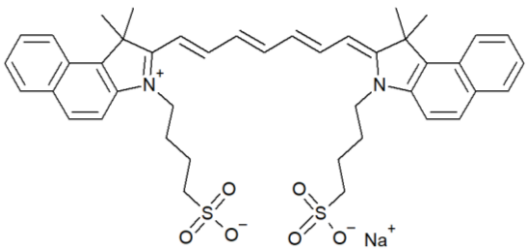

Figure 5.4 Chemical structure of indocyanine green.

An investigation into the potential PDT activity of ICG was first reported in 2002,[456] where an 830 nm diode laser was used to irradiate human melanoma cells in the presence of ICG. It was shown that after approximately 500 seconds of irradiation at a power density of 0.2 W / cm^2 (which is under the MPE value), the cell viability decreased to only 10 % relative to cells which were treated with ICG but not irradiated. Though the authors in this instance did not measure the ROS generation or temperature change, this significant decrease in viability inspired many subsequent investigations into the PDT/PTT activity of ICG.

On several occasions, LDH-ICG intercalates have been reported,[307,457] as well as a rare-earth doped LDH-ICG intercalate,[458] with highly promising results. An LDH-ICG intercalate co-loaded with doxorubicin[457] showed exceptional tumour suppression properties in mice (Figure 5.5a), after only 2 minutes total irradiation with an 808 nm laser at 0.3 W/cm^2. This result is attributed to the synergistic effect of ROS production, DOX release, and photothermal response. The authors report enhanced ROS production by LDH-ICG compared with pure ICG, but do not offer insight as to why this is the case. Perhaps more impressively, a Gd/Yb doped LDH-ICG intercalate system has been reported, which is capable of trimodal imaging contrast (MR, CT, and NIRF) in addition to trimodal therapy (PTT, PDT, and chemotherapeutic release).[458] The combined effect of these treatment modalities lead to complete tumour suppression in mice (Figure 5.5b).

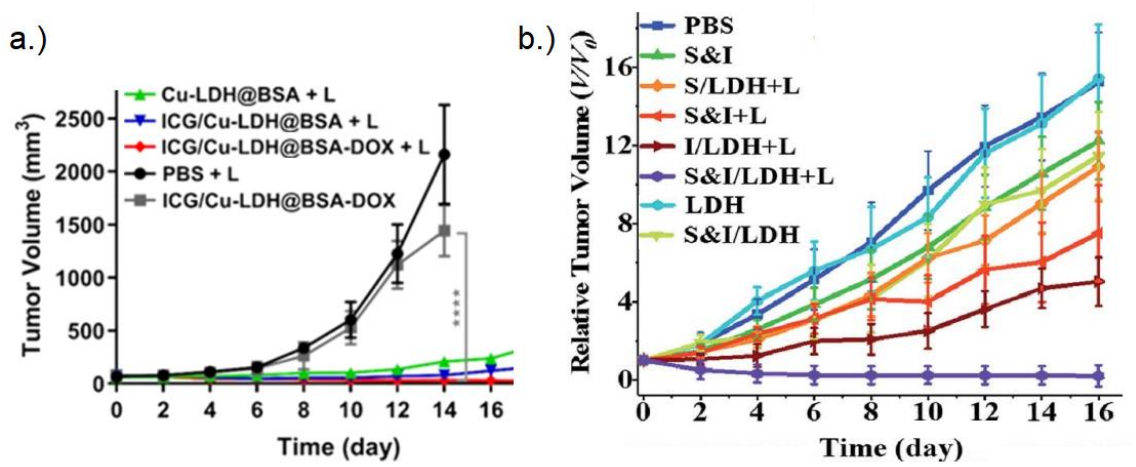

Figure 5.5 a.) Diagram (reprinted with permission from reference [457]. Copyright 2021, American Chemical Society) showing tumour volume change in mice under different treatment conditions; 'L' denotes irradiation at 808 nm, 0.3 W/cm2 for a total of 2 minutes. 'BSA', 'DOX', and 'PBS' denote bovine serum albumin, doxorubicin, and phosphate buffered saline respectively. b.) Diagram (adapted from reference [458] with permission from the Royal Society of Chemistry) showing tumour volume change in mice under different treatment conditions; 'L' denotes irradiation at 808 nm, 1 W/cm2 for a total of 3 minutes. 'S', 'I', and 'PBS' denote SN38 (a chemotherapeutic drug), indocyanine green, and phosphate buffered saline respectively.

Many first window NIR absorbing molecules suffer from poor commercial availability, high costs, and stability/toxicity issues.[459,460] There is therefore continuing interest in discovering new entities which efficiently absorb NIR light, particularly if they are readily available or simple to synthesise. There exist reports of organic compounds which, in their crystalline form, are able to achieve long lived (>1 s) triplet excitation states.[461] One of these compounds, isophthalic acid (IPA, Figure 5.6), was shown to exhibit phosphorescence up to 4 seconds after exposure to a UV illumination source. Another group hypothesised that it may be possible to achieve similar long-lived triplet excitation states by intercalating such compounds into an LDH matrix.[1] In this way, the regular arrangement of those organic molecules, which is necessary for the long-lived excitation state, is provided by their intercalation within the LDH matrix. In turn, this allows such long-lived excitation states to be exploited (in liquid suspensions) to generate ROS for PDT applications.

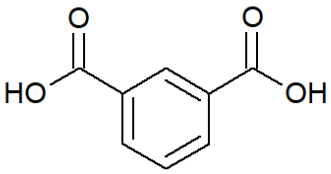

Figure 5.6 The chemical structure of isophthalic acid.

It has been demonstrated that an LDH-IPA compound was able to successfully generate ROS species in response to laser irradiation.[1] Moreover, as the mechanism of absorption in this case proceeded via a two-photon process, the photodynamic effect was achieved using NIR irradiation (808 nm) as opposed to UV.[1] This LDH-IPA intercalate, when tested in mice irradiated for 10 minutes (0.7 W / cm^2),[1] was also able to elicit complete or near-complete tumour suppression in all cases. It was noted in the study that irradiation only effected a < 5 °C temperature increase, which is insufficient for PTT and therefore such systems are only suitable as PDT agents.

To date, no reports of LRH materials intercalated with ICG or IPA exist, nor any LRH-based systems for photothermal applications. Only one recent work mentions photodynamic therapy in the context of LRHs. In this report, a photodynamic pro-drug, 5-aminolevulinic acid (5-ALA) is intercalated into a Gd/Eu based LRH.[420] When internalised by cells, 5-ALA[462] is converted into a porphyrin-like metabolite, which is capable of absorbing a range of wavelengths up to approximately 650 nm to subsequently produce ROS.[463] Since 5-ALA is a prodrug and does not produce ROS outside of living cells, it is not suitable the purposes of the present study as the irradiation equipment is not configured for biological studies.

5.2 Aims

The work described in this chapter aims to investigate the potential use of LRH materials in photothermal and photodynamic therapy applications. To do this, a laser assembly will be first be constructed according to the required specifications and tested to verify its functionality. The lead formulation of LRH ($LGd_{1.41}Tb_{0.59}H$) will then be intercalated with indocyanine green (ICG) and isophthalic acid (IPA), and the intercalates subsequently irradiated using 808 nm laser light to evaluate their ability to act as photothermal/photodynamic platforms (Figure 5.7). It is predicted based on available literature that the resultant intercalates should exhibit the ability to generate reactive oxygen species for photodynamic therapy or heat for photothermal applications. The influence of the intercalation of ICG/IPA into the selected LRH systems will also be evaluated in terms of their luminescence performance.

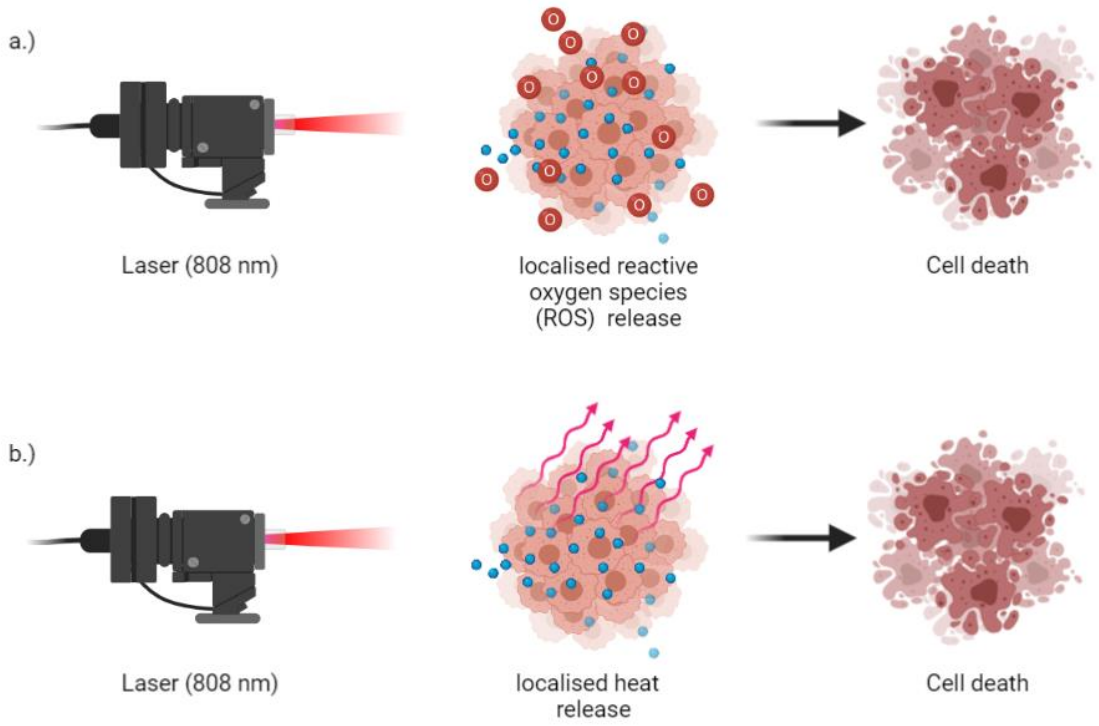

Figure 5.7 Illustration of the a.) photodynamic and b.) photothermal response of nanoparticles causing cell death in response to laser illumination.

5.3 Experimental

5.3.1 Materials

Isophthalic acid and indocyanine green were sourced from Sigma Aldrich. 1,3-diphenylisobenzofuran was obtained from Merck. All water used was deionised, and ethanol was of analytical grade.

5.3.2 Laser apparatus assembly

The lasing apparatus was assembled in-house, with help from Ryan Mellor (3D printing) and John Frost (external laser housing) using various components as follows.

A single-mode, fibre-coupled laser (ThorLabs, 808 nm, part number S1FC808) was used as the source of light. A fibre patch cable (ThorLabs, part number P5-830A-PCAPC-1 S) and mating sleeve (ThorLabs, part number ADAFC4) were used to connect the laser source to an aspheric collimator (ThorLabs, part number CFS18-850-APC). The external laser housing was made by John Frost from 3 mm thick, black polyethylene sheet (RS components) cut to form a box consisting of two parts – a base and a removable lid. The lid and base were fitted with a magnetic interlock connected to the laser. The base was built to house a miniature stirring plate (MIXdrive 1 XS, 2Mag), which was connected to an external control unit (MIXcontrol Eco, 2Mag).

The internal components of the laser housing were designed, and 3D printed by Ryan Mellor to allow the collimator to be aligned at the necessary focal distance and height to a quartz cuvette, containing a cuvette stirring bar. A temperature probe (RS Components, part number 204-8390) was inserted through a hole drilled into the top of the housing, and a circular clamp was used to affix the probe

at the necessary height to avoid the laser beam path and the stirring bar in the cuvette. The temperature probe was connected to an external digital thermometer and data logger (RS components, part number 123-3217).

An NIR detector card (ThorLabs, part number VRC4) was used to visualise the laser beam. Digital images of the NIR detector card were then used to measure the approximate spot size using ImageJ software.

5.3.3 Ion exchange reaction

LRH-Cl (150 mg, R = Tb/Gd) was dispersed in water (15 ml), and ICG (10 mg) or IPA (150 mg) was added to the solution. To aid dissolution of IPA, water was basified to pH 9 or 12 with NaOH (1M) solution. The mixture was heated at 60 °C for 24 h, with stirring. The product was collected by centrifugation, washed with water (2 x 30 ml) and ethanol (2 x 30 ml), and subsequently dried at 40 °C for 24 h.

A further intercalation experiment was performed in an analogous manner, using $LGd_{1.41}Tb_{0.59}H$-ICG (150 mg) and ibuprofen sodium (223 mg) dispersed in water (15 ml).

5.3.4 Characterisation

Characterisation procedures used in this chapter are identical to those described in Section 2.3.3; any differences and additional methods are described in this section.

5.3.4.1 Nuclear Magnetic Resonance

^{1}H NMR spectra were collected using a Bruker Advance Neo 500 MHz instrument. All samples were prepared 24 h prior to testing. Solutions of ICG and

DPBF were prepared in deuterated ethanol (EtOD) at concentrations of 1 mg/ml and 3 mg/ml respectively. A mixture of ICG and DPBF was made using the respective solutions in equal volumes (with the resultant final concentration of 0.5 mg / ml for each component). Part of the mixture was then irradiated under 808 nm wavelength laser light (25 mW power) for 1 hour. NMR peak positions and assignments are listed in the caption for Figure 5.29.

5.3.4.2 Solid state photoluminescence

Photoluminescence measurements were performed on a Renishaw inVia Qontor microscope at an excitation wavelength of 325 nm, at 0.05 % laser intensity to limit sample degradation and avoid exceeding the intensity limit. Measurements were taken over the range 326 - 700 nm at a resolution of 0.026 nm.

5.3.5 Photodynamic response testing

A stock solution of 1,3-diphenylisobenzofuran (DPBF, 0.1 mM in EtOH) was made in a darkened room, and the container wrapped in aluminium foil for storage at room temperature. The dye solution gradually deactivates upon storage, so fresh stock was prepared periodically. As DPBF is light sensitive, all transfers/mixing were also carried out in a darkened room. A calibration curve was generated using DPBF in EtOH/H_2O (1:1, the solvent system used for further testing).

Aqueous LRH suspensions were prepared immediately prior to testing at a concentration of 1 mg / ml and diluted to prepare a stock solution with concentration of 0.05 mg / ml to minimise particle interference with the UV-vis measurement. At the point of measurement, the stock solution was diluted with water or DPBF dye as needed, such that the final concentration was 0.025 mg /

ml. A solution of ICG for use as a positive control was prepared at a concentration of 0.5 mg / ml and subsequently diluted to a final concentration of 0.016 mg / ml (0.02 mM). ICG solutions were prepared fresh each time when required.

For ROS generation assays, 1.5 ml of the DPBF solution was mixed with 1.5 ml of aqueous stock suspension of sample directly in a quartz cuvette (such that the final concentration of DPBF was 0.05 mM, of LRH suspension was 0.025 mg / ml, and of ICG was 0.016 mg / ml). A cuvette stirring bar was added to ensure even mixing during illumination. The absorption spectrum of the sample (300 – 800 nm) was then measured immediately after mixing using a Jenway 7205 UV/Visible Diode Array Scanning Spectrophotometer. The sample was then transferred to the laser assembly to be illuminated for the required amount of time, with stirring at 200 rpm, after which the absorbance spectrum was measured again.

To test the stability of DPBF to the illumination in the UV-vis spectrophotometer, a solution was made using 1.5 ml of DPBF stock and 1.5 ml water. The cuvette was transferred to the UV-vis spectrometer and spectra recorded at 1 minute time intervals without laser illumination. The process was then repeated, with laser illumination at 808 nm and 25 mW between measurement intervals to ensure DPBF stability under 808 nm laser illumination. The stability of ICG was evaluated in the same manner, using a solution of ICG in water (0.016 mg / ml).

5.3.6 Photothermal response testing

To test the photothermal response of samples, the equipment described in Section 5.2.3 was used. Briefly, a quartz cuvette containing a stirring bar was filled with the required aqueous suspension (3 ml) and transferred to the laser assembly. LRH suspensions were made in water at a concentration of 1 mg / ml.

An aqueous ICG solution (1 or 0.03 mg / ml) were used as a positive control, and pure water was used as a negative control. Depending on the experiment, the stirring bar was either set to 200 rpm or not turned on. At the required timepoint, the laser was switched on at the desired power, and temperature data collected for as long as needed.

5.4 Results and discussion

5.4.1 Initial laser assembly

The laser assembly is described in detail in the experimental section and is illustrated in Figure 5.8. To verify that the beam is being produced and is in the correct position, a near-infrared laser detection card was used. The card is coated in a material which produces visible luminescence when exposed to near-infrared wavelengths (790 - 1590 nm), and has a printed reticule pattern on it, which allows the approximate measurement of the beam spot size by using it as a scale bar. The card was inserted into the position where the cuvette would be, and several digital images were taken to measure the beam diameter (representative example shown in Figure 5.8, inset).

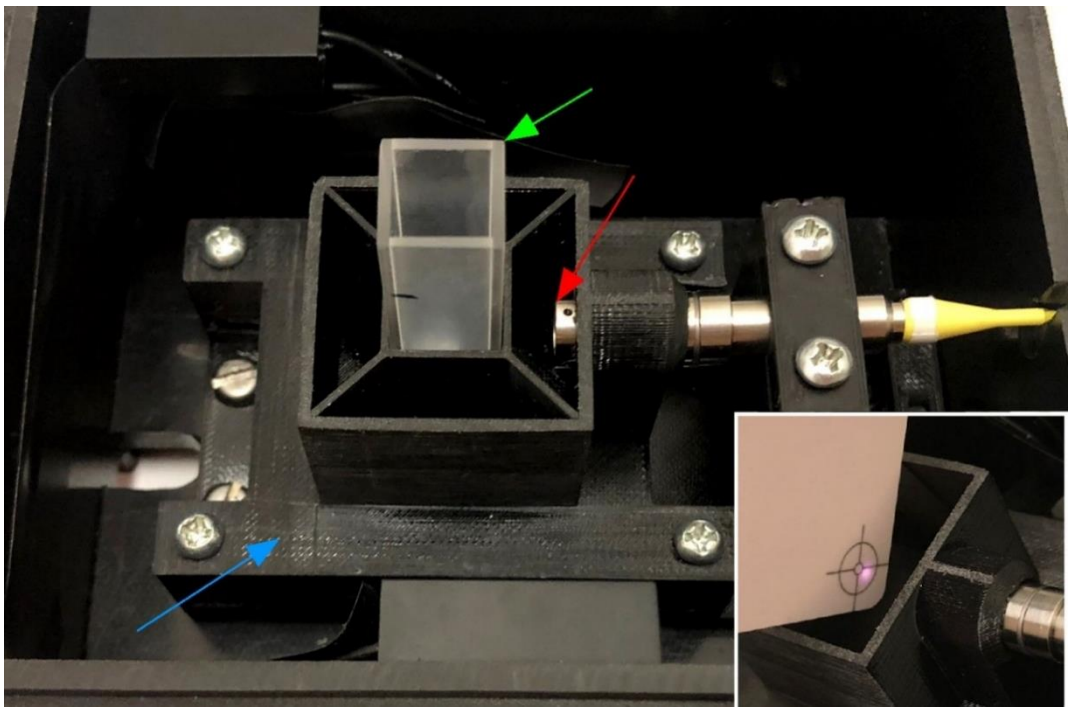

Figure 5.8 Interior of the laser housing, illustrating the position of the cuvette (green arrow) and collimator (beam source, red arrow). The 3D printed assembly holding the cuvette in place has a circular cut-out to allow the beam through (not visible). The stirring plate is built into the stage below the cuvette (blue arrow). Inset: the laser beam visualised on a NIR detector card.

A laser beam striking an object at 90° can be thought of as forming a 'spot' on the surface of the object, where the intensity of the light is strongest at the centre of the spot and fades towards the edges. This is referred to as a Gaussian beam, because plotting the intensity of light against distance from centre of the spot results in a Gaussian curve (Figure 5.9). The total beam spot diameter is therefore not well defined, but the beam spot diameter at a specified intensity can be defined. Frequently, 50 % intensity is selected, and this gives a spot diameter which is called the full width at half-maximum (FWHM). Another measure of beam diameter often quoted is the $1/e^2$ width, which is the full width of the spot at the point where the beam intensity diminishes to the fraction $1/e^2$ (13.53 % intensity).

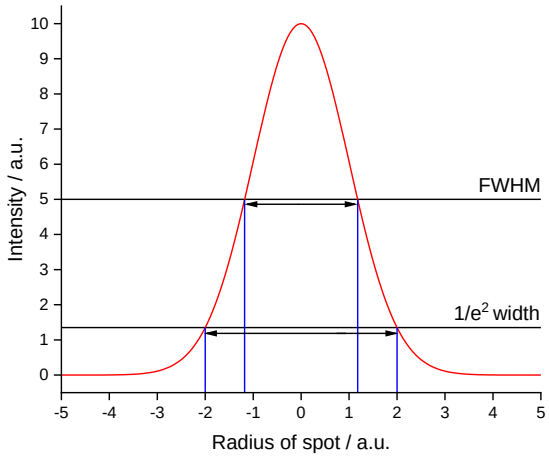

Figure 5.9 Gaussian beam intensity graph illustrating the spot radius at 50 % intensity (FWHM) and at 13.5 % intensity ($1/e^2$).

The theoretical maximum beam diameter at the focal length quoted by the manufacturer for the beam collimator was 3.99 mm ($1/e^2$ width). This is equivalent to approximately 2.35 mm for the FWHM value, as calculated by Equation 5.3 (where ω is the $1/e^2$ width). The beam spot measured from the digital images using the NIR visualisation card was 2.95 + 0.38 mm. Since the images were taken in a lit room, the edges of the beam spot are not easily visible, therefore it is reasonable to expect that the beam spot size measured by this method would be smaller than the $1/e^2$ width. This shows that the set-up is functioning well, and the beam position is suitable (because it is pointed directly at where the cuvette would be).

$$\omega = \frac{FWHM\sqrt{2}}{\sqrt{ln2}} \tag{5.3}$$

The output power of the laser is not possible to measure without a specialist laser power output meter. The attenuation value for the specific fibre type used in this set-up is quoted as < 0.5 dB per kilometre by the manufacturer, which is essentially negligible when considering a fibre cable length of only 1 metre. Therefore, the output power of the laser in this setup is likely very close to the maximum power of the laser source (25 mW).

5.4.2 LRH intercalate synthesis and characterisation

5.4.2.1 LRH-IPA

5.4.2.1.1 Synthesis at elevated pH

To prepare $LGd_{1.41}Tb_{0.59}H$-IPA for PDT applications, it was necessary to basify the reaction solution to aid the dissolution of IPA. To this end, IPA intercalates were prepared at pH 9 and pH 12 (weak and strong base conditions); the resultant diffractograms are shown in Figure 5.10a. Unexpectedly, in both cases, the (010) reflection was seen to shift to a higher diffraction angle (11.03 and 11.81° respectively, relative to 10.39° before intercalation); this indicates that the intercalation of IPA into the precursor LRH caused a contraction in the interlayer distance.

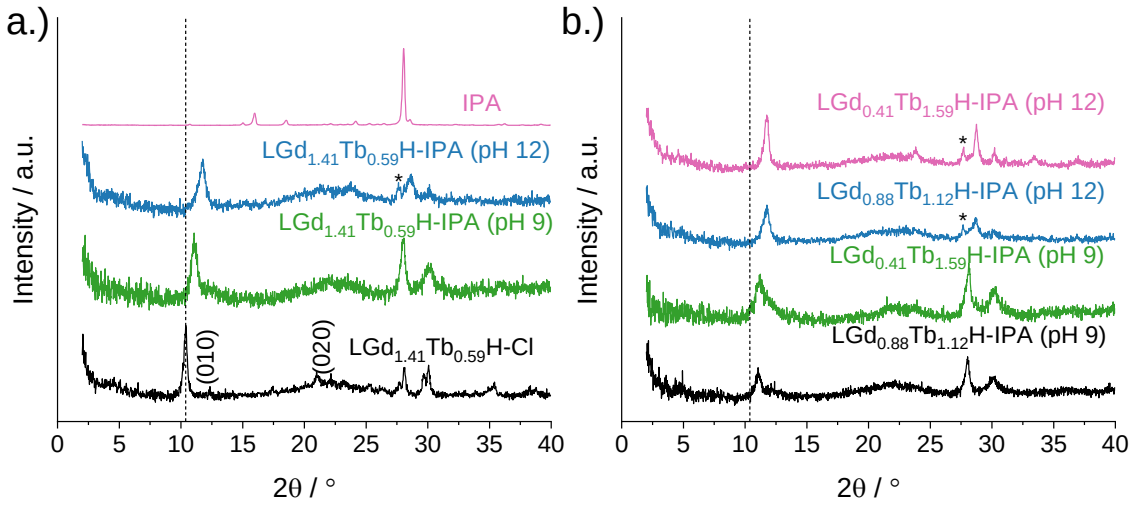

Figure 5.10 XRD patterns for a.) IPA, $LGd_{1.41}Tb_{0.59}H$-Cl and the resulting intercalation compounds LRH-IPA generated at pH 9, pH 12; b.) $LGd_{0.41}Tb_{1.59}H$-Cl and $LGd_{0.88}Tb_{1.12}H$-Cl and the resulting intercalation compounds LRH-IPA generated at pH 9, pH 12. Dotted line shows the (010) reflection of the precursor $LGd_{1.41}Tb_{0.59}H$-Cl for reference.

When IPA intercalation was attempted into the two other mixed metal systems (Figure 5.10b) a contraction was also observed. In all cases, the intercalate generated at pH 12 exhibits the (010) reflection at a slightly higher diffraction angle than that of the intercalates made at pH 9, indicating that the contraction

effect is somewhat stronger under more alkaline conditions. Moreover, all intercalates synthesised at pH 12 exhibit an additional reflection around 27.0 - 27.6° (indicated by an asterisk) which may indicate the presence of an additional phase or pure IPA (which shows a primary reflection at 28 °).

Based on the (010) reflection positions (2θ = 10.39°, 11.03°, and 11.81°), the interlayer spacing was calculated to be 8.55 Å in the precursor LRH, and 7.53-8.06 Å in the IPA-loaded LRHs respectively. This intercalate layer spacing is notably smaller than that reported in LDH-IPA (13.0 Å).[1] The individual LRH layer thickness can be approximated as 6.0 Å,[311] giving a gallery height of 1.53 – 2.06 Å in the present LRH-IPA intercalates.

The height and width of individual IPA molecules have been previously reported as approximately 7.4 and 8.5 Å respectively,[464] both of which are larger than the derived gallery heights. This may suggest that unlike in the reported LDH-IPA intercalate which postulated a vertical arrangement of IPA molecules between the LDH layers, the LRH-IPA intercalate may instead comprise IPA molecules arranged in a planar fashion within the LRH layers. This is feasible as such an arrangement would allow the delocalised π – electron cloud of the IPA molecules to interact with the positively charged LRH layers. Additionally, since rotation of the carboxylate groups is free about the C-C bond, such a planar arrangement would still facilitate the electrostatic interaction between the LRH layers and the anionic carboxylate groups. Similar planar/tilted arrangements of molecules containing π – systems within LDH materials have been reported previously.[465,466] Planar arrangement of IPA molecules between the LRH layers may explain the unexpected contraction in layer spacing seen.

The formulae of both LRH intercalates (Table 5.2) was calculated using EM and TGA data (Table 5.1, Figure 5.11), and the IPA loading was determined to be 6.12 % (pH 9) and 1.92 % (pH 12) by mass. The intercalate synthesised at pH 12 does not appear to exhibit two distinct dehydroxylation/dehydration phases typical of LRH materials, instead showing one mass loss event up to 400 °C associated with water loss. This may indicate that the nature of the interaction of interlayer water/hydroxyl groups in this material may be slightly different than that in the pH 9 intercalate, though the total water content is approximately the same (ca. 15 %). Therefore, synthesis under higher alkalinity conditions appears to hinder IPA loading, possibly through competitive intercalation of hydroxide anions. It may also be the case that the post-synthesis washing steps may be removing some of the intercalated IPA via rapid release, so further syntheses with a reduced number of washes will be attempted to improve IPA loading.

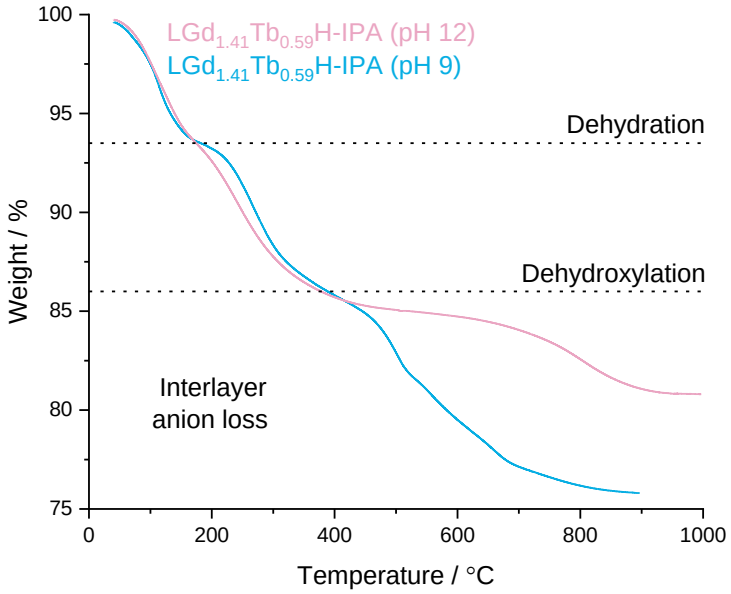

Figure 5.11 Thermogram of LRH-IPA intercalates synthesised at pH 9 and pH 12 (reference lines correspond to weight % at calculated mass for each phase).

Table 5.1 Summary of observed (and calculated from formulae, Table 5.2) values for elemental analysis and TGA data for the LRH-IPA intercalates synthesised at pH 9 and pH 12.

Material	*pH 9*	*pH 12*
% C	3.74 (3.71)	1.28 (1.25)
% H	1.43 (1.90)	1.40 (1.81)
Mass loss % (H_2O)	6.54 (6.34)	n/a (6.14)

Table 5.2 Summary of formulae derived from TGA/elemental analysis data.

Material	*Formula*	*Drug loading / % mass*
LRH-IPA, pH 9	$Gd_{1.41}Tb_{0.59}(OH)_5(CO_3)_{0.05}(Cl)_{0.54}(C_8H_4O_4)_{0.18}\cdot 1.7H_2O$	6.12
LRH-IPA, pH 12	$Gd_{1.41}Tb_{0.59}(OH)_5(CO_3)_{0.05}(Cl)_{0.79}(C_8H_4O_4)_{0.055}\cdot 1.6H_2O$	1.92

5.4.2.1.2 Synthesis with reduced washes and prolonged drying time

Since the basis of ROS generation in reported LDH-IPA materials relies on the regularity of distribution of IPA within the LDH matrix, it was desirable to increase the crystallinity of IPA intercalates. One possible route to achieve this is heat treatment. The basis for this process is that heating provides the necessary energy for components within a solid to rearrange, gradually transforming disordered solids into more ordered structures. For instance, this has been previously reported for LDH materials, with calcination between 100 - 250 °C resulting in notable reflection narrowing in the diffraction pattern after 6 hours of treatment.[467]

At temperatures above 100 °C, significant changes due to the dehydration and subsequent dehydroxylation of the LRH layers are expected to occur. It was reasoned that treatment at a milder temperature for a longer period may be preferrable. It was therefore attempted to prepare L$Gd_{1.41}Tb_{0.59}$H-IPA with the

drying time extended from 24 hours to 7 days (at 40 °C). Additionally, since the washing step after synthesis may be causing low IPA loading, the washing was limited to a single rinse with water.

The diffractograms of the resultant compound, pure IPA, and precursor LRH are shown in Figure 5.12. While the material generated by this method does exhibit a strong reflection at 8.35°, the position is not consistent with those of the intercalates generated at pH 9 or 12.8 (ca. 11 °). Additionally, the reflections between ca. 27 - 31° in the parent LRH material (arising from the (400), (112), (320), and (410) planes), which are present to some degree in all LRH intercalates generated in prior chapters, appears to be absent in the 7-day dried sample, providing more evidence that it is unlikely to be an analogous phase. It is therefore likely that the main reflection at 8.35° may be arising from an unknown phase. It is possible that the IPA molecules have become ligated directly to the individual Tb/Gd^{3+} centres or to individual Tb/Gd (OH) polyhedra; similar coordination polymer structures have been reported in the literature.[468,469]

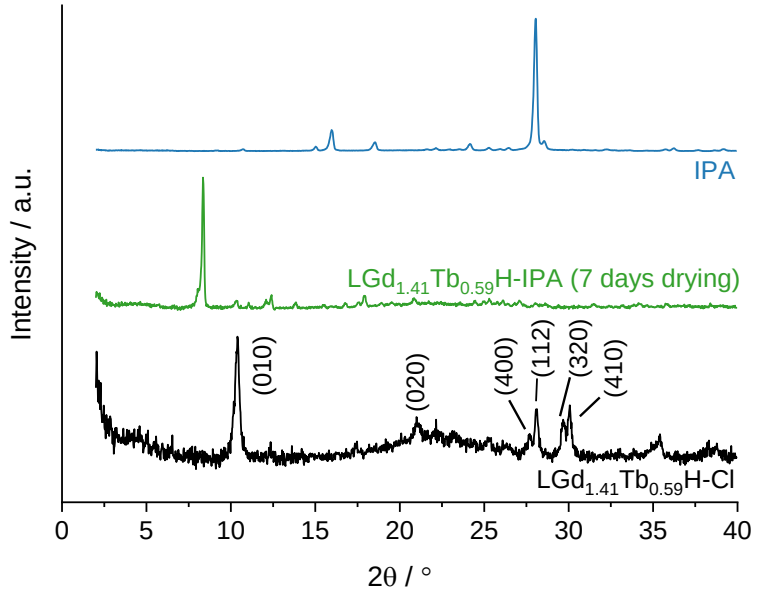

Figure 5.12 XRD patterns for IPA, LGd1.41Tb0.59H-Cl and the resulting compound generated by reducing the post-synthetic washing and increasing the drying time to 7 days (168 hours).

EM and TGA data for this compound are shown in Table 5.3, Figure 5.13. The carbon content of this phase is much higher than for the LRH-IPA intercalates generated in Section 5.4.2.1.1 (ca. 36 % as opposed to 1-4 %). The material exhibits two mass loss events which coincide with dehydration/dehydroxylation as is typical for LRH materials. The total water/hydroxyl content corresponds to approximately 15 % which is also consistent with the other LRH-IPA intercalates (Section 5.4.2.1.1).

The remaining material after heating to 900 °C corresponds to the mixed Gd/Tb(III) oxide form ($Gd_{1.41}Tb_{0.59}O_3$, RMM = 363.5 g mol^{-1}). As this form accounts for ca. 38 % of the mass of the initial material, the total formula unit mass can be approximated as 956.6 g mol^{-1}, which in turn is approximately 48.6 % heavier than the precursor LRH (RMM = 463.60 g mol^{-1}). If the material was an LRH, the theoretical loading of the IPA dianion based on charge balance considerations would be ca. 16 % (assuming the same level of hydration as the precursor LRH). The presence of a further 32 % mass equivalent of IPA in the material implies the presence of excess pure IPA (which is unlikely, as a reflection corresponding to pure IPA is not seen on the XRD pattern); or that the material exhibits alternative coordination to IPA anions than simple electrostatic interaction. Based on the shape of the TGA curve, it is likely that the IPA molecules are all in a similar environment because they burn off within a short temperature range (at 550 – 650° C). It is therefore not unreasonable that a coordination compound may have formed as opposed to an intercalate. Under the alkaline synthetic conditions, each IPA molecule forms a dianion and may act as a bis-bidentate ligand; one or more IPA molecules may then bridge adjacent Ln^{3+} centres, with the remaining free coordination sites occupied by hydroxyl

anions. Regardless, since the structure/identity of the compound cannot be verified, it was not used for further study.

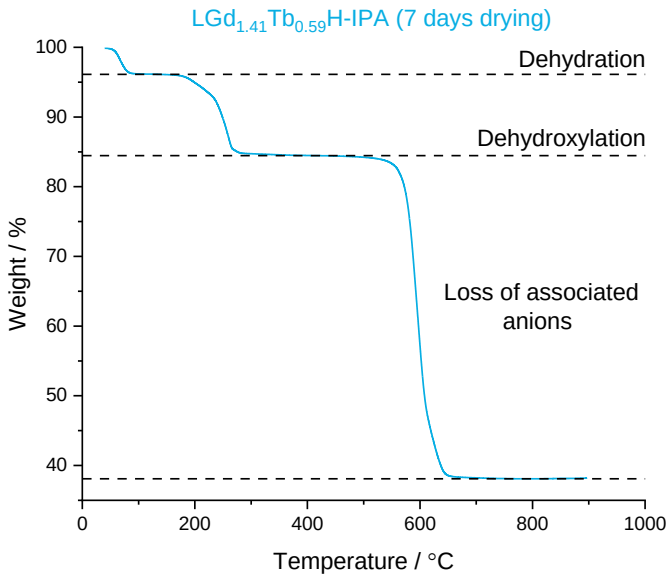

Figure 5.13 Thermogram of LRH-IPA compound (reference lines correspond to weight % at calculated mass for each phase).

Table 5.3 Summary of observed values for elemental analysis and TGA data for the LRH-IPA complex generated with reduced washing and increased drying time (7 days).

Material	*% C*	*% H*	*Mass loss % (H_2O)*
LRH-IPA complex	36.07	1.98	3.879

5.4.2.2 LRH-ICG

Since ICG is a vividly coloured compound, the coupling of ICG to LRH during the attempted ion exchange reaction was easily confirmed visually (Figure 5.14). Prior to the addition of LRH, the ICG solution was a deep, dark green colour. Immediately after the addition of the LRH, the mixture became opaque due to the suspension of the white LRH particles. After 24 hours, particulate matter within the flask appeared as dark green, and the supernatant was almost colourless – indicating that ICG was no longer in solution, and that the previously white LRH

particles had coupled to the available ICG molecules resulting in their colour change.

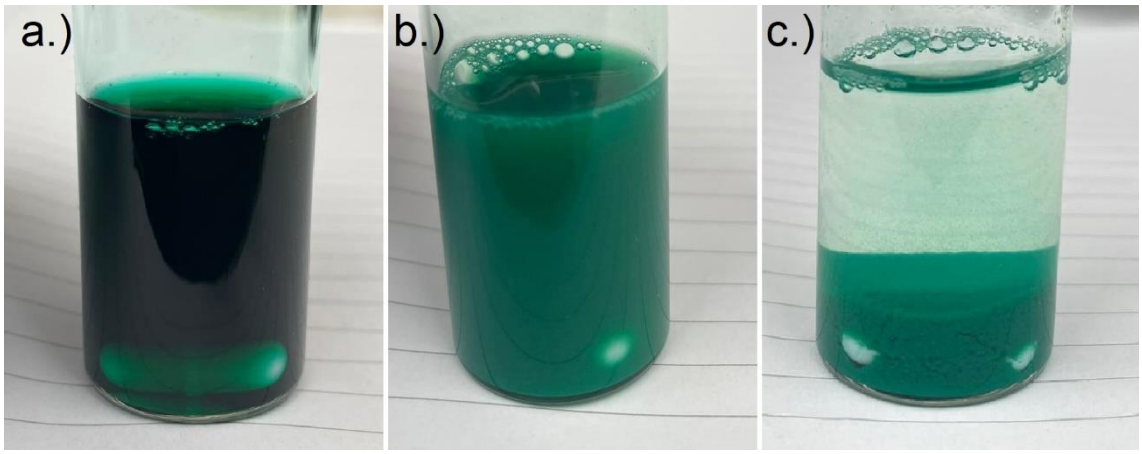

Figure 5.14 Images of a.) solution of ICG prior to addition of LRH; b.) ICG and LRH suspension immediately after mixing; c.) LRH-ICG composite after 24 hours of mixing.

XRD patterns of the precursor LRH ($LGd_{1.41}Tb_{0.59}H$-Cl), ICG, and their resultant composites prepared by attempted ion exchange are shown in Figure 5.15. The reflections present in the precursor LRH are identical to those present in the LRH/ICG composite. This may indicate that the coupling of LRH and ICG did not proceed *via* intercalation, as intercalation is expected to result in a change of the interlayer spacing (and therefore a shift in the corresponding reflections). It is possible that due to the large size of individual ICG molecules, the layers of the LRH were not able to shift apart sufficiently to accommodate the guest molecule, or that the amount of ICG intercalated was very little. It may be possible that ICG has instead adsorbed to the surface of the LRH particles, possibly by electrostatic attraction of the negative sulfonate groups on ICG to the positively charged surface layers of the LRH particles.

Surface adsorption is not expected to result in a change in interlayer spacing and would therefore not result in changes to the diffraction pattern relative to unloaded LRH. To test if the LRH-ICG composite could still display intercalation behaviour whilst retaining the coupled ICG molecules, a further ion-exchange reaction was

performed using ibuprofen sodium, and the resulting pattern is shown in Figure 5.15. The (010) reflection is seen to shift to a higher angle, indicating a contraction in the interlayer distance which is consistent with what was observed for the intercalation of IPA into the same precursor LRH described in Section 5.4.2.1. However, this was unexpected as intercalation of ibuprofen into LTbH (Section 2.4.3) resulted in an increase in the interlayer distance, as expected based on the hydrophobic nature of the ibuprofen ion. It is therefore unclear whether the nature of the LRH composition may be influencing the intercalation behaviour. In any case, it was evident from the vivid green colour of the resultant particles that the coupled ICG molecules were not lost during the synthesis, indicating that it is possible to co-load ICG and a small molecule API. However, the degree of crystallinity in the resultant compound

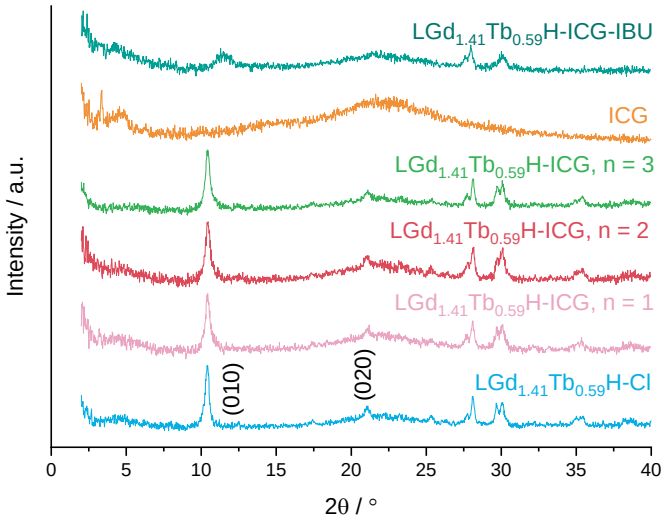

Figure 5.15 XRD patterns for ICG, $LGd_{1.41}Tb_{0.59}H$-Cl, the resulting composites of LRH-ICG prepared on three separate occasions, and the ion-exchange product LRH-ICG-IBU.

FTIR spectra for ICG, $LGd_{1.41}Tb_{0.59}H$-Cl, and the resulting LRH-ICG composite were measured and are shown in Figure 5.16. The precursor LRH spectrum is consistent with that of LTbH described in Section 2.4.4, and most prominently exhibits multiple broad stretches over the range 3650 - 3330 cm^{-1} ascribed to O-

H stretching vibrations arising from intercalated water molecules and hydroxide groups coordinated to Gd^{3+}/Tb^{3+}.

The FTIR spectrum of pure ICG shows broad, diffuse absorption above approximately 1750 cm^{-1}, most likely associated with various overlapping C-H/C=C stretching and bending modes. Stretching bands arising from the S=O bonds in the sulfonate groups are seen at 1398 and 1350 cm^{-1} respectively.

The LRH-ICG compound shows the band positions arising from the S=O sulfonate stretches are shifted to higher wavenumbers (1416 and 1355 cm^{-1}) relative to pure ICG (Figure 5.16b). This shifting is presumed to be the result of electrostatic interactions between the anionic sulfonate groups of ICG and the cationic LRH layers, therefore supporting the possibility of surface adsorption of ICG onto the LRH surface.

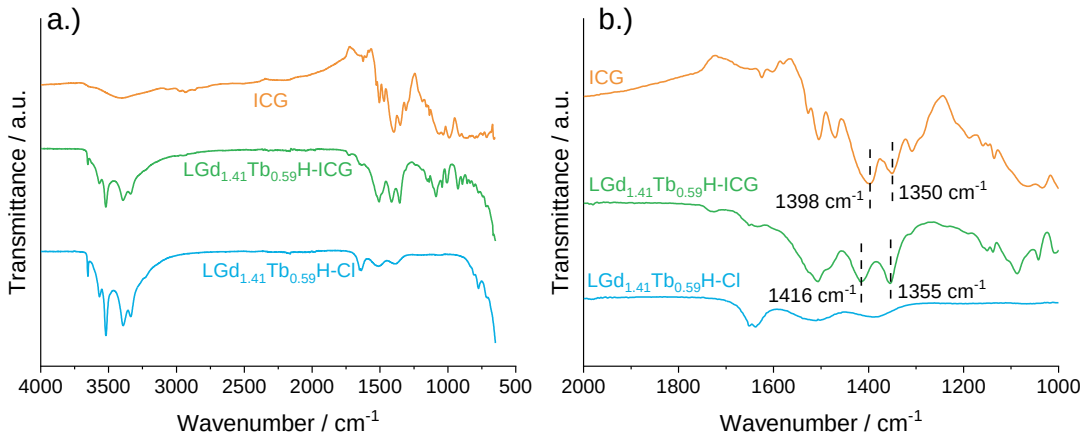

Figure 5.16 a.) FTIR spectra for ICG, $LGd_{1.41}Tb_{0.59}H$-Cl and the resulting LRH/ICG composite prepared by ion exchange. b.) Enlarged view showing band shifting in LRH-ICG composite relative to the pure ICG spectrum.

As the ICG loading is limited by the amount of ICG initially present during the attempted intercalation (10 mg of ICG to 150 mg of precursor LRH), the theoretically possible ICG loading in the LRH/ICG particles is only ca. 6.6 % by mass. Elemental analysis and TGA were employed to verify the actual ICG loading of the LRH-/ICG composite.

Since the only source of nitrogen in the LRH-ICG composite is the ICG molecule, the elemental analysis data (Table 5.4) was a convenient way to determine ICG loading with reasonable certainty. The amount of nitrogen detected by elemental analysis corresponds to approximately 6.9 % ICG loading (by mass). This value is slightly higher than the theoretical 6.6 % (based available amount of ICG present during synthesis), though the difference is slight enough to be explained by weighing or measurement errors. The thermogram of LRH-ICG (Figure 5.17) displays the expected initial intercalated water loss around 100 – 150 °C, corresponding to approximately 1.5 water molecules per formula unit. The second mass loss event, occurring between approximately 200 – 300 °C, is ascribed to dehydroxylation of the LRH layers, which is consistent with data obtained in previous chapters. Above around 400 °C, mass loss is ascribed to the gradual loss of intercalated ions (CO_3, Cl, ICG, and H) to form the mixed Gd/Tb oxide. The combined TGA and elemental analysis data was used to calculate the approximate formula of LRH-ICG (Table 5.5).

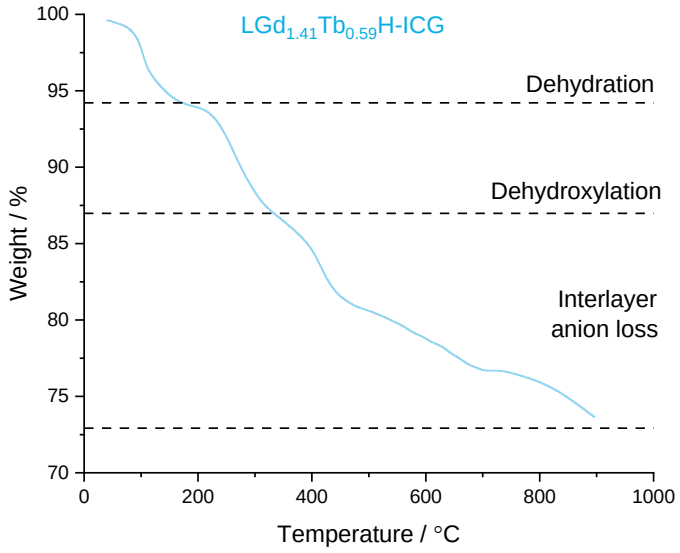

Figure 5.17 Thermogram of LRH-ICG composite (reference lines correspond to weight % at calculated mass for each phase).

*Table 5.4 Summary of observed (and calculated from formula, Table 5.5) values for elemental analysis and TGA data. *: Data presented in Chapter 4, Section 4.4.2).*

Material	*% C*	*% H*	*% N*	*Mass loss % (H_2O)*
*LRH-Cl precursor **	0.35 (0.32)	1.58 (1.74)	-	5.94 (5.83)
LRH-ICG	6.81 (5.70)	1.50 (2.07)	0.27 (0.26)	6.03 (5.49)

Table 5.5 Formula derived from TGA/elemental data for the LRH-ICG composite.

Material	*Formula*	*Drug loading / % mass*
LRH-ICG	$Gd_{1.41}Tb_{0.59}(OH)_5(Cl)_{0.55}(CO_3)_{0.2}$ $(C_{43}H_{47}N_2O_6S_2)_{0.05}(H_2O)_{1.6}$	7.54

5.4.3 Luminescence response

The solid-state photoluminescence spectra of $LGd_{1.41}Tb_{0.59}H$, IPA, and the LRH-IPA intercalate generated at pH 9 are shown in Figure 5.18.

Under UV excitation with the 325 nm laser, pure IPA is seen to display molecular phosphorescence across a broad range of wavelengths (particularly between 475 – 600 nm, Figure 5.18b). The spectrum of precursor LRH exhibits peaks consistent with the characteristic terbium transitions ($^5D_4$ to $^7F_{6\text{-}3}$). Considering the IPA intercalate, it can be seen that the intensity of the terbium emissions is vastly increased relative to the precursor LRH.

The strong intensity enhancement provided by the IPA in the intercalate is also evident by the appearance of the remaining terbium transitions ($^5D_4$ to $^7F_{3\text{-}0}$), which are too low in intensity to be seen in the precursor LRH. This implies that the overall energy transfer flows from the intercalated IPA molecules to the terbium centres. As explained in Section 5.1.2, the presence of a strongly radiative relaxation pathway in a compound intended for PDT applications is

undesirable and prevents efficient ROS generation. It is therefore unlikely that the LRH-IPA intercalate will exhibit significant PDT activity.

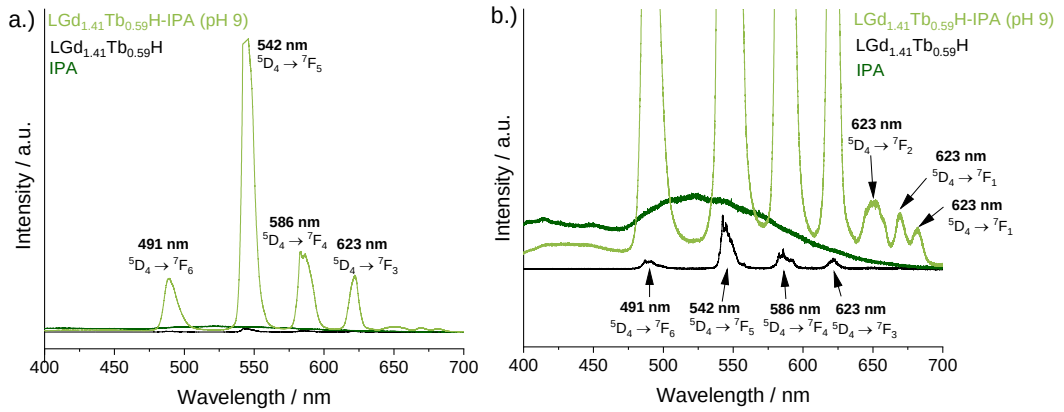

Figure 5.18 Solid state photoluminescence emission spectra of IPA, $LGd_{1.41}Tb_{0.59}H$-Cl, $LGd_{1.41}Tb_{0.59}H$-IPA (synthesised at pH 9); b.) enhanced view for clarity; obtained at an excitation wavelength of 325 nm and laser power of 0.05 %.

The solid-state photoluminescence spectra of ICG, $LGd_{1.41}Tb_{0.59}H$, $LGd_{1.41}Tb_{0.59}H$-ICG, and $LGd_{1.41}Tb_{0.59}H$-ICG-IBU are shown in Figure 5.19. Pure ICG exhibits no detectable molecular luminescence in the range of wavelengths measured under UV excitation (325 nm). Likewise, the LRH-ICG composite shows negligible emission intensity between 400 – 700 nm. It is evident that the presence of ICG in the composite quenches the characteristic terbium transitions seen in the precursor LRH, and that the relaxation of the excited composite is primarily non-radiative. By extension, this implies that the net flow of energy is likely from the LRH matrix to the ICG molecule, which is desirable for PDT applications.

It was demonstrated in Section 2.4.12 that intercalation of ibuprofen anions into LTbH leads to an enhancement in the emission intensities associated with terbium. It was therefore of interest to determine if the signal from LRH-ICG would be recovered following the intercalation of ibuprofen. This was found to be the case – the composite $LGd_{1.41}Tb_{0.59}H$-ICG-IBU exhibits vastly higher emission

intensity relative to the precursor LRH. Such co-loaded systems could potentially find use as a pathway for dual treatment – an initial drug release stage where an intercalated small molecule API shows loading-dependent luminescence; followed by a second stage, whereby the remaining LRH-ICG composite switches to a non-radiative relaxation mode, allowing efficient ROS generation for PDT.

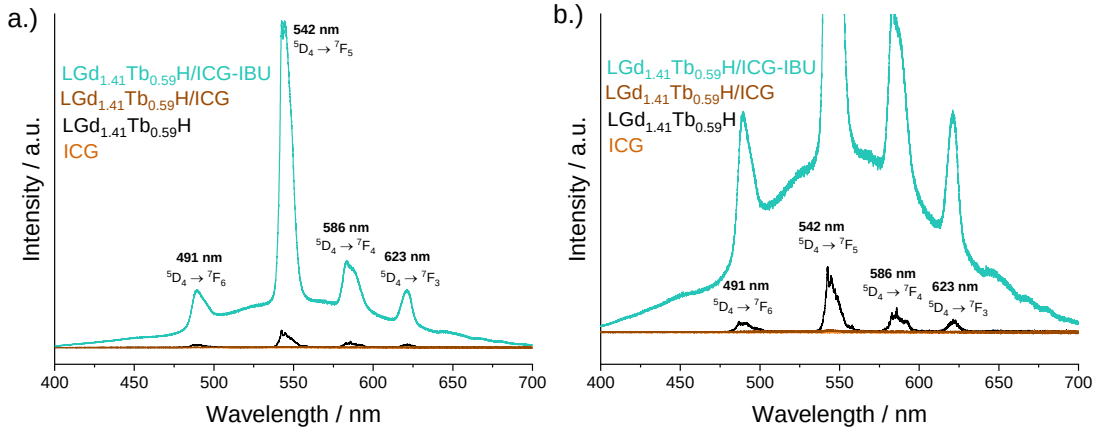

Figure 5.19 a.) Solid state photoluminescence emission spectra of ICG, $LGd_{1.41}Tb_{0.59}H$-Cl, $LGd_{1.41}Tb_{0.59}H$-ICG, and $LGd_{1.41}Tb_{0.59}H$-ICG-IBU intercalates; b.) enhanced view for clarity; obtained at an excitation wavelength of 325 nm and laser power of 0.05 %.

5.4.4 Photothermal response

5.4.4.1 Negative control tests with water

Since the absorbance of water at 808 nm is low,[470] and samples tested will be in aqueous suspension, water was selected as the medium for negative control thermal response tests. It was reasoned that, due to the lack of absorption at the laser wavelength, there should be no change in temperature measured within the cuvette with the laser on. In other words, the graph of temperature versus time should look the same before and after the laser is turned on and should be approximately horizontal.

The first test consisted of turning on the stirring (200 rpm) and measuring the temperature of the water without irradiation. Unexpectedly, the temperature did

not appear to be stable and showed a continuous increase. The experiment was repeated three times on different days, and allowed to continue for 1 h, 2 h, and just under 3 h respectively. The resultant graphs are shown in Figure 5.20. The rate of temperature change appears to show a decay-type pattern and is estimated to reach equilibrium at approximately 32° C (according to the limit of the fitted decay curve, not shown).

Since the temperature increase occurred with the laser powered off, it was assumed that the heat must be either be generated electrically by the stirring plate built into the enclosure, or by friction arising from the magnetic stirrer. Unfortunately, it was not possible to set the rate of stirring lower than 200 rpm because at lower rotation rates there was not enough power to overcome the weight of the magnetic stirrer bar.

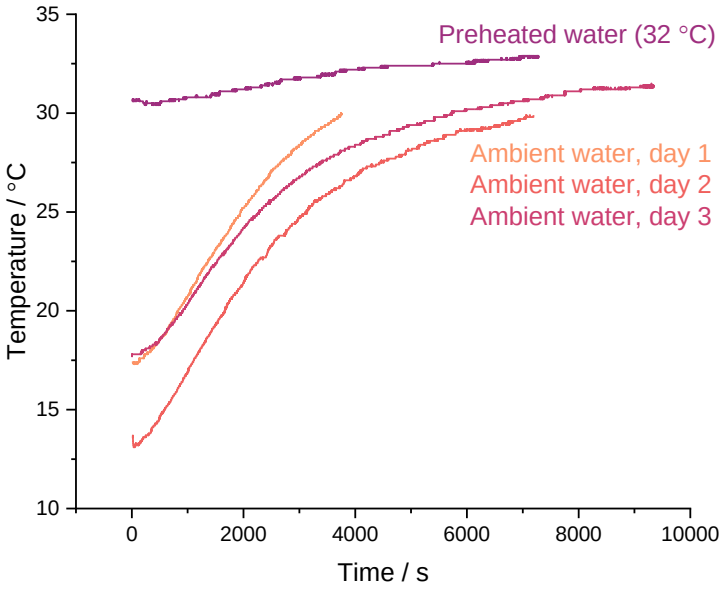

Figure 5.20 Graph illustrating the increase in temperature measured for water without laser illumination, with stirring at 200 rpm.

Preheating samples to 32° C showed an improvement in the resulting plot (Figure 5.20); however, on colder days the sample cooled rapidly and would thereafter begin to heat again, leading to inconsistent results. Therefore, further

photothermal response measurements will be conducted in the absence of stirring to achieve a stable temperature baseline. Consequentially, the vertical mixing of liquid within the cuvette would be relatively poor and the total change in the temperature of samples may be expected to represent a slight overestimate as the warmer liquid rises towards the temperature probe.

The experiment was therefore repeated without magnetic stirring, on 3 separate days, and the resulting graphs are shown in Figure 5.21. In all cases there is a slight temperature decrease at the start of the measurement, presumably due to the sample temperature equilibrating with the internal temperature of the laser enclosure. After approximately 20 min, the temperature is seen to stabilise, and remains stable (± 0.1 °C) for the next 1.5 h of measurement.

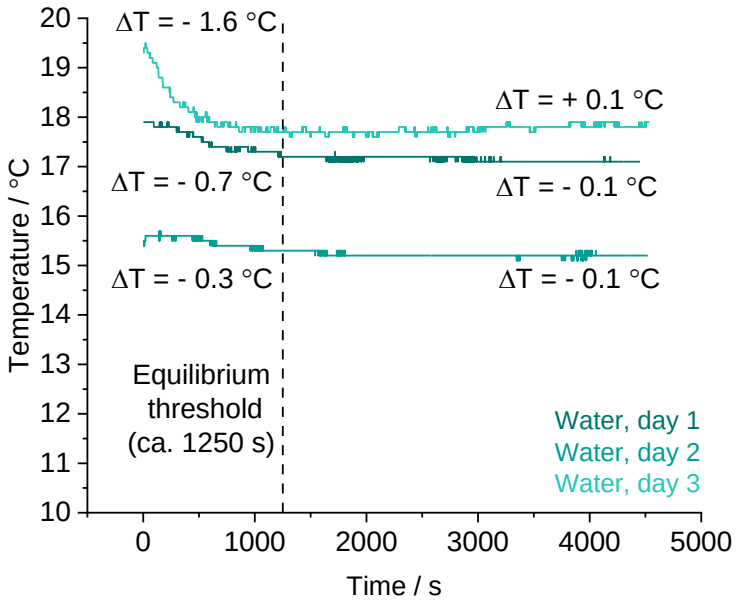

Figure 5.21 Graph illustrating the change in temperature measured for water without laser illumination and without magnetic stirring. Individual sample temperature change is shown.

To establish the effect of the laser on the temperature of water, further experiments were conducted in which the samples were allowed to equilibrate for 20 min without illumination, illuminated at 25 mW for 10 min, and subsequently allowed to equilibrate for a period of 20 min with no illumination. The resultant

graphs are shown in Figure 5.22. As with previous samples, the initial stage shows slight cooling as the samples equilibrate with the equipment, with an average cooling of 0.5 °C. During illumination, an average temperature increase of 0.4 °C was seen, with subsequent cooling of similar magnitude (- 0.3 °C) after the laser was turned off. This temperature increase is very small, and within the range of the tolerance of the temperature probe (1.5° C). Furthermore, photothermally responsive materials generate localised heat at vastly higher temperatures (typically 40 – 60 °C).[471] Therefore, temperature increases of this magnitude will not present an issue in further experiments.

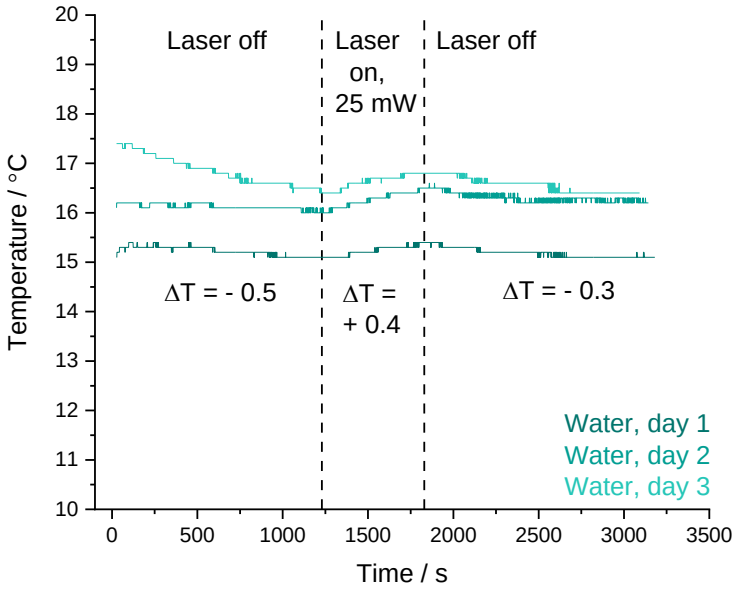

Figure 5.22 The change in temperature measured for water before, during, and after laser illumination at 25 mW and without magnetic stirring. Average sample temperature change is shown for each segment.

Overall, based on the results obtained with water, further experiments will be conducted without stirring, and with a period of at least 20 minutes of equilibration to ensure a stable temperature baseline.

5.4.4.2 Tests with indocyanine green and LRH-ICG

As ICG is a well-known NIR chromophore for PTT applications, it was selected for use as a positive control for this series of experiments. An initial solution of ICG at a concentration of 0.03 mg / ml was tested (Figure 5.23), effecting only a 0.2 ºC rise in temperature after illumination at maximum power (25 mW) for 10 minutes. Such a small temperature increase is comparable in magnitude to that seen for pure water (0.4 ºC). This is inconsistent with the literature, with some reports of solutions of ICG at much lower concentrations (2.5 µg / ml) resulting in a temperature change of ca. 5 ºC after illumination at a similar laser power density (0.5 W cm^{-2}) after only 3 min.[458]

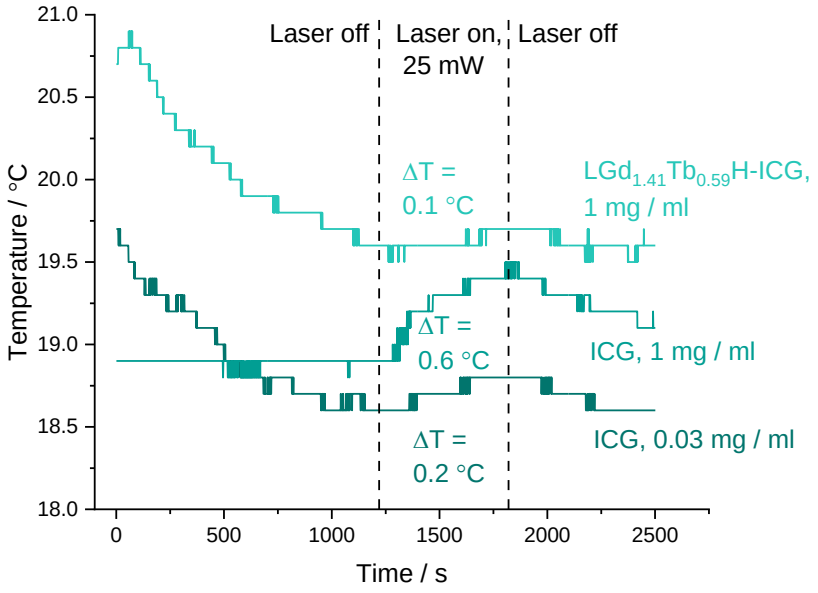

Figure 5.23 The change in temperature measured for aqueous solutions of ICG (1 mg/ml and 0.03 mg/ml) and an aqueous suspensions of LRH-ICG (1 mg/ml) before, during, and after laser illumination at 25 mW and without magnetic stirring. Average sample temperature change is shown for each segment.

The testing concentration was therefore increased to 1 mg / ml, and the resultant temperature change under identical illumination conditions (Figure 5.23) was 0.6 ºC. Though marginally higher than the negative control, the magnitude of the photothermal response seen was still not in line with what would be expected at

such a high concentration. Finally, the $LGd_{1.41}Tb_{0.59}H$-ICG sample (at a concentration of 1 mg / ml) was tested. Given the calculated drug loading (7.54 % by mass), the total ICG content of this suspension was approximately 0.075 mg / ml. It was therefore expected that if this material exhibited any enhanced PTT effect relative to pure ICG, that the temperature increase should be at least double that of the 0.03 mg / ml ICG solution. However, the total measured temperature change during illumination was only 0.1 ºC.

Taken together, it is likely that the present experimental apparatus is in some way unsuitable to adequately elicit or measure the photothermal response. In many instances of similar work, the temperature response of samples on irradiation is measured using a thermal camera instead of an immersion probe.[31,203,472] Such an approach may have been more suitable for this work, as the lack of stirring may have prevented the immersion probe from detecting much of any potential temperature change. Since it is not certain how far the laser beam may penetrate into the cuvette, and to what extent penetration depth is affected by the concentration or colour of sample solutions/suspensions, a thermal camera would have also provided more consistent measurements between samples. Unfortunately, due to a combination of factors arising from the COVID-19 pandemic, it was not possible to acquire a thermal camera and conduct further photothermal experiments.

5.4.5 Photodynamic response

5.4.5.1 DPBF dye stability

Due to the light sensitivity of the DPBF dye, it was first necessary to determine how stable the dye is with respect to illumination by a spectrophotometer during measurement. Therefore, a solution of DPBF was prepared at a final concentration of 0.05 mM (the same as would be used in further experiments). The solution absorbance spectrum was then measured once per minute, over 18 minutes. The results of this experiment are shown in Figure 5.24a.

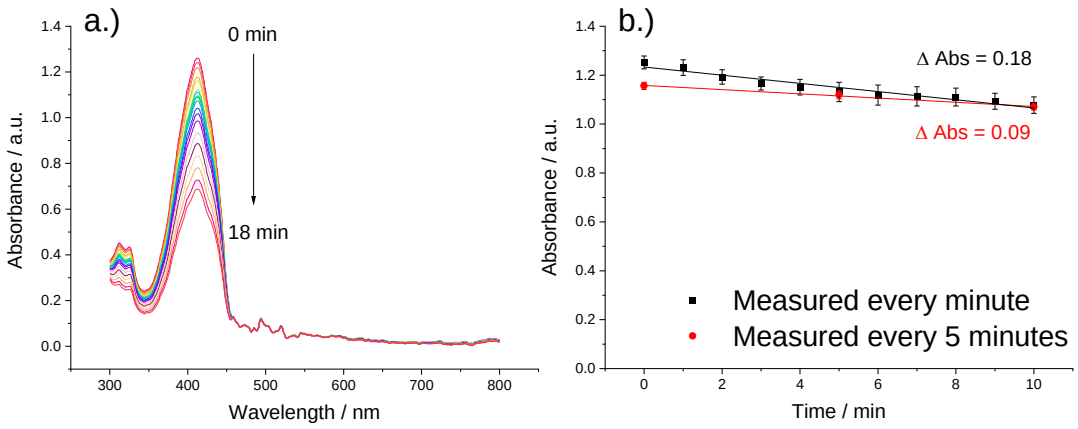

Figure 5.24 a.) Change in absorbance spectrum of DPBF (0.05 mM) over repeated measurements; b.) single point absorbance measurements of DPBF at 412 nm, showing decline in absorbance intensity with repeated measurements. Three independent experiments were performed, and the results are shown as mean ± standard deviation.

A significant decrease in the absorbance intensity of DPBF (approximately 50 %, Figure 5.24a) is seen as a result of repeated measurements. Further experiments were conducted in which sample absorbance at 412 nm was measured either once per minute, or once every five minutes. The results of these experiments are shown in Figure 5.24b. Fewer measurements lead to a smaller decrease in absorbance of DPBF (0.09 units vs. 0.18 units), indicating that repeated exposure to the broad-spectrum illumination by the spectrophotometer lamp results in minor DPBF photobleaching. Therefore, further experiments will aim to minimise the number of absorbance measurements as far as practicable.

To verify that illumination from the laser does not cause degradation of DPBF, sample absorbance was measured before, during, and after a total of 10 minutes laser illumination (at full power, 25 mW). The outcome of this experiment is shown in Figure 5.25. The average change in absorbance (0.03 units) is very low, even compared to DPBF without laser illumination (Figure 5.24b). It can therefore be concluded that light at 808 nm does not have any detrimental effect on the performance of DPBF, and that this is a suitable dye to use for singlet oxygen detection in this context.

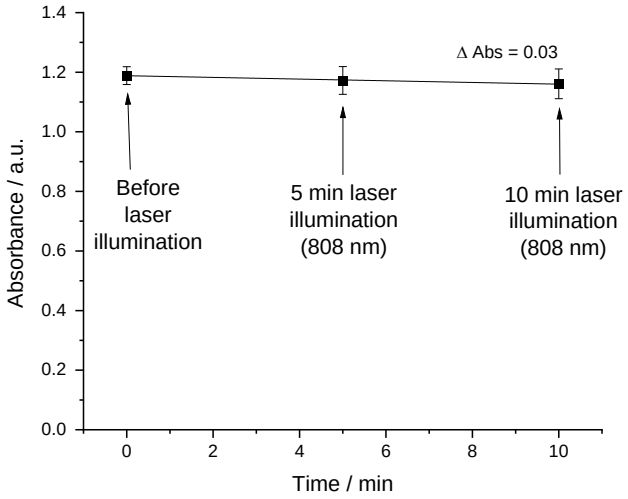

Figure 5.25 Single point absorbance measurements at 412 nm of DPBF (0.05 mM), before and after laser illumination (808 nm, 25 mW power). Three independent experiments were performed, and the results are shown as mean ± standard deviation.

5.4.5.2 Positive control tests with indocyanine green

To determine the optimal concentration of ICG to use, a series of solutions were made (0.25 – 0.016 mg / ml) and their absorbance measured over 300 – 800 nm (Figure 5.26). It was desirable that the optimal concentration solution should have low absorbance at 412 nm (so as not to interfere with DPBF and allow accurate ROS detection), but also high absorbance at around 800 nm to ensure good absorption of NIR laser irradiation. The optimum final ICG concentration was chosen to be 0.016 mg / ml, as further dilution resulted in significant reduction in

absorbance around 800 nm, which was not desirable. To verify the dye stability towards illumination by the spectrophotometer, a fresh solution was prepared at 0.016 mg / ml and the absorbance spectrum was measured once per minute for 20 minutes, shown in Figure 5.26b. The change in absorbance over the course of the experiment is negligible and can therefore be disregarded.

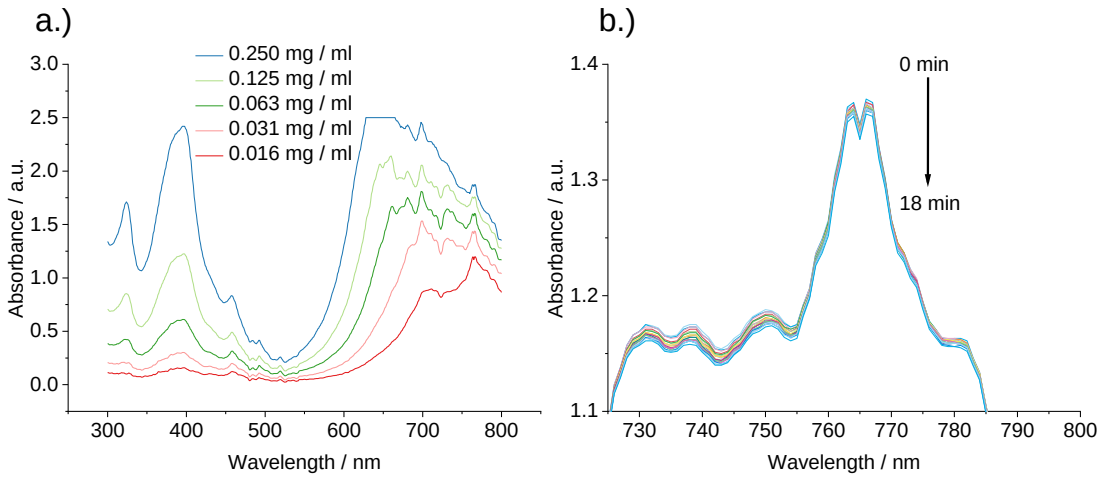

Figure 5.26 a.) Absorbance spectra of aqueous solutions of ICG at various concentrations. b.) Enlarged view of the change in absorbance spectrum of a 0.016 mg / ml aqueous solution of ICG due to repeated measurements.

To measure the ROS production by pure ICG under 808 nm laser illumination, samples were prepared containing both ICG and DPBF at the final concentrations derived above (0.016 mg / ml and 0.05 mM respectively). Sample absorbance spectra were taken at 10-minute intervals of laser irradiation at 25 mW power (up to a total of 30 minutes irradiation), as depicted in Figure 5.27a. For comparison, the same experiment was performed with pure DPBF and pure ICG (Figure 5.27b-c).

The samples containing both ICG and DPBF (before irradiation) show slightly altered absorbance profiles relative to their pure, unmixed, counterparts. Firstly, pure ICG exhibits two prominent absorbance maxima – 713 nm and 765 nm, with intensity of 0.73 and 1.06 units respectively. These maxima are consistent with the oligomer and monomer forms of ICG respectively.[473] Upon mixing with DPBF,

the monomer maximum at 765 nm increases in intensity to ca. 1.29 units. Secondly, the absorbance maximum of pure DPBF (412 nm, intensity 0.95 units) is also seen to increase in intensity upon mixing with ICG (to 1.1 units). In the case of the DPBF peak, this difference is most likely additive in nature, as ICG shows some absorbance (0.1 a.u.) at 412 nm. However, the increase in intensity for the ICG peak at 765 nm (a change of 0.23 units) is difficult to explain, as the absorbance of DPBF at that wavelength is only around 0.08 a.u.

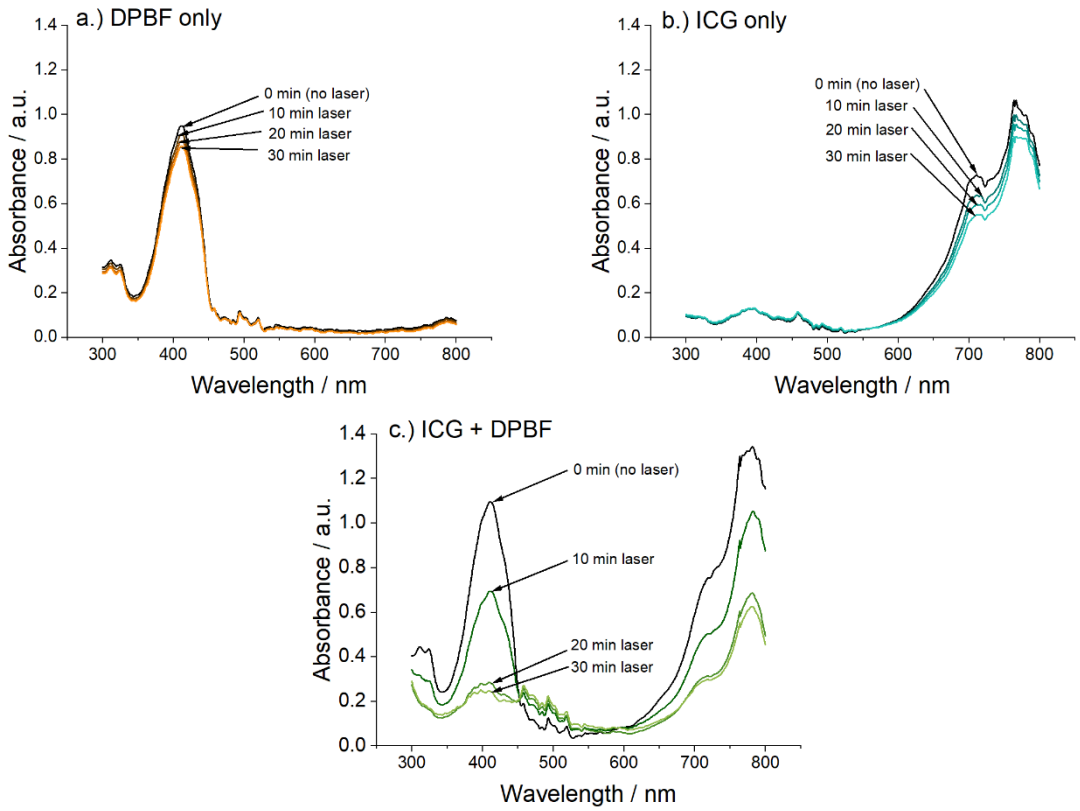

Figure 5.27 Absorbance spectra of solutions of a.) DPBF, 0.05 mM; b.) ICG, 0.016 mg / ml; and c.) ICG + DPBF (0.05 mM and 0.016 mg / ml respectively) after several 10 minute intervals of irradiation with 808 nm laser light (25 mW); d.) Graph showing the total remaining amount of DPBF (in nmol) in the cuvette at specified time intervals of irradiation, as calculated using a DPBF calibration curve.

Pure ICG is seen to lose some intensity with irradiation – this is likely due to photodecomposition as has been reported.[474] For the mixed ICG/DPBF samples, the mean absorbance before irradiation and at each irradiation time interval is summarised in Table 5.6. After 30 minutes of irradiation, the DPBF peak has decreased in intensity by approximately 79 %, whereas the ICG peak decreases

in intensity by approximately 54 %. In both cases, this decrease is much higher than that seen for pure DPBF or pure ICG (Figure 5.27b), meaning that it exceeds the natural signal decay that is seen due to deactivation of DPBF/ICG by the laser and spectrophotometer. Additionally, while the decrease in absorbance of DPBF was expected (due to the production of ROS species and the subsequent conversion of DPBF to DBB), such a dramatic absorbance loss arising from ICG was not expected.

A calibration curve was used to convert the absorbance arising from DPBF to the amount of DPBF reacted (nmol), and these values are summarised in Table 5.6.

Table 5.6 Summary of the absolute absorbance and % change in absorbance of solutions containing ICG and DPBF (0.016 mg / ml and 0.05 mM respectively) after different laser irradiation intervals.

Irradiation time	*DPBF absorbance at 412 nm*	*Loss / %*	*DPBF reacted / nmol*	*ICG absorbance at 782 nm*	*Loss / %*
0 min	1.08 ± 0.01	0	0	1.33 ± 0.01	0
10 min	0.75 ± 0.04	31	53.37 ± 8.54	1.11 ± 0.04	17
20 min	0.30 ± 0.02	72	129.35 ± 4.31	0.70 ± 0.02	47
30 min	0.23 ± 0.01	79	141.25 ± 0.42	0.61 ± 0.02	54

These results may be explained by one of three proposed scenarios:

1.) During irradiation, ICG produces ROS which then react with DPBF, producing DBB (thereby reducing the DPBF peak intensity); ROS, the reaction intermediate epoxide, and/or product DBB subsequently reacts with ICG, thereby reducing ICG peak intensity;

2.) ICG produces ROS, which then react with DPBF to form DBB as above; the ICG peak loses intensity because ICG has some signal enhancing interaction with DPBF, which is now diminishing;

3.) ICG does not produce ROS, instead it reacts directly with DPBF until it is consumed.

For the purposes of ROS detection using DPBF, scenarios 1 and 2 are equally acceptable, because the intensity of absorption arising from DPBF is still directly related to the amount of ROS produced, and the intensity arising from ICG is of no consequence to the result. However, scenario 3 is undesirable because the loss in intensity for the DPBF peak in that case would not yield information about the quantity of ROS production. Therefore, to exclude this possibility, ICG and DPBF were mixed and stirred (without irradiation) for the same time intervals as the irradiation test. The resulting absorbance spectra are shown in Figure 5.28a.

No photobleaching is seen in the mixture of DPBF and ICG without laser irradiation, even after 30 minutes of stirring. Therefore, it is unlikely that ICG and DPBF are reacting chemically. This supports the conclusion that the process involved in diminishing the respective absorbance of both ICG and DPBF in mixture is photochemical in nature (either scenario 1 or 2). This can also be seen visually by the change in colour of the ICG + DPBF mixture with irradiation as opposed to without (Figure 5.28b). This is in agreement with other literature sources which investigated the use of ICG/DPBF systems under laser irradiation,[475,476] though in those cases the absorption decay of ICG was not addressed.

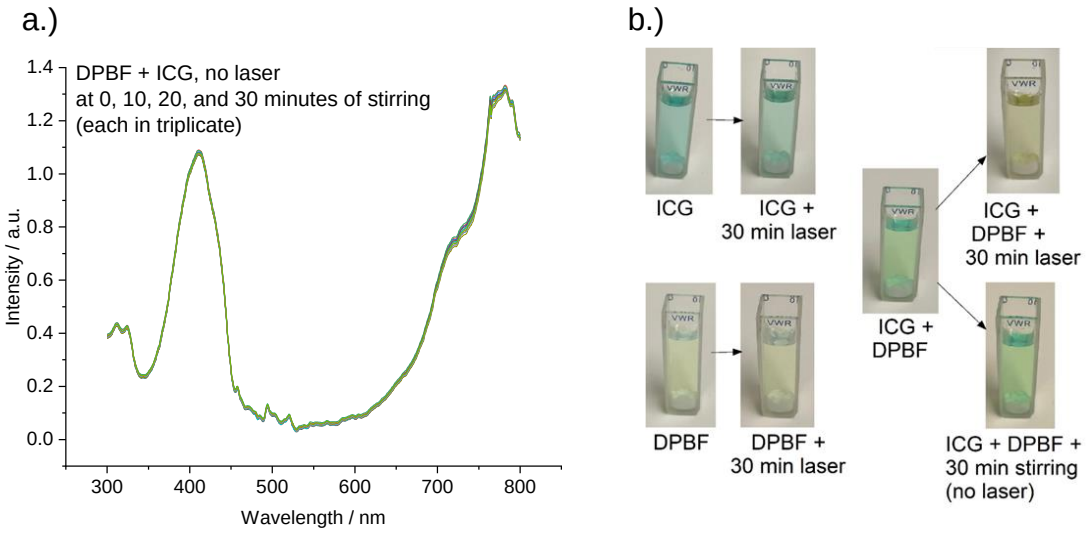

Figure 5.28 a.) Absorbance spectra of aqueous solutions of ICG + DPBS without irradiation, stirring for 10-minute intervals over the course of 30 minutes. Experiment was performed in triplicate and the absorbance spectra overlaid. b.) representative photographs of sample solutions before and after 30 minutes of irradiation to illustrate photobleaching effect.

To investigate the nature of this photoconversion further, solutions of ICG, DPBF, and their mixture before and after irradiation were used to conduct ^{1}H NMR analysis. Due to the dilute concentrations of samples used, it was not possible to obtain FTIR and ^{13}C NMR data. ^{1}H NMR data for the pure solutions of ICG and DPBF are presented in Figure 5.29, and for the ICG/DPBF mixture before and after irradiation in Figure 5.30. The spectrum of pure ICG is largely consistent with the literature,[477] and shows a prominent, poorly resolved multiplet at δ 2.02 ppm (14H m, $H_g/H_m/H_n$, Figure 5.29a) with an integration value that solves for six protons less than expected (20H). It is presumed that this is a consequence of proton exchange with the solvent or the poor resolution of the multiplet resulting in incorrect integration. The spectrum of DPBF (Figure 5.29b), is also consistent with the literature[478] but exhibits several multiplets (highlighted in green, Figure 5.29b) which can be assigned to its photodegradation product, DBB,[479] as a result of light exposure during transit/measurement.

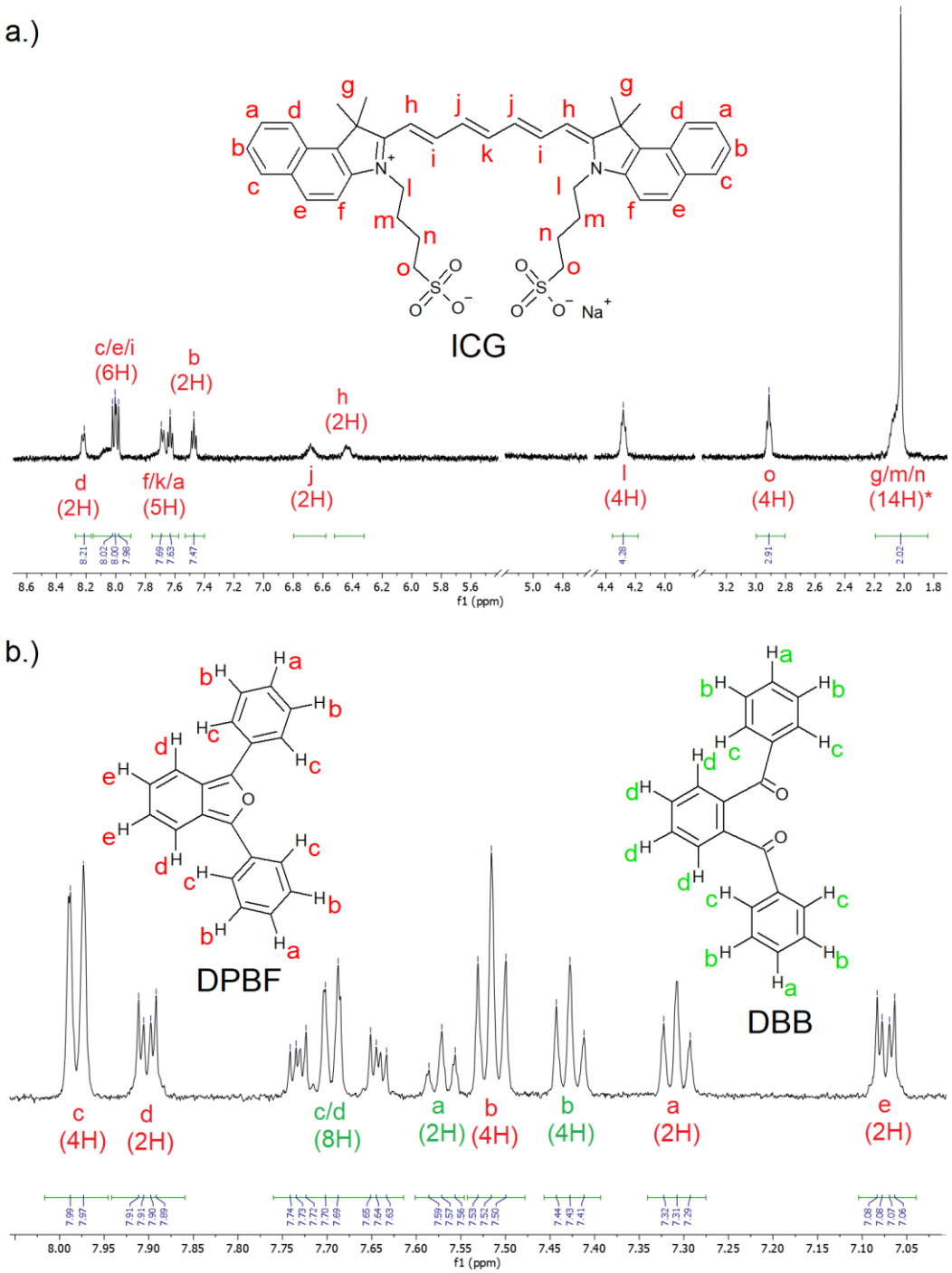

Figure 5.29 ^{1}H NMR spectra and assignments for a.) ICG and b.) DPBF solutions in deuterated ethanol (1 mg / ml concentration). Large amount of DBB present in DPBF sample due to exposure to light during measurement/transfer. Hydrogen atoms not shown in ICG for clarity. Ethanol-d6 (solvent; δ = 5.30, 3.58, 1.14 ppm) and contaminant water (ca. δ = 4.56 ppm) peaks removed for clarity. Where peaks have been removed, a break in the X-axis is shown.

^{1}H NMR, ICG: δ (ppm) 8.21 (2H, d, H_d), 8.00 (6H, m, H_c/H_e/H_i), 7.69 (5H, m, H_f/H_k/H_a), 6.66 (2H, poorly resolved triplet, H_j), 6.44 (2H, poorly resolved triplet, H_h), 4.28 (4H, t, H_l), 2.91 (4H, t, H_o), 2.02 (14H, m, H_g/H_m/H_n). *: peak intensity does not integrate to the expected 20H, presumably due to non-gaussian shape of peak.*

^{1}H NMR, DPBF: δ (ppm) 7.99 (4H, dd, H_c), 7.91 (2H, dd, H_d), 7.52 (4H, t, H_b), 7.31 (2H, t, H_a), 7.08 (2H, dd, H_e). Spectrum contained additional peaks arising from the photodegradation product of DPBF (DBB) due to exposure to light during transportation and measurement.

The spectrum of the ICG/DPBF mixture (Figure 5.30a) displays a combination of the features of the pure ICG and DPBF solutions, with no associated chemical shifts relative to the pure solutions (Figure 5.29). After irradiation, the peak arising from ICG (δ 2.02 ppm, $H_g/H_m/H_n$, Figure 5.30a) is seen to split into a well-resolved multiplet. This is similar to what has previously been reported for pure solutions of ICG,[480] wherein the splitting was ascribed to the removal of symmetry of the methyl groups (H_g) within the molecule as a result of dimerization at the j/k carbon atoms over time. In the present case, since all four samples were prepared at the same time, and splitting was not observed in the spectrum of pure ICG, it is unlikely that dimerization of ICG alone was responsible for the change. It is more likely that some kind of reaction has occurred at the same position (j/k carbon atoms). Singlet oxygen is known to be reactive towards alkenes,[481] and ICG has also been reported to react with the ROS species it generates.[482]

Two of the peaks arising from DPBF (δ 7.90, 7.07 ppm, H_d and H_e) are significantly diminished after radiation, which is consistent with the formation of DBB (whereby the expected intensity increase at δ 7.70 ppm is observed).

In summary, DPBF is stable to the measurement conditions and is therefore an appropriate choice for further ROS detection tests. ICG was, as expected, successfully able to elicit a ROS generation response under 808 nm irradiation. Specifically, 20 minutes of irradiation at full power led to over 70 % reduction in absorbance intensity by DPBF at the concentrations tested (0.05 mM and 0.02 mM respectively). The absorbance intensity arising from ICG was found to also diminish with irradiation, though to a lesser extent than DPBF, likely due to reaction with the generated ROS species.

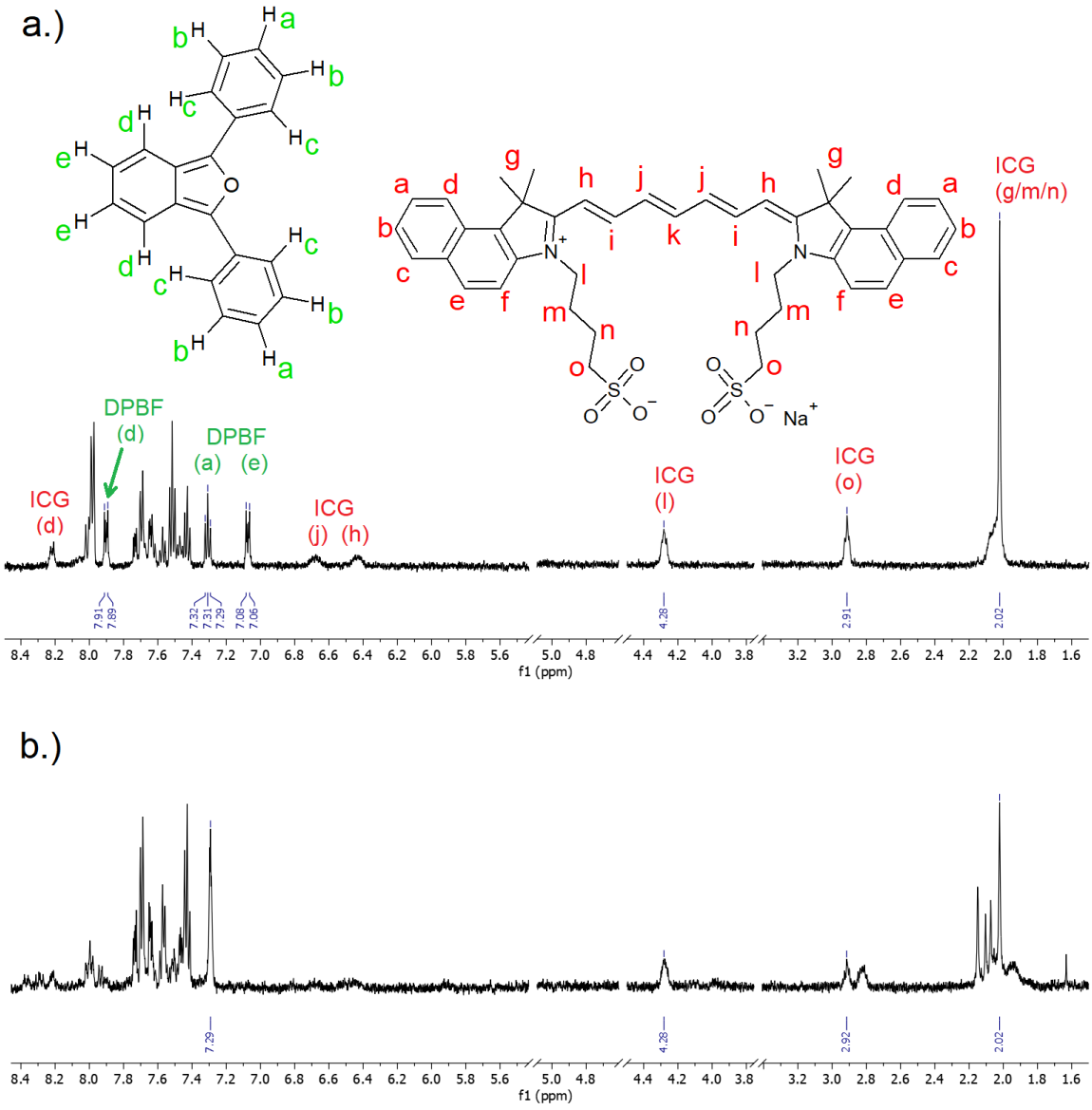

Figure 5.30 ^{1}H NMR spectra for mixtures of ICG/DPBF (0.5 mg / ml each) a.) without irradiation, and b.) with 30 minutes of irradiation with a laser at 808 nm, and 25 mW power. Hydrogen atoms not shown in ICG for clarity. Ethanol-d6 (solvent; δ = 5.30, 3.58, 1.14 ppm) and contaminant water (ca. δ = 4.56 ppm) peaks removed for clarity. Where peaks have been removed, a break in the X-axis is shown. Prominent peaks arising from DPBF and ICG are highlighted for illustrative purposes; peaks arising from DBB are present but not highlighted in the overlapping region between ca. δ = 7.8 – 7.4 ppm.

5.4.5.3 LRH materials

It is important to account for light scattering by particles when using UV-vis as a technique to test suspensions. Briefly, a UV-vis measurement consists of illuminating a cuvette containing a sample solution from one side, and a detector on the opposite side of the cuvette is used to quantify the intensity of light which has passed through the sample. Any light intensity lost to the sample is due to the sample absorbing light of that wavelength.

However, when the sample is a suspension containing particles, light is also scattered away from the detector by the particles, in random directions. In this way, light intensity lost to the sample is now a combination of absorbance and scattering. The resultant absorbance spectrum of a suspension hence overestimates the absorptivity of suspensions, particularly at shorter wavelengths.[483] Therefore, to determine the optimal concentration of LRH suspensions to use for PDT effect screening, a series of suspensions of $LGd_{1.41}Tb_{0.59}H$ at different concentrations was made and their resultant absorption spectra are shown in Figure 5.31.

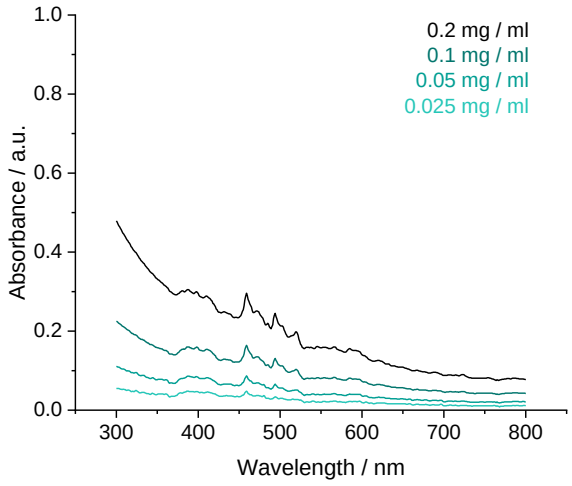

Figure 5.31 Absorbance spectra of aqueous suspensions of LRH at various concentrations, illustrating a pronounced Rayleigh scattering effect towards the shorter wavelength end of the spectrum.

Based on these results, final concentrations of LRH samples of 0.025 mg / ml were chosen as optimal, giving limited absorbance (ca. 0.05 units) at the DPBF absorbance wavelength (412 nm). It is expected based on previous results (Figure 5.27) that the absorbance intensity at 412 nm will range from ca. 0.2 – 1 absorbance units, therefore competing absorbance of only 0.05 units should not present a problem. It was not desirable to further decrease the concentration of LRH samples, because the amount of ROS produced may be too low to detect.

Suspensions of LRH formulations (LTbH, LGdH, and $LGd_{1.41}Tb_{0.59}H$) at 0.025 mg / mL were tested for ROS production using DPBF before and after irradiation for 10 minutes, and the resultant spectra are shown in Figure 5.32. In each case, no significant change in the absorbance peak of DPBF is seen – at least at this concentration. This is in line with what was expected, considering that the spectra of LRH materials (Figure 5.31) do not show any absorbance around 800 nm. Therefore, LRH alone is not expected to absorb energy and produce ROS which can then react with DPBS, and hence no change in DPBS absorbance is seen.

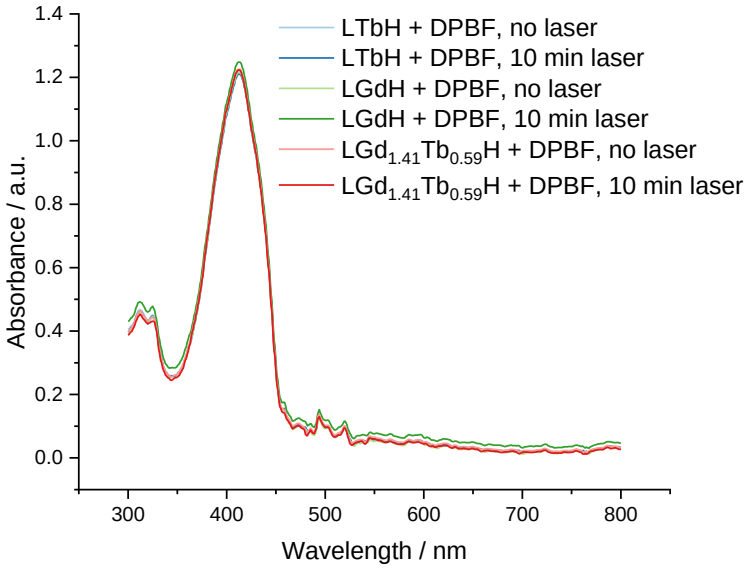

Figure 5.32 Absorbance spectra of aqueous suspensions of LRH materials (0.025 mg / ml) with DPBF before and after 10 minutes of irradiation with 808 nm laser light (25 mW).

The results of the ROS production test for $LGd_{1.41}Tb_{0.59}H$-IPA are shown in Figure 5.33. No significant decrease in the absorbance intensity arising from DPBF is seen, and therefore the IPA intercalate does not exhibit photodynamic activity. Considering the results of the photoluminescence tests in Section 5.4.3, this is unsurprising as intercalation of IPA resulted in a vast terbium luminescence enhancement, implying net energy transfer from the IPA molecules to the LRH matrix. Therefore, the intercalate was unlikely to exhibit photodynamic activity, as the excited IPA molecules would rapidly transfer their excess energy to the LRH matrix instead of nearby oxygen molecules.

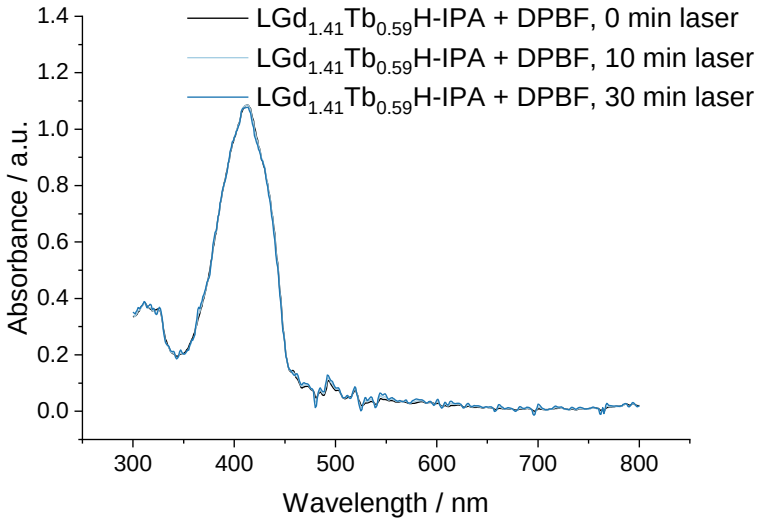

Figure 5.33 Absorbance spectra of $LGd_{1.41}Tb_{0.59}H$-IPA with DPBF, at selected irradiation intervals (808 nm, 25 mW). No change in absorbance is observed, indicating no ROS generation by the intercalate.

The same test was conducted for suspensions of $LGd_{1.41}Tb_{0.59}H$-ICG, and the results are shown in Figure 5.34. Unlike the precursor LRH (Figure 5.32), the LRH-ICG composite shows significant ROS production as measured by the decrease in absorbance of the DPBF peak. This confirms that the photodynamic capacity of ICG is preserved upon conjugation with the LRH matrix.

Considering the ICG loading within the LRH (7.54 % by mass), the ICG concentration in the samples tested was approximately 0.002 mg / ml. When

compared to the free ICG solution tested (Figure 5.27c, 0.016 mg / ml), the present LRH-ICG intercalates show comparable ROS generating activity, even at only a fraction of the ICG content. A calibration curve was used to convert the absorbance arising from DPBF to the amount of DPBF reacted (nmol), and these values are summarised in Table 5.7. On average, after 30 minutes of irradiation, around 105 nmol of the DPBF was deactivated by LRH-ICG compared to 141 nmol by free ICG (at approximately 8 times the ICG content).

It therefore seems that conjugation to the LRH matrix may improve the photodynamic activity of ICG relative to free ICG. It was established in Section 5.4.3 that the LRH matrix efficiently transfers excitation energy to the associated ICG molecules. Therefore, ICG molecules associated with the LRH are not expected to relax efficiently by energy loss via the LRH matrix. Additionally, it is possible that the LRH matrix may be absorbing vibrational energy lost by the ICG molecule and donating it back to the ICG molecule which then generates ROS. Such a mechanism would explain both the increased conversion efficiency and poor photothermal performance of this material.

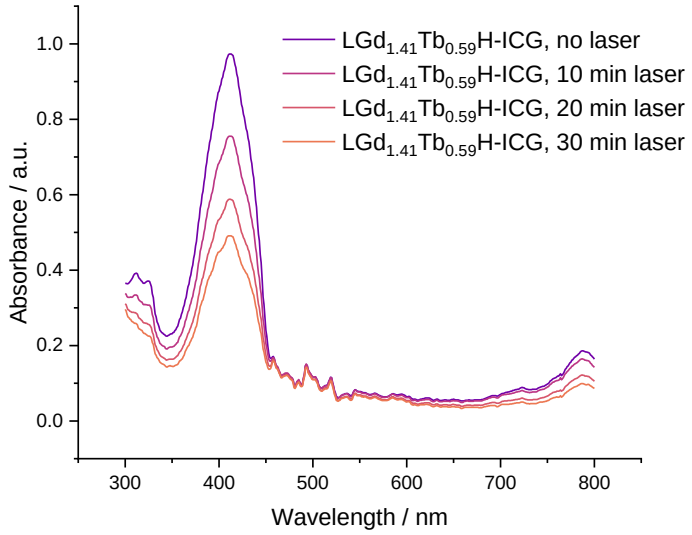

Figure 5.34 Representative absorbance spectra of aqueous suspensions of LRH-ICG (0.025 mg / ml) with DPBF before and after several intervals of irradiation with 808 nm laser light (25 mW).

Table 5.7 Summary of the absolute absorbance and % change in absorbance of suspensions containing LRH-ICG and DPBF (0.016 mg / ml and 0.05 mM respectively) after different laser irradiation intervals.

Irradiation time	*DPBF absorbance at 412 nm*	*Loss / %*	*DPBF reacted / nmol*
0 min	0.884 ± 0.06	0	0
10 min	0.678 ± 0.05	23.3	65.61 ± 7.85
20 min	0.529 ± 0.04	40.2	90.89 ± 5.74
30 min	0.446 ± 0.03	49.5	104.92 ± 4.10

5.5 Conclusions

The work presented in this chapter sought to investigate LRH materials with potential PTT and PDT applications. A near-infrared laser assembly was first designed, constructed, and tested to facilitate these experiments. The lead LRH formulation, $LGd_{1.41}Tb_{0.59}H$, was loaded with known PTT/PDT dye indocyanine green (ICG), and isophthalic acid (IPA) which has recently been reported to act as an efficient PDT agent when intercalated into a structurally similar LDH system.[1] It was found that the loading of ICG onto the LRH matrix does not proceed *via* ion-exchange, and the resulting LRH-ICG composite retains its ion-exchange capacity; this was demonstrated by co-loading ibuprofen (IBU) to produce LRH-ICG-IBU.

Solid-state luminescence measurements under UV excitation revealed that the loading of ICG onto the precursor LRH caused a significant quenching in the characteristic terbium transitions relative to the unloaded LRH; in turn, this suggested that the main relaxation pathway of the system is non-radiative, which is conducive to high PDT efficiency. Co-loading with IBU lead to terbium signal enhancement relative to the parent LRH, leading to the possibility of a sequential treatment system – an initial drug release stage where an intercalated small molecule API shows loading-dependent luminescence; followed by a second stage, whereby the remaining LRH-ICG composite switches to a non-radiative

relaxation mode, allowing efficient ROS generation for PDT. Conversely, loading with IPA resulted in a vast increase in the intensity of terbium transitions, implying that energy absorbed by the intercalated IPA molecules is rapidly transferred to the LRH matrix. It was therefore expected that LRH-IPA would not exhibit efficient ROS generation. Despite this, the luminescence enhancement seen in LRH-IPA compounds may be of potential use for imaging applications.

The measurement of photothermal response in this work was unfortunately not successful, due to a combination of experimental equipment factors. However, the photodynamic response measurements resulted in some promising findings. As expected, the precursor LRH systems and the LRH-IPA intercalates exhibited no significant ROS generation ability. On the other hand, LRH-ICG exhibited greatly enhanced ROS generation efficiency relative to free ICG – deactivating a comparable amount of DPBF to pure ICG (105 nmol 141 nmol), at only 1/8th of the ICG content.

6 Conclusions

6.1 Summary of findings

The work presented in this thesis aimed to investigate the potential of layered rare-earth hydroxides (LRHs) as theranostic platforms. To date, the structurally related layered double hydroxides (LDHs) have received considerable attention in theranostics and the wider field of biomedical literature, with many promising results and high-impact publications. The layered structure of LRHs/LDHs is particularly attractive for theranostics as it can efficiently and reversibly uptake anionic drug or photosensitiser molecules, thereby enabling drug delivery or phototherapy.

The rare-earth (RE) elements possess inherent magnetic and luminescent properties, and there exists a wealth of biomedical literature exploring the RE elements as dopants to enhance other systems, mainly for imaging applications. Despite this, research exploring LRHs for theranostic applications is still nascent. To this end, our research group has previously explored the potential of LGdH as a theranostic agent.[87] Building on these findings, **Chapter 2** of this thesis described the hydrothermal synthesis, characterisation, and functional performance assessment of LTbH as a theranostic platform.[318]

The synthesis of LTbH-Cl and subsequent intercalation of the model drugs diclofenac, ibuprofen, and naproxen (dic, ibu, nap) was confirmed by XRD; elemental microanalysis and TGA experiments revealed high drug loadings of 80-100 % based on charge balance considerations (*ca.* 33 wt %). The haemo- and cytocompatibility of the LTbH formulations was found to be high. Photoluminescence studies revealed that intercalation of ibu and nap resulted in

a significant increase in luminescence intensity, whereas the intercalation of dic lead to the quenching of the luminescence signal associated with Tb^{3+}. Moreover, it was demonstrated using LTbH-ibu that it is feasible to use the changing luminescence emission spectrum upon drug release to quantify the extent of drug which had de-intercalated. This property could provide a non-invasive way to quantify the real-time drug release kinetics *in vivo*.

To ensure consistent performance and safety for potential *in vivo* applications, homogeneous particles with an average size below ca. 200 nm are required. The particles prepared by the method described in Chapter 2 were found to be non-uniform and exceed this size requirement (670 ± 564 nm). Aiming to resolve this, the work described in **Chapter 3** concerns the optimisation of the hydrothermal synthesis method to reproducibly yield LTbH particles with a smaller average particle size and higher morphological consistency. The synthetic parameters of temperature, incubation time, and vessel fill volume were systematically varied. It was shown that temperature exhibits a dominant effect in determining resultant particle morphology. The optimised, low temperature (90 °C) method was demonstrated to be highly consistent and reproducible, resulting in particles with a mean size of 152 ± 59 nm, ideally suited to theranostic applications.

To establish if other, theranostic-compatible LRHs can be produced in an analogous way, **Chapter 4** begins by describing the application of the size-optimised hydrothermal method to produce a small family of LRH systems (R = R = Pr, Nd, Gd, Dy, Er, Yb). The synthesis was successful for R = Pr, Nd, Gd, and Dy, in all cases yielding particles with mean size under 200 nm. In the case of LErH, the resultant mean particle size was somewhat larger at 442 ± 246 nm, which is thought to be related to the smaller ionic size of Er^{3+}. In the case of LYbH, synthesis at 90 °C was not facile, resulting instead in the formation of a colloidal

dispersion; increasing synthetic temperature to 150 °C resulted in a biphasic solid with mean particle size 20 ± 14 μm. Lead elements Gd and Tb were selected based on their favourable properties for theranostic applications – high magnetic activity, intense photoluminescence, similarity in ion dimensions and resultant particle size, as well as relatively high biocompatibility. Three additional formulations containing the elements Gd and Tb were created, at varying composition ratios. Relaxometry studies revealed that while the LRH materials exhibit low r_1 relaxivities (r_1 = 0.02 – 0.38 $mM^{-1}s^{-1}$), their r_2 relaxivities are promising (r_2 = 1.6 – 3.48 $mM^{-1}s^{-1}$). The photoluminescence of the various LRH formulations was assessed in aqueous suspension, and it was found that $LGd_{1.41}Tb_{0.59}H$-Cl exhibited higher luminescence intensity arising from Tb than would be expected based on Tb content, which was attributed to the minimised Tb-Tb quenching and additional energy transfer from Gd to Tb.

Based on these results, a lead formulation ($LGd_{1.41}Tb_{0.59}H$-Cl) was selected for photodynamic and photothermal capacity testing in **Chapter 5**. A near-infrared laser assembly was first designed, constructed, and tested to facilitate these experiments. The lead LRH formulation, $LGd_{1.41}Tb_{0.59}H$, was loaded with known PTT/PDT dye indocyanine green (ICG), and isophthalic acid (IPA) which has recently been reported to act as an efficient PDT agent when intercalated into a structurally similar LDH system.[1] The measurement of photothermal response in this work was unfortunately not successful, due to a combination of experimental equipment factors. However, the photodynamic response measurements resulted in some promising findings. Though the $LGd_{1.41}Tb_{0.59}$-IPA intercalate did not exhibit any photodynamic activity, $LGd_{1.41}Tb_{0.59}$-ICG exhibited greatly enhanced ROS generation efficiency relative to free ICG – an 8-fold improvement in DPBF deactivation compared to the equivalent free IGC concentration.

Additionally, it was found that the loading of ICG onto the LRH matrix does not proceed *via* ion-exchange, and the resulting LRH-ICG composite retains its ion-exchange capacity; therefore, this system may be able to carry a drug load in addition to high photodynamic activity and bimodal imaging capacity.

Overall, the work presented in this thesis contributes to the body of knowledge regarding LRH materials for potential biomedical applications, an area which holds great promise but has thus far not been addressed in depth. This work serves as an introductory exploration into the theranostic facets of several LRH systems – their cytocompatibility, capacity for morphological control, drug loading and release properties, as well as their potential for acting as imaging contrast agents and facilitating phototherapy.

6.2 Future work

Firstly, and perhaps most importantly, the cytocompatibility of LRH systems should be investigated more thoroughly. It was found in the work presented here that the HEK 293 cell line (used as a healthy cell model) was more sensitive to the presence of LRH materials than the cancerous Caco-2 cell line. Therefore, it would be of interest to investigate how LRH materials (without additional pharmaceutically active ingredients) may affect the viability and proliferation in other human cell lines (particularly healthy cells). Additionally, such studies would help to ascertain the local concentration level at which LRH particles begin to exhibit cytotoxicity, which would be essential knowledge for further development of LRH materials as potential theranostic agents. Confocal imaging studies of LRH-treated cells should also be conducted to understand the LRH particle uptake behaviour and how it may differ depending on LRH composition and particle morphology. Further down the line, it would also be necessary to conduct

studies to investigate the ultimate fate and safety of LRH particles *in vivo*, and whether metabolic elimination results in LRH dissolution (and therefore release of potentially toxic free Ln^{3+} ions), if there is any bioaccumulation, or if LRH particles are excreted intact.

Secondly, further intercalation studies could be undertaken to better understand the nature of LRH matrix interaction with guest molecules. Ostensibly, there may be readily accessible, small molecule moieties which when intercalated into LRH matrices may exhibit strong photothermal or photodynamic effects. Studies should also be conducted using LRH materials loaded with anti-cancer drugs (for example, methotrexate or doxorubicin) instead of model drugs. It would also be of interest to investigate if targeting moieties (antibodies or small molecules) could be functionalised onto the surface of LRH materials, to facilitate better selectivity towards cancerous cells (and presumably mitigate against off-target toxicity towards healthy cells). Such surface functionalisation would enable the LRH particles to retain their ability to carry a chemotherapeutic drug load *via* intercalation. Furthermore, studies on the use of polymer coatings to modulate drug release behaviour from LRH matrices would be beneficial, as they would enable the development of sustained-release formulations and potentially expand the use of LRH theranostic systems beyond cancer therapy. Additionally, investigating enteric coatings to protect LRH formulations from the acidic stomach environment may enable their delivery *via* the oral route, which is currently precluded due to the instability of LRH materials under acidic conditions. Such formulations may be useful for the image-guided treatment of localised gastrointestinal diseases such as cancer, Crohn's disease, or ulcerative colitis, though oral delivery of LRH formulations is unlikely to be effective as a systemic treatment.

Thirdly, there is scope to improve the imaging contrast abilities of LRH materials. The luminescence properties of the other rare-earth elements as part of LRH systems should be investigated in more detail. For instance, LRHs comprising one or more strongly luminescent rare-earth elements may enable multi-channel luminescent imaging or exhibit synergistic effects that further enhance the viability of LRH materials as biomedically relevant luminescent probes. Strategies to improve MRI relaxivity, such as delamination of bulk LRH materials to improve water access, could also be investigated. Delamination may also be a strategy to further enhance the photodynamic capabilities of LRH-ICG materials, as ICG presumably grafts onto the LRH *via* surface adsorption, and delamination would expose more surface area available for adsorption.

The laser apparatus presented in this work could be further configured to enable more thorough photo-therapy characterisations. The photothermal activity of LRH materials (and LRH-photosensitiser intercalates) could be investigated with the use of a thermal camera. Additionally, if the laser equipment were to be configured to enable *in vitro* studies, the photothermal/photodynamic response could be quantified in terms of the resultant cytotoxic effect, rather than indirectly *via* assay methods or temperature measurements.

Overall, LRH systems show great promise as potential theranostic agents. There is limitless scope for fine-tuning LRH performance, from their inherent properties such as composition, luminescence and magnetism, through to their diverse intercalation chemistry and potential surface functionalisation or incorporation into composite materials. Though research interest into LRH materials for biomedical applications is only beginning to gather momentum, it is certain that the potential benefits and discoveries in this field will be abundant in the coming years, leading to exciting new possibilities in the realm of personalised medicine.

7 References

1. Gao, R., Mei, X., Yan, D., Liang, R. & Wei, M. Nano-photosensitizer based on layered double hydroxide and isophthalic acid for singlet oxygenation and photodynamic therapy. *Nat. Commun.* **9**, 2798 (2018).

2. Usman, M. S., Hussein, M. Z., Fakurazi, S., Fikri, F. & Saad, A. Gadolinium-based layered double hydroxide and graphene oxide nano-carriers for magnetic resonance imaging and drug delivery. *Chem. Cent. J.* **11**, 47 (2017).

3. Liu, Y. *et al.* Gold nanorods/mesoporous silica-based nanocomposite as theranostic agents for targeting near-infrared imaging and photothermal therapy induced with laser. *Int. J. Nanomedicine* **10**, 4747–4761 (2015).

4. Cheng, L. *et al.* Multifunctional nanoparticles for upconversion luminescence/MR multimodal imaging and magnetically targeted photothermal therapy. *Biomaterials* **33**, 2215–2222 (2012).

5. Wang, T., Vineberg, J. G., Honda, T. & Ojima, I. Design and synthesis of tumor-targeting theranostic drug conjugates for SPECT and PET imaging studies. *Bioorg. Chem.* **76**, 458–467 (2018).

6. Huang, X., El-Sayed, I. H., Qian, W. & El-Sayed, M. A. Cancer cell imaging and photothermal therapy in the near-infrared region by using gold nanorods. *J. Am. Chem. Soc.* **128**, 2115–2120 (2006).

7. Duman, F. D. *et al. Biomedical Applications of Inorganic Materials*. (Royal Society of Chemistry, 2021). doi:https://doi.org/10.1039/9781788019293-00014

8. Parkin, D. M., Bray, F., Ferlay, J. & Pisani, P. Estimating the world cancer burden: Globocan 2000. *Int. J. Cancer* **94**, 153–156 (2001).

9. Ferlay, J. *et al.* Estimating the global cancer incidence and mortality in 2018: GLOBOCAN sources and methods. *Int. J. Cancer* **144**, 1941 (2019).

10. Tomasetti, C. & Vogelstein, B. Variation in cancer risk among tissues can be explained by the number of stem cell divisions. *Science* **347**, 78–81 (2015).

11. zur Hausen, H. Papillomaviruses and cancer: from basic studies to clinical application. *Nat. Rev. Cancer* **2**, 342–350 (2002).

12. Kolonel, L. N., Altshuler, D. & Henderson, B. E. The multiethnic cohort study: exploring genes, lifestyle and cancer risk. *Nat. Rev. Cancer* **4**, 519–527 (2004).

13. Weber, G. F., Lett, G. S. & Haubein, N. C. Osteopontin is a marker for cancer aggressiveness and patient survival. *Br. J. Cancer* **103**, 861 (2010).

14. Soldati, L. *et al.* The influence of diet on anti-cancer immune responsiveness. *J. Transl. Med.* **16**, 1–18 (2018).

15. Mahvi, D. A., Liu, R., Grinstaff, M. W., Colson, Y. L. & Raut, C. P. Local Cancer Recurrence: The Realities, Challenges, and Opportunities for New Therapies. *CA. Cancer J. Clin.* **68**, 488–505 (2018).

16. Cuccurullo, V. & Mansi, L. AJCC Cancer Staging Handbook: from the AJCC Cancer Staging Manual (7th edition). *Eur. J. Nucl. Med. Mol. Imaging* **38**, 408–408 (2011).

17. Gangadhar, T. C. & Vonderheide, R. H. Mitigating the toxic effects of anticancer immunotherapy. *Nat. Rev. Clin. Oncol.* **11**, 91–99 (2014).

18. Dy, G. K. & Adjei, A. A. Understanding, recognizing, and managing toxicities of targeted anticancer therapies. *CA. Cancer J. Clin.* **63**, 249–279 (2013).

19. Coffman, A., Torgeson, A. & Lloyd, S. Correlates of Refusal of Surgery in the Treatment of Non-metastatic Pancreatic Adenocarcinoma. *Ann. Surg. Oncol.* **26**, 98–108 (2019).

20. Richardson, J. L., Marks, G. & Levine, A. The influence of symptoms of disease and side effects of treatment on compliance with cancer therapy. *J. Clin. Oncol.* **6**, 1746–1752 (1988).

21. Mohanty, C., Das, M. & Sahoo, S. K. Emerging role of nanocarriers to increase the solubility and bioavailability of curcumin. *Expert Opin. Drug Deliv.* **9**, 1347–64 (2012).

22. Bilia, A. R., Isacchi, B., Righeschi, C., Guccione, C. & Bergonzi, M. C.

Flavonoids Loaded in Nanocarriers: An Opportunity to Increase Oral Bioavailability and Bioefficacy. *Food Nutr. Sci.* **2014**, 1212–1327 (2014).

23. Luzuriaga, M. A. *et al.* Enhanced Stability and Controlled Delivery of MOF-Encapsulated Vaccines and Their Immunogenic Response in Vivo. *ACS Appl. Mater. Interfaces* **11**, 9740–9746 (2019).

24. Van Vlerken, L. E., Vyas, T. K. & Amiji, M. M. Poly(ethylene glycol)-modified nanocarriers for tumor-targeted and intracellular delivery. *Pharm. Res.* **24**, 1405–1414 (2007).

25. Xiao, M. *et al.* Programming Drug Delivery Kinetics for Active Burst Release with DNA Toehold Switches. *J. Am. Chem. Soc.* **141**, 20354–20364 (2019).

26. Natarajan, J. V. *et al.* Sustained drug release in nanomedicine: A long-acting nanocarrier-based formulation for glaucoma. *ACS Nano* **8**, 419–429 (2014).

27. Al_Bayati, A. M. K., Munef, R. A. & Al_Haddad, R. M. S. Shape and Size Effect of Surface Plasmons on Gold Nanoparticles. *Syst. Rev. Pharm.* **11**, 507–514 (2020).

28. Farokhi, M., Mottaghitalab, F., Saeb, M. R. & Thomas, S. Functionalized theranostic nanocarriers with bio-inspired polydopamine for tumor imaging and chemo-photothermal therapy. *J. Control. Release* **309**, 203–219 (2019).

29. Xie, Z. *et al.* Black phosphorus analogue tin sulfide nanosheets: Synthesis and application as near-infrared photothermal agents and drug delivery platforms for cancer therapy. *J. Mater. Chem. B* **6**, 4747 (2018).

30. Liu, Z. *et al.* 2D Superparamagnetic Tantalum Carbide Composite MXenes for Efficient Breast-Cancer Theranostics. *Theranostics* **8**, 1648–1664 (2018).

31. Ma, R. *et al.* Indocyanine Green-Based Theranostic Nanoplatform for NIR Fluorescence Image-Guided Chemo/Photothermal Therapy of Cervical Cancer. *Int. J. Nanomedicine* **16**, 4847 (2021).

32. Bai, J., Jia, X., Ruan, Y., Wang, C. & Jiang, X. Photosensitizer-Conjugated Bi2Te3 Nanosheets as Theranostic Agent for Synergistic Photothermal and

Photodynamic Therapy. *Inorg. Chem.* **57**, 10180–10188 (2018).

33. Juarranz, Á., Jaén, P., Sanz-Rodríguez, F., Cuevas, J. & González, S. Photodynamic therapy of cancer. Basic principles and applications. *Clin. Transl. Oncol.* **10**, 148–154 (2008).

34. Allison, R. R. *et al.* Photosensitizers in clinical PDT. *Photodiagnosis Photodyn. Ther.* **1**, 27–42 (2004).

35. Zhang, H. *et al.* Self-assembled minimalist multifunctional theranostic nanoplatform for magnetic resonance imaging-guided tumor photodynamic therapy. *ACS Nano* **12**, 8266–8276 (2018).

36. Tian, G. *et al.* Engineered design of theranostic upconversion nanoparticles for tri-modal upconversion luminescence/magnetic resonance/X-ray computed tomography imaging and targeted delivery of combined anticancer drugs. *J. Mater. Chem. B* **2**, 1379–1389 (2014).

37. Haque, A., Faizi, M. S. H., Rather, J. A. & Khan, M. S. Next generation NIR fluorophores for tumor imaging and fluorescence-guided surgery: A review. *Bioorg. Med. Chem.* **25**, 2017–2034 (2017).

38. Yi, X., Wang, F., Qin, W., Yang, X. & Yuan, J. Near-infrared fluorescent probes in cancer imaging and therapy: an emerging field. *Int. J. Nanomedicine* **9**, 1347 (2014).

39. Quan, B., Choi, K., Kim, Y.-H., Kang, K. W. & Chung, D. S. Near infrared dye indocyanine green doped silica nanoparticles for biological imaging. *Talanta* **99**, 387–93 (2012).

40. Wang, J.-H. *et al.* Bimodal optical diagnostics of oral cancer based on Rose Bengal conjugated gold nanorod platform. *Biomaterials* **34**, 4274–4283 (2013).

41. Chen, H. *et al.* Characterization of a fluorescence probe based on gold nanoclusters for cell and animal imaging. *Nanotechnology* **24**, 055704 (2013).

42. Gareth, E. D. *et al.* MRI breast screening in high-risk women: Cancer detection and survival analysis. *Breast Cancer Res. Treat.* **145**, 663–672 (2014).

43. van Zijl, P. C. *et al.* Quantitative assessment of blood flow, blood volume and blood oxygenation effects in functional magnetic resonance imaging. *Duodecim.* **114**, 808–809 (1998).

44. Krohn, S. *et al.* Real-time MRI of the temporomandibular joint at 15 frames per second—A feasibility study. *Eur. J. Radiol.* **85**, 2225 (2016).

45. Hu, H. H., Li, Y., Nagy, T. R., Goran, M. I. & Nayak, K. S. Quantification of Absolute Fat Mass by Magnetic Resonance Imaging: a Validation Study against Chemical Analysis. *Int. J. Body Compos. Res.* **9**, 111–122 (2011).

46. T.S., S. K., Kalidoss, M., Y, R. & Doble, M. Theranostic calcium phosphate nanoparticles with potential for multimodal imaging and drug delivery. *Front. Bioeng. Biotechnol.* **7**, 126 (2019).

47. Ramalho, J. *et al.* Gadolinium-Based Contrast Agent Accumulation and Toxicity: An Update. *Am. J. Neuroradiol.* **37**, 1192–1198 (2016).

48. Huang, X. *et al.* pH-responsive theranostic nanocomposites as synergistically enhancing positive and negative magnetic resonance imaging contrast agents. *J. Nanobiotechnology* **16**, 1–12 (2018).

49. Beeran, A. E. *et al.* Multifunctional nano manganese ferrite ferrofluid for efficient theranostic application. *Colloids Surfaces B Biointerfaces* **136**, 1089–1097 (2015).

50. Foster, A. *et al.* Novel theranostic agent for PET imaging and targeted radiopharmaceutical therapy of tumour-infiltrating immune cells in glioma. *eBioMedicine* **71**, 103571 (2021).

51. Shi, J. *et al.* Transforming a Targeted Porphyrin Theranostic Agent into a PET Imaging Probe for Cancer. *Theranostics* **1**, 363–370 (2011).

52. Polyak, A. & Ross, T. L. Nanoparticles for SPECT and PET Imaging: Towards Personalized Medicine and Theranostics. *Curr. Med. Chem.* **25**, 4328–4353 (2018).

53. Moeendarbari, S. *et al.* Theranostic Nanoseeds for Efficacious Internal Radiation Therapy of Unresectable Solid Tumors. *Sci. Rep.* **6**, (2016).

54. Song, Z. *et al.* Decorated ultrathin bismuth selenide nanosheets as

targeted theranostic agents for in vivo imaging guided cancer radiation therapy. *NPG Asia Mater.* **9**, e439–e439 (2017).

55. Li, L., Lin, H., Li, D., Zeng, Y. & Liu, G. Ultrasound activated nanosensitizers for sonodynamic therapy and theranostics. *Biomed. Mater.* **16**, 022008 (2021).

56. Liu, X. *et al.* Iron-Based Theranostic Nanoplatform for Improving Chemodynamic Therapy of Cancer. *ACS Biomater. Sci. Eng.* **6**, 4834–4845 (2020).

57. Wang, X., Zhong, X., Liu, Z. & Cheng, L. Recent progress of chemodynamic therapy-induced combination cancer therapy. *Nano Today* **35**, 100946 (2020).

58. Wu, Y.-F. *et al.* Multi-functionalized carbon dots as theranostic nanoagent for gene delivery in lung cancer therapy. *Sci. Rep.* **6**, 21170 (2016).

59. Andersen, V. L. *et al.* A self-assembled, modular nucleic acid-based nanoscaffold for multivalent theranostic medicine. *Theranostics* **9**, 2662 (2019).

60. Li, T. *et al.* Photo-Fenton-like Metal–Protein Self-Assemblies as Multifunctional Tumor Theranostic Agent. *Adv. Healthc. Mater.* **8**, 1900192 (2019).

61. Ye, Y. *et al.* Synergistic Transcutaneous Immunotherapy Enhances Antitumor Immune Responses through Delivery of Checkpoint Inhibitors. *ACS Nano* **10**, 8956–8963 (2016).

62. Knipe, J. M., Peters, J. T. & Peppas, N. A. Theranostic agents for intracellular gene delivery with spatiotemporal imaging. *Nano Today* **8**, 21–38 (2013).

63. Peng, T. *et al.* Functional nucleic acids for cancer theranostics. *Coord. Chem. Rev.* **403**, (2020).

64. Li, Y. *et al.* Gram-scale synthesis of highly biocompatible and intravenous injectable hafnium oxide nanocrystal with enhanced radiotherapy efficacy for cancer theranostic. *Biomaterials* **226**, 119538 (2020).

65. Wyszogrodzka-Gaweł, G. *et al.* An Inhalable Theranostic System for Local Tuberculosis Treatment Containing an Isoniazid Loaded Metal Organic Framework Fe-MIL-101-NH2—From Raw MOF to Drug Delivery System. *Pharmaceutics* **11**, 687 (2019).

66. Ramachandran, R. *et al.* Theranostic 3-Dimensional nano brain-implant for prolonged and localized treatment of recurrent glioma. *Sci. Rep.* **7**, 43271 (2017).

67. Zhang, Z. *et al.* Polydopamine-coated nanocomposite theranostic implants for localized chemotherapy and MRI imaging. *Int. J. Pharm.* **615**, 121493 (2022).

68. Yang, B., Lin, H., Dai, C., Chen, Y. & Shi, J. “Stepwise Extraction” strategy-based injectable bioresponsive composite implant for cancer theranostics. *Biomaterials* **166**, 38–51 (2018).

69. Demchenko, A. P. Photobleaching of organic fluorophores: quantitative characterization, mechanisms, protection*. *Methods Appl. Fluoresc.* **8**, 022001 (2020).

70. Knights, O. & McLaughlan, J. Gold Nanorods for Light-Based Lung Cancer Theranostics. *Int. J. Mol. Sci.* **19**, 3318 (2018).

71. Liu, B. *et al.* 808-nm-Light-Excited Lanthanide-Doped Nanoparticles: Rational Design, Luminescence Control and Theranostic Applications. *Adv. Mater.* **29**, 1605434 (2017).

72. Bourne, G. W. & Trifaró, J. M. The gadolinium ion: A potent blocker of calcium channels and catecholamine release from cultured chromaffin cells. *Neuroscience* **7**, 1615–1622 (1982).

73. Zhou, H. *et al.* Biodegradable Inorganic Nanoparticles for Cancer Theranostics: Insights into the Degradation Behavior. *Bioconjug. Chem.* **31**, 315–331 (2020).

74. McKinney, R. W., Gorai, P., Manna, S., Toberer, E. & Stevanović, V. Ionic: Vs. van der Waals layered materials: Identification and comparison of elastic anisotropy. *J. Mater. Chem. A* **6**, 15828–15838 (2018).

75. Fejér, I., Kata, M., Erös, I., Berkesi, O. & Dékány, I. Release of cationic

drugs from loaded clay minerals. *Colloid Polym. Sci.* **279**, 1177–1182 (2001).

76. Joshi, G. V., Kevadiya, B. D., Patel, H. A., Bajaj, H. C. & Jasra, R. V. Montmorillonite as a drug delivery system: Intercalation and in vitro release of timolol maleate. *Int. J. Pharm.* **374**, 53–57 (2009).

77. Aguzzi, C. *et al.* Intercalation of tetracycline into layered clay mineral material for drug delivery purposes. *Mater. Technol.* **29**, B96–B99 (2014).

78. Ghidiu, M. *et al.* Alkylammonium Cation Intercalation into Ti3C2 (MXene): Effects on Properties and Ion-Exchange Capacity Estimation. *Chem. Mater.* **29**, 1099–1106 (2017).

79. Díaz, A. *et al.* Zirconium phosphate nano-platelets: A novel platform for drug delivery in cancer therapy. *Chem. Commun.* **48**, 1754–1756 (2012).

80. Lin, D., Zhang, Y. & Zhou, B. pH-responsive drug delivery system based on AIE luminogen functionalized layered zirconium phosphate nano-platelets. *J. Solid State Chem.* **225**, 427–430 (2015).

81. Manos, M. J., Malliakas, C. D. & Kanatzidis, M. G. Heavy-Metal-Ion Capture, Ion-Exchange, and Exceptional Acid Stability of the Open-Framework Chalcogenide $(NH_4)_4In_{12}Se_{20}$. *Chem. - A Eur. J.* **13**, 51–58 (2007).

82. Li, B., He, J., Evans, D. G. & Duan, X. Inorganic layered double hydroxides as a drug delivery system - Intercalation and in vitro release of fenbufen. *Appl. Clay Sci.* **27**, 199–207 (2004).

83. Wang, L. *et al.* A Gd-doped Mg-Al-LDH/Au nanocomposite for CT/MR bimodal imagings and simultaneous drug delivery. *Biomaterials* **34**, 3390–3401 (2013).

84. Figueiredo, M. P. *et al.* Iron-Based Layered Double Hydroxide Implants: Potential Drug Delivery Carriers with Tissue Biointegration Promotion and Blood Microcirculation Preservation. *ACS Omega* **3**, 18263–18274 (2018).

85. Ryu, S. J., Jung, H., Oh, J. M., Lee, J. K. & Choy, J. H. Layered double hydroxide as novel antibacterial drug delivery system. *J. Phys. Chem. Solids* **71**, 685–688 (2010).

86. Choi, S. J., Oh, J. M. & Choy, J. H. Anticancer drug-layered hydroxide nanohybrids as potent cancer chemotherapy agents. *J. Phys. Chem. Solids* **69**, 1528–1532 (2008).

87. Xu, Y. *et al.* Layered gadolinium hydroxides for simultaneous drug delivery and imaging. *Dalt. Trans.* **47**, 3166 (2018).

88. Ju, R. & Gu, Q. Biohybrid based on layered terbium hydroxide and applications as drug carrier and biological fluorescence probe. *Appl. Organomet. Chem.* **32**, e3926 (2018).

89. Kaassis, A. Y. A. A., Wei, M. & Williams, G. R. New biocompatible hydroxy double salts and their drug delivery properties. *J. Mater. Chem. B* **4**, 5789–5793 (2016).

90. Richardson-Chong, S. S. D., Patel, R. & Williams, G. R. Intercalation and controlled release of bioactive ions using a hydroxy double salt. *Ind. Eng. Chem. Res.* **51**, 2913–2921 (2012).

91. Cheng, H., Liu, Q., Zhang, J., Yang, J. & Frost, R. L. Delamination of kaolinite-potassium acetate intercalates by ball-milling. *J. Colloid Interface Sci.* **348**, 355–359 (2010).

92. Oh, J. The effect of synthetic conditions on tailoring the size of hydrotalcite particles. *Solid State Ionics* **151**, 285–291 (2002).

93. Nava Andrade, K. *et al.* Assembly of folate-carbon dots in GdDy-doped layered double hydroxides for targeted delivery of doxorubicin. *Appl. Clay Sci.* **192**, 105661 (2020).

94. Gunawan, P. & Xu, R. Synthesis of unusual coral-like layered double hydroxide microspheres in a nonaqueous polar solvent/surfactant system. *J. Mater. Chem.* **18**, 2112–2120 (2008).

95. Bekaroğlu, M. G., Nurili, F. & İşçi, S. Montmorillonite as imaging and drug delivery agent for cancer therapy. *Appl. Clay Sci.* **162**, 469–477 (2018).

96. Xu, Z. P. *et al.* Subcellular compartment targeting of layered double hydroxide nanoparticles. *J. Control. Release* **130**, 86–94 (2008).

97. Constantino3, V. R. L. & Pinnavaia, T. J. Basic Properties of Mg2+i-jAl3+x

Layered Double Hydroxides Intercalated by Carbonate, Hydroxide, Chloride, and Sulfate Anions. *Inorg. Chem* **34**, 883–892 (1995).

98. Santos, R. M. M., Tronto, J., Briois, V. & Santilli, C. V. Thermal decomposition and recovery properties of ZnAl–CO 3 layered double hydroxide for anionic dye adsorption: insight into the aggregative nucleation and growth mechanism of the LDH memory effect. *J. Mater. Chem. A* **5**, 9998–10009 (2017).

99. Radha, A. V., Vishnu Kamath, P. & Shivakumara, C. Mechanism of the anion exchange reactions of the layered double hydroxides (LDHs) of Ca and Mg with Al. *Solid State Sci.* **7**, 1180–1187 (2005).

100. Zhao, Y., Li, J.-G., Guo, M. & Yang, X. Structural and photoluminescent investigation of LTbH/LEuH nanosheets and their color-tunable colloidal hybrids. *J. Mater. Chem. C* **1**, 3584 (2013).

101. Lee, B. Il, Lee, K. S., Lee, J. H., Lee, I. S. & Byeon, S. H. Synthesis of colloidal aqueous suspensions of a layered gadolinium hydroxide: A potential MRI contrast agent. *Dalt. Trans.* **14**, 2490–2495 (2009).

102. Jung, S. Y., Gwak, G. H., Park, J. K. & Oh, J. M. Finely crafted quasi-core-shell gadolinium/layered double hydroxide hybrids for switching on/off bimodal CT/MRI contrasting nanodiagnostic platforms. *RSC Adv.* **10**, 5838–5844 (2020).

103. Jin, M., Spillane, D. E. M., Geraldes, C. F. G. C., Williams, G. R. & Bligh, S. W. A. Gd(III) complexes intercalated into hydroxy double salts as potential MRI contrast agents. **44**, 20728 (2015).

104. Gándara, F. *et al.* Layered rare-earth hydroxides: A class of pillared crystalline compounds for intercalation chemistry. *Angew. Chemie - Int. Ed.* **45**, 7998–8001 (2006).

105. Wang, Y. *et al.* Multifunctional mesoporous silica-coated graphene nanosheet used for chemo-photothermal synergistic targeted therapy of glioma. *J. Am. Chem. Soc.* **135**, 4799–4804 (2013).

106. Sun, X. *et al.* Nano-Graphene Oxide for Cellular Imaging and Drug Delivery. *Nano Res* **1**, 203–212 (2008).

107. Naguib, M. *et al.* Two-Dimensional Nanocrystals Produced by Exfoliation of Ti3AlC2. *Adv. Mater.* **23**, 4248–4253 (2011).

108. Ghidiu, M. *et al.* Ion-Exchange and Cation Solvation Reactions in Ti 3 C 2 MXene. *Chem. Mater.* **28**, 3507–3514 (2016).

109. Liu, G. *et al.* Surface Modified Ti3C2 MXene Nanosheets for Tumor Targeting Photothermal/Photodynamic/Chemo Synergistic Therapy. *ACS Appl. Mater. Interfaces* **9**, 40077–40086 (2017).

110. Chae, S. H. *et al.* Oxidation effect in octahedral hafnium disulfide thin film. *ACS Nano* **10**, 1309–1316 (2016).

111. Wang, X. *et al.* Chemical vapor deposition of trigonal prismatic NbS2 monolayers and 3R-polytype few-layers. *Nanoscale* **9**, 16607–16611 (2017).

112. Zhang, C. *et al.* Polyphenol-Assisted Exfoliation of Transition Metal Dichalcogenides into Nanosheets as Photothermal Nanocarriers for Enhanced Antibiofilm Activity. *ACS Nano* **12**, 12347–12356 (2018).

113. Liu, T. *et al.* Combined photothermal and photodynamic therapy delivered by PEGylated MoS2nanosheets. *Nanoscale* **6**, 11219–11225 (2014).

114. Qian, X., Shen, S., Liu, T., Cheng, L. & Liu, Z. Two-dimensional TiS2 nanosheets for in vivo photoacoustic imaging and photothermal cancer therapy. *Nanoscale* **7**, 6380–6387 (2015).

115. Wan, C. *et al.* Flexible n-type thermoelectric materials by organic intercalation of layered transition metal dichalcogenide TiS 2. *Nat. Mater.* **14**, 622–627 (2015).

116. Crepaldi, E. L., Pavan, P. C. & Valim, J. B. Comparative Study of the Coprecipitation Methods for the Preparation of Layered Double Hydroxides. *J. Braz. Chem. Soc.* **11**, 64–70 (2000).

117. Zhi, P. X. & Guo, Q. L. Hydrothermal synthesis of layered double hydroxides (LDHs) from mixed MgO and Al2O3: LDH formation mechanism. *Chem. Mater.* **17**, 1055–1062 (2005).

118. Zhang, F., Du, N., Song, S., Liu, J. & Hou, W. Mechano-hydrothermal

synthesis of Mg2Al-NO3 layered double hydroxides. *J. Solid State Chem.* **206**, 45–50 (2013).

119. Liang, H. *et al.* Hydrothermal continuous flow synthesis and exfoliation of NiCo layered double hydroxide nanosheets for enhanced oxygen evolution catalysis. *Nano Lett* **15**, 1421–1427 (2015).

120. Gu, Z., Wu, A., Li, L. & Xu, Z. P. Influence of hydrothermal treatment on physicochemical properties and drug release of anti-inflammatory drugs of intercalated layered double hydroxide nanoparticles. *Pharmaceutics* **6**, 235–248 (2014).

121. Geng, F., Ma, R. & Sasaki, T. Anion-Exchangeable Layered Materials Based on Rare-Earth Phosphors: Unique Combination of Rare-Earth Host and Exchangeable Anions. *Acc. Chem. Res.* **43**, 1177–1185 (2010).

122. Mcintyre, L. J., Jackson, L. K. & Fogg, A. M. Ln2(OH)5NO3·xH2O (Ln = Y, Gd-Lu): A Novel Family of Anion Exchange Intercalation Hosts. *Chem. Mater.* **20**, 335–340 (2008).

123. Gu, Q., Chen, W., Duan, F. & Ju, R. Fabrication of a nano-drug delivery system based on layered rare-earth hydroxides integrating drug-loading and fluorescence properties. *Dalt. Trans.* **45**, 12137–12143 (2016).

124. Kannan, S., Vinitha, P., Mohanraj, K. & Sivakumar, G. Antibacterial studies of novel Cu2WS4 ternary chalcogenide synthesized by hydrothermal process. *J. Solid State Chem.* **258**, 376–382 (2018).

125. Miao, J., Xue, M., Itoh, H. & Feng, Q. Hydrothermal synthesis of layered hydroxide zinc benzoate compounds and their exfoliation reactions. *J. Mater. Chem.* **16**, 474–480 (2006).

126. Cai, X. *et al.* Solvothermal synthesis of NiCo-layered double hydroxide nanosheets decorated on RGO sheets for high performance supercapacitor. *Chem. Eng. J.* **268**, 251–259 (2015).

127. Lee, J., Rhee, S. & Jung, D.-Y. Orientation-controlled assembly and solvothermal ion-exchange of layered double hydroxide nanocrystals. *Chem. Commun.* **21**, 2740 (2003).

128. Higashi, K., Watanabe, Y., Iso, Y. & Isobe, T. Synthesis of Y2O3:Bi3+,Yb3+

nanosheets from layered yttrium hydroxide precursor and their photoluminescence properties. *RSC Adv.* **7**, 6671–6678 (2017).

129. Song, J. *et al.* Solvothermal growth of bismuth chalcogenide nanoplatelets by the oriented attachment mechanism: An in situ PXRD study. *Chem. Mater.* **27**, 3471–3482 (2015).

130. Deng, Y. P. *et al.* Layered/spinel heterostructured Li-rich materials synthesized by a one-step solvothermal strategy with enhanced electrochemical performance for Li-ion batteries. *J. Mater. Chem. A* **4**, 257–263 (2015).

131. Rabenau, A. The Role of Hydrothermal Synthesis in Preparative Chemistry. *Angew. Chemie Int. Ed. English* **24**, 1026–1040 (1985).

132. Anandan, S., Wu, J. J. & Ashokkumar, M. Sonochemical Synthesis of Layered Copper Hydroxy Nitrate Nanosheets. *ChemPhysChem* **16**, 3389–3391 (2015).

133. Jeevanandam, P., Koltypin, Y. & Gedanken, A. Preparation of nanosized nickel aluminate spinel by a sonochemical method. *Mater. Sci. Eng. B Solid-State Mater. Adv. Technol.* **90**, 125–132 (2002).

134. Bharali, D. & Deka, R. C. Adsorptive removal of congo red from aqueous solution by sonochemically synthesized NiAl layered double hydroxide. *J. Environ. Chem. Eng.* **5**, 2056–2067 (2017).

135. Darvishi, Z. & Morsali, A. Synthesis and characterization of Nano-bentonite by sonochemical method. *Ultrason. Sonochem.* **18**, 238–242 (2011).

136. Chen, H., Hu, L., Chen, M., Yan, Y. & Wu, L. Nickel-cobalt layered double hydroxide nanosheets for high-performance supercapacitor electrode materials. *Adv. Funct. Mater.* **24**, 934–942 (2014).

137. Qu, J. *et al.* Synthesis of Li-Al layered double hydroxides via a mechanochemical route. *Appl. Clay Sci.* **120**, 24–27 (2016).

138. Tongamp, W., Zhang, Q. & Saito, F. Mechanochemical route for synthesizing nitrate form of layered double hydroxide. *Powder Technol.* **185**, 43–48 (2008).

139. Iwasaki, T., Yoshii, H., Nakamura, H. & Watano, S. Simple and rapid synthesis of Ni-Fe layered double hydroxide by a new mechanochemical method. *Appl. Clay Sci.* **58**, 120–124 (2012).

140. Thomas, N. Mechanochemical synthesis of layered hydroxy salts. *Mater. Res. Bull.* **47**, 3568–3572 (2012).

141. Yang, W., Li, Q., Zheng, X., Li, X. & Li, X. Luminescent sensing film based on sulfosalicylic acid modified Tb(III)-doped yttrium hydroxide nanosheets. *J. Adv. Ceram.* **7**, 352–361 (2018).

142. Li, H. *et al.* Mechanical Exfoliation and Characterization of Single- and Few-Layer Nanosheets of WSe_2, TaS_2, and $TaSe_2$. *Small* **9**, 1974–1981 (2013).

143. Warner, J. H., Rümmeli, M. H., Bachmatiuk, A. & Büchner, B. Atomic resolution imaging and topography of boron nitride sheets produced by chemical exfoliation. *ACS Nano* **4**, 1299–1304 (2010).

144. Zhang, L. *et al.* Size-controlled synthesis of graphene oxide sheets on a large scale using chemical exfoliation. *Carbon* **47**, 3365–3368 (2009).

145. Allen, M. R. *et al.* Evolution of physical and photocatalytic properties in the layered titanates A2Ti4O9 (A = K, H) and in nanosheets derived by chemical exfoliation. *Chem. Mater.* **22**, 1220–1228 (2010).

146. Li, J. G. *et al.* Two-step crystallization of a phase-pure Ln2(OH)5NO3·nH2O layered compound for the smallest Ln ions of Tm, Yb and Lu, anion exchange, and exfoliation. *Dalt. Trans.* **46**, 12683–12691 (2017).

147. Ge, W., Kawahara, K., Tsuji, M. & Ago, H. Large-scale synthesis of NbS2 nanosheets with controlled orientation on graphene by ambient pressure CVD. *Nanoscale* **5**, 5773–5778 (2013).

148. Wang, K. K., Wang, F. X., Liu, Y. D. & Pan, G. B. Vapor growth and photoconductive property of single-crystalline MoO 3 nanosheets. *Mater. Lett.* **102**–**103**, 8–11 (2013).

149. Qiao, C. *et al.* One-step synthesis of zinc-cobalt layered double hydroxide (Zn-Co-LDH) nanosheets for high-efficiency oxygen evolution reaction. *J.*

Mater. Chem. A **3**, 6878–6883 (2015).

150. Yu, J., Martin, B. R., Clearfield, A., Luo, Z. & Sun, L. One-step direct synthesis of layered double hydroxide single-layer nanosheets. *Nanoscale* **7**, 9448–9451 (2015).

151. Oyler, K. D., Ke, X., Sines, I. T., Schiffer, P. & Schaak, R. E. Chemical synthesis of two-dimensional iron chalcogenide nanosheets: FeSe, FeTe, Fe(Se,Te), and FeTe2. *Chem. Mater.* **21**, 3655–3661 (2009).

152. Han, X., Kuang, Q., Jin, M., Xie, Z. & Zheng, L. Synthesis of titania nanosheets with a high percentage of exposed (001) facets and related photocatalytic properties. *J. Am. Chem. Soc.* **131**, 3152–3153 (2009).

153. Barahuie, F., Hussein, M. Z., Arulselvan, P., Fakurazi, S. & Zainal, Z. Drug delivery system for an anticancer agent, chlorogenate-Zn/Al-layered double hydroxide nanohybrid synthesised using direct co-precipitation and ion exchange methods. *J. Solid State Chem.* **217**, 31–41 (2014).

154. Aisawa, S., Takahashi, S., Ogasawara, W., Umetsu, Y. & Narita, E. Direct intercalation of amino acids into layered double hydroxides by coprecipitation. *J. Solid State Chem.* **162**, 52–62 (2001).

155. Monteforte, F. *et al.* Meloxicam-LDH hybrid compound: A successful strategy to improve solubility. *J. Inorg. Organomet. Polym. Mater.* **30**, 637–648 (2020).

156. Geng, F. *et al.* New Layered Rare-Earth Hydroxides with Anion-Exchange Properties. *Chem. - A Eur. J.* **14**, 9255–9260 (2008).

157. Nakayama, H., Wada, N. & Tsuhako, M. Intercalation of amino acids and peptides into Mg–Al layered double hydroxide by reconstruction method. *Int. J. Pharm.* **269**, 469–478 (2004).

158. TAJIMA, T., SUZUKI, N., WATANABE, Y. & KANZAKI, Y. Intercalation Compounds of Layered Titanium Phosphate for Drug Delivery Use. *J. Ion Exch.* **14**, 177–180 (2003).

159. Liu, S.-Q., Li, S.-P. & Li, X.-D. Intercalation of methotrexatum into layered double hydroxides via exfoliation-reassembly process. *Appl. Surf. Sci.* **330**, 253–261 (2015).

160. Ansy, K. M., Lee, J.-H., Piao, H., Choi, G. & Choy, J.-H. Stabilization of antioxidant gallate in layered double hydroxide by exfoliation and reassembling reaction. *Solid State Sci.* **80**, 65–71 (2018).

161. Paek, S. M. *et al.* Exfoliation and reassembling route to mesoporous titania nanohybrids. *Chem. Mater.* **18**, 1134–1140 (2006).

162. Kamada, K., Tsukahara, S. & Soh, N. Magnetically applicable layered iron-titanate intercalated with biomolecules. *J. Mater. Chem.* **20**, 5646 (2010).

163. Choi, S. J., Oh, J. M. & Choy, J. H. Toxicological effects of inorganic nanoparticles on human lung cancer A549 cells. *J. Inorg. Biochem.* **103**, 463–471 (2009).

164. Saifullah, B. *et al.* Development of a biocompatible nanodelivery system for tuberculosis drugs based on isoniazid-Mg/Al layered double hydroxide. *Int. J. Nanomedicine* **9**, 4749–4762 (2014).

165. Saifullah, B. *et al.* Antimycobacterial, antimicrobial, and biocompatibility properties of para-aminosalicylic acid with zinc layered hydroxide and Zn/Al layered double hydroxide nanocomposites. *Drug Des. Devel. Ther.* **8**, 1029–1036 (2014).

166. Wu, Y. *et al.* Layered double hydroxide nanoparticles promote self-renewal of mouse embryonic stem cells through the PI3K signaling pathway. *Nanoscale* **7**, 11102–11114 (2015).

167. Barik, S., Khandual, A., Behera, L., Badamali, S. K. & Luximon, A. Nano-Mg–Al-layered double hydroxide application to cotton for enhancing mechanical, UV protection and flame retardancy at low cytotoxicity level. *Cellulose* **24**, 1107–1120 (2017).

168. Wei Su, L., Lin, D. J. & Yen Uan, J. Novel dental resin composites containing LiAl-F layered double hydroxide (LDH) filler: Fluoride release/recharge, mechanical properties, color change, and cytotoxicity. *Dent. Mater.* **35**, 663–672 (2019).

169. Gu, Z. *et al.* Layered double hydroxide nanoparticles: Impact on vascular cells, blood cells and the complement system. *J. Colloid Interface Sci.* **512**, 404–410 (2018).

170. Cunha, V. R. R., De Souza, R. B., Da Fonseca Martins, A. M. C. R. P., Koh, I. H. J. & Constantino, V. R. L. Accessing the biocompatibility of layered double hydroxide by intramuscular implantation: Histological and microcirculation evaluation. *Sci. Rep.* **6**, 1–10 (2016).

171. Duda, F. *et al.* Highly biocompatible behaviour and slow degradation of a LDH (layered double hydroxide)-coating on implants in the middle ear of rabbits. *J. Mater. Sci. Mater. Med.* **26**, 9 (2015).

172. Perioli, L., Nocchetti, M., Giannelli, P., Pagano, C. & Bastianini, M. Hydrotalcite composites for an effective fluoride buccal administration: A new technological approach. *Int. J. Pharm.* **454**, 259–268 (2013).

173. Shafik, H. M., Ayoub, S. M., Ebeid, N. H. & Someda, H. H. New adjuvant design using layered double hydroxide for production of polyclonal antibodies in radioimmunoassay techniques. *J. Radioanal. Nucl. Chem.* **301**, 81–89 (2014).

174. Wang, J. *et al.* The enhanced immune response of hepatitis B virus DNA vaccine using SiO2@LDH nanoparticles as an adjuvant. *Biomaterials* **35**, 466–478 (2014).

175. Li, A. *et al.* Signalling pathways involved in the activation of dendritic cells by layered double hydroxide nanoparticles. *Biomaterials* **31**, 748–756 (2010).

176. Li, A. *et al.* The use of layered double hydroxides as DNA vaccine delivery vector for enhancement of anti-melanoma immune response. *Biomaterials* **32**, 469–477 (2011).

177. Yan, S. *et al.* The Pathways for Layered Double Hydroxide Nanoparticles to Enhance Antigen (Cross)-Presentation on Immune Cells as Adjuvants for Protein Vaccines. *Front. Pharmacol.* **9**, 1060 (2018).

178. Chen, W. *et al.* Clay Nanoparticles Elicit Long-Term Immune Responses by Forming Biodegradable Depots for Sustained Antigen Stimulation. *Small* **14**, 1704465 (2018).

179. Williams, G. R. *et al.* Immunity induced by a broad class of inorganic crystalline materials is directly controlled by their chemistry. *J. Exp. Med.*

211, 1019–1025 (2014).

180. Yan, S., Gu, W., Zhang, B., Rolfe, B. E. & Xu, Z. P. High adjuvant activity of layered double hydroxide nanoparticles and nanosheets in anti-tumour vaccine formulations. *Dalt. Trans.* **47**, 2956–2964 (2018).

181. Yoon, Y. S. *et al.* Surface modification of exfoliated layered gadolinium hydroxide for the development of multimodal contrast agents for MRI and fluorescence imaging. *Adv. Funct. Mater.* **19**, 3375–3380 (2009).

182. Gu, Q.-Y. *et al.* Nanostructured layered terbium hydroxide containing NASIDs: in vitro physicochemical and biological evaluations. *J. Nanosci. Nanotechnol.* **18**, 5320–5326 (2018).

183. Kaassis, A. Y. A., Al-Jamal, W. T., Strimaite, M., Severic, M. & Williams, G. R. Biocompatible hydroxy double salts as delivery matrices for non-steroidal anti-inflammatory and anti-epileptic drugs. *Appl. Clay Sci.* **221**, 106456 (2022).

184. Baek, M., Lee, J. A. & Choi, S. J. Toxicological effects of a cationic clay, montmorillonite in vitro and in vivo. *Mol. Cell. Toxicol.* **8**, 95–101 (2012).

185. Salcedo, I. *et al.* In vitro biocompatibility and mucoadhesion of montmorillonite chitosan nanocomposite: A new drug delivery. *Appl. Clay Sci.* **55**, 131–137 (2012).

186. Zhuang, H., Zheng, J. P., Gao, H. & De Yao, K. In vitro biodegradation and biocompatibility of gelatin/montmorillonite-chitosan intercalated nanocomposite. *J. Mater. Sci. Mater. Med.* **18**, 951–957 (2007).

187. Liu, X., Duan, G., Li, W., Zhou, Z. & Zhou, R. Membrane destruction-mediated antibacterial activity of tungsten disulfide (WS 2). *RSC Adv.* **7**, 37873–37880 (2017).

188. Yu, Y. *et al.* Dispersible MoS2 Nanosheets Activated TGF-β/Smad Pathway and Perturbed the Metabolome of Human Dermal Fibroblasts. *ACS Biomater. Sci. Eng.* **3**, 3261–3272 (2017).

189. Appel, J. H. *et al.* Low Cytotoxicity and Genotoxicity of Two-Dimensional MoS 2 and WS 2. *ACS Biomater. Sci. Eng.* **2**, 361–367 (2016).

190. Hao, J. *et al.* In Vivo Long-Term Biodistribution, Excretion, and Toxicology of PEGylated Transition-Metal Dichalcogenides MS_2 (M = Mo, W, Ti) Nanosheets. *Adv. Sci.* **4**, 1600160 (2017).

191. Teo, W. Z., Chng, E. L. K., Sofer, Z. & Pumera, M. Cytotoxicity of exfoliated transition-metal dichalcogenides (MoS 2, WS2, and WSe2) is lower than that of graphene and its analogues. *Chem. - A Eur. J.* **20**, 9627–9632 (2014).

192. Huang, X. W. *et al.* Silk fibroin-assisted exfoliation and functionalization of transition metal dichalcogenide nanosheets for antibacterial wound dressings. *Nanoscale* **9**, 17193–17198 (2017).

193. Kurapati, R. *et al.* Enzymatic Biodegradability of Pristine and Functionalized Transition Metal Dichalcogenide MoS_2 Nanosheets. *Adv. Funct. Mater.* **27**, 1605176 (2017).

194. Yang, K. *et al.* Graphene in mice: Ultrahigh in vivo tumor uptake and efficient photothermal therapy. *Nano Lett.* **10**, 3318–3323 (2010).

195. Yang, K. *et al.* In vivo pharmacokinetics, long-term biodistribution, and toxicology of pegylated graphene in mice. *ACS Nano* **5**, 516–522 (2011).

196. Duch, M. C. *et al.* Minimizing oxidation and stable nanoscale dispersion improves the biocompatibility of graphene in the lung. *Nano Lett.* **11**, 5201–5207 (2011).

197. Zhang, X. *et al.* Distribution and biocompatibility studies of graphene oxide in mice after intravenous administration. *Carbon N. Y.* **49**, 986–995 (2011).

198. Chong, Y. *et al.* The in vitro and in vivo toxicity of graphene quantum dots. *Biomaterials* **35**, 5041–5048 (2014).

199. Ren, C., Hu, X. & Zhou, Q. Graphene Oxide Quantum Dots Reduce Oxidative Stress and Inhibit Neurotoxicity In Vitro and In Vivo through Catalase-Like Activity and Metabolic Regulation. *Adv. Sci.* **5**, 1700595 (2018).

200. Wang, F., Yang, C. H., Duan, M., Tang, Y. & Zhu, J. F. TiO2 nanoparticle modified organ-like Ti3C2 MXene nanocomposite encapsulating hemoglobin for a mediator-free biosensor with excellent performances.

Biosens. Bioelectron. **74**, 1022–1028 (2015).

201. Chen, K. *et al.* Strong and biocompatible poly(lactic acid) membrane enhanced by Ti3C2Tz (MXene) nanosheets for Guided bone regeneration. *Mater. Lett.* **229**, 114–117 (2018).

202. Jastrzębska, A. M. *et al.* In vitro studies on cytotoxicity of delaminated Ti3C2 MXene. *J. Hazard. Mater.* **339**, 1–8 (2017).

203. Dai, C. *et al.* Biocompatible 2D Titanium Carbide (MXenes) Composite Nanosheets for pH-Responsive MRI-Guided Tumor Hyperthermia. *Chem. Mater.* **29**, 8637–8652 (2017).

204. Kjellin, P., Vikingsson, L., Danielsson, K., Johansson, P. & Wennerberg, A. A nanosized zirconium phosphate coating for PEEK implants and its effect in vivo. *Materialia* **10**, 100645 (2020).

205. Kurashina, K. *et al.* In vivo study of calcium phosphate cements: Implantation of an α-tricalcium phosphate/dicalcium pbosphate dibasic/tetracalcium phosphate monoxide cement paste. *Biomaterials* **18**, 539–543 (1997).

206. Uzeda, M. J. *et al.* Randomized clinical trial for the biological evaluation of two nanostructured biphasic calcium phosphate biomaterials as a bone substitute. *Clin. Implant Dent. Relat. Res.* **19**, 802–811 (2017).

207. Park, J. B. *et al.* Piezoelectric ceramic implants:in vivo results. *J. Biomed. Mater. Res.* **15**, 103–110 (1981).

208. Mallik, P. K. & Basu, B. Better early osteogenesis of electroconductive hydroxyapatite-calcium titanate composites in a rabbit animal model. *J. Biomed. Mater. Res. Part A* **102**, 842–851 (2014).

209. Saha, S., Bhattacharjee, A., Rahaman, S. H., Basu, A. & Chakraborty, J. Synergistic anti-cancer activity of etoposide drug loaded calcium aluminium layered double hydroxide nanoconjugate for possible application in non small cell lung carcinoma. *Appl. Clay Sci.* **188**, 105496 (2020).

210. Senapati, S. *et al.* Layered double hydroxides as effective carrier for anticancer drugs and tailoring of release rate through interlayer anions. *J. Control. Release* **224**, 186–198 (2016).

211. Gil, O. M., Rocha, M. A., Constantino, V. R. L., Koh, I. H. J. & de Faria, D. L. A. Modified drug release system based on sulindac and layered double hydroxide: An in vivo Raman investigation. *Vib. Spectrosc.* **87**, 60–66 (2016).

212. Delarco, M., Fernandez, A., Martin, C. & Rivers, V. Release studies of different NSAIDs encapsulated in Mg,Al,Fe-hydrotalcites. *Appl. Clay Sci.* **42**, 538–544 (2009).

213. Rojas, R., Palena, M. C., Jimenez-Kairuz, A. F., Manzo, R. H. & Giacomelli, C. E. Modeling drug release from a layered double hydroxide-ibuprofen complex. *Appl. Clay Sci.* **62**–**63**, 15–20 (2012).

214. Gao, X. *et al.* Intercalation and controlled release properties of vitamin C intercalated layered double hydroxide. *J. Solid State Chem.* **203**, 174–180 (2013).

215. Fayyazbakhsh, F. *et al.* Release behavior and signaling effect of vitamin D3 in layered double hydroxides-hydroxyapatite/gelatin bone tissue engineering scaffold: An in vitro evaluation. *Colloids Surf. B Biointerfaces* **158**, 697–708 (2017).

216. Li, L., Gu, W., Chen, J., Chen, W. & Xu, Z. P. Co-delivery of siRNAs and anti-cancer drugs using layered double hydroxide nanoparticles. *Biomaterials* **35**, 3331–3339 (2014).

217. Li, Y. *et al.* Delaminated layered double hydroxide delivers DNA molecules as sandwich nanostructure into cells via a non-endocytic pathway. *Sci. Bull.* **62**, 686–692 (2017).

218. Yu, X., Wen, T., Cao, P., Shan, L. & Li, L. Alginate-chitosan coated layered double hydroxide nanocomposites for enhanced oral vaccine delivery. *J. Colloid Interface Sci.* **556**, 258–265 (2019).

219. Kim, M. H. *et al.* Theranostic Bioabsorbable Bone Fixation Plate with Drug-Layered Double Hydroxide Nanohybrids. *Adv. Healthc. Mater.* **5**, 2765–2775 (2016).

220. Yasaei, M., Khakbiz, M., Ghasemi, E. & Zamanian, A. Synthesis and characterization of ZnAl-NO 3 (-CO 3) layered double hydroxide: A novel

structure for intercalation and release of simvastatin. *Appl. Surf. Sci.* **467–468**, 782–791 (2019).

221. Li, X. *et al.* Double-carrier drug delivery system based on polyurethane-polyvinyl alcohol/layered double hydroxide nanocomposite hydrogel. *Mater. Lett.* **243**, 1–4 (2019).

222. Mishra, G., Dash, B., Pandey, S., Sethi, D. & Kumar, C. G. Comparative evaluation of synthetic routes and antibacterial/antifungal properties of Zn-Al layered double hydroxides containing benzoate anion. *Environ. Eng. Sci.* **35**, 247–260 (2018).

223. Liu, X. *et al.* The synthesis of a DHAD/ZnAlTi-LDH composite with advanced UV blocking and antibacterial activity for skin protection. *RSC Adv.* **10**, 9786–9790 (2020).

224. Wang, Z. *et al.* Layered double hydroxide eliminate embryotoxicity of chemotherapeutic drug through BMP-SMAD signaling pathway. *Biomaterials* **230**, 119602 (2020).

225. Zhu, R. *et al.* PH sensitive nano layered double hydroxides reduce the hematotoxicity and enhance the anticancer efficacy of etoposide on non-small cell lung cancer. *Acta Biomater.* **29**, 320–332 (2016).

226. Hakeem, A. *et al.* Facile synthesis of pH-responsive doxorubicin-loaded layered double hydroxide for efficient cancer therapy †. *This J. is Cite this J. Mater. Chem. B* **5768**, 5768 (2018).

227. Ma, R., Wang, Z., Yan, L., Chen, X. & Zhu, G. Novel Pt-loaded layered double hydroxide nanoparticles for efficient and cancer-cell specific delivery of a cisplatin prodrug. *J. Mater. Chem. B* **2**, 4868–4875 (2014).

228. Wang, Y. *et al.* Magnesium-based layered double hydroxide nanosheets: a new bone repair material with unprecedented osteogenic differentiation performance. *Nanoscale* **12**, 19075–19082 (2020).

229. Wang, A. *et al.* MgAl monolayer hydrotalcite increases the hypoglycemic effect of berberine by enhancing its oral bioavailability. *Biomed. Pharmacother.* **127**, 110140 (2020).

230. Kong, X., Jin, L., Wei, M. & Duan, X. Antioxidant drugs intercalated into

layered double hydroxide: Structure and in vitro release. *Appl. Clay Sci.* **49**, 324–329 (2010).

231. Wang, W.-R. *et al.* Dexamethasone sodium phosphate intercalated layered double hydroxides and their therapeutic efficacy in a murine asthma model. *RSC Adv.* **5**, 23826–23834 (2015).

232. Cardonick, E. & Iacobucci, A. Use of chemotherapy during human pregnancy. *Lancet Oncology* **5**, 283–291 (2004).

233. Yang, J. H., Lee, S. Y., Han, Y. S., Park, K. C. & Choy, J. H. Efficient transdermal penetration and improved stability of L-ascorbic acid encapsulated in an inorganic nanocapsule. *Bull. Korean Chem. Soc.* **24**, 499–503 (2003).

234. Hwang, S.-H., Han, Y.-S. & Choy, J.-H. *Intercalation of Functional Organic Molecules with Pharmaceutical, Cosmeceutical and Nutraceutical Functions into Layered Double Hydroxides and Zinc Basic Salts*. *Intercalation of Functional Organic Molecules Bull. Korean Chem. Soc* **22**, (2001).

235. Biswick, T., Park, D. H., Shul, Y. G. & Choy, J. H. P-coumaric acid-zinc basic salt nanohybrid for controlled release and sustained antioxidant activity. *J. Phys. Chem. Solids* **71**, 647–649 (2010).

236. Yang, J.-H. *et al.* New Inorganic-Based Drug Delivery System of Indole-3-Acetic Acid-Layered Metal Hydroxide Nanohybrids with Controlled Release Rate. *Compr. Supramol. Chem.* **7**, 129 (1996).

237. Bull, R. M. R., Markland, C., Williams, G. R. & O'Hare, D. Hydroxy double salts as versatile storage and delivery matrices. *J. Mater. Chem.* **21**, 1822–1828 (2011).

238. Gu, Q. *et al.* Intercalation of amino acids into Eu 3+-doped layered gadolinium hydroxide and quenching of Eu 3+ luminescence. *Eur. J. Inorg. Chem.* **2012**, 4407–4412 (2012).

239. Iborra, C. V. *et al.* Characterisation of northern Patagonian bentonites for pharmaceutical uses. *Appl. Clay Sci.* **31**, 272–281 (2006).

240. Modabberi, S. *et al.* Characterization of Iranian bentonites to be used as

pharmaceutical materials. *Appl. Clay Sci.* **116**–**117**, 193–201 (2015).

241. Joshi, G. V., Kevadiya, B. D. & Bajaj, H. C. Design and evaluation of controlled drug delivery system of buspirone using inorganic layered clay mineral. *Microporous Mesoporous Mater.* **132**, 526–530 (2010).

242. Choy, J.-H. *et al.* A nanohybrid system for taste masking of sildenafil. *Int. J. Nanomedicine* **7**, 1635 (2012).

243. Tan, D., Yuan, P., Annabi-Bergaya, F., Liu, D. & He, H. High-capacity loading of 5-fluorouracil on the methoxy-modified kaolinite. *Appl. Clay Sci.* **100**, 60–65 (2014).

244. Abukhadra, M. R. & Allah, A. F. Synthesis and characterization of kaolinite nanotubes (KNTs) as a novel carrier for 5-fluorouracil of high encapsulation properties and controlled release. *Inorg. Chem. Commun.* **103**, 30–36 (2019).

245. Tan, D. *et al.* Selective loading of 5-fluorouracil in the interlayer space of methoxy-modified kaolinite for controlled release. *Appl. Clay Sci.* **159**, 102–106 (2018).

246. Zhang, Y. *et al.* Intercalated 2D nanoclay for emerging drug delivery in cancer therapy. *Nano Res.* **10**, 2633–2643 (2017).

247. Zhang, Y. *et al.* Emerging integrated nanoclay-facilitated drug delivery system for papillary thyroid cancer therapy. *Sci. Rep.* **6**, 1–10 (2016).

248. Holešová, S. *et al.* Antibacterial kaolinite/urea/chlorhexidine nanocomposites: Experiment and molecular modelling. *Appl. Surf. Sci.* **305**, 783–791 (2014).

249. Jou, S. K. & Malek, N. A. N. N. Characterization and antibacterial activity of chlorhexidine loaded silver-kaolinite. *Appl. Clay Sci.* **127**–**128**, 1–9 (2016).

250. Deb, A., Andrews, N. G. & Raghavan, V. Natural polymer functionalized graphene oxide for co-delivery of anticancer drugs: In-vitro and in-vivo. *Int. J. Biol. Macromol.* **113**, 515–525 (2018).

251. Yin, T. *et al.* Redox Sensitive Hyaluronic Acid-Decorated Graphene Oxide

for Photothermally Controlled Tumor-Cytoplasm-Selective Rapid Drug Delivery. *Adv. Funct. Mater.* **27**, (2017).

252. Gong, P. *et al.* Fluorescence-switchable ultrasmall fluorinated graphene oxide with high near-infrared absorption for controlled and targeted drug delivery. *Chem. Eng. J.* **348**, 438–446 (2018).

253. González-Villegas, J. *et al.* Poly(ethylene glycol)-modified zirconium phosphate nanoplatelets for improved doxorubicin delivery. *Inorganica Chim. Acta* **468**, 270–279 (2017).

254. Kalita, H. *et al.* Sonochemically synthesized biocompatible zirconium phosphate nanoparticles for pH sensitive drug delivery application. *Mater. Sci. Eng. C* **60**, 84–91 (2016).

255. Hosseinzadeh, R. & Khorsandi, K. Photodynamic effect of Zirconium phosphate biocompatible nano-bilayers containing methylene blue on cancer and normal cells. *Sci. Rep.* **9**, 14899 (2019).

256. Ueoka, H., Shimomura, O., Pica, M., Donnadio, A. & Nomura, R. Immobilization of Anti-Inflammatory Drug on Exfoliated α-Zirconium Phosphate as a pH-Responsive Carrier. *Colloids Interface Sci. Commun.* **28**, 29–33 (2019).

257. Safari, M., Kamari, Y., Ghiaci, M., Sadeghi-aliabadi, H. & Mirian, M. Synthesis and characterization of insulin/zirconium phosphate@TiO $_2$ hybrid composites for enhanced oral insulin delivery applications. *Drug Dev. Ind. Pharm.* **43**, 862–870 (2017).

258. Ozkizilcik, A. *et al.* Synthesis of Biocompatible Titanate Nanofibers for Effective Delivery of Neuroprotective Agents. in *Methods in Molecular Biology* **1727**, 433–442 (Humana Press Inc., 2018).

259. Ozkizilcik, A. *et al.* Timed release of cerebrolysin using drug-loaded titanate nanospheres reduces brain pathology and improves behavioral functions in Parkinson's disease. *Mol. Neurobiol.* **55**, 359–369 (2018).

260. Tee, J. K. *et al.* Nanoparticles' interactions with vasculature in diseases. *Chem. Soc. Rev.* **48**, 5381–5407 (2019).

261. Suk, J. S., Xu, Q., Kim, N., Hanes, J. & Ensign, L. M. PEGylation as a

strategy for improving nanoparticle-based drug and gene delivery. *Adv. Drug Deliv. Rev.* **99**, 28–51 (2016).

262. Gu, Z. *et al.* Antibody-Targeted Drug Delivery to Injured Arteries Using Layered Double Hydroxide Nanoparticles. *Adv. Healthc. Mater.* **1**, 669–673 (2012).

263. Oh, J.-M., Choi, S.-J., Lee, G.-E., Han, S.-H. & Choy, J.-H. Inorganic Drug-Delivery Nanovehicle Conjugated with Cancer-Cell-Specific Ligand. *Adv. Funct. Mater.* **19**, 1617–1624 (2009).

264. Toffoli, G. *et al.* Overexpression of folate binding protein in ovarian cancers. *Int. J. Cancer* **74**, 193–198 (1997).

265. Boogerd, L. S. F. *et al.* Concordance of folate receptor-α expression between biopsy, primary tumor and metastasis in breast cancer and lung cancer patients. *Oncotarget* **7**, 17442–17454 (2016).

266. Yan, L. *et al.* Folic acid conjugated self-assembled layered double hydroxide nanoparticles for high-efficacy-targeted drug delivery. *Chem. Commun.* **49**, 10938–10940 (2013).

267. Mei, X. *et al.* Layered double hydroxide monolayers for controlled loading and targeted delivery of anticancer drugs. *Nano Res.* **11**, 195–205 (2018).

268. Dong, J. *et al.* Application of graphene quantum dots for simultaneous fluorescence imaging and tumor-targeted drug delivery. *Sensors Actuators, B Chem.* **256**, 616–623 (2018).

269. Iannazzo, D. *et al.* Graphene quantum dots for cancer targeted drug delivery. *Int. J. Pharm.* **518**, 185–192 (2017).

270. Depan, D., Shah, J. & Misra, R. D. K. Controlled release of drug from folate-decorated and graphene mediated drug delivery system: Synthesis, loading efficiency, and drug release response. *Mater. Sci. Eng. C* **31**, 1305–1312 (2011).

271. Huang, P. *et al.* Folic Acid-conjugated Graphene Oxide loaded with Photosensitizers for Targeting Photodynamic Therapy. *Theranostics* **1**, 240 (2011).

272. Qin, X. C. *et al.* Folic acid-conjugated graphene oxide for cancer targeted chemo-photothermal therapy. *J. Photochem. Photobiol. B Biol.* **120**, 156–162 (2013).

273. Tian, J. *et al.* Pegylated folate and peptide-decorated graphene oxide nanovehicle for in vivo targeted delivery of anticancer drugs and therapeutic self-monitoring. *Biosens. Bioelectron.* **80**, 519–524 (2016).

274. Wei, Y., Zhou, F., Zhang, D., Chen, Q. & Xing, D. A graphene oxide based smart drug delivery system for tumor mitochondria-targeting photodynamic therapy. *Nanoscale* **8**, 3530–3538 (2016).

275. Han, S. *et al.* A molecularly imprinted composite based on graphene oxide for targeted drug delivery to tumor cells. *J. Mater. Sci.* **54**, 3331–3341 (2019).

276. Deng, W. *et al.* Development of biocompatible and VEGF-targeted paclitaxel nanodrugs on albumin and graphene oxide dual-carrier for photothermal-triggered drug delivery in vitro and in vivo. *Int. J. Nanomedicine* **13**, 439–453 (2018).

277. Zhang, C. *et al.* Glycyrrhetinic Acid Functionalized Graphene Oxide for Mitochondria Targeting and Cancer Treatment In Vivo. *Small* **14**, 1703306 (2018).

278. Li, R., Liu, T. & Wang, K. Hyaluronic acid-modified zirconium phosphate nanoparticles for potential lung cancer therapy. *Biomed. Tech.* **62**, 67–73 (2017).

279. Xu, T., Zhang, J., Chi, H. & Cao, F. Multifunctional properties of organic-inorganic hybrid nanocomposites based on chitosan derivatives and layered double hydroxides for ocular drug delivery. *Acta Biomater.* **36**, 152–163 (2016).

280. Wang, Y., Zhou, L., Fang, L. & Cao, F. Multifunctional carboxymethyl chitosan derivatives-layered double hydroxide hybrid nanocomposites for efficient drug delivery to the posterior segment of the eye. *Acta Biomater.* **104**, 104–114 (2020).

281. Wu, J., Deng, A., Jiang, W., Tian, R. & Shen, Y. Synthesis and in vitro

evaluation of pH-sensitive magnetic nanocomposites as methotrexate delivery system for targeted cancer therapy. *Mater. Sci. Eng. C* **71**, 132–140 (2017).

282. Ma, X. *et al.* A Functionalized Graphene Oxide-Iron Oxide Nanocomposite for Magnetically Targeted Drug Delivery, Photothermal Therapy, and Magnetic Resonance Imaging. *Nano Res* **2012**, 199–212

283. Shirvalilou, S. *et al.* Development of a magnetic nano-graphene oxide carrier for improved glioma-targeted drug delivery and imaging: In vitro and in vivo evaluations. *Chem. Biol. Interact.* **295**, 97–108 (2018).

284. Kuo, Y.-M. *et al.* Layered double hydroxide nanoparticles to enhance organ-specific targeting and the anti-proliferative effect of cisplatin †. *J. Mater. Chem. B* **3**, 3447 (2015).

285. Hibino, T. Acid Treatment of Layered Double Hydroxides Containing Carbonate. *Eur. J. Inorg. Chem.* **2014**, 5311–5321 (2014).

286. Panda, H. S., Srivastava, R. & Bahadur, D. In-vitro release kinetics and stability of anticardiovascular drugs-intercalated layered double hydroxide nanohybrids. *J. Phys. Chem. B* **113**, 15090–15100 (2009).

287. Barkhordari, S., Yadollahi, M. & Namazi, H. pH sensitive nanocomposite hydrogel beads based on carboxymethyl cellulose/layered double hydroxide as drug delivery systems. *J. Polym. Res.* **21**, 454 (2014).

288. Barkhordari, S. & Yadollahi, M. Carboxymethyl cellulose capsulated layered double hydroxides/drug nanohybrids for cephalexin oral delivery. *Appl. Clay Sci.* **121**–**122**, 77–85 (2016).

289. Asiabi, H., Yamini, Y., Alipour, M., Shamsayei, M. & Hosseinkhani, S. Synthesis and characterization of a novel biocompatible pseudo-hexagonal NaCa-layered double metal hydroxides for smart pH-responsive drug release of dacarbazine and enhanced anticancer activity in malignant melanoma. *Mater. Sci. Eng. C* **97**, 96–102 (2019).

290. Yun, Y. *et al.* Facile synthesis of Ca2+-crosslinked sodium alginate/graphene oxide hybrids as electro- and pH-responsive drug carrier. *Mater. Sci. Eng. C* **108**, 110380 (2020).

291. Hu, H., Yu, J., Li, Y., Zhao, J. & Dong, H. Engineering of a novel pluronic F127/graphene nanohybrid for pH responsive drug delivery. *J. Biomed. Mater. Res. Part A* **100A**, 141–148 (2012).

292. Song, E. *et al.* Hyaluronic acid-decorated graphene oxide nanohybrids as nanocarriers for targeted and pH-responsive anticancer drug delivery. *ACS Appl. Mater. Interfaces* **6**, 11882–11890 (2014).

293. Anirudhan, T. S., Chithra Sekhar, V. & Athira, V. S. Graphene oxide based functionalized chitosan polyelectrolyte nanocomposite for targeted and pH responsive drug delivery. *Int. J. Biol. Macromol.* **150**, 468–479 (2020).

294. Shahabadi, N., Razlansari, M., Zhaleh, H. & Mansouri, K. Antiproliferative effects of new magnetic pH-responsive drug delivery system composed of Fe 3 O 4 , CaAl layered double hydroxide and levodopa on melanoma cancer cells. *Mater. Sci. Eng. C* **101**, 472–486 (2019).

295. Lv, O. *et al.* Highly fluorescent and morphology-controllable graphene quantum dots-chitosan hybrid xerogels for in vivo imaging and pH-sensitive drug carrier. *Mater. Sci. Eng. C* **67**, 478–485 (2016).

296. Weaver, C. L., Larosa, J. M., Luo, X. & Cui, X. T. Electrically controlled drug delivery from graphene oxide nanocomposite films. *ACS Nano* **8**, 1834–1843 (2014).

297. Liu, K. H., Liu, T. Y., Chen, S. Y. & Liu, D. M. Drug release behavior of chitosan-montmorillonite nanocomposite hydrogels following electrostimulation. *Acta Biomater.* **4**, 1038–1045 (2008).

298. Kim, J., Kim, H. & Kim, W. J. Single-Layered MoS_2 -PEI-PEG Nanocomposite-Mediated Gene Delivery Controlled by Photo and Redox Stimuli. *Small* **12**, 1184–1192 (2016).

299. Zhang, X. *et al.* Dual-responsive molybdenum disulfide/copper sulfide-based delivery systems for enhanced chemo-photothermal therapy. *J. Colloid Interface Sci.* **539**, 433–441 (2019).

300. Li, B. *et al.* Novel theranostic nanoplatform for complete mice tumor elimination via MR imaging-guided acid-enhanced photothermo-/chemo-therapy. *Biomaterials* **177**, 40–51 (2018).

301. Lin, H., Gao, S., Dai, C., Chen, Y. & Shi, J. A Two-Dimensional Biodegradable Niobium Carbide (MXene) for Photothermal Tumor Eradication in NIR-I and NIR-II Biowindows. *J. Am. Chem. Soc.* **139**, 16235–16247 (2017).

302. Yu, X. *et al.* Fluorine-free preparation of titanium carbide MXene quantum dots with high near-infrared photothermal performances for cancer therapy. *Nanoscale* **9**, 17859–17864 (2017).

303. Xing, C. *et al.* Two-Dimensional MXene (Ti3C2)-Integrated Cellulose Hydrogels: Toward Smart Three-Dimensional Network Nanoplatforms Exhibiting Light-Induced Swelling and Bimodal Photothermal/Chemotherapy Anticancer Activity. *ACS Appl. Mater. Interfaces* **10**, 27631–27643 (2018).

304. Deng, L. *et al.* Hybrid Iron Oxide-Graphene Oxide-Polysaccharides Microcapsule: A Micro-Matryoshka for On-Demand Drug Release and Antitumor Therapy in Vivo. *ACS Appl. Mater. Interfaces* **8**, 6859–6868 (2016).

305. Huang, G. *et al.* Manganese-iron layered double hydroxide: a theranostic nanoplatform with pH-responsive MRI contrast enhancement and drug release. *J. Mater. Chem. B* **5**, 3629–3633 (2017).

306. Yan, L. *et al.* Firmly anchored photosensitizer Chlorin e6 to layered double hydroxide nanoflakes for highly efficient photodynamic therapy in vivo. *Chem. Commun.* **53**, 2339–2342 (2017).

307. Wei, P.-R., Kuthati, Y., Kankala, R. & Lee, C.-H. Synthesis and Characterization of Chitosan-Coated Near-Infrared (NIR) Layered Double Hydroxide-Indocyanine Green Nanocomposites for Potential Applications in Photodynamic Therapy. *Int. J. Mol. Sci.* **16**, 20943–20968 (2015).

308. Shen, W. *et al.* Defect engineering of layered double hydroxide nanosheets as inorganic photosensitizers for NIR-III photodynamic cancer therapy. *Nat. Commun. 2022 131* **13**, 1–14 (2022).

309. Werner, S. *et al.* Cationically charged MnIIAlIII LDH nanosheets by chemical exfoliation and their use as building blocks in graphene oxide-based materials. *Langmuir* **29**, 9199–9207 (2013).

310. Poudret, L., Prior, T. J., McIntyre, L. J. & Fogg, A. M. Synthesis and crystal structures of new lanthanide hydroxyhalide anion exchange materials, Ln2(OH)5X·1.5H2O (X = Cl, Br; Ln = Y, Dy, Er, Yb). *Chem. Mater.* **20**, 7447–7453 (2008).

311. Geng, F. *et al.* General synthesis and structural evolution of a layered family of Ln 8 (OH) 20 Cl 4 · n H 2 O (Ln = Nd, Sm, Eu, Gd, Tb, Dy, Ho, Er, Tm, and Y). *J. Am. Chem. Soc.* **130**, 16344–16350 (2008).

312. Wang, Y. *et al.* SiO2-coated layered gadolinium hydroxides for simultaneous drug delivery and magnetic resonance imaging. *J. Solid State Chem.* **286**, 121291 (2020).

313. Li, L., Gu, W., Liu, J., Yan, S. & Xu, Z. P. Amine-functionalized SiO2 nanodot-coated layered double hydroxide nanocomposites for enhanced gene delivery. *Nano Res.* **8**, 682–694 (2015).

314. Wu, X. *et al.* One-step freezing temperature crystallization of layered rare-earth hydroxide (Ln2(OH)5NO3·nH2O) nanosheets for a wide spectrum of Ln (Ln = Pr-Er, and Y), anion exchange with fluorine and sulfate, and microscopic coordination probed via photoluminescence. *J. Mater. Chem. C* **3**, 3428–3437 (2015).

315. Wang, Z., Li, J. G., Zhu, Q., Li, X. & Sun, X. Sacrificial conversion of layered rare-earth hydroxide (LRH) nanosheets into (Y1-xEux)PO4 nanophosphors and investigation of photoluminescence. *Dalt. Trans.* **45**, 5290–5299 (2016).

316. Yoon, Y. S. *et al.* Fabrication of a silica sphere with fluorescent and MR contrasting GdPO4 nanoparticles from layered gadolinium hydroxide. *Chem. Commun.* **46**, 3654–3656 (2010).

317. Muir, B. W. *et al.* Metal-free and MRI visible theranostic lyotropic liquid crystal nitroxide-based nanoparticles. *Biomaterials* **33**, 2723–2733 (2012).

318. Strimaite, M. *et al.* Layered terbium hydroxides for simultaneous drug delivery and imaging. *Dalt. Trans.* **50**, 10275–10290 (2021).

319. Whan, R. E. & Crosby, G. A. Luminescence studies of rare earth complexes: Benzoylacetonate and dibenzoylmethide chelates. *J. Mol.*

Spectrosc. **8**, 315–327 (1962).

320. Manna, P., Bhar, M. & Mukherjee, P. Lanthanide photoluminescence lifetimes reflect vibrational signature of local environment: Lengthening duration of emission in inorganic nanoparticles. *J. Lumin.* **235**, 118052 (2021).

321. Soini, E., Lövgren, T. & Reimer, C. B. Time-Resolved Fluorescence of Lanthanide Probes and Applications in Biotechnology. *Crit Rev Anal Chem* **18**, 105–154 (2008).

322. Liu, L. L. *et al.* Intercalation assembly of optical hybrid materials based on layered terbium hydroxide hosts and organic sensitizer anions guests. *Chinese Chem. Lett.* **24**, 93–95 (2013).

323. Su, F. *et al.* Enhanced Tb3+ luminescence in layered terbium hydroxide by intercalation of benzenepolycarboxylic species. *Mater. Res. Bull.* **88**, 301–307 (2017).

324. Mestre, A. S., Pires, J., Nogueira, J. M. F. & Carvalho, A. P. Activated carbons for the adsorption of ibuprofen. *Carbon N. Y.* **45**, 1979–1988 (2007).

325. Chu, N. *et al.* Intercalation of organic sensitisers into layered europium hydroxide and enhanced luminescence property. *Dalt. Trans.* **41**, 7409 (2012).

326. Kandare, E. & Hossenlopp, J. M. Thermal degradation of acetate-intercalated hydroxy double and layered hydroxy salts. *Inorg. Chem.* **45**, 3766–3773 (2006).

327. Rives, V. Characterisation of layered double hydroxides and their decomposition products. *Mater. Chem. Phys.* **75**, 19–25 (2002).

328. Kovanda, F. *et al.* Mixed oxides obtained from Co and Mn containing layered double hydroxides: Preparation, characterization, and catalytic properties. *J. Solid State Chem.* **179**, 812–823 (2006).

329. Lee, S.-S., Lee, B.-I., Kim, S.-J., Byeon, S.-H. & Kang, J.-K. Thermal decomposition and recovery behaviors of layered gadolinium hydroxychloride. *Inorg. Chem.* **51**, 10222–10232 (2012).

330. Ay, A. N., Zümreoglu-Karan, B. & Temel, A. Boron removal by hydrotalcite-like, carbonate-free Mg-Al-NO3-LDH and a rationale on the mechanism. *Microporous Mesoporous Mater.* **98**, 1–5 (2007).

331. DICLOFENAC SODIUM - BNF content published by NICE. Available at: https://bnf.nice.org.uk/drug/diclofenac-sodium.html#indicationsAndDoses. (Accessed: 8th February 2021)

332. IBUPROFEN - BNF content published by NICE. Available at: https://bnf.nice.org.uk/drug/ibuprofen.html#indicationsAndDoses. (Accessed: 8th February 2021)

333. NAPROXEN - BNF content published by NICE. Available at: https://bnf.nice.org.uk/drug/naproxen.html#indicationsAndDoses. (Accessed: 8th February 2021)

334. EMC. Doxorubicin solution - summary of product characteristics. Available at: https://www.medicines.org.uk/emc/product/6184/smpc. (Accessed: 8th February 2021)

335. EMC. Paclitaxel solution - summary of product characteristics. Available at: https://www.medicines.org.uk/emc/product/3891/smpc. (Accessed: 8th February 2021)

336. Al-Nimer, M. S. M., Hameed, H. G. & Mahmood, M. M. Antiproliferative effects of aspirin and diclofenac against the growth of cancer and fibroblast cells: In vitro comparative study. *Saudi Pharm. J.* **23**, 483–486 (2015).

337. Akrami, H., Aminzadeh, S. & Fallahi, H. Inhibitory effect of ibuprofen on tumor survival and angiogenesis in gastric cancer cell. *Tumor Biol.* **36**, 3237–3243 (2015).

338. Kim, M. S. *et al.* Naproxen induces cell-cycle arrest and apoptosis in human urinary bladder cancer cell lines and chemically induced cancers by targeting PI3K. *Cancer Prev. Res.* **7**, 236–245 (2014).

339. Parello, M. L., Rojas, R. & Giacomelli, C. E. Dissolution kinetics and mechanism of Mg-Al layered double hydroxides: A simple approach to describe drug release in acid media. *J. Colloid Interface Sci.* **351**, 134–139 (2010).

340. Young, L. K., Matthew, S. Z. & Houston, J. G. Absence of potential gadolinium toxicity symptoms following 22,897 gadoteric acid (Dotarem®) examinations, including 3,209 performed on renally insufficient individuals. *Eur. Radiol.* **29**, 1922–1930 (2019).

341. Rohwer, H. & Hosten, E. pH dependence of the reactions of arsenazo III with the lanthanides. *Anal. Chim. Acta* **339**, 271–277 (1997).

342. Dressman, J. B. *et al.* Upper Gastrointestinal (GI) pH in Young, Healthy Men and Women. *Pharm. Res. An Off. J. Am. Assoc. Pharm. Sci.* **7**, 756–761 (1990).

343. Jalalvand, E., Robertson, B., Tostivint, H., Wallén, P. & Grillner, S. The spinal cord has an intrinsic system for the control of pH. *Curr. Biol.* **26**, 1346–1351 (2016).

344. Griffiths, J. Are cancer cells acidic? *Br. J. Cancer* **64**, 425–427 (1991).

345. CHEMWATCH. Gadolinium (III) chloride hexahydrate - material safety data sheet. (2009). Available at: https://datasheets.scbt.com/sc-202617.pdf. (Accessed: 17th May 2021)

346. Henderson, D. W. Experimental analysis of non-isothermal transformations involving nucleation and growth. *J. Therm. Anal.* **15**, 325–331 (1979).

347. De Bruijn, T. J. W., De Jong, W. A. & Van Den Berg, P. J. Kinetic parameters in Avrami-Erofeev type reactions from isothermal and non-isothermal experiments. *Thermochim. Acta* **45**, 315–325 (1981).

348. Bhaskar, R., Murthy, R. S. R., Miglani, B. D. & Viswanathan, K. Novel method to evaluate diffusion controlled release of drug from resinate. *Int. J. Pharm.* **28**, 59–66 (1986).

349. Aw, M. S., Gulati, K. & Losic, D. Controlling drug release from titania nanotube arrays using polymer nanocarriers and biopolymer coating. *J. Biomater. Nanobiotechnol.* **02**, 477–484 (2011).

350. Ribeiro, L. N. M. *et al.* Pectin-coated chitosan-LDH bionanocomposite beads as potential systems for colon-targeted drug delivery. *Int. J. Pharm.* **463**, 1–9 (2014).

351. Lis, S. Luminescence spectroscopy of lanthanide(III) ions in solution. *J. Alloys Compd.* **341**, 45–50 (2002).

352. Lai, J., Shah, B. P., Garfunkel, E. & Lee, K. B. Versatile fluorescence resonance energy transfer-based mesoporous silica nanoparticles for real-time monitoring of drug release. *ACS Nano* **7**, 2741–2750 (2013).

353. Dong, X., Wei, C., Liu, T., Lv, F. & Qian, Z. Real-time fluorescence tracking of protoporphyrin incorporated thermosensitive hydrogel and its drug release in vivo. *ACS Appl. Mater. Interfaces* **8**, 5104–5113 (2016).

354. Choi, J. S. *et al.* Size-controlled biodegradable nanoparticles: Preparation and size-dependent cellular uptake and tumor cell growth inhibition. *Colloids Surf. B* **122**, 545–551 (2014).

355. Kreuter, J. Nanoparticles and microparticles for drug and vaccine delivery. *J. Anat.* **189**, 503–505 (1996).

356. Maitani, Y. *et al.* Higher lung accumulation of intravenously injected organic nanotubes. *Int. J. Nanomedicine* **8**, 315–323 (2013).

357. Myerson, J. W. *et al.* Non-affinity factors modulating vascular targeting of nano- and microcarriers. *Adv. Drug Deliv. Rev.* **99**, 97–112 (2016).

358. Hobbs, S. K. *et al.* Regulation of transport pathways in tumor vessels: Role of tumor type and microenvironment. *Proc. Natl. Acad. Sci. U. S. A.* **95**, 4607–4612 (1998).

359. Sarin, H. Physiologic upper limits of pore size of different blood capillary types and another perspective on the dual pore theory of microvascular permeability. *J. Angiogenes. Res.* **2**, (2010).

360. Decuzzi, P., Causa, F., Ferrari, M. & Netti, P. A. The Effective Dispersion of Nanovectors Within the Tumor Microvasculature. *Ann. Biomed. Eng.* **34**, 633–641 (2006).

361. Hollis, C. P. *et al.* Biodistribution and bioimaging studies of hybrid paclitaxel nanocrystals: Lessons learned of the EPR effect and image-guided drug delivery. *J. Control. Release* **172**, 12–21 (2013).

362. Goldman, A. J., Cox, R. G. & Brenner, H. Slow viscous motion of a sphere

parallel to a plane wall—II Couette flow. *Chem. Eng. Sci.* **22**, 653–660 (1967).

363. Cooley, M. *et al.* Influence of particle size and shape on their margination and wall-adhesion: implications in drug delivery vehicle design across nano-to-micro scale. *Nanoscale* **10**, 15350–15364 (2018).

364. Ta, H. T., Truong, N. P., Whittaker, A. K., Davis, T. P. & Peter, K. The effects of particle size, shape, density and flow characteristics on particle margination to vascular walls in cardiovascular diseases. *Expert Opin. Drug Deliv.* **15**, 33–45 (2018).

365. Chithrani, B. D. & Chan, W. C. W. Elucidating the mechanism of cellular uptake and removal of protein-coated gold nanoparticles of different sizes and shapes. *Nano Lett.* **7**, 1542–1550 (2007).

366. Banerjee, A., Qi, J., Gogoi, R., Wong, J. & Mitragotri, S. Role of nanoparticle size, shape and surface chemistry in oral drug delivery. *J. Control. Release* **238**, 176–185 (2016).

367. Langevin, D. *et al.* Towards reproducible measurement of nanoparticle size using dynamic light scattering: Important controls and considerations. *NanoImpact* **10**, 161–167 (2018).

368. Lynch, I. & Dawson, K. A. Protein-nanoparticle interactions. *Nano Today* **3**, 40–47 (2008).

369. Guerra, L. F., Muir, T. W. & Yang, H. Single-Particle Dynamic Light Scattering: Shapes of Individual Nanoparticles. *Nano Lett.* **19**, 5530–5536 (2019).

370. Hayashi, H. & Hakuta, Y. Hydrothermal Synthesis of Metal Oxide Nanoparticles in Supercritical Water. *Materials (Basel).* **3**, 3794–3817 (2010).

371. Dang, L. X. Intermolecular interactions of liquid dichloromethane and equilibrium properties of liquid–vapor and liquid–liquid interfaces: A molecular dynamics study. *J. Chem. Phys.* **110**, 10113 (1999).

372. Schäf, O., Ghobarkar, H. & Knauth, P. Hydrothermal Synthesis of Nanomaterials. in *Nanostructured Materials* 23–41 (Kluwer Academic

Publishers, 2005). doi:10.1007/0-306-47722-X_2

373. Tong, M. L., Hu, S., Wang, J., Kitagawa, S. & Seik, W. N. Supramolecular isomerism in cadmium hydroxide phases. Temperature-dependent synthesis and structure of photoluminescent coordination polymers of α- and β-Cd2(OH)2(2,4-pyda). *Cryst. Growth Des.* **5**, 837–839 (2005).

374. Panda, H. S., Srivastava, R. & Bahadur, D. Synthesis and in situ mechanism of nuclei growth of layered double hydroxides. *Bull. Mater. Sci. 2012 347* **34**, 1599–1604 (2012).

375. Sharma, S. K., Kushwaha, P. K., Srivastava, V. K., Bhatt, S. D. & Jasra, R. V. Effect of hydrothermal conditions on structural and textural properties of synthetic hydrotalcites of varying Mg/Al ratio. *Ind. Eng. Chem. Res.* **46**, 4856–4865 (2007).

376. Jose, N. A., Zeng, H. C. & Lapkin, A. A. Hydrodynamic assembly of two-dimensional layered double hydroxide nanostructures. *Nat. Commun. 2018 91* **9**, 1–12 (2018).

377. Wang, J. *et al.* Pressure-induced oriented attachment growth of large-size crystals for constructing 3D ordered superstructures. *ACS Nano* **10**, 405–412 (2016).

378. Kim, J. S. *et al.* Effect of hydrothermal condition on the formation of multi-component oxides of Ni-based metallic glass under high temperature water near the critical point. *AIP Adv.* **5**, 077132 (2015).

379. Byrappa, K., Keerthiraj, N. & Byrappa, S. M. Hydrothermal Growth of Crystals—Design and Processing. in *Handbook of Crystal Growth* **2**, 535–575 (Elsevier, 2015).

380. Xu, C., Lee, J. & Teja, A. S. Continuous hydrothermal synthesis of lithium iron phosphate particles in subcritical and supercritical water. *J. Supercrit. Fluids* **44**, 92–97 (2008).

381. Hayashi, H. *et al.* Hydrothermal synthesis of BaTiO3 nanoparticles using a supercritical continuous flow reaction system. *J. Cryst. Growth* **312**, 1968–1972 (2010).

382. Adschiri, T., Kanazawa, K. & Arai, K. Rapid and Continuous Hydrothermal

Synthesis of Boehmite Particles in Subcritical and Supercritical Water. *J. Am. Ceram. Soc.* **75**, 2615–2618 (1992).

383. Laquerriere, P. *et al.* Importance of hydroxyapatite particles characteristics on cytokines production by human monocytes in vitro. *Biomaterials* **24**, 2739–2747 (2003).

384. Doshi, N. & Mitragotri, S. Needle-shaped polymeric particles induce transient disruption of cell membranes. *J. R. Soc. Interface* **7**, s403 (2010).

385. Lebre, F. *et al.* The shape and size of hydroxyapatite particles dictate inflammatory responses following implantation. *Sci. Rep.* **7**, 2922 (2017).

386. Bialik, M., Sedin, P. & Theliander, H. Boiling point rise calculations in sodium salt solutions. *Ind. Eng. Chem. Res.* **47**, 1283–1287 (2008).

387. Yudina, E., Frolova, A., Krivtsov, I. & Avdin, V. Analysis of products formed in hydrothermal processing of yttrium nitrate and yttrium chloride. *Вестник ЮУрГУ. Серия: Химия* **7**, 51–54 (2015).

388. Xu, Y. *et al.* Reverse microemulsion synthesis of layered gadolinium hydroxide nanoparticles. *J. Solid State Chem.* **258**, 320–327 (2018).

389. Wu, X. *et al.* Structure characterization and photoluminescence properties of (Y 0.95-xGdxEu0.05)2O 3 red phosphors converted from layered rare-earth hydroxide (LRH) nanoflake precursors. *J. Alloys Compd.* **559**, 188–195 (2013).

390. Feng, Y. *et al.* Synthesis of Cu-containing layered double hydroxides with a narrow crystallite-size distribution. *Clays Clay Miner.* **51**, 566–569 (2003).

391. Dukes, L. D. *et al.* Dependence on NADH produced during glycolysis for β-cell glucose signaling. *J. Biol. Chem.* **269**, 10979–10982 (1994).

392. Candeias, L. P. *et al.* The catalysed NADH reduction of resazurin to resorufin. *J. Chem. Soc. Perkin Trans. 2* **11**, 2333–2334 (1998).

393. Cheng, J. *et al.* The vacuolization of macrophages induced by large amounts of inorganic nanoparticle uptake to enhance the immune response. *Nanoscale* **11**, 22849–22859 (2019).

394. Herd, H. L., Malugin, A. & Ghandehari, H. Silica nanoconstruct cellular

toleration threshold in vitro. *J. Control. Release* **153**, 40–48 (2011).

395. González-Polo, R. A. *et al.* The apoptosis/autophagy paradox: autophagic vacuolization before apoptotic death. *J. Cell Sci.* **118**, 3091–3102 (2005).

396. Codogno, P. & Meijer, A. J. Autophagy and signaling: their role in cell survival and cell death. *Cell Death Differ. 2005 122* **12**, 1509–1518 (2005).

397. Cordani, M. & Somoza, Á. Targeting autophagy using metallic nanoparticles: a promising strategy for cancer treatment. *Cell. Mol. Life Sci.* **76**, 1215–1242 (2019).

398. Neufeld, B. H., Tapia, J. B., Lutzke, A. & Reynolds, M. M. Small Molecule Interferences in Resazurin and MTT-Based Metabolic Assays in the Absence of Cells. *Anal. Chem.* **90**, 6867–6876 (2018).

399. Robbins, A. K. & Horlick, R. A. Macrophage Scavenger Receptor Confers an Adherent Phenotype to Cells in Culture. *Biotechniques* **25**, 240–244 (1998).

400. Tsao, Y. S., Condon, R., Schaefer, E., Lio, P. & Liu, Z. Development and improvement of a serum-free suspension process for the production of recombinant adenoviral vectors using HEK293 cells. *Cytotechnology* **37**, 189 (2001).

401. Wakefield, G., Keron, H. A., Dobson, P. J. & Hutchison, J. L. Structural and optical properties of terbium oxide nanoparticles. *J. Phys. Chem. Solids* **60**, 503–508 (1999).

402. Bünzli, J.-C. G. Lanthanides. in *Kirk-Othmer Encyclopedia of Chemical Technology* 1–43 (John Wiley & Sons, Inc., 2013).

403. Seitz, M., Oliver, A. G. & Raymond, K. N. The lanthanide contraction revisited. *J. Am. Chem. Soc.* **129**, 11153–11160 (2007).

404. Dangelo, P. *et al.* Revised ionic radii of lanthanoid(III) ions in aqueous solution. *Inorg. Chem.* **50**, 4572–4579 (2011).

405. Pereira, C. C. L., Lima, J. C., Moro, A. J. & Monteiro, B. Layered europium hydroxide system for phosphorous sensing and remediation. *Appl. Clay Sci.* **146**, 216–222 (2017).

406. Wang, C. *et al.* Gold Nanoparticles on Nanosheets Derived from Layered Rare-Earth Hydroxides for Catalytic Glycerol-to-Lactic Acid Conversion. *ACS Appl. Mater. Interfaces* **13**, 522–530 (2021).

407. Ren, Y. & Feng, J. Skin-inspired multifunctional luminescent hydrogel containing layered rare-earth hydroxide with 3D printability for human motion sensing. *ACS Appl. Mater. Interfaces* **12**, 6797–6805 (2020).

408. Liu, L. *et al.* Facile fabrication of color-tunable and white light emitting nano-composite films based on layered rare-earth hydroxides. *J. Mater. Chem. C* **3**, 2326–2333 (2015).

409. Su, F. *et al.* Delaminated layered rare-earth hydroxide composites with ortho-coumaric acid: color-tunable luminescence and blue emission due to energy transfer. *J. Mater. Chem. C* **3**, 7143–7152 (2015).

410. Liu, L. *et al.* Dramatically Enhanced Luminescence of Layered Terbium Hydroxides as Induced by the Synergistic Effect of Gd^{3+} and Organic Sensitizers. *J. Phys. Chem. C* **118**, 14511–14520 (2014).

411. Teplonogova, M. A., Yapryntsev, A. D., Baranchikov, A. E. & Ivanov, V. K. High-Entropy Layered Rare Earth Hydroxides. *Inorg. Chem.* **61**, 19817–19827 (2022).

412. Geng, F. *et al.* Synthesis and Properties of Well-Crystallized Layered Rare-Earth Hydroxide Nitrates from Homogeneous Precipitation. *Inorg. Chem* **48**, 6724–6730 (2009).

413. Viswanathan, S., Kovacs, Z., Green, K. N., Ratnakar, S. J. & Sherry, A. D. Alternatives to gadolinium-based metal chelates for magnetic resonance imaging. *Chem. Rev.* **110**, 2960–3018 (2010).

414. Alsaadi, B. M., Rossotti, F. J. C. & Williams, R. J. P. Electron relaxation rates of lanthanide aquo-cations. *J. Chem. Soc. Dalt. Trans.* **11**, 2147–2150 (1980).

415. Caravan, P., Ellison, J. J., Mcmurry, T. J. & Lauffer, R. B. Gadolinium(III) chelates as MRI contrast agents: structure, dynamics, and applications. *Chem. Rev.* **99**, 2293–2352 (1999).

416. McIntyre, L. J., Jackson, L. K. & Fogg, A. M. Synthesis and anion exchange

chemistry of new intercalation hosts containing lanthanide cations, Ln2(OH)5(NO3)·xH2O (Ln=Y, Gd-Lu). *J. Phys. Chem. Solids* **69**, 1070–1074 (2008).

417. Xiang, Y. *et al.* Synthesis of highly luminescent and anion-exchangeable cerium-doped layered yttrium hydroxides for sensing and photofunctional applications. *Adv. Funct. Mater.* **21**, 4388–4396 (2011).

418. Hibino, T. Anion Selectivity of Layered Double Hydroxides: Effects of Crystallinity and Charge Density. *Eur. J. Inorg. Chem.* **2018**, 722–730 (2018).

419. Bruce, D. W., Hietbrink, B. E. & DuBois, K. P. The acute mammalian toxicity of rare earth nitrates and oxides. *Toxicol. Appl. Pharmacol.* **5**, 750–759 (1963).

420. Gu, Q. *et al.* Fabrication of novel bifunctional nanohybrid based on layered rare-earth hydroxide with magnetic and fluorescent properties. *Front. Mater. Sci* **2020**, 488–496 (2020).

421. Jeon, S. & Hwang, H. Effect of hygroscopic nature on the electrical characteristics of lanthanide oxides (Pr2O3, Sm2O3, Gd2O3, and Dy2O3). *J. Appl. Phys.* **93**, 6393 (2003).

422. Mikawa, M. *et al.* Paramagnetic Water-Soluble Metallofullerenes Having the Highest Relaxivity for MRI Contrast Agents. *Bioconjug. Chem.* **12**, 510–514 (2001).

423. Li, Y., Chen, T., Tan, W. & Talham, D. R. Size-Dependent MRI Relaxivity and Dual Imaging with Eu 0.2 Gd 0.8 PO 4 ·H 2 O Nanoparticles. *Langmuir* **30**, 5873–5879 (2014).

424. Vuong, Q. L. *et al.* Paramagnetic nanoparticles as potential MRI contrast agents: Characterization, NMR relaxation, simulations and theory. *Magn. Reson. Mater. Physics, Biol. Med.* **25**, 467–478 (2012).

425. Caro, C., Paez-Muñoz, J. M., Beltrán, A. M., Pernia Leal, M. & García-Martín, M. L. PEGylated Terbium-Based Nanorods as Multimodal Bioimaging Contrast Agents. *ACS Appl. Nano Mater.* **4**, 4199–4207 (2021).

426. Debasu, M. L., Ananias, D., Rocha, J., Malta, O. L. & Carlos, L. D. Energy-

transfer from Gd(III) to Tb(III) in (Gd,Yb,Tb)PO4 nanocrystals. *Phys. Chem. Chem. Phys.* **15**, 15565–15571 (2013).

427. Jiang, C. *et al.* One-pot aqueous synthesis of gadolinium doped CdTe quantum dots with dual imaging modalities. *Talanta* **155**, 14–20 (2016).

428. Forte, A. *et al.* Mesoporous silica nanoparticles with manganese and lanthanide salts: synthesis, characterization and cytotoxicity studies. *Dalt. Trans.* **50**, 8588–8599 (2021).

429. Liu, X. *et al.* Nanotoxic Effects of Silver Nanoparticles on Normal HEK-293 Cells in Comparison to Cancerous HeLa Cell Line. *Int. J. Nanomedicine* **16**, 753 (2021).

430. Zhou, L. *et al.* DNA-mediated biomineralization of rare-earth nanoparticles for simultaneous imaging and stimuli-responsive drug delivery. *Biomaterials* **35**, 8694–8702 (2014).

431. Urban, C., Urban, A. S., Charron, H. & Joshi, A. Externally modulated theranostic nanoparticles. *Transl. Cancer Res.* **2**, 292 (2013).

432. Da Moura Semedo, C., Webb, M., Waller, H., Khunti, K. & Davies, M. Skin autofluorescence, a non-invasive marker of advanced glycation end products: clinical relevance and limitations. *Postgrad. Med. J.* **93**, 289–294 (2017).

433. Hemmer, E., Benayas, A., Légaré, F. & Vetrone, F. Exploiting the biological windows: current perspectives on fluorescent bioprobes emitting above 1000 nm. *Nanoscale Horizons* **1**, 168–184 (2016).

434. Smith, A. M., Mancini, M. C. & Nie, S. Second window for in vivo imaging. *Nat. Nanotechnol. 2009 411* **4**, 710–711 (2009).

435. Kraft, J. C. & Ho, R. J. Y. Interactions of indocyanine green and lipid in enhancing near-infrared fluorescence properties: The basis for near-infrared imaging in vivo. *Biochemistry* **53**, 1275–1283 (2014).

436. Owens, E. A., Henary, M., El Fakhri, G. & Choi, H. S. Tissue-Specific Near-Infrared Fluorescence Imaging. *Acc. Chem. Res.* **49**, 1731–1740 (2016).

437. Hintersteiner, M. *et al.* In vivo detection of amyloid-β deposits by near-

infrared imaging using an oxazine-derivative probe. *Nat. Biotechnol.* **23**, 577–583 (2005).

438. Del Rosal, B., Villa, I., Jaque, D. & Sanz-Rodríguez, F. In vivo autofluorescence in the biological windows: the role of pigmentation. *J. Biophotonics* **9**, 1059–1067 (2016).

439. Peng, Q. *et al.* Lasers in medicine. *Reports Prog. Phys.* **71**, 056701 (2008).

440. IEC 60825-1 INTERNATIONAL STANDARD NORME INTERNATIONALE Safety of laser products-Part 1: Equipment classification and requirements Sécurité des appareils à laser-Partie 1: Classification des matériels et exigences.

441. Chen, W. R., Adams, R. L., Higgins, A. K., Bartels, K. E. & Nordquist, R. E. Photothermal effects on murine mammary tumors using indocyanine green and an 808-nm diode laser: An in vivo efficacy study. *Cancer Lett.* **98**, 169–173 (1996).

442. Pasparakis, G. & Pasparakis, G. Light-Induced Generation of Singlet Oxygen by Naked Gold Nanoparticles and its Implications to Cancer Cell Phototherapy. *Small* **9**, 4130–4134 (2013).

443. Hatef, A., Fortin-Deschênes, S., Boulais, E., Lesage, F. & Meunier, M. Photothermal response of hollow gold nanoshell to laser irradiation: Continuous wave, short and ultrashort pulse. *Int. J. Heat Mass Transf.* **89**, 866–871 (2015).

444. Garcia-Diaz, M., Huang, Y. Y. & Hamblin, M. R. Use of fluorescent probes for ROS to tease apart Type I and Type II photochemical pathways in photodynamic therapy. *Methods* **109**, 158 (2016).

445. Entradas, T., Waldron, S. & Volk, M. The detection sensitivity of commonly used singlet oxygen probes in aqueous environments. *J. Photochem. Photobiol. B Biol.* **204**, (2020).

446. Carloni, P. *et al.* On the use of 1,3-diphenylisobenzofuran (DPBF). Reactions with carbon and oxygen centered radicals in model and natural systems. *Res. Chem. Intermed.* **19**, 395–405 (1993).

447. Jain, A. *et al.* Blue light triggered generation of reactive oxygen species

from silica coated Gd3Al5O12:Ce3+ nanoparticles loaded with rose Bengal. *Data Br.* **20**, 1023–1028 (2018).

448. Uthaman, S. *et al.* Self-Quenched Polysaccharide Nanoparticles with a Reactive Oxygen Species-Sensitive Cascade for Enhanced Photodynamic Therapy. *ACS Appl. Mater. Interfaces* **12**, 28004 (2020).

449. Weng, X. L. & Liu, J. Y. Strategies for maximizing photothermal conversion efficiency based on organic dyes. *Drug Discov. Today* **26**, 2045–2052 (2021).

450. Zhao, L., Liu, Y., Chang, R., Xing, R. & Yan, X. Supramolecular Photothermal Nanomaterials as an Emerging Paradigm toward Precision Cancer Therapy. *Adv. Funct. Mater.* **29**, 1806877 (2019).

451. Fan, X. *et al.* MXene Ti 3 C 2 T x for phase change composite with superior photothermal storage capability. *J. Mater. Chem. A* **7**, 14319–14327 (2019).

452. Wang, D. *et al.* Boosting Non-Radiative Decay to Do Useful Work: Development of a Multi-Modality Theranostic System from an AIEgen. *Angew. Chemie Int. Ed.* **58**, 5628–5632 (2019).

453. Xu, C. *et al.* Molecular Motion and Nonradiative Decay: Towards Efficient Photothermal and Photoacoustic Systems. *Angew. Chemie* **134**, e202204604 (2022).

454. Benya, R., Quintana, J. & Brundage, B. Adverse reactions to indocyanine green: A case report and a review of the literature. *Cathet. Cardiovasc. Diagn.* **17**, 231–233 (1989).

455. Chen, W. R. *et al.* Chromophore-enhanced laser-tumor tissue photothermal interaction using an 808-nm diode laser. *Cancer Lett.* **88**, 15–19 (1995).

456. Urbanska, K. *et al.* Indocyanine green as a prospective sensitizer for photodynamic therapy of melanomas. *Acta Biochim. Pol.* **49**, 387–391 (2002).

457. Liu, J., Sun, L., Li, L., Zhang, R. & Xu, Z. P. Synergistic Cancer Photochemotherapy via Layered Double Hydroxide-Based Trimodal

Nanomedicine at Very Low Therapeutic Doses. *ACS Appl. Mater. Interfaces* **13**, 7115–7126 (2021).

458. Mei, X. *et al.* A bottom-up synthesis of rare-earth-hydrotalcite monolayer nanosheets toward multimode imaging and synergetic therapy. *Chem. Sci.* **9**, 5630–5639 (2018).

459. Luo, S., Zhang, E., Su, Y., Cheng, T. & Shi, C. A review of NIR dyes in cancer targeting and imaging. *Biomaterials* **32**, 7127–7138 (2011).

460. Li, J. Bin *et al.* Recent Progress in Small-Molecule Near-IR Probes for Bioimaging. *Trends Chem.* **1**, 224–234 (2019).

461. Kuno, S., Akeno, H., Ohtani, H. & Yuasa, H. Visible room-temperature phosphorescence of pure organic crystals via a radical-ion-pair mechanism. *Phys. Chem. Chem. Phys.* **17**, 15989–15995 (2015).

462. Kennedy, J. C., Pottier, R. H. & Pross, D. C. Photodynamic therapy with endogenous protoporphyrin: IX: Basic principles and present clinical experience. *J. Photochem. Photobiol. B Biol.* **6**, 143–148 (1990).

463. Gold, M. H. & Goldman, M. P. 5-Aminolevulinic Acid Photodynamic Therapy: Where We Have Been and Where We Are Going. *Dermatologic Surg.* **30**, 1077–1084 (2004).

464. Li, Z. & Wandlowski, T. Structure formation and annealing of isophthalic acid at the electrochemical au(111)-electrolyte interface. *J. Phys. Chem. C* **113**, 7821–7825 (2009).

465. Qin, L. *et al.* In vitro antioxidant activity and in vivo antifatigue effect of layered double hydroxide nanoparticles as delivery vehicles for folic acid. *Int. J. Nanomedicine* **9**, 5701–5710 (2014).

466. Saliba, D. & Al-Ghoul, M. Kinetics of intercalation of fluorescent probes in magnesiumaluminium layered double hydroxide within a multiscale reactiondiffusion framework. *Philos. Trans. R. Soc. A Math. Phys. Eng. Sci.* **374**, (2016).

467. Ahsan Iqbal, M. & Fedel, M. Ordering and disordering of in situ grown MgAl-layered double hydroxide and its effect on the structural and corrosion resistance properties. *Int. J. Miner. Metall. Mater.* **26**, 1570 (2019).

468. Liu, L. J., Zhang, M. Y., Guo, Q. Z., Zhang, Z. H. & Guo, J. F. A terbium(iii) lanthanide-organic framework as a selective and sensitive iodide/bromide sensor in aqueous medium. *Dalt. Trans.* **50**, 1697–1702 (2021).

469. Wang, H.-M. *et al.* A luminescent terbium coordination polymer for sensing methanol. *RSC Adv.* **4**, 14035–14041 (2014).

470. Palmer, K. F. & Williams, D. Optical properties of water in the near infrared*. *J. Opt. Soc. Am.* **64**, 1107 (1974).

471. Liu, R., Xiao, W., Hu, C., Xie, R. & Gao, H. Theranostic size-reducible and no donor conjugated gold nanocluster fabricated hyaluronic acid nanoparticle with optimal size for combinational treatment of breast cancer and lung metastasis. *J. Control. Release* **278**, 127–139 (2018).

472. Ruan, Y., Jia, X., Wang, C., Zhen, W. & Jiang, X. Mn–Fe layered double hydroxide nanosheets: a new photothermal nanocarrier for O 2 -evolving phototherapy. *Chem. Commun.* **54**, 11729–11732 (2018).

473. Zhou, J. F., Chin, M. P. & Schafer, S. A. Aggregation and degradation of indocyanine green. in *Laser Surgery: Advanced Characterization, Therapeutics, and Systems IV* (ed. Anderson, R. R.) **2128**, 495–505 (SPIE, 1994).

474. Diaz Tovar, J. S., Kassab, G., Inada, N. M., Salvador Bagnato, V. & Kurachi, C. Photodegradation in the infrared region of indocyanine green in aqueous solution. in *2019 SBFoton International Optics and Photonics Conference, SBFoton IOPC 2019* 1–5 (IEEE, 2019).

475. Cui, T. *et al.* “Stealth” dendrimers with encapsulation of indocyanine green for photothermal and photodynamic therapy of cancer. *Int. J. Pharm.* **600**, 120502 (2021).

476. Wang, X. hui *et al.* Polylysine modified conjugated polymer nanoparticles loaded with the singlet oxygen probe 1,3-diphenylisobenzofuran and the photosensitizer indocyanine green for use in fluorometric sensing and in photodynamic therapy. *Microchim. Acta* **186**, 1–8 (2019).

477. Rüttger, F., Mindt, S., Golz, C., Alcarazo, M. & John, M. Isomerization and Dimerization of Indocyanine Green and a Related Heptamethine Dye.

European J. Org. Chem. **2019**, 4791–4796 (2019).

478. 1,3-Diphenylisobenzofuran(5471-63-6) 1H NMR spectrum. Available at: https://www.chemicalbook.com/SpectrumEN_5471-63-6_1HNMR.htm. (Accessed: 24th February 2023)

479. 1,2-DIBENZOYLBENZENE(1159-86-0) 1H NMR spectrum. Available at: https://www.chemicalbook.com/SpectrumEN_1159-86-0_1HNMR.htm. (Accessed: 24th February 2023)

480. Mindt, S., Karampinis, I., John, M., Neumaier, M. & Nowak, K. Stability and degradation of indocyanine green in plasma, aqueous solution and whole blood †. *Cite this Photochem. Photobiol. Sci* **17**, 1189 (2018).

481. Uchoa, A. F., Severino, D. & Baptista, M. S. Antioxidant properties of singlet oxygen suppressors. in *Natural antioxidants and biocides from wild medicinal plants* 65–91 (CABI, 2013). doi:10.1079/9781780642338.0065

482. Engel, E. *et al.* Light-Induced Decomposition of Indocyanine Green. *Invest. Ophthalmol. Vis. Sci.* **49**, 1777–1783 (2008).

483. Fayet-Bonnel, M. Influence of the Size of the Precipitates in NaCl:Pb2+ Crystals on Rayleigh Scattering and UV Absorption. *Phys. status solidi* **60**, 713–719 (1973).